



HAL
open science

Interaction between armenian-clay-based ceramics and model wines

Syuzanna Esoyan

► **To cite this version:**

Syuzanna Esoyan. Interaction between armenian-clay-based ceramics and model wines. Agronomy. Université Bourgogne Franche-Comté; Université d'État d'Erevan (Erevan, Arménie), 2022. English. NNT : 2022UBFCK102 . tel-04031632

HAL Id: tel-04031632

<https://theses.hal.science/tel-04031632v1>

Submitted on 16 Mar 2023

HAL is a multi-disciplinary open access archive for the deposit and dissemination of scientific research documents, whether they are published or not. The documents may come from teaching and research institutions in France or abroad, or from public or private research centers.

L'archive ouverte pluridisciplinaire **HAL**, est destinée au dépôt et à la diffusion de documents scientifiques de niveau recherche, publiés ou non, émanant des établissements d'enseignement et de recherche français ou étrangers, des laboratoires publics ou privés.



**THESE DE DOCTORAT DE L'ETABLISSEMENT UNIVERSITE BOURGOGNE
FRANCHE-COMTE
PREPARED at Institute Agro Dijon**

Doctoral school n°554
Doctoral school – Environments and Health

Doctor of Agri-Food Biotechnology

By

ESOYAN Syuzanna

The interaction between Armenian clay-based ceramic and model wine

Thesis presented and defended in Dijon, December 12, 2022

Composition of the Jury:

Mr. GOUGEON Regis	Professor, University of Burgundy, IUVV	President
Ms. JABER Maguy	Professor, Sorbonne University, Faculty of Science	Rapporteur
Mr. JEANDET Philippe	Professor, University of Reims Champagne-Ardenne, Faculty of Science	Rapporteur
Ms. MARMARYAN Gayane	Associate Professor, Armenian National Agrarian University	Examiner
Mr. GHAZARYAN Karen	Associate Professor, Yerevan State University, Faculty of Biology	Examiner
Ms. HOVHANNISYAN Nelli	Associate Professor, Yerevan State University, Faculty of Biology	Co-Director
Ms. LOUPIAC Camille	Associate Professor, Institute Agro Dijon	Co-Director
Mr. BODART Philippe	Associate Professor, University of Burgundy, Institute Agro Dijon	Director

Acknowledgments

I would like to express my deepest gratitude to my supervisors, Dr. Philippe Bodart, Dr. Camille Loupiac, and Dr. Nelli Hovhannisyan for their invaluable support, advice, and motivation during my study.

I also wish to acknowledge all those who supported us doing the research to be performed. This includes Mr. Zorik GHARIBYAN founding director of the Winery of ZORAH WINES for providing the clay samples, Dr. Jean-Marc DACHICOURT of the University of Burgundy the department of ESIREM for performing the XRF analysis, Dr. Marie-Laure LEONARD of the University of Burgundy of the department of ESIREM for performing the TGA analysis, Prof. Claude FONTAINE and Prof. Sabine VALANGE from the University of Poitiers for performing the XRD analysis, Dr. Aline BONNOTTE and Dr. Laure AVOSCAN of the University of Burgundy of the Research center of INRAE for performing the analysis of SEM/EDX, Prof. Bernhard Michalke and Prof. Philippe Schmitt-Kopplin of the Helmholtz Zentrum München for performing ICP-AES analysis, Prof. Jean-Pierre Bellat and Dr. Igor Bezverkhyy for He-pycnometry and BET measurements respectively of the University of Burgundy of the Research laboratory of Interdisciplinaire Carnot de Bourgogne, UMR 6303 CNRS.

This work is part of the project VALVIGNE (2020-2022, SYNERGIE BG0027582) supported by the conseil régional Bourgogne Franche Comté and the European Union through the PO FEDER - FSE Bourgogne 2014-2020 program.

I would also like to convey thanks to Ms. Bernadette ROLLIN and Ms. Anne-Sophie VIAUX for their continues support in the laboratory.

Special thanks go to Prof. Régis Gougeon and As. Prof. Ali Assifaoui for their advice.

I would also like to thank my UMR PAM (Institute Agro Dijon) Lab family for the friendship.

The moral support of all my Armenian friends in Dijon is also gratefully acknowledged.

Finally, I wish to express my love and gratitude to my beloved family for their love and care.

Abstract

The use of ceramics for the transformation or conservation of wine has existed since the origins of wine, but the impact of ceramics on wine has not received much attention.

However, in contact with the wine, ceramics are generally not neutral materials, and the constituent minerals of ceramics are led to dissolve. This work mainly aims to study the migration of elements from ceramics to wine.

To our knowledge, this question has so not been addressed so far, at least with our chosen approach.

This study required the prior characterization of the materials and the ceramics produced in the laboratory.

The analyzes (XRF, XRD and SEM/EDX) revealed that the natural material used for the manufacture of ceramics contains a large amount of silicon oxide (~ 60%) and calcium oxide (15-21%). The clay is composed mainly of smectite, kaolinite, mixed-layer clay and illite. After firing, the ceramic is mainly composed of diopside, hematite, gehlenite and minerals from the plagioclase family. The interaction of the ceramic with a model wine has been studied: the natural acidity of the model wine favors the dissolution of the ceramic, and in response, the pH of the model wine increases and the migration of all types of elements present in the ceramic occurs rapidly. The ICP-AES made it possible to follow the migration of 26 elements over 16 months. NMR (Time Domain) is used to guide the approach to questions regarding the impact of headspace volume and oxygen concentration on iron and ethanol redox processes in wine concomitant with the dissolution of the ceramic.

The coating of ceramic tablets (for example with beeswax) can greatly reduce and limit the dissolution of the ceramic. Most of the results presented are original and address certain aspects of the interactions between ceramics and wine.

Résumé

L'utilisation de céramiques (terres cuites) pour la transformation ou la conservation du vin existe depuis les origines du vin, mais l'impact de la céramique sur le vin n'a pas reçu beaucoup d'attention. Pourtant, au contact du vin, les céramiques ne sont généralement pas des matériaux neutres, les minéraux constitutifs des céramiques sont amenés à se dissoudre. Ce travail vise principalement à étudier la migration des éléments de la céramique vers le vin.

A notre connaissance, cette question n'a pas été abordée jusqu'à présent, du moins avec l'approche que nous avons choisie.

Cette étude a nécessité la caractérisation préalable des matériaux et de la céramique produite en laboratoire.

Les analyses (XRF, XRD et SEM/EDX) ont révélé que le matériau naturel utilisé pour la fabrication de la céramique contient une grande quantité d'oxyde de silicium (~60%) et d'oxyde de calcium (15-21%). L'argile est composée principalement de smectite, de kaolinite, d'argile à couches mixtes et d'illite. Après cuisson la céramique est composée principalement de diopside, hématite, gehlénite et de minéraux de la famille des plagioclases. L'interaction de la céramique avec un vin modèle a été étudiée : l'acidité naturelle du vin favorise la dissolution de la céramique, en réponse le pH du vin augmente et la migration de tous les types d'éléments présents dans la céramique se produit rapidement. L'ICP-AES a permis de suivre la migration de 26 éléments sur 16 mois. La RMN (Time Domain) est utilisée pour orienter l'approche vers des questions concernant l'impact du volume de l'espace de tête et de la concentration en dioxygène sur les processus d'oxydoréduction du fer et de l'éthanol dans le vin concomitant à la dissolution de la céramique.

L'enrobage des tablettes céramiques (par exemple par la cire d'abeille) peut fortement diminuer et limiter la dissolution de la céramique. La plupart des résultats présentés sont originaux et adressent certains aspects des interactions entre céramiques et vin.

Table of content

Acknowledgments	iii
Abstract	v
Table of content	vii
List of Figures	x
List of Tables	xvi
Foreword	18
Chapter 1. Introduction	21
1.1. Clays, clay-minerals, Armenian clay deposits, and Clay-based ceramics.....	21
1.1.1. Structure and classification of clay minerals.....	22
1.1.2. Armenian Clay Deposits.....	24
1.1.2.1. Armenian clay deposits genesis	24
1.1.2.2. Shahumyan Clay deposit	26
1.1.3. Clay-based ceramics	27
1.2. Contextualization of ceramics in the wine industry.....	27
Chapter 2. Materials and Methods	31
2.1. Materials.....	31
2.1.1. Sampling of clay powder and clay paste.....	31
2.1.2. Kaolinite	31
2.1.3. Model wine	31
2.1.4. Preparation of clay-based ceramics	31
2.1.4.1. Shaping of the tablets	32
2.1.4.2. Drying.....	33
2.1.4.3. Thermal treatment of the tablets	33
2.1.5. Shrinkage of the tablets.....	36
2.1.6. Sample geometry (surface of tablet, volume of wine).....	37
2.1.6.1. Volume to surface ratio in real containers	37
2.1.6.2. Geometries of fired ceramic samples in contact with model wine.....	39
2.1.6.3. Geometrical constraints on the volume to surface ratio for the relaxometric measurements (small tablets)	40
2.2. Methods.....	42
2.2.1. Thermal Gravimetric Analysis (TGA).....	42
2.2.2. X-ray fluorometry (XRF).....	43

2.2.3. X-ray powder diffraction (XRD).....	43
2.2.4. Gas Pycnometry.....	44
2.2.5. The nitrogen adsorption/desorption isotherm.....	45
2.2.6. Scanning electron microscopy (SEM)	45
2.2.7. Inductively coupled plasma atomic emission spectrometry (ICP-AES).....	46
2.2.8. Oxygen measurement.....	47
2.2.9. Time domain nuclear magnetic resonance (TD NMR) relaxometry	48
2.2.10. pH-measurements.....	48
Chapter 3. Characterization of clay and ceramic	49
3.1. Thermal gravimetric analysis of row clay powders from Shahumyan deposit	49
3.1.1. Literature review	49
3.1.2. TGA results	49
3.1.3. Conclusion	50
3.2. WD-XRF (Wavelength Dispersive X-ray fluorescence) analysis of Armenian clay chemical composition	51
3.2.1. Literature review	51
3.2.2. XRF results	52
3.2.3. Conclusion	53
3.3. XRD (X-ray diffraction) analysis of Armenian clay minerals in row clay powder and in ceramics.....	53
3.3.1. Literature review	53
3.3.2. Results	55
3.3.3. Total mineralogy of raw (from Shahumyan deposit) and purified clay	56
3.3.3.1. Raw clay	56
3.3.3.2. Purified clay	57
3.3.4. Clay fraction mineralogy of raw Shahumyan sample	57
3.3.5. Mineralogy of ceramic tablet fired at peak temperature 930°C (FP930).....	60
3.3.6. Conclusion	62
3.4. Determination of porosity of clay-based ceramic by He-pycnometry	62
3.4.1. Results	63
3.4.2. Discussion.....	63
3.5. BET (Brunner-Emmett-Teller) characterization of ceramic tablets.....	64
3.5.1. Results	64
3.5.2. Conclusion	64

3.6. Characterization and chemical analysis of ceramic by scanning electron microscopy (SEM)	65
3.6.1. Results	65
3.6.1.1. SEM analyses of raw clay powder from Shahumyan's deposit	65
3.6.1.2. SEM analyses of ceramic	67
3.6.1.3. SEM/EDX elemental analysis of ceramic.....	67
3.6.2. Discussion.....	69
3.6.2.1. Image analysis of ceramic tablets.....	69
3.6.2.2. Qualitative analyses	70
3.6.3. Conclusion	71
Chapter 4. Ion migrations from ceramic to wine	72
4.1. Ion migrations from ceramic to model wine followed by ICP-AES.....	72
4.1.1. Sample preparation.....	72
4.1.2. Results	73
4.1.3. Discussion.....	77
4.1.3.1. Evolution of calcium concentration	78
4.1.3.2. Evolution of iron and magnesium concentration	85
4.1.4. Conclusion	86
4.2. Ion migration from ceramic to wine followed by time domain nuclear magnetic resonance.....	88
4.2.1. Sample preparation.....	88
4.2.2. The benefit of proton time domain nuclear magnetic resonance (TD NMR).....	89
4.2.3. Representation of relaxograms	93
4.2.4. Relaxation rate of solutions in contact with a ceramic	95
4.2.5. Relaxogram of model wine in contact with a ceramic, small headspace in sealed environment	97
4.2.6. Relaxograms of model wine in contact with a ceramic, large headspace	102
4.2.7. Relaxogram of model wine in contact with a ceramic, large headspace, second contact.....	107
4.2.8. Evolution of the relaxation rate of model wine in contact with a ceramic in a low dioxygen environment.....	110
4.2.9. Evolution of the relaxation rate of model wine in contact with a coated ceramic	112
4.2.10. Evolution of pH during a contact period	114

4.3. Comparison of TD NMR with ICP-AES.....	116
4.4. Conclusion.....	118
Final conclusion.....	119
Perspectives.....	121
Lexicon.....	122
References.....	124
Annex I. Mathematical code for calculating the ratio ρ for an axial symmetrical container.....	136
Annex II. XRF spectroscopy.....	138
Annex III. Scanning electron microscopy (SEM).....	142
Annex IV. X-ray diffraction.....	148
Annex V. Shrinking measurement on Shahumyan ceramics and Kaolin-based ceramics.....	151
Annex VI. ICP-AES.....	159
Annex VII. TD NMR relaxometry.....	167
Annex VIII. Pourbaix diagrams (Fe, Ca, Mn).....	179
Annex IX. Publications.....	181

List of Figures

Figure 1. (a) Four octahedrons sketching the octahedral sheet in gibbsite. (b) Tetrahedral sheet composed of six tetrahedrons (adapted from [11]).....	22
Figure 2. Classification of clay minerals (adapted from [18]).....	23
Figure 3. Geological location of Armenian Highland [22].....	24
Figure 4. Geological map of the Republic of Armenia and its geologic time scale (left, adapted from [26]). Position (📍) of Shahumyan clay deposit (left bottom) and geotectonic zonation scheme (right) of the Republic of Armenia (adapted from [24]).....	25
Figure 5. Illustrating Armenian pithoi (karases) buried in the sand. The volume of one pithos can reach 1000 L [37].....	28
Figure 6. The tablet and their average dimensions before (a) and after (b) heat treatment.....	32
Figure 7. The heating of the tablets by two firing programs.....	34
Figure 8. Shrinkage and weight loss between the dried and fired stages on (big and small) Armenian and kaolin tablets. Number in brackets correspond to the tablet population, FP correspond to the firing protocol (800 or 930 °C), the number preceded by a # is the batch number. Error bars correspond to standard deviations (see Annex V for further detail).....	37
Figure 9. Volume versus weight of three batches of big and small tablets FP930.....	37

Figure 10. Original drawing used to calculate the equation of the revolution curve; units are dm (right). Reconstruction of the pithos to calculate its volume and surface (left).	38
Figure 11. Dimensions of a cylinder immersed in 600 μ L of wine that would satisfy a ρ ratio of 1.8 m.	41
Figure 12. Thermogram of Shahumyan clay recorded under air flow at 15°C/min TG (blue), DTG (green) curves, as well as the cumulated weight loss (%) are reported with indication on the structural clay mineral modification as a function of temperature.....	50
Figure 13. Representative histogram of Table 7.....	53
Figure 14. Diffractogram of Armenian clay powder from Shahumyan/Yuva deposit as received. Minerals: (C) Chlorite, (Ca) Calcite, (Do) Dolomite (?), (Gy) Gypsum, (I) Illite, (K) Kaolinite, (P) Plagioclase (Albite-type), (Q) Quartz, (Sm) Smectite.	56
Figure 15. Diffractogram of Armenian purified clay powder (Shahumyan/Yuva deposit). Minerals: (C) Chlorite, (I) Illite, (K) Kaolinite, (P) Plagioclase (Albite-type), (Q) Quartz.	57
Figure 16. Diffractograms of oriented preparation of purified Armenian clay from Shahumyan. Air-dried (AD), ethylene-glycol (EG) saturated and thermal treatments at 350°C and 550°C. Minerals: (C) Chlorite, (I) Illite, (K) Kaolinite, (ML) Mixed-layer (C/S type), (P) Plagioclase, (Q) Quartz, (Sm) Dioctahedral smectite, (X) Non identified (zeolite or amphibole probably).	59
Figure 17. Diffractogram of the ceramic (FP930). Minerals: (Di) Diopside, (Gh) Gehlenite, (P) Plagioclase, (Q) Quartz, (He) Hematite	60
Figure 18. Porosity of big (big triangle) and small (small triangle) ceramic tablets fired at 800 °C (open triangle) or 930° C (filled triangles).	63
Figure 19. Microstructure of raw clay powder from Sh1 sample (Shahumyan deposit)	65
Figure 20. SEM images of clay powder from Shahumyan deposit (Armenia). Diatomite (Bacillariophyta) (a) (~ 5 μ m in diameter, and ~ 15 μ m in length) Coccolithophore - Coccolithus pelagicus (b) remains (~ 8 μ m in diameter). ..	66
Figure 21. The change of the microstructure of tablet before (a) and after (b) firing at 930°C.	67
Figure 22. SEM image of ceramic tablet fired at 930°C showing the melting process.....	69
Figure 23. SEM images of ceramic tablet fired at 930°C. The surface of the tablet (a) and interior part (b).	69
Figure 24. Elemental average concentration in ceramic, measured with 26 points from seven areas. Blue columns represent elements identified only by SEM/EDX. Green columns represent elements identified by both ICP-AES and SEM/EDX methods.	70
Figure 25. Elemental analysis of model wine alone (without contact with ceramic). Open columns correspond to elements below the limit of quantification (e.g. [Cu] < 11.7 μ g/L).	74

- Figure 26. Concentrations of elements released from 1 g of ceramic tablet during aging from 1h (1 hour) up to 16m (16 months), d stands for days. Model wine elements concentration is subtracted.75
- Figure 27. The concentration of elements released from 1 g of ceramic after 11 hours of contact with the model wine. Wine elements are subtracted. Elements with zero values were present in the model wine but their concentration did not increase after the contact with the ceramic. Open columns correspond to elements below the limit of quantification (e.g. [Hg] < 28.4 µg/L).77
- Figure 28. Blue: the evolution of calcium concentration in the model wine measured by ICP-AES (in mM) versus the contact time between the model wine and the ceramic (model wine subtracted). Red: evolution of pH. Because of few model wine was available the measurements were done by pouring a few drops of model wine onto some pH-paper, it is subject to significant uncertainties estimated as ± 0.5 and reported by error bars. The dotted line corresponds to the pH of the starting model wine (2.35).78
- Figure 29. The mass of elements (µg) released from one tablet, measured in 2.8 ml of model wine by ICP-AES (full circles). Simulated dissolution from literature data of an equivalent tablet (same surface area, average mass of 679 mg) are reported with dotted lines. The upper horizontal dashed black line figures the level corresponding to a mass of 679 mg.81
- Figure 30. Refinement of the dissolution of calcium during the first 12 hours contacts with an Avrami law: $Ct = Cmax 1 - e - k tn$83
- Figure 31. Evolution of calcium concentration (in linear scale) (a) from 12 to 350 hours and (b) from 300 to 15300 hours released from 1g of ceramic tablet. Potassium, magnesium, and iron concentrations are reported for comparison.85
- Figure 32. Metallic element concentration (µg/L) per mg of ceramic immersed in 2.8 mL of model wine in sealed glass 10-mm NMR tubes, measured during aging by ICP-AES. For each element, from left to right, one bar chronologically corresponds to a contact time (1 hour to 16 months).90
- Figure 33. Ratios (in percent) of paramagnetic ions concentration with respect to the Fe concentration (extracted for ICP-AES data) versus aging time, with ponderations relative to their relaxivity (Table 15). Model wine elements concentrations are subtracted. It is assumed that all elements are in the reported oxidation states. The horizontal dotted black line represents the calculated quantity for iron (100 %).91
- Figure 34. Titration of O₂ concentration in ultrapure water (blue) and 12 % (alcohol by volume - ABV) hydroalcoholic solution (red), at 25 °C. Abscise of open symbol has been calculated from [137], the open symbol is only reported and not used in the linear regression.92
- Figure 35. Typical proton relaxogram of a model wine in contact with a ceramic. The ceramic is dropped in the wine at ~ 2 hours and initiate the increase of the relaxation rate.93
- Figure 36. Titration of ferric ions concentration in a model wine. This curve has been obtained by individual synthesise, (no dilution of a stock solution was used).

Number in brackets are the incertitude given by the linear regression on the previous digit.....	94
Figure 37. First hours of Fe^{3+} titration diagram of a model wine in contact with a ceramic.	95
Figure 38. Relaxation rate of water (green ●), hydroalcoholic solution (blue ◆) (12% ABV), and tartaric acid solution (purple ▲) before (up to 2 hours) and after contact (after 2 hours) with ceramic.....	96
Figure 39. Experimental design of the flame sealed environment.....	97
Figure 40. Three repetitions of the evolution of the relaxation rate of model wine solutions in contact with a ceramic. Samples are in a sealed 7mm-NMR tube with a limited headspace. W_{tablet} is the weight of the ceramic tablet, V_{wine} is the volume of model wine added, $V_{\text{air}}/V_{\text{wine}}$ is an estimation of the ratio of the headspace over the volume of wine. ρS is the volume of the model wine to surface of the ceramic tablet. pH of the model wine is given at initial time....	99
Figure 41. ρS (black) and ρW (orange) ratios versus the delay to reach the steady state. The point at 40 hours is obtained from Figure 71 of Annex VII.	101
Figure 42. Evolution of the relaxation rate of model wine in contact with a ceramic. Samples are placed in 10mm-NMR tube with a large headspace. (a) in a closed tube (b) in an open tube (infinite headspace). Reported values on the right have the same meaning as in Figure 40.....	103
Figure 43. ρS (black) and ρW (orange) ratios versus the delay to reach the relaxation rate of pure model wine, open symbols correspond to experiment with a large headspace.....	105
Figure 44. Relaxogram of a solution of tartaric acid (5g/L) in ultra-pure water.	106
Figure 45. ρS (black) and ρW (orange) ratios versus the delay to reach the relaxation rate of pure model wine. The open symbols correspond to 5g/L of tartaric acid in ultra-pure water.	106
Figure 46. Relaxogram of model wine during first and second contact of ceramic with fresh model wine. The ceramic was washed between the two contacts. (a) second contact, (b) superposition of relaxogram recorded during the first contact (red from Figure 42 a) and relaxogram of the second contact(blue). (c) (●) raw tablet in contact with ultrapure water (extension from Figure 38), (●) washed tablet (after the first contact of experiment (a) in Figure 42) in contact with ultrapure water. Arrows mark the insertion of the ceramic in the water.	108
Figure 47. ρS (black) and ρW (orange) ratios versus the delay to reach the relaxation rate of pure model wine the open symbols correspond to 5g/L of tartaric acid in ultra-pure water.	109
Figure 48. Relaxogram of a model wine in contact with a ceramic in an environment containing 1/3 of atmospheric dioxygen concentration. $[O_2]_{\text{wineint}}$ is the initial dioxygen concentration in the model wine. Model wine pH=2.31 (at t=0)	111
Figure 49. ρS (black) and ρW (orange) ratios versus the delay to reach the relaxation rate of pure model, big and small symbols correspond to the large and small	

headspace experiments respectively. Open symbols are N ₂ degassed experiments.....	112
Figure 50. Relaxograms of model wine solution containing (a) a ceramic tablet coated with one (a, ●) and two (a & b, ●) layers of natural beeswax, or beeswax alone (b, ▲)	113
Figure 51. Model wine aged with ceramic coated beeswax. a) 3 months aged, b) 1 year aged.	114
Figure 52. Relaxogram of model wine in contact with ceramic tablet (●) and pH of the solution (●). White star indicates the observation of white precipitation, the vertical yellow arrow, apparition of a yellowish color of one out of three repetitions, the yellow star observation of yellowish crystals in one of three repetitions.....	115
Figure 53. (a) Comparison of the equivalent ferric ion concentration calculated from a relaxogram (blue) and the ICP measurement (green) on the left numbers refer to the statistics performed on all the ceramic tablets used for the ICP experiment. The relaxogram correspond to the one displayed in Figure 42.b. Diagram in (b) additionally reports (continuous red line) the theoretical labile iron resulting of the dissolution of hematite (estimated as 5% of the mass of the ceramic) . (c) is an expansion of (b).	117
Figure 54. Original drawing from [1], fig 139, p 102 (Figure 10) and the revolution curve (red dots) with its digitalization reported in the two columns on the left.	136
Figure 55. XRF spectrum of elements [148]	140
Figure 56. Emission of X-rays [150]	141
Figure 57. Plant remains in clay powder from Armenian clay deposit Shahumyan.	142
Figure 58. Illustration of the Bragg Law	148
Figure 59. XRD Diffractogram of a clay	149
Figure 60. Typical weight loss of two big tablets as function of the time.....	151
Figure 61. Schematic representation of a typical Bigot's curve [154].....	152
Figure 62. Total shrinkage and weight loss on big and small Armenian and kaolin tablets. Number in brackets correspond to the tablet population, FP correspond to the firing protocol (800 or 930 °C), the number preceded by a # is the batch number. Error bars correspond to standard deviation.	153
Figure 63. Shrinkage and weight lost on big and small Armenian and kaolin tablets between drying and firing stages. Symbolism is as described in Figure 62.	154
Figure 64. Weight in function of volume of tablets for various batches. FP correspond to the firing protocol (800 or 930 °C), the number preceded by a # is the batch number	155
Figure 65. Schematic representation of a water molecule with the internuclear vector r and the energy levels of the coupled system that depend on the angle β between r and the direction of the static magnetic field B_0	167
Figure 66. The two types of dynamics modulating the dipolar interactions.....	168
Figure 67. Simulation of the isotropic rotational diffusion relaxation rate for water molecules ($\tau r = 2.6 \cdot 10^{-12}$ s) versus the proton Larmor frequency of the magnetic field.....	169

- Figure 68. Simulation of the isotropic translational diffusion relaxation rate for water molecules ($\tau t = 9 * 2.6 10^{-12} s$) versus the proton Larmor frequency of the magnetic field..... 170
- Figure 69. Simulation of the relaxation profile of water with translational and rotational contribution..... 171
- Figure 70. Simulation of the proton profile of a model wine solution containing 1.28 mg of Mn^{2+} (black). In red model wine contribution rotation and translation, green dipolar contribution (with its two dispersions) blue contact interaction..... 173
- Figure 71. Relaxogram of a flame sealed sample, the ceramic has been washed with HPLC water and Na exchanged before contact with the model wine..... 175
- Figure 72. (a) Relaxogram of a model wine with a weak ethanol concentration (estimated around 1 % ABV) in a low oxygen content (initial dioxygen content in the headspace 14 $\mu g/L$). (b) Evolution with time of the dioxygen content in the headspace..... 177
- Figure 73. Evolution of relaxation time of hydroalcoholic solution with ABV, from..... 178

List of Tables

Table 1. Composition of model wine	31
Table 2. Firing stages of the clay [40], [43], [44], [45]	35
Table 3. Estimation of ρ and equivalent surface area/vol ratios for three containers, calculation were performed according to geometrical formulae for volume and surface calculation (barrel and bottle) [46], [47] or by integration of a revolution curve (pithos) [2].....	39
Table 4. Example of different experiments with tablet diameters and heights, model wine volumes, and associated ρ ratios.....	42
Table 5. Lines used for determination of elements with ICP-AES.....	47
Table 6. Chemical composition of Armenian clay powder from Shahumyan reported from 1960-2001.	51
Table 7. Chemical components of two clay powders from Shahumyan (Sh1 & Sh2) and a clay body obtained by XRF.	52
Table 8. Comparative table of the proposed mineral compositions (%) of Shahumyan clay deposit (m.c.: main constituent, s.q.: small quantity, a.: all together. dominant minerals are in red. Mmt, ML, carb. stand for Montmorillonite, Mixed layer, and carbonate respectively.	55
Table 9. Mineralogical composition of clay fraction of the raw Shahumyan sample	59
Table 10. Minerals identified in Shahumyan row and purified clay materials and ceramic products (minerals for chlorite and smectite groups are reported as possible minerals in clay), Mmt stands for Montmorillonite.	61
Table 11. Mean of the SEM/EDX analysis of ceramic fired at 930°C. The observations have been performed at the point levels on a scale of 10 μm . The number of points analyzed is 26. The results are expressed in atom and weight (%).	68
Table 12. Evolution of concentration (mg/L) of elements released from 1 g of ceramic to the model wine (wine elements are subtracted). Diagrams for elements with concentration lower then 1 mg/L are not reported. The time sampling is as follow: {1h, 2h, 3h, 4h, 5h, 6h, 7h, 8h, 9h, 10h, 11h, 2d, 4d, 8d, 15d, 2m, 4m, 8m, 16m, (where h, d, m stand for hour, day month)}, but for the sake of visibility only one contact time over two is reported in the label of abscise axis. Red diagrams correspond to paramagnetic elements.....	76
Table 13. Dissolution constant (K_d) of some minerals identified in the ceramic. The reported values are generally obtained by a flow experiment. Quartz is given for comparison. l stands for low (not measured) dissolutions constants in bold were used for the calculations of Figure 29.	80
Table 14. Comparison of materials and some results obtained on ceramsites by Qin et al [119] and those of this work on ceramic.	82
Table 15. Relaxivity (r) of aquaions at 20 MHz, 25°C. Grey cells report non-majoritarian forms. It is worth noting that at a lower magnetic field (1 MHz or lower) or different temperature the relaxivity may strongly vary particularly for Mn^{2+} and V^{4+}	90

Table 16. Amount (mmol) of ethanol and dioxygen (estimation) present in the 10 mm tube during the large-headspace-closed experiment (Figure 42(a)).....	104
Table 17. Mechanical composition of the clay.....	141
Table 18. SEM/EDX semiquantitative analysis of ceramic fired at 930°C measured for seven different areas at 26 points (pt1, pt2 ...). The results are presented in atomic %. Numbers in brackets [(1), (2),...] represent areas.	143
Table 19. Elemental mapping of ceramic fired at 930°C. Magnification: 800x.....	144
Table 20. Elemental mapping of ceramic fired at 930°C. Magnification: 400x.....	146
Table 21. Tablets dimensions (in mg, mm; mm ² and mm ³ for the weight, length, surface, and volume respectively) and shrinkage between the dried and fired stages of the firing protocols.....	155
Table 22. Tablets dimensions (in mg, mm; mm ² and mm ³ for the weight, length, surface and volume respectively) and shrinkage between the shaped and fired stages of the firing protocols.....	157
Table 23. Concentrations (mg/L) of elements released from ceramic to model wine determined by ICP-AES. Samples are aged from 1 hour (1h) up to 16 months (16m), h, d, m stand for hour, day month respectively. Sample 0 corresponds to model wine alone (without contact with the ceramic). The ratio ρ corresponds to the ratio of the volume of model wine (V_w) to the surface of the tablet (S_t). The colormap highlights the concentration of elements from lowest value (red) to the highest value (green).	159
Table 24. The concentration (mg/L) of each element released from 1 g of ceramic to the model wine after contact with the ceramic (wine element subtracted). Open columns correspond to elements below the limit of quantification (e.g. [Hg]). Red diagrams indicate paramagnetic elements. The time sampling is as follow: {1h, 2h, 3h, 4h, 5h, 6h, 7h, 8h, 9h, 10h, 11h, 2d, 4d, 8d, 15d, 2m, 4m, 8m, 16m, (where h, d, m stand for hour, day month)}, but for the sake of visibility only one contact time over two is reported in the label of abscise axis.	161
Table 25. The concentration (mg/L) of elements released from 1 g of ceramic to the model wine (wine elements subtracted), sample by sample. Open columns correspond to elements below the limit of quantification (e.g. [Hg]). Red columns correspond to paramagnetic elements. Elements are ordered as follow: {Al, B, Ba, Be, Ca, Cd, Co, Cr, Cu, Fe, Hg, K, Li, Mg, Mn, Mo, Na, Ni, P, Pb, S, Sr, Ti, V, W, Zn} but for the sake of visibility only one over two is reported in the label of abscise axis.....	164

Foreword

It is difficult to mention exactly when the first ceramic vessels appeared and widespread. The fact is that their use has a history of tens of millennium. These vessels were most likely used to store and transport water, various types of liquids, grain and other foods, and later wine [1]. Since these ancient times, the technology and applications of ceramics are steadily increasing.

Archaeological excavations in Armenian Highlands discovered numerous finds that proved winemaking (winepresses, wine cellars, vessels for practical and ritual uses found in Adablur, Karmir Blur, Areni, and other sites), which describe the primary phases and patterns of development of cultivation and production. The winemaking complexes came to prove that Armenian Highlands was a powerful center of winemaking which later contributed that Armenian people played a great role in spreading viticulture and winemaking in the world. Among the mentioned finds, especially important were hundreds of grape sprouts, barks, fruit stems, seeds, pressed fruits and pulp remains found in Areni-1 cave in Vayots Dzor Province of Armenia, together with the oldest known wine producing facility, which is at least 6.000 years old [2].

The existence of this winery speaks about the fact that in ancient times in Armenia, like in different countries of the world, such as Greece, Italy, France, etc., ceramic containers were used to make wine. This ancient method of making wine remains traditional in Armenia and is still relevant today. Nowadays there is an increasing interest of the recourse of ceramic for wine production [3].

However, ceramic jars are not the only way for wine to ferment and age. Over time, containers made of wood (mainly oak), glass, stainless steel, and concrete came into use, each with their own advantages and disadvantages and the character of the interaction between the wine and the container where it is fermented and/or aged will differ.

Concrete tanks combine the porosity characteristic of wood barrels and ceramic vessels. When coated (e.g., with epoxy paint for decreasing porosity and avoid undesired chemical reactions), concrete tanks are more flavor-neutral than oak barrels. There are

winemakers who think that concrete gives the wine an earthy taste, but opinions about flavor neutrality are not consensual.

Physically, concrete tanks are thermally stable: as opposed to stainless steel, concrete has slower heat exchange, due to a lower thermal conductivity ($0.5 \text{ Wm}^{-1}\text{K}^{-1}$; $20.5 \text{ Wm}^{-1}\text{K}^{-1}$ for concrete and stainless steel respectively) and the thickness of its walls. The disadvantage of concrete tanks can be their big size, which makes them difficult to be moved from one place to another [4].

Stainless steel tanks are more manageable and help monitor the fermentation process. As a neutral, nonporous material, steel tanks are chemically stable, which allows for preserving the flavor and aroma properties of wine, thereby producing more stable and homogenous wine. Their major disadvantages are high thermal conductivity and sensitivity to temperature fluctuations [5].

Unlike concrete, ceramic, and wood barrels, in which chemical exchange or reaction with the container can be significant (further amplified by the inherent porosity) vinification in glass vessels is more like to stainless steel. They keep the natural flavor of the wine like steel tanks. The disadvantages of glass vessels are their fragility and small volume. This method of winemaking is mainly used to make wine at home in small volumes.

If ceramics, concrete, glass and stainless steel are considered to be neutral flavor, **wood barrels** stand out for their influence on the taste of wine. During interaction with the wood, due to the chemical reactions that take place, the wine is enriched with the phenolic, aromatic compounds of the wood thereby influencing the organoleptic profile of the wine and increasing antioxidant stability (oak barrels) [6], [7]. Ellagitannins impact the intensity of astringency and bitterness [8] and wine metabolome [6]. Wood barrels play an important role also in the point of view of oxygen exchange during oxidative aging in barrels [9]. Wood barrels have also a low thermal conductivity (for oak $0.17 \text{ Wm}^{-1}\text{K}^{-1}$).

Summarizing the available information on the interactions between the containers and the wine, we can state that in contrast to the influence of wood barrels on the texture and taste of wine, which has been widely studied, the effects of alternative containers is

hardly studied and little is known about their impact on the chemical composition of the resulting wines [5], [10].

The precise aim of this thesis is "the characterization of the interactions between Armenian clay-based ceramic and model wine".

Various aspects have been studied to achieve this goal. They are:

- Identification of the chemical composition of Armenian clay
- Identification of the mineralogical composition of Armenian clay (before heating) and ceramics (after heating)
- Characterization the morphology and the porosity of ceramics
- The impact of clay-based ceramic on the pH of model wine
- Change in the chemical composition of the model wine as a result of the migration of elements from ceramics into the liquid phase.

Considering "The interaction between Armenian clay-based ceramic and model wine" the scientific questions could be reformulated as:

- the impact of model wine on the ceramic,
- the response of the ceramic to the attack of the model wine,
- the resulting evolution of the model wine.

Chapter 1. Introduction

1.1. Clays, clay-minerals, Armenian clay deposits, and Clay-based ceramics

Clay is a mineral mixture that is the result of the *weathering* of the earth's crust over vast spans of time. The clay is mainly formed from the content of *feldspar* [11] present in igneous rocks (primarily granite) hydrolyzed during weathering. Those clay deposits which are at or near the site of the parent material (granite) are called residual or primary clays. These so-called residual clays are grainy and lack the smoothness necessary for applicability. These clays are said to be rough because they do not shape easily. Those clays which have been transported by water, wind, and ice and deposited in locations distant from the source material (*erosion*) are called sedimentary or secondary clays. Compared to residual clays, sedimentary clays are characterized with higher plasticity, the particles are smaller, more uniform, and more mixed with other materials, this is the clay used by potters [12]. More precisely, Murray [13] stipulated that the term clay has no genetic significance because it is used for residual weathering products, hydrothermally altered products, and sedimentary deposits and referred to the definition of Grim "as any fine-grained, natural, earthy, argillaceous material" [14]. Clay is a rock term, but it is also used as a particle size term: the size fraction comprised of the smallest particles is called the clay fraction. The Wentworth scale defines the clay grade as finer than 4 μm [15] which is used by many engineers and soil scientists whereas clay scientists generally consider 2 μm as the upper limit of the clay size grade [11].

Due to weathering, the hydrolysis of feldspar is the major source of clay-minerals, which are the main constituents of clays. Grim summarized the clay mineral concept: "clays are composed essentially of a small group of extremely small crystalline particles of one or more members of a group of minerals that are commonly known as the clay minerals" [16]. The clay minerals are primarily constituted of hydrous aluminum silicates SiO_2 (30-70 wt%), Al_2O_3 (10-40 wt%) and H_2O (5-10 wt%). Numerous additional elements may substitute aluminum (Fe, Mg, Si, Ti, Mn, Li), silicon (Al and lesser Fe) or hydroxyl groups (F) [17] or present in the interlayer spaces giving rise to a huge variety of similar minerals with extensive chemical version [12] [14] [16]. The clay mineral groups are *kaolin*

(the primary minerals in kaolin clays), *smectite* (the primary minerals in bentonite clays), *palygorskite-sepiolite*, *illite*, *chlorite*. *Mixed-layered clays variations exist for most of the above groups*. The properties of these clays, which are related to their structure and composition may strongly differ from one clay to another [11].

Clay also contains organic impurities. The type and amount of organic matter present in clay influences its properties. Organic material is found in clays in two forms: in the form of plant particles, leaf scraps, spores, etc., or in the form of organic molecules adsorbed on the surface of particles of clay minerals [15].

1.1.1. Structure and classification of clay minerals

Basic crystalline units of the clay minerals are of two types, tetrahedral or octahedral. Tetrahedral units consist of silicon surrounding by four oxygen atoms and combine to form the silica sheet. Aluminum (or magnesium) octahedron consists of aluminum surrounding by six oxygen atoms and unite to form octahedral sheets like in gibbsite ($\text{Al}(\text{OH})_3$) or brucite ($\text{Mg}(\text{OH})_2$) (Figure 1).

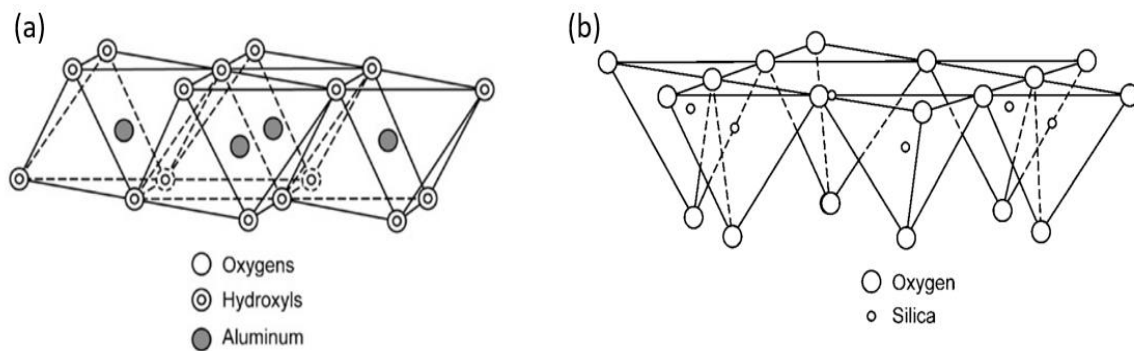


Figure 1. (a) Four octahedrons sketching the octahedral sheet in gibbsite. (b) Tetrahedral sheet composed of six tetrahedrons (adapted from [11])

There are diverse ways to classify clay minerals. One of the approaches used to classify the clay minerals is based on the way the tetrahedral and octahedral sheets are packed into layers. The major groups of clay minerals include layer and chain silicates, sesquioxides, and other inorganic minerals as shown in Figure 2.

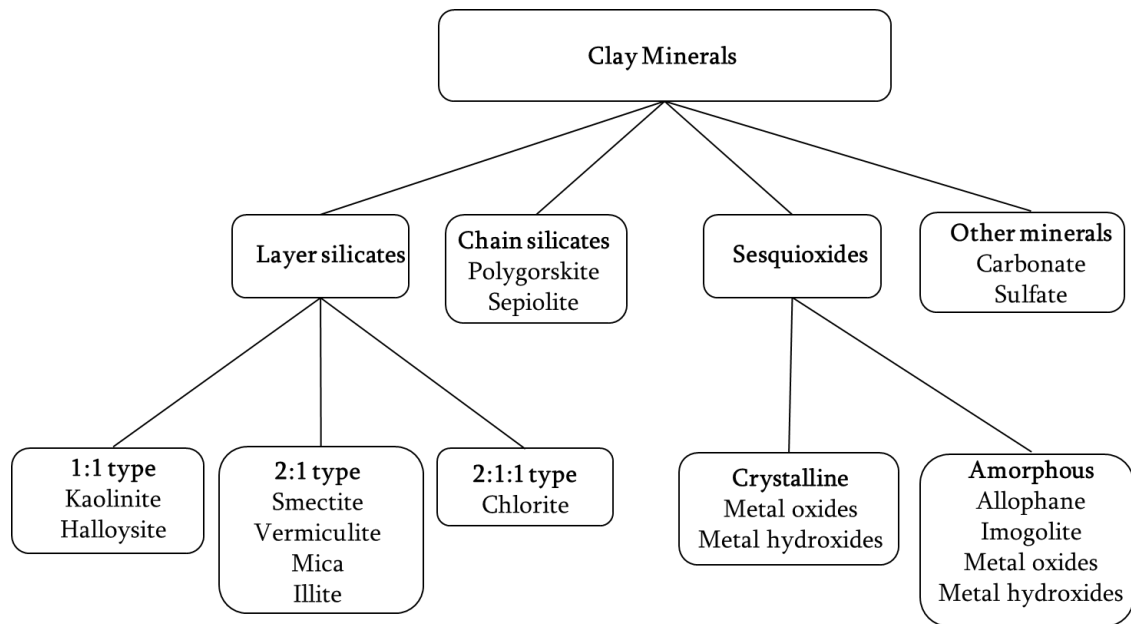


Figure 2. Classification of clay minerals (adapted from [18])

Based on the number and arrangements of tetrahedral and octahedral sheets present in the clay, the layered silicates are divided into three categories:

1:1 type of clay mineral. Each individual layer is assembled from one tetrahedral (SiO_4) and one octahedral (AlO_6) sheet. The sheets are bonded together by sharing of O^{2-} ions. Kaolinite and halloysite are examples under this category [19]

2:1 type of clay mineral. These types of clay minerals consist of one octahedral layer sandwiched between two tetrahedral layers. Smectite group, and vermiculite and illite are typical examples.

2:1:1 type of clay mineral. It is formed of 2:1 layer separated by one octahedral sheet giving rise to 2:1:1 ratio. Chlorite group minerals are the main constituent of the 2:1:1 silicate group which are basically iron magnesium silicates with some aluminum atoms [20]. The typical chlorite clay crystal composed of 2:1 layers, such as in vermiculites clay mineral alternate with a magnesium dominated tri-octahedral sheet (brucite-like) [21].

1.1.2. Armenian Clay Deposits

1.1.2.1. Armenian clay deposits genesis

The current territory of the Republic of Armenia is part of the Armenian Highlands, located between the Anatolian and Iranian plateau and Caucasus and Middle East (Figure 3).



Figure 3. Geological location of Armenian Highland [22]

To Armenia scale, according to the timeline of the formation of the geological structural units, three¹/four² largest structural-formational zones are namely: the Somkheto-Karabakh complex or Somkhet-Kapan undulated tectonic zone, the Armenian folded zone (by K.N. Paffenholz) [25] or Bazum-Zangezur intensively folded suture zone, the Near-Araks zone or Superpositioned orogenic basin zone, and Trans-araksian moderately folded zone (by Ed. Kharazian). Among above mentioned geotectonic zones, the Superpositioned orogenic basin zone [24] is of our interest, since it includes the Shahumyan clay deposit (from which the clay used for this work was taken). According to the scheme of tectonic zoning of the Lesser Caucasus, the Near-Araks tectonic zone, is situated between the rivers of Hrazdan and Vedi (Figure 4).

The accumulations of sediments in the Near-Araks zone, including the Shahumyan clay deposit has long history and can be related to several stages starting from Devonian-

¹ by I. Petrosov [23]

² by Ed. Kharazian [24]

Early Carbone (380-420 million years ago) with terrigenous-carbonate formations and ending Maeotic-Anthropogenic stages expressed by terrestrial volcanogenic formations (from 500 000 years ago). Considering all the stages during which the Shahumyan clay deposit was formed, it can be considered that the deposit results, mainly from sedimentary and partially from volcanogenic formations [23].

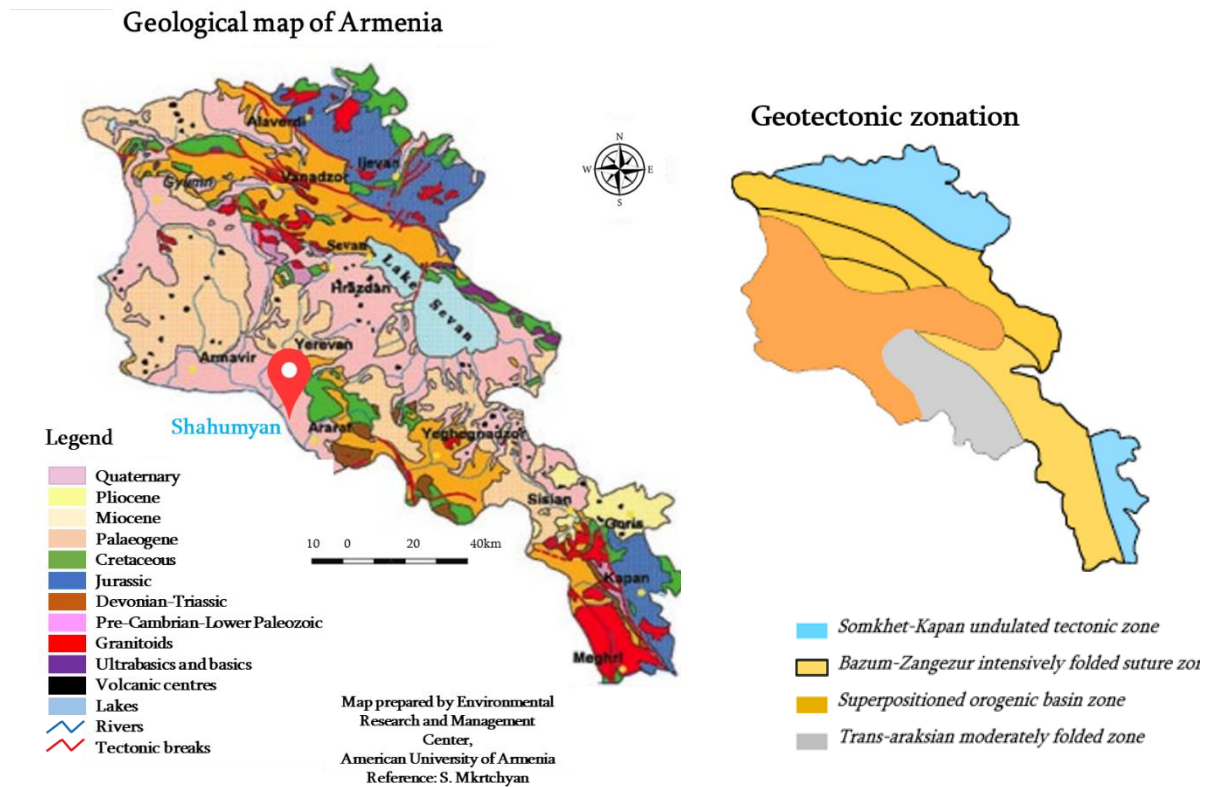


Figure 4. Geological map of the Republic of Armenia and its geologic time scale (left, adapted from [26]). Position (📍) of Shahumyan clay deposit (left bottom) and geotectonic zonation scheme (right) of the Republic of Armenia (adapted from [24]).

More precisely, according to Tumanyan N. [27] and Kazaryan M. M. [28] Shahumyan clay deposit resulted of the formation of a basin in the Ararat Valley (Near-Araks zone) at the Riss-Würm period (2.6 million to 11 700 years ago) characterized by the rather long existence of a lake. During this period clay settled on the lake bottom, forming

Shahumyan and adjacent clay deposits [23]. With river-lake sediments, many rest of flora and fauna are encountered in these deposits [27].

Additionally, the important volcanic activity (Figure 4) of the Armenian highlands [29] is responsible for the presence of volcanogenic-sedimentary and volcanogenic rocks in the territory of Shahumyan [23]. Both metallic and non-metallic minerals are widespread in distinct parts of the plateau.

It is worth to mention that in general clays and clay minerals are not limited to Shahumyan deposit, but they are quite widespread in the territory of Armenia (Gyumri, Noyemberyan, Ijevan, Sevan, Shahumyan (Yuva), Saritagh, etc.) and are used for various purposes (bricks, dishes, pots, tandoor, roof tiles, drainage pipes) [30]. For pottery making, Shahumyan is reputed as the best quality deposit (and its clay has wide range of application) because of the refractory properties of the clay, able to withstand relatively high firing temperatures.

1.1.2.2. Shahumyan Clay deposit

Shahumyan clay deposit is located on the territory of the Ararat Province of the Republic of Armenia, 30 km south of Yerevan the capital of the Republic [30]. The geological location of the deposit is defined by the coordinates: 39°52'40"-39°53'10"N 44°32'30"-44°33'20"E.

Although the deposit has long been used by the locals, it was first explored in 1960 by M. M. Kazaryan [28]. During the subsequent soviet expeditions lead by G.M. Abramyan and A. O. Martirosyan (1969) [31], and by Tumanyan N. et al., (1982-1983) [27] the geological composition, hydrogeological features, qualitative-technological characteristics of the clay were evaluated. In parallel assessment of the suitability of the clay to produce drainage pipes, bricks, pottery, and tiles were conducted.

Shahumyan clay deposit is stratified by layers (from bottom to top) of rocks, sands, loams, carbonate clays (with a high content of carbonates) and modern alluvial-diluvial sediments.

The deposit is composed of two layers of clay: gray clays with a yellowish tint and gray clays, but it is not always possible to accurately prove the transition from one variety

to another. The yellowish gray clay lies near the surface (starting from a depth of 0.1m) of the deposit, the gray clay lies under the first yellowish layer. The difference in shades is noticeable only when wet. After drying, they are almost indistinguishable from each other. Both types of clay are fatty.

Overall, clays of these two varieties do not differ from each other in terms of chemical composition and physicochemical properties. Microscopic studies have shown presence of different minerals, such a quartz, carbonate, feldspar, mica, chlorite in the rocks [27]. The clay of this deposit is fusible (low melting) and semi-acidic ($5 < \text{pH} < 7$) [28], [30].

1.1.3. Clay-based ceramics

It is commonly accepted that ceramics are inorganic nonmetallic material obtained through thermal processing of natural raw materials at relatively high temperature [19] (from 600 to 1200°C [32], [33] depending on the composition of the material). In general, ceramic materials are hard, brittle, and wear and corrosion resistant. These properties reflect the strong atomic bonds that exist between atoms in ceramic materials. Ceramics include crystalline materials and non-crystalline amorphous glasses, which are commonly composed of oxides [34].

The term clay-based ceramics is self-explanatory: it refers to ceramics produced from clay, which is also known as traditional ceramics. It results of a firing process applied to extruded, molded, or shaped pottery. Studies show that the sintering can start at a relatively low temperature (600°C) and may be conditioned by the mineral composition and structure of the clay [35], [36]. After firing, the clay soluble in water, is transformed into an insoluble stone-like and durable ceramic material [19]. The ceramic properties (in particular porosity) depend on the starting material but also on the heating technique.

1.2.Contextualization of ceramics in the wine industry

If the first indications of the use of ceramics in the Paleolithic period (~29000 BC) fall within the realm of worship, domestic use (dishes and jars) appears in the Neolithic period (~10000 BC), with the sedentarization of the populations. Ceramic production has

been one of the oldest and most active types of industrial activity that played an important role in the life of mankind. Since ancient days Armenia has been famous for its wine-making traditions, the ready wine was stored in ceramic pithoi («կարաս» – [karas]) half buried³ in the ground or set along the walls of wine cellars. These practices are still in use to this day (Figure 5). But, if the usage of clay and ceramics in Armenia has ancient roots, the scientific study of the impact of clay-based ceramics (jars) on their contents like grain, dairy products (buttermilk, yogurt, cheese, etc.), honey, beer, wine etc. is almost missing. In particular, the effect of clay-based ceramics on winemaking, aging, or storage has not been widely studied.



Figure 5. Illustrating Armenian pithoi (karases) buried in the sand. The volume of one pithos can reach 1000 L [37]

Nowadays, while wood (primarily oak) and stainless steel are the usual materials for winemaking, clayware ceramics and concrete are gaining in interest because of the increasingly popular natural wine movement in which traditional (even ancient) winemaking techniques are practiced.

In the recent web-literature, one can find several mention of the benefit of using clay-based ceramic for winemaking; in particular, Peter Weltman reported in 2018 (non-

³ which creates natural movement in the wine while aging

exhaustively) contemporary use of clay-based ceramic container for the winemaking in Georgia, Italy, USA [3]:

- (i) Georgian winemakers, who use clay jars to make wine by the traditional methods, believe that wines made in this way are distinguished for their stability and exceptional taste which is achieved without the use of chemicals or preservatives [38].
- (ii) In the new world, A. Beckham (Oregon's Beckham Estate Vineyard), who came to winemaking after 17 years as a ceramicist, calls out the temperature-regulating properties of clay as one of its primary benefits (like Georgian winemakers). "Two tons of grapes will ferment for 30 to 35 days with peak temperatures around 20° to 22°C in clay. While the same two tons of grapes in non-temperature-controlled wood or steel will finish fermenting in 10 or 11 days. The temperatures will max out around 30°C!" The lower temperatures for clay-fermented wines create brighter and fresher wines. He found that the clay allows oxygen into the wine twice as fast as wood. However, the subtleties of oxygen transfer at each temperature constitute additional variables that winemakers can use to their advantage. A. Beckham also notes that the clay reacts enzymatically with wine and raises its pH by pulling out acids. "I took a Riesling with a pH of 2.8, and in just two months, it went to 4." [3] Moreover, as a ceramicist, A. Beckham experienced firing temperatures to make vessels with distinct levels of porosity. He varied the firing temperature in a range of 100 degrees. He reported that at low temperature, pots are porous, they "weep and sweat"— the wines have more gas exchange and are the most expressive," at high temperature, "the vessels are vitrified and tight, the wines are much more reductive".
- (iii) In contrast to all this, in the opinion of the Armenian winemaker Zorik Gharibian "amphorae doesn't bring or take anything from the wine, it creates a space for the wine to keep it alive" [39].

Summarizing the empirical results of the above-mentioned observation, it is possible to list the reported possible advantages of using ceramic jars in winemaking. These are:

temperature regulation, natural cooling system, favorable oxygen exchange, change in pH, that are different from those of stainless steel, wood barrels, or concrete. In addition, other advantages as the absence of chemicals, wine clarification, flavor neutral are also pointed out.

However, since the ceramic jars used in traditional or contemporary winemaking have not been studied, nor have their effects on the wine stored in them, despite their ancestral uses. We considered that it could be culturally, oenologically, economically, and scientifically worthwhile attempting to reveal some of the interactions between clay-based ceramics and model wine.

Of course, it would seem ambitious to wish to study the whole spectrum of interactions in a single thesis.

Chapter 2. Materials and Methods

2.1. Materials

2.1.1. Sampling of clay powder and clay paste

The clay body for the preparation of ceramic tablets was kindly provided by potters from Shahumyan (Armenia) village. The row clay samples (powders taken from Shahumyan deposit) were donated by the owner of winery “ZORAH WINES” Zorik Gharibyan. The clay body is a mixture of clay, well ground sand (particle size close to the particle size of clay) and water.

2.1.2. Kaolinite

Natural kaolinite (Sigma Aldrich) was used as a reference for its non-swelling property. Sand (Sigma Aldrich) was mixed to kaolinite to obtain a clay body for tablet preparation. This is used for the preparation of the model tablets.

2.1.3. Model wine

The model wine (Table 1) used in the study is composed from L-(+)-tartaric acid (Sigma Aldrich $\geq 99.7\%$), ultra-pure water (VWR, LS-MS grade) and ethanol (Sigma Aldrich $\geq 99.9\%$). Model wine was prepared by dissolving tartaric acid (5 g/L) in water, followed by the addition of ethanol to give a final concentration of 12% (v/v). Then the needed volume was adjusted by adding water. The pH of the solution varies 2.3-2.4.

Table 1. Composition of model wine

Model wine
Tartaric acid – 5g/L
Ultra-pure water
Ethanol – 12%
pH 2.3-2.4

2.1.4. Preparation of clay-based ceramics

For studying the interaction of ceramic and model wine, ceramic tablets (Figure 6) were shaped and then baked. Tablets were prepared from the clay past. According to the

Armenian potter, a clay-sand fraction of less than 4 μm in a ratio of 2:1 respectively was used to prepare the past.

The preparation of clay-based ceramic tablets is based on the traditional technology of pottery. The starting paste was composed of 500 g of mixture (clay+sand) and 128 g (130 ml) of water. Over time, with natural drying, a little water was added to keep the plasticity of the paste allowing shaping the tablets.

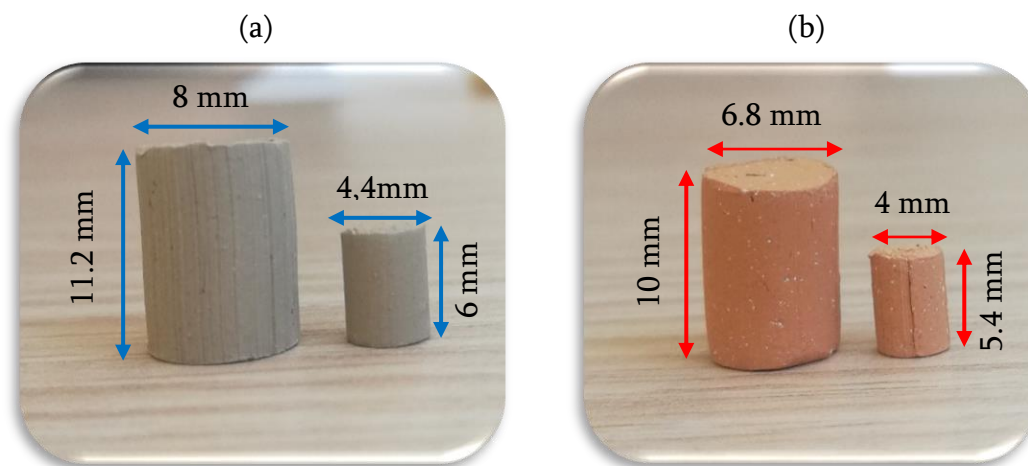


Figure 6. The tablet and their average dimensions before (a) and after (b) heat treatment

The suitable clay for pottery needs to be homogenous, free from air bubbles. When the clay was ready for using, cylinder-shape tablets were prepared. Like Armenian clay-based ceramic tablets the model tablets were prepared with kaolinite clay.

2.1.4.1. Shaping of the tablets

The tablets were cylindrically shaped by using handmade extruder made out of plastic syringe (contact of the clay with metal tools was excluded in order to avoid the addition of paramagnetic elements, which could interfere during relaxometric measurements). Two sets of tablets with targeted distinct dimensions were produced. The height, the diameter, and the surface of the tablets are critical dimensions since the tablets must fit into the experimental receptacles (i.e., 10 mm NMR tube), covered by the wine in a controlled volume-of-wine/surface-of-the-tablet (V/S) ratio in regards of real dimensions

encountered in Armenian ceramic-pots winemaking technologies. The details of these calculations are given in the "Sample geometry" section.

2.1.4.2. Drying

After shaping, the tablets were air dried at room temperature. Depending on the size of the subject, the temperature and RH in the room the drying time may vary. In our case, tablets were dried in 3-4 days (due to their small size), till a stable weight. Tablets were weighed on a precision balance (Sartorius Quintix®, with an accuracy of 0.01mg).

2.1.4.3. Thermal treatment of the tablets

Thermal treatment of the clay is a process, as a result of which clay is transformed into ceramics under the influence of high temperatures (up to 1300°C). In general, thermal treatment of traditional ceramic includes the following stages:

Heating – In this step well dried⁴ ("bone dried") samples are heated from ambient temperature to about 600-800°C (depending on the raw materials composition) [40]. Various transformations take place in the material during heating, such as the removal of free water, combustion of organic matter, transformation of α -quartz to β -quartz, loss of OH⁻ groups in the clays, and carbonate decomposition (if it contains carbonates). All these chemical reactions lead to gas release, changes in volume, etc.

Firing - The actual firing process begins at temperatures above 800°C [40] (depending on the type of clay minerals) to the peak temperature (depending on the final purpose). The main physico-chemical transformations, take place in this step, reduce the porosity of ceramics due to the sintering of the material and lead to the dimensional changes (shrinkage). Firing gives a strength to the material and increases water resistance. It also changes the color of the final product. The final composition, microstructure and properties of the ceramic depends on the composition of clay paste and the firing process. In our case, the clay from Shahumyan belongs to the low-melting type of clay and the firing

⁴ The sample is considered as well dried when there is no more significant weight loss

protocol used for the heating of the tablets is based on the Armenian pottery making technology. In this work two firing protocols are reported:

- Firing protocol 930 - (FP930),
- Firing protocol 800 - (FP800).

Firing protocol FP930 (Figure 7) is composed of three steps. First step includes the heating of the samples during 4 hours from ambient temperature (20°C) to 600°C (heating rate of 2.4°C/min). The second step includes fast increase of temperature from 600°C to 930°C (firing rate of 20°C/min) and then firing at 930°C for 2 hours. The last third step is free cooling process. As mentioned above the firing protocol mimics the technique used in Armenia to produce such jars.

Firing protocol FP800 – This firing protocol is identical to FP930 except for the peak temperature (800 °C instead of 930°C, Figure 7).

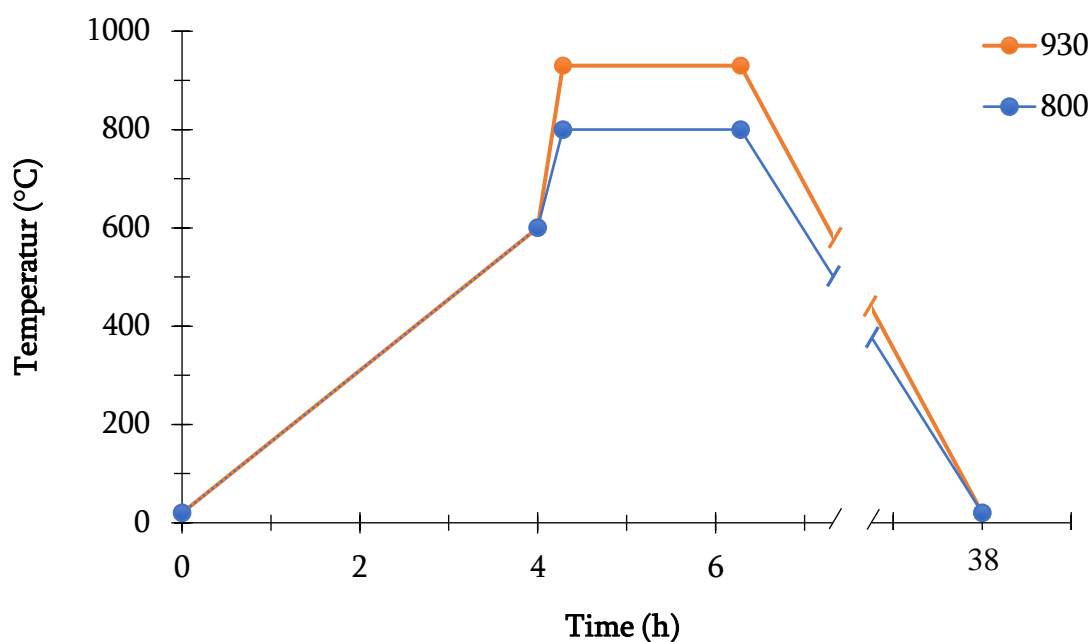


Figure 7. The heating of the tablets by two firing programs

Heating rate plays a significant role in the ceramic sintering process. During heating process, the rate of temperature rise was chosen to avoid unwanted effects, such as cracking due to heat stress. On the one hand, the clay object cannot be immediately burned at high temperature; it must be heated gradually, smoothly, avoiding jumps. On the other hand,

too slow heating at this stage can lead to a “steaming” effect, where water-soluble salts condense on the surface of the products, which can later stain. In our study we have used slow heating rate (2.4°C/min - first step), and fast heating rate (20°C/min) for the second step of heating (proposed by Armenian potters). The heating rate was important from point of view of the porosity. It is known, that fast (5-10°C/min) [41] and especially ultra-fast (up to 1200°C/min) heating rate reduce the pore area, while slow heating rate (until 5°C/min) promotes the increase of total pore area [42].

The pottery always should be almost "bone dried" before being placed into the kiln. However, there is still water trapped within the spaces between the clay particles. During slowly heating of the clay, this water evaporates. If the clay is heated too quickly, the water will turn to steam right inside the clay body, expanding with an explosive effect on the pot. Before the boiling point of the water (100°C) is reached, all the atmospheric water should have evaporated out of the clay body. This will result in the clay compacting and some minimal shrinkage. During the firing process several phase transformations happens with clay and ceramic as presented in Table 2.

During the *sintering* process, calcium carbonates (CaCO_3) and magnesium carbonates (MgCO_3) actively interact with the decomposition products of clay minerals - amorphous silica SiO_2 and alumina Al_2O_3 . These reactions proceed with the release of carbon dioxide CO_2 .

Table 2. Firing stages of the clay [40], [43], [44], [45]

	T/°C	Stage of firing
Heating	20-200	Desorption of free water
	200-400	The removal of adsorbed water is completed. Burning of organic matters contained in the mass.
	400-600	Dehydration of clay minerals begins and the release of chemically bound water entering their crystal lattice.
	573	Quartz inversion- a phase transition of quartz from β to a higher temperature α -form takes place. This process is accompanied by volumetric changes.
	600-800	Most clay minerals have already decomposed by this point, and the sintering process has not yet been completed - new minerals have not yet formed.

Firing	600-900	Organic and inorganic matters of the clay are being burned off out.
	800-1000	Sintering process of the ceramic mass begins, new minerals are formed: clay is becoming ceramic material. These processes can continue with the release of gaseous substances
	1100-1300	Mullit crystals begin forming in porcelain
	1100-20	Free cooling
Cooling	573-230	The sudden shrinkage of cristobalite - a crystalline form of silica. High-temperature forms of quartz pass into low-temperature crystalline forms, with a notable change in volume

2.1.5. Shrinkage of the tablets

It was beyond the scope of this work to study the shrinkage of the paste during the ceramic production, but weight, diameter, and height of the tablets were systematically recorded as an indicator of the repeatability of the drying and fire protocol. Detailed results are reported in Annex V but illustrative charts are reported in Figure 8 and Figure 9.

In Figure 8, a strong shrinking is revealed in the Armenian tablets with respect to model kaolinite ones (used as a reference for the non-swelling property of kaolinite), suggesting the likely presence of smectic clays in Shahumyan deposit. The shrinking upon firing of the three batches of Armenian tablets is fairly reproducible. This is likely to be a valued property of Armenian clay for traditional potters and may contribute to the high quality reputation of the Shahumyan deposit.

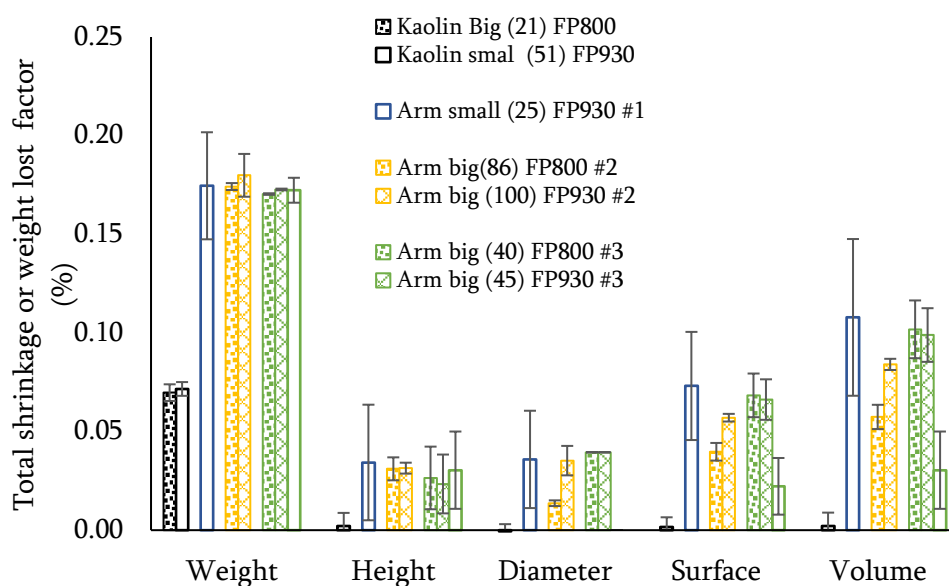


Figure 8. Shrinkage and weight loss between the dried and fired stages on (big and small) Armenian and kaolin tablets. Number in brackets correspond to the tablet population, FP correspond to the firing protocol (800 or 930 °C), the number preceded by a # is the batch number. Error bars correspond to standard deviations (see Annex V for further detail).

Figure 9 reports the volume versus weight of three batches of big and small tablets FP930 the slope indicates a fairly stable density of 1.88.

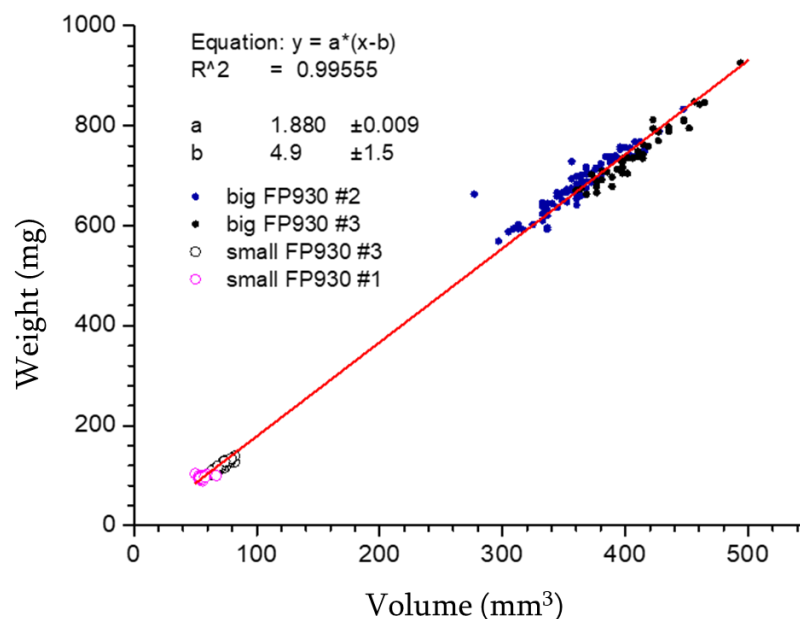


Figure 9. Volume versus weight of three batches of big and small tablets FP930

2.1.6. Sample geometry (surface of tablet, volume of wine)

2.1.6.1. Volume to surface ratio in real containers

To quantitatively study the interaction between ceramic and wine, the surface of the ceramic in contact with the wine and the volume of the wine are critical dimensions. It was difficult to study the system at a real scale, and the ratio of the volume of wine in contact with the container can vary strongly with the size and the geometry of the container. As a reference for ceramic container, we estimate this ratio from a drawing of

an ancient pithos [1], fig 139, p 102 (Figure 10). The calculations are numerically performed by integration in space of the surface of revolution describing the container (see Annex I)

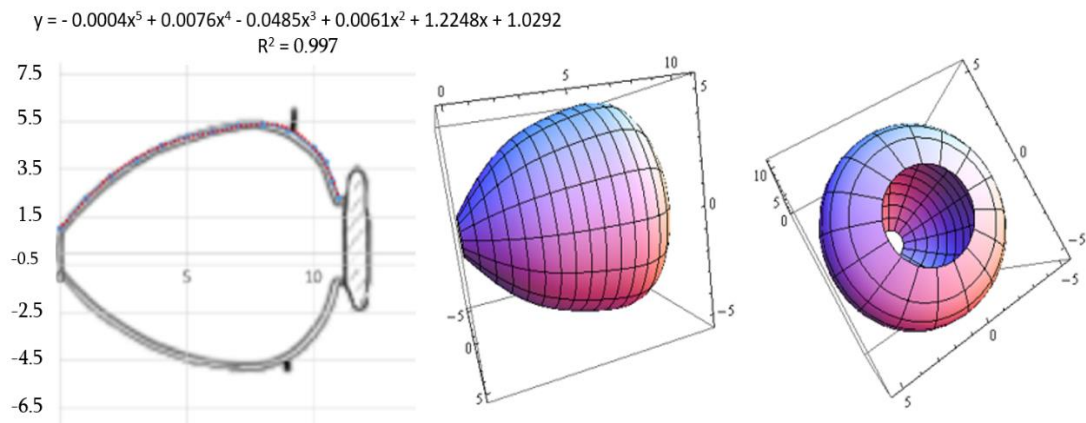





Figure 10. Original drawing used to calculate the equation of the revolution curve; units are dm (right). Reconstruction of the pithos to calculate its volume and surface (left).

We reduce the geometry of the container to a single parameter ρ defined as:

$$\rho = \frac{\text{volume of the container}}{\text{surface of the container in contact with the wine}} \quad (1)$$

When expressed in meter, the ρ ratio can be related to the inverse of the normalized surface-area-to-volume-ratio (surface area/volume), which is the amount of surface area of an object per unit volume of this object. For illustrative purposes Table 3 reports the estimated ρ ratio for Bordeaux bottle and barrel, and for the pithos of Figure 10.

Table 3. Estimation of ρ and equivalent surface area/vol ratios for three containers, calculation were performed according to geometrical formulae for volume and surface calculation (barrel and bottle) [46], [47] or by integration of a revolution curve (pithos) [2].

<i>Container</i>	<i>Volume (L)</i>	ρ <i>(m)</i>	<i>Surface area/vol (m⁻¹)</i>
<p><i>Bottle</i> ^(a) <i>(Bordeaux type)</i></p> 	0.75	0.0157	63.67
<p><i>Barrel</i> ^(b) <i>Bordeaux transport</i></p>  <p>Height 95 cm Wide 27 mm ϕ Head 56 cm ϕ Middle 70 cm</p>	225	0.128	7.82
<p><i>Pithos</i> ^(c)</p> 	660	0.186	5.38

2.1.6.2. Geometries of fired ceramic samples in contact with model wine

For practical reasons, (easiness of production) a cylindrical shape (tablet) for the ceramic sample was chosen. Two type of tablets were produced (big and small, Figure 6 and Table 4).

As previously mentioned, to analyze the interactions of model wine with the ceramic tablet, that we assume occurring primarily at its surface, the dimension of the ceramic tablet with respect to the volume of model wine are of prime importance. However, at the laboratory scale these dimensions are limited or constrained by experimental designed.

2.1.6.3. Geometrical constraints on the volume to surface ratio for the relaxometric measurements (small tablets)

Relaxometry experiments are performed in 10 mm diameter tubes (8.8 mm interior diameter), and the sample has to be situated in the homogeneous magnetic field: the height (H_s) of the sample (ceramic in the wine) should not exceed 1 cm and the total volume of the sample (V_s) should not exceed 0.6 mL. The geometrical constraints are therefore:

- (i) the ceramic must be completely immersed in the wine
- (ii) diameter of the tablet: $D_c \leq 8.8$ mm
- (iii) height of sample (ceramic & wine): $H \leq 1$ cm.
- (iv) volume of the sample (volume of ceramic (V_c) plus volume of wine (V_w)):

$$V_s = V_c + V_w \leq 0.6 \text{ mL}$$
- (v) targeted ρ ratio: $\sim 0.18 \text{ m } V_c$

Neglecting the penetration of wine in the ceramic, the volume of the sample is given by (constraint (iv)):

$$V_s = V_c + V_w = \frac{\pi D_c^2}{4} H_c + V_w. \quad (2)$$

Since,

$$\rho = \frac{V_w}{S_c}, \quad (3)$$

and

$$S_t = \pi D_c H_c + 2 \frac{\pi D_c^2}{4} \quad (4)$$

We obtain, that for a given ρ ratio and sample volume V_s , the dimensions of the ceramic cylinder of diameter D_c and height H_c , fulfill the following equation:

$$H_c = 2 \frac{(\pi D_c^2 R - 2V_s)}{\pi D_c (D_c + 4R)} \quad (5)$$

Figure 11 reports the graph of Eq.(5) for $\rho = 0.18 \text{ m}$ and $V_s = 600 \text{ } \mu\text{L}$ that would reproduce the dimensions occurring in the reference pithos. The size of the ceramic tablet

should by example have a diameter of 1mm and a height of 0.5 mm, which is certainly not easily achievable in practice.

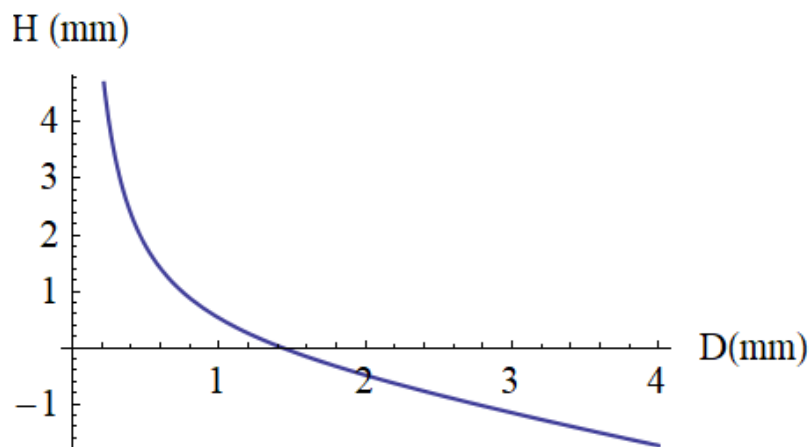





Figure 11. Dimensions of a cylinder immersed in 600 μL of wine that would satisfy a ρ ratio of 1.8 m.

To fulfill the above relaxometric experiment constraints, omitting the ρ ratio criteria, with tractable ceramic dimension we produced tablets of ~ 3.9 mm diameter and ~ 5.4 mm height. A typical experiment would require 470 mL of wine. However, the ρ ratio is now 0.0052 m, 36 times lower than the ratio for the reference pithos. This means that the kinetic of chemical reaction are expected to be quite different in the NMR tubes with respect reactions occurring in the reference pithos.

Small tablets were specially designed for relaxometric experiments but other experiments for which, more wine or more ceramic surfaces were required, were performed with big tablets (Table 4) and other experimental constraints. The resulting ρ ratio may vary significantly from one type of experiment to another one (Table 4), but for each experiment, we pay attention to report systematically the ρ ratio as a scaling factor.

Table 4. Example of different experiments with tablet diameters and heights, model wine volumes, and associated ρ ratios.

Small tablet in a sealed 7 mm tube, inside a 10 mm tube	Small tablet in a 10 mm tube	Eight big tablets in 10 mL of wine
		
Diameter : 3.7 mm	Diameter : 3.5 mm	Diameter : 7 mm
Height : 5.2 mm	Height : 5.3 mm	Height : 8 mm
Surface : 81.95 mm ²	Surface : 77.52 mm ²	Σ surfaces : 2505 mm ²
Wine volume : 200 mm ³	Wine volume : 700 mm ³	Wine volume : 10000 mm ³
ρ ratio : 0.0024 m	ρ ratio : 0.009 m	ρ ratio : 0.004 m

2.2. Methods

There are diverse analytical tools and methods available for the identification and characterization of clays, clay minerals, and ceramics but also for studying the ceramic-wine interactions. The most suitable methods to answer our research questions were the following, which are reported below.

2.2.1. Thermal Gravimetric Analysis (TGA)

Thermal gravimetry is a thermal analysis technique used to determine the change in the physical and chemical properties of the materials upon heating. The TGA measurement is usually performed by considering the mass loss, either as a function of temperature rise with a constant heating rate, or in isothermal conditions as a function of time [48].

Analysis of the clay samples taken from the Shahumyan deposit has been performed in the laboratory of École supérieure d'ingénieurs numérique et matériaux (ESIREM). The instrument SDT Q600 V20.9 Build 20 thermal analyzer is used with a heating rate of 15°C

min⁻¹ over a temperature range of 28–920°C under flowing air or nitrogen conditions. Around 14 mg of powder was used for each analysis. Several samples were run in triplicates.

2.2.2. X-ray fluorometry (XRF)

X-ray Fluorometry is a non-destructive analytical technique that allows to determine the chemical compositions of the materials.

For chemical analysis of clayey materials, we performed wavelength dispersive X-ray fluorescence analysis in the laboratory of École supérieure d'ingénieurs numérique et matériaux (ESIREM) on a Bruker S8 Tiger instrument with the detection limit of 0.1 ppm - 100% and resolution (Mn-K α) 35eV. X-rays were generated using a 3 kW rhodium anode X-ray tube under helium. The parameters of X-ray tube are 50 kV and 60 mA.

Two Shahumyan clay samples and the potter clay body (2:1) hereafter referred as clay body were analyzed. For each, 5g of fine-grained homogenous sample was placed on single-use sample holder with a prolene membrane.

2.2.3. X-ray powder diffraction (XRD)

X-ray powder diffraction method is used for identification and characterization of crystallized clay-minerals present in clayey samples and ceramics.

The samples have been characterized by X-ray diffraction in the laboratory of Université de Poitiers / Ecole Nationale Supérieure d'Ingénieurs de Poitiers Institut de Chimie des Milieux et Matériaux de Poitiers (IC2MP)⁵. The ceramic was produced in the laboratory from the clay body provided by the Armenian potter with the firing protocol FP930 (Figure 7). After elaboration, the tablet was crushed in an agate mortar to avoid sample's contamination.

A Bruker D8 Advance diffractometer, equipped with a copper anticathode (radiation $\lambda_{\text{CuK}\alpha} = 1.541838 \text{ \AA}$ after filtering through a nickel blade), mounted in θ/θ

⁵ First XRD, exploratory experiments were performed at Ecole Supérieure d'Ingénieurs Numérique et Matériaux (ESIREM, Dijon) and in the Institut de Science des Matériaux de Mulhouse –(IS2M), and a precise analyze was performed at the Institut de Chimie des Milieux et Matériaux de Poitiers (IC2MP).

Bragg-Brentano configuration was used. The optical system eliminating the divergent components of the incident and diffracted beams consists of anti-divergence $1/4^{\circ}2\theta$ slits and a Soller slit system (0.04 rd). The spinner type sample holder has been used (rotation speed 4 rpm). The detector is of solid semiconductor type allowing simultaneous counting over an angular sector of $3^{\circ}2\theta$. The analytical conditions are 40 kV, 40 mA, angular range 2.5 to $65^{\circ}2\theta$ (powders), 2.5 to $35^{\circ}2\theta$ (oriented clay preparations), counting time of $45\text{s}/2^{\circ}2\theta$.

Approximately 500 mg of material was placed on a hollowed-out support. Ethylene-glycol saturation and heat treatments were carried out on the clay samples in order to identify all the *phyllosilicates* present. The principle is based on monitoring the variations in their interfoliar space by studying the positions of their reflections ($00l$) during conventional treatments [49], [50].

The diffractograms were processed with HighScore software. The minerals present in clay sample from deposit and in ceramic FP930°C (Table 10) were identified by comparison of a given powder diffractogram with the references contained in the international database of minerals JCPDS ICDD PdF3.

2.2.4. Gas Pycnometry

Generally helium pycnometer is used to determine the volume—and thus the open porosity and the density—of granular, porous compounds (rocks, ceramic etc.) [51].

Helium pycnometry measures the volume (or the density) of materials based on a pressure equalization principle [52]. To determine the open porosity of ceramic tablets a handmade helium pycnometer was used in the laboratory of Interdisciplinaire Carnot de Bourgogne UMR 6303 CNRS.

Pure helium (99.9%) was employed to determine the volume of the samples by measuring the pressure change of helium in a calibrated volume. The tablet of known mass is placed in a chamber of known volume, maintained at a constant temperature (25°C). A calibrated volume of helium (99.9%) is then added to the system. The resulting equilibrium pressures are used to determine the apparent volume of the ceramic tablet.

Five big tablets were used for each firing protocol FP800 and FP930. Five small tablets were also used for the too firing protocols but they were too small to be measured individually. For each firing protocol, all small tablets were put together in the cell. In all cases measurements were repeated five times.

The incertitude on small tablets is significant because of unfavorable error propagation. Incertitude on big tablets was done from the standard deviation of an average of five measurements on five tablets.

2.2.5. The nitrogen adsorption/desorption isotherm

The pore characteristics of porous materials are determined by the application of several adsorption models such as the Brunauer–Emmett–Teller (BET) theory [53]. The nitrogen adsorption/desorption isotherm is used to characterize porous materials, allowing for the determination of specific surface area.

The measurement was performed in the Laboratoire of Interdisciplinaire Carnot de Bourgogne (UMR 6303 CNRS – Université de Bourgogne) with an ASAP2020 Micromeritics device by measuring nitrogen adsorption and desorption ($T = 77$ K up to 1 atm). The samples (5 ceramic big tablets with the mass of about 5g were kept in vacuum ($P \leq 0.7$ Pa) at 350°C for 4 hours prior to the measurements.

2.2.6. Scanning electron microscopy (SEM)

Scanning electron microscopy used to study the surface topology of clay minerals such as the size of platelets and their shape mainly describes the surface morphology down to few nm (0.5 to 4nm) [53]. Scanning electron microscopy can be associated with an Energy Dispersive X-ray (EDX) analysis allowing for a qualitative⁶ and quantitative (10 -20 % relative error) elemental analysis.

The microstructure and elemental composition of the samples were analyzed using Hitachi SU-8230 scanning electron microscopy equipped with an energy dispersive X-ray

⁶ H, Li, He and Be are not observable

spectrometer. The combination of SEM and EDX analysis is used for the qualitative analyses of the elemental composition of the samples. EDX analysis measures the ionization energy and intensity distribution of X-ray signals generated by the electron beam. Secondary electrons by converting into electronic signals give rise to images of the area scanned. The samples were coated with a thin layer of carbon or gold to increase the surface conductive and improve the image quality. The determination of elements was performed directly on the ceramic tablet without homogenization. For statistical purpose, different measurement areas and points were selected depending on the homogeneity/heterogeneity of samples.

The morphology of clay from Shahumyan deposit and tablets before (crude) and after firing (ceramic) were observed by secondary electrons (SE) under a scanning electron microscopy at an acceleration voltage of 2.0 kV, after either carbon or gold coating.

Elemental analysis of ceramic was performed on unpolished samples by using EDX at an acceleration voltage of 20.0 kV.

X-ray mapping and data analysis have been performed using Pathfinder 1.2 software.

2.2.7. Inductively coupled plasma atomic emission spectrometry (ICP-AES)

The ICP-AES is an analytical technique based on the principles of atomic spectroscopy for the determination of more than 70 elements with detection limits in the parts per billion to parts per million range [54]. The technique was used for the complete screening of elements in the model wine after contacts with the ceramic.

Elemental analysis of the samples was conducted by using an ICP-AES Spectro ARCOS system (SPECTRO Analytical Instruments GmbH & Co. KG, Kleve, Germany). 26 elements (namely: Al, B, Ba, Be, Ca, Cd, Co, Cr, Cu, Fe, Hg, K, Li, Mg, Mn, Mo, Na, Ni, P, Pb, S, Sr, Ti, V, W, and Zn) were investigated and the corresponding wavelength are reported in Table 5. Sample introduction was carried out using a peristaltic pump connected to a Meinhard nebuliser with a cyclone spray chamber. The RF power was set to 1250 W, the plasma gas was 15 L Ar/min, whereas the nebuliser gas was 0.6 L Ar/min.

Table 5. Lines used for determination of elements with ICP-AES.

Element	ICP-AES (λ) (nm)	Element	ICP-AES (λ) (nm)
Al	396.152	Mg	279.553
B	249.773	Mn	257.611
Ba	455.403	Mo	202.03
Be	313,042	Na	589.592
Ca	317.933	Ni	231.614
Cd	214,438	P	214.914
Co	228,616	Pb	220.353
Cr	267.716	S	182,036
Cu	324.754	Sr	407.771
Fe	259.941	Ti	334.941
Hg	194.164	V	292.402
K	769.869	W	207,911
Li	670.784	Zn	213.856

2.2.8. Oxygen measurement

The concentration of O₂ in NMR tube was measured by chemiluminescence using Presens Pst3 oxygen sensors (PreSens GmbH, Regensburg, Germany) [55] containing a luminophore spot sensitive to oxygen, with a detection range between 0.03– 100% O₂.

The sensor was glued inside NMR tube in the headspace area then model wine was added in NMR tube and ceramic tablet was dropped in. Then tube was closed with NMR cap and vacuum grease was used at the 1 cm interface between the cap and the tube. The oxygen headspace concentration was measured in NMR tube during T₁ measurement. Measurements were performed by applying an optical fiber in front of the spot and by emitting excitation light through the glass wall [56]. The whole procedure of sample preparation was conducted in glove bag where the amount of O₂ was reduced to a minimum (≤ 0.03 mg/L) with N₂. The concentration of O₂ in glove bag was measured by using oximeter Portavo 907 Multi Oxy with digital sensor SE340 (Knick, GmbH & Co. KG Beuckestraße, Germany) with an oxygen measuring range of 0 μ g/L-20 mg/L.

2.2.9. Time domain nuclear magnetic resonance (TD NMR) relaxometry

Nuclear magnetic resonance using proton relaxometry measures the time needed by a population of spins placed in an external magnetic field to recover from a resonant radiofrequency excitation. Two relaxation parameters (T_1 and T_2) are of great interest because they are often used to obtain information on molecular mobility of molecules ranging from small molecular groups and domains size [57], [58], [59], [60] for quantification of elements in liquids (wine) etc. [61]. The technique was used to follow in situ migration of elements, reduction of iron, but also the consumption of dioxygen in the model wine in contact with the ceramic.

^1H time domain NMR measurements were performed to characterize the processes occurring in model wine being in contact with ceramic through spin-lattice (longitudinal) relaxation processes (T_1). Low-field NMR experiments were recorded at 25°C on a minispec mq20 (Bruker) operating at 19.65 MHz equipped with static probe. Longitudinal relaxation times were measured with an inversion recovery pulse sequence. For the 90° and 180°, the pulse lengths were set to 2.8 μs and 4.4 μs respectively. The receiving gain was set to 68 dB, except for the flame-sealed sample (Figure 40(c)). The recycling delay was set 6 times to T_1 . Sixteen points were scanned for building the relaxation curves for all the experiments except for three samples (Figure 35, Figure 40 (a, b,)). For each acquisition, four scans were collected. Total measuring time varies from 10 to 20 min.

2.2.10. pH-measurements

The pH of the model wine being in contact with ceramic tablets were performed with a Five Easy F20 bench pH-meter, using a LE438 3-in-1 plastic electrode with integrated temperature sensor.

Chapter 3. Characterization of clay and ceramic

3.1. Thermal gravimetric analysis of row clay powders from Shahumyan deposit

3.1.1. Literature review

From the TGA analysis of the Shahumyan clay performed by several scientists show, that the main constituent clay minerals are montmorillonite and hydromica in various proportions, as well as kaolin in small quantities. As impurities in the clay sample, there are fine-grained carbonate and silty material 0.05 mm in size, represented by grains of quartz, feldspar, chloride, mica and ore minerals [31], [62].

3.1.2. TGA results

The results of the analysis of the thermal stability of the row clay powder are presented on Figure 12. The thermogram composed of the weight loss or TG curve (green) and its derivative (DTG, blue). The weight loss curve, showing the mass variation with temperature presented three steps.

The first weight loss (4%) is observed in the range 28°-196°C. The second mass decrease occurs between 270°C to 630°C, is very slow (9% up to here). A fast and sharp weight loss starts at about 650°C up to 750°C. A cumulative mass loss of 19% is eventually measured.

On the DTG curve the first endothermic peaks with a maximum at a temperature of 38°C and 105°C, reflect the removal of physisorbed water. The relatively small endothermic peak (439°C) could be associated with the removal of hydroxyl groups from clay minerals and destruction their crystal lattice.

During the third mass loss (650-750°C) the changes are related to the decomposition of clay material, burning of the organic materials and maybe beginning of the transformation of clay minerals.

Exothermic peak at 715°C coincides with the formation of high-temperature phases. It reflects the crystallization of amorphous decomposition products of a clay minerals.

Small exothermic peaks in temperature range (370-470°C), apparently due to the oxidation of organic matter contained in these clays.

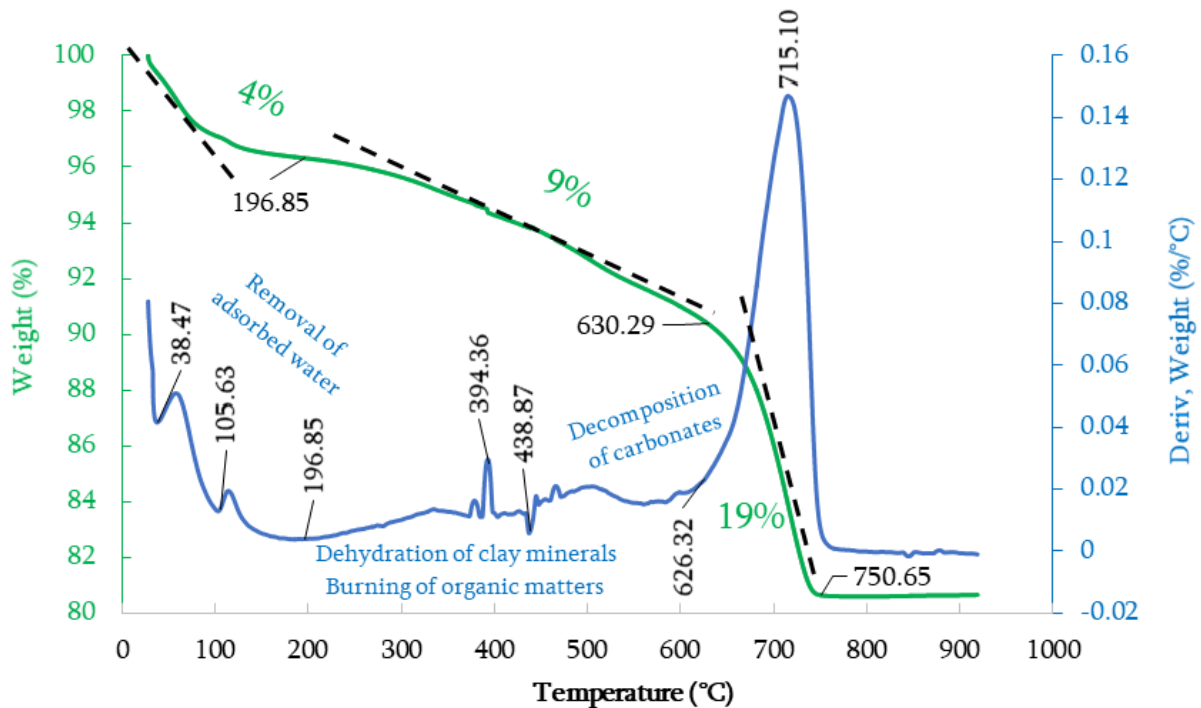


Figure 12. Thermogram of Shahumyan clay recorded under air flow at 15°C/min TG (blue), DTG (green) curves, as well as the cumulated weight loss (%) are reported with indication on the structural clay mineral modification as a function of temperature.

3.1.3. Conclusion

The thermograms patterns are correlating with previously reported literature data and the usual decomposition and recomposition stages described in the literature are satisfactorily observed.

3.2.WD-XRF (Wavelength Dispersive X-ray fluorescence) analysis of Armenian clay chemical composition

3.2.1. Literature review

Table 6 resumes the chemical compositions of Shahumyan clay (reported in the literature)⁷. Main components are SiO₂ (41-51 %), CaO (13-18%), and Al₂O₃ (12-14%). Significant amount of Fe₂O₃ (5.5-7%) and MgO (2.3-5.1%) are also quantified. The other elements consist in small and trace amounts. The loss on ignition (LOI) is almost the same for all experiments (16%).

Table 6. Chemical composition of Armenian clay powder from Shahumyan reported from 1960-2001.

Oxides	Concentration (% w/w)						
	1963 [28]	1966 [30]	1970 [31]	1983 [27]	1991 [63]	2000 [64]	2001 [62]
SiO ₂	42.22	44.2	41.22	44.2	44.0	43.0	51.30
Al ₂ O ₃	14.08	14,3	12.78	14.3	12.20	14,05	13.15
CaO	13.96	14.0	13.99	14.0	18.21	13.44	18.00
Fe ₂ O ₃	6.61	6.6	5.86	6.6	5.49	5.90	7.00
MgO	5.06	5.1	4.21	3.36	2.28	3.67	4.10
MnO	0.12	0.1	-	0.1	-	-	-
TiO ₂	0.96	0.9	-	0.9	0.8	0.6	-
Na ₂ O	-	-	1.2	1.19	1.88	1.80	-
K ₂ O	-	-	1.47	1.63	2.04	1.10	-
LOI	16.64	16.6	15.52	15.96	16.8	-	16.00

⁷ The method used for chemical composition analysis is not mentioned.

3.2.2. XRF results

Results are presented in Table 7 and Figure 13. The chemical compositions of both clay samples are similar. The overall composition is comparable to the previously reported data (Table 6), the most abundant components in the samples are SiO₂, CaO and Al₂O₃. However, the amount of SiO₂ in the current study is slightly higher (58-63%) than in previous studies (41-51%). As expected, the amount of SiO₂ in clay body is higher, than in raw clay powders, and more interesting the obtained clay body SiO₂ concentration is in supporting with the 2:1 clay/sand ratio claimed by the potter (according to SiO₂ concentrations of Table 7, a 2:1 mixture of clay/sand gives 75% or 72% of SiO₂ for Sh1 or Sh2 sample respectively). It should be noted, that clay samples are characterized by a rather high content of calcium oxide (18%), however, it does not effect on the quality of the ceramics, because it is in a finely dispersed states [31]. The presence of CO₂, SO₃, S, P in clays is associated with the presence of various impurities in them (organic substances, for example) [30].

Table 7. Chemical components of two clay powders from Shahumyan (Sh1 & Sh2) and a clay body obtained by XRF.

Composition	Concentration (% w/w)		
	Sh 1	Sh 2	Clay body
SiO ₂	62.78	58.21	73.77
CaO	15.04	21.93	9.69
Al ₂ O ₃	8.75	8.18	6.57
Fe ₂ O ₃	5.42	4.98	3.95
MgO	2.94	3.23	2.53
K ₂ O	1.95	1.49	1.53
Na ₂ O	1.15	0.83	1.05
TiO ₂	0.67	0.70	0.48
MnO	0.09	0.08	<0.01

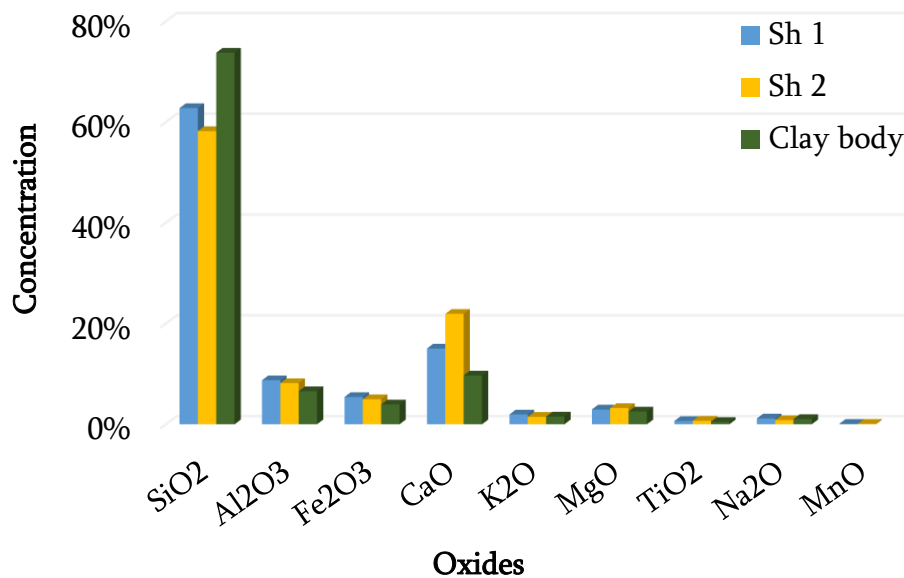


Figure 13. Representative histogram of Table 7

3.2.3. Conclusion

Our XRF data agree well with the previously reported literature data with however, an increase of the amount of reported SiO₂. The clay is characterized by a high silicon (~ 60%), and calcium oxide (15-21%) content, that could qualify as the clay of sandstone marl rather than fatty, as reported in the literature [27], [28], [31].

Alternatively, the 2:1 clay/sand ratio claimed by the potter in the clay body seems confirmed.

3.3.XRD (X-ray diffraction) analysis of Armenian clay minerals in row clay powder and in ceramics

3.3.1. Literature review

The first description of the constituents of the Shahumyan clay was produced by Gulyan E. et al, in 1970 (the method is not mentioned) [65] which later was confirmed by Tumanyan et al, in 1983 by “X-ray thermal analysis” [27]. The main constituents reported are montmorillonite and hydromica in different quantitative ratios, as well as kaolinite in small quantities. Fine-grained carbonate and silty material represented by grains of quartz,

feldspar, chlorite, mica and ore mineral are present as impurities. According to the XRD study of Petrosov I. (1983) [23], Shahumyan clay contains the following clay minerals: montmorillonite, mixed layer clay (H/M) and chlorite (all together 20%), hydromica (50-80%) and kaolinite (20%). But, as he mentioned, the distribution of clay minerals is inhomogeneous in the vertical section of the deposit. It allows us to assume that depending on the depth of sampling the mineralogical composition of the deposit can varies.

In 1991, Navasardyan K. [63] (by XRD) presented the following mineralogical composition of Shahumyan clay: plagioclase (26.35%), kaolinite (2.10%), Illite (24.79%), chlorite (4.82%), quartz (11.28%), calcite (24.5%) and accessory minerals, such an apatite, sphene, magnetite and hematite (2.68%).

In 2000 (by “roentgenography”), Hakobyan R. et al [64], reported montmorillonite (23%), hydromica (5%), kaolinite (5%), feldspar (15%), carbonates (22.5%), quartz (11.2%).

In the last study (2001), carried out by Hamamchyan M. et al [62], by thermographic and X-ray-phase analysis the following clay minerals were established: montmorillonite, goethite, quartz (the quantity of the minerals is not mentioned). Calcite was not detected.

There are clear discrepancies among mineral compositions reported in Table 8. This can be due the improvement of the analytical techniques used for the studies (more than 30 years separate the first to the last analysis), but the heterogeneity of the deposit sections as mentioned by Petrosov I. [23], is also very likely to contribute to the diversity of results in Table 8. In any cases it was desirable to undertake a characterization of our samples.

Table 8. Comparative table of the proposed mineral compositions (%) of Shahumyan clay deposit (m.c.: main constituent, s.q.: small quantity, a.: all together. dominant minerals are in red. Mmt, ML, carb. stand for Montmorillonite, Mixed layer, and carbonate respectively.

	Gulyan E. et al. (1970) [65]	Petrosov I. (1983) [23]	Navasardya n K. (1991) [63]	Hakobyan R. et al. (2000) [64]	Hamamchya n M. et al. (2001) [62]
Technics	The method is not mentioned	XRD	XRD	Petrography and Roentgenography	Thermographic and X-ray-phase analysis
Smectite					
Mmt	m.c.	20 a		23	yes
Hydromica					
Illite	m.c.	50-80	24.8	5	
Kaolinite	s. q.	20	2.1	5	
ML clay		20 a			
Chlorite		20 a	4.8		
Feldspar				15	
Plagioclase			26.3		
Quartz			11.3	11.2	yes
Calcite			24.5	22 (carb.)	no
Apatite					
Sphene			2.7		
Magnetite					
Hematite					(goethite)

3.3.2. Results

Three types of material were analyzed: a raw clayey sample from the Shahumyan deposit, a purified Shahumyan sample, and a ceramic fired up to 930°C (FP930). For the two clay samples, a total mineral (material analyzed as received) and mineralogy of the clay fraction (after an orientational preparation and four treatments: air drying, vapor ethylene glycol solvation, heat treatment at 350°C and 550°C) have been performed.

3.3.3. Total mineralogy of raw (from Shahumyan deposit) and purified clay

3.3.3.1. Raw clay

The mineral composition of the raw clay (Figure 14) seems quite close to sandstone marl. The marly part consists of a mixture of carbonates, mainly calcite (3.04 Å) associated with a little dolomite (2.90 Å) and a complex assembly of clays (4.51 Å) (probable smectite-chlorite mixture (broad reflection at ≈ 14.5 Å), kaolinite (7.16 Å) and illite (10.0 Å)), the sandstone part is composed of quartz (3.34 Å and 4.26 Å) and feldspar from the plagioclase group (albite type (3.20 Å)). The two main phases are therefore calcite and quartz. Traces of gypsum ($\text{CaSO}_4 \cdot 2\text{H}_2\text{O}$) were observed (7.62 Å). Finally, very weak reflection at 9.04 Å unidentified.

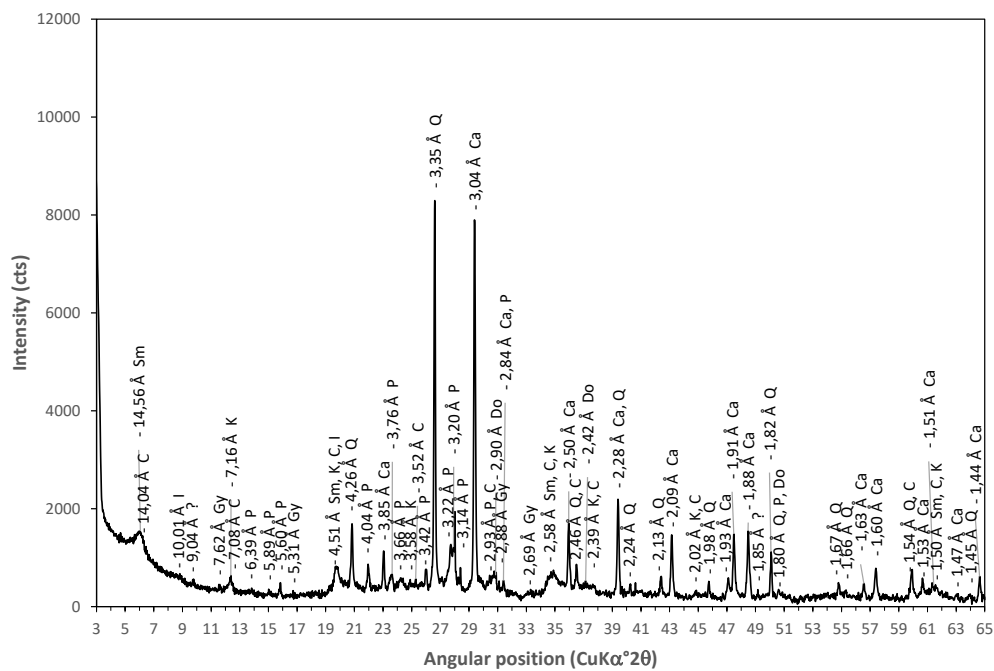


Figure 14. Diffractogram of Armenian clay powder from Shahumyan/Yuva deposit as received. Minerals: (C) Chlorite, (Ca) Calcite, (Do) Dolomite (?), (Gy) Gypsum, (I) Illite, (K) Kaolinite, (P) Plagioclase (Albite-type), (Q) Quartz, (Sm) Smectite.

3.3.3.2. Purified clay

60 g of clay mixture (clay-sand) was used for the purification. The yield of clay after purification is 1.7% by weight. The diffractogram of purified clay (Figure 15) reveals a sample mainly clayey with a small amount of quartz and traces of plagioclase (albite). Therefore, the “purification” process led rather successfully to the elimination of carbonates and the concentration of clay minerals. Amongst which, probable smectite-chlorite mixture (broad reflection at $\approx 14.5 \text{ \AA}$), kaolinite (7.16 \AA), and illite (10.0 \AA), in agreement with the analysis of the raw sample (Figure 14).

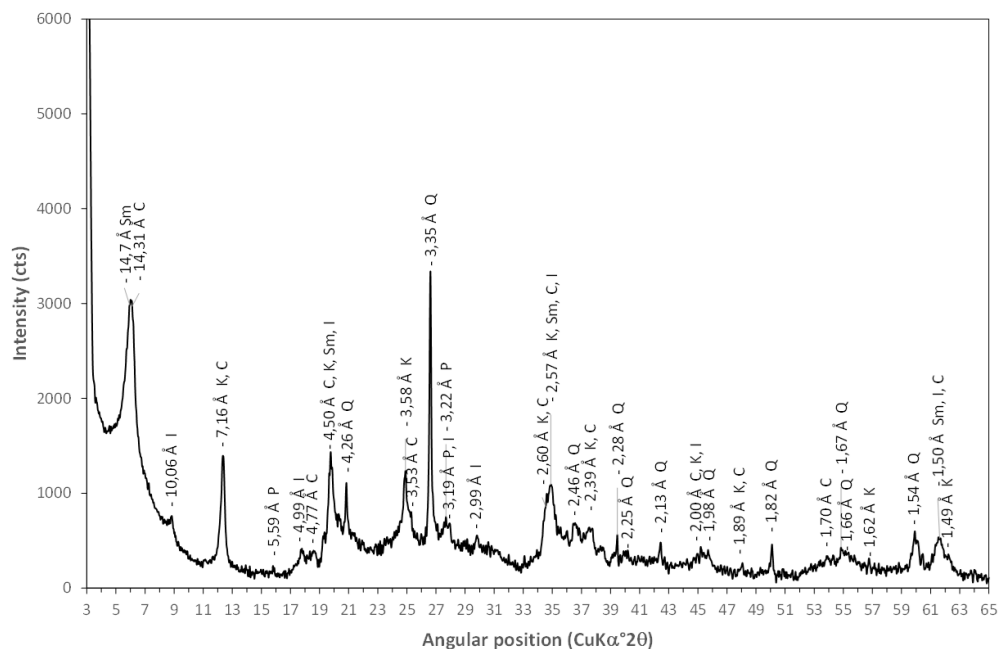


Figure 15. Diffractogram of Armenian purified clay powder (Shahumyan/Yuva deposit). Minerals: (C) Chlorite, (I) Illite, (K) Kaolinite, (P) Plagioclase (Albite-type), (Q) Quartz.

3.3.4. Clay fraction mineralogy of raw Shahumyan sample

Besides identifying clay mineralogical composition, heat and ethylene-glycol treatments were carried out to determine the nature (swelling properties) of the clay (Figure 16). The goal of this analysis is to precisely determine the nature of the clay minerals that make up the “clayey” materials used to manufacture ceramics. Moreover,

from the surface of the major reflections (001) of each of the clay minerals, and assuming that their reflection index is close to 1, it is possible to estimate their respective proportions.

Very close results have been obtained for the raw and purified samples and we only discuss the result of the purified sample.

Smectite is the main (49%) mineral group of the clay minerals in the clay Table 9.

A series of basal reflexes are fixed on the X-ray patterns of the samples (Figure 16). An intense reflection (14.5 Å) is fixed on the air-dried sample. After ethylene-glycol saturation, the interlayer distance increases to (16.7 Å) due to the swelling properties of the smectite. After thermal treatment decreases (9.6 Å). Next intense reflection (10 Å), as well as two weak (4.45 Å; 3.22 Å) reflections, remain after all treatments.

Kaolinite, which is the second mineral in the clay composition (19%) by its quantity Table 9), on the diffractogram (Figure 16) X-ray diffraction patterns of air-dried, ethylene-glycol-saturated, and thermal treated samples show two intense reflections (7.15Å and 3.58Å), that disappear after heat treatment at 550°C and one weak reflection (4.45Å) which is fixed also after all type of treatments.

Chlorite constitutes about 9% (16% in the raw sample) of the clay fraction (Table 9). On the diffractograms (Figure 16) of the samples is fixed an intense reflection (14 Å), which does not change after its treatment, but is shifted (14.3 Å; 14.2 Å; 13.8 Å), then it shows one more intense peak (7.1 Å) a and small peak (4.7 Å) which disappear after heat treatment at 550°C. The fourth peak (3.52 Å) also disappears after heat treatment at 550°C.

Mixed-layered clay (chlorite/smectite type) makes up 14% of the clay composition (Table 9).

On the diffractograms, the air-dried sample shows an intense reflection (14.5 Å). After ethylene-glycol saturation the interlayer distance increases (15.1 Å) due to the swelling clay smectite in its composition. After thermal treatment (550 °C) the interlayer distance decreases (12.1 Å). A weak reflection (4.45 Å) remains in all treated samples.

Illite (hydromica group) is a non-expanding clay mineral. Our sample contains 9% of Illite (Table 9). On the (Figure 16), the basal reflections (10 Å, 5 Å) are fixed, which do not change after saturation of the samples with ethylene-glycol and heat treatment at

550°C. Weak reflections, (5 Å; 4.5 Å; 3.3 Å) fixed for air-dried sample, remain during the ethylene-glycol and heat treatment.

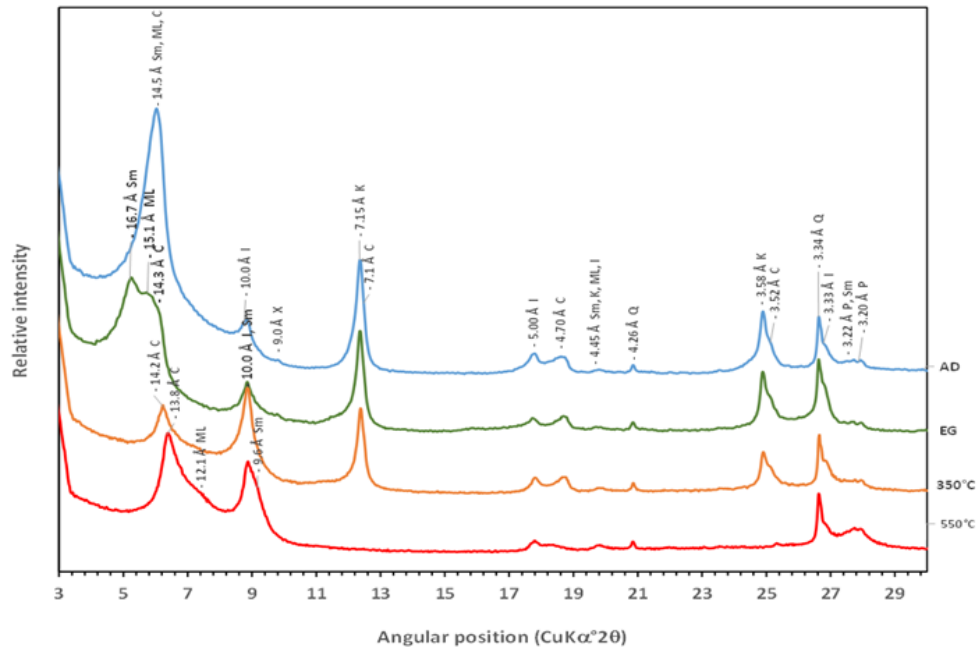


Figure 16. Diffractograms of oriented preparation of purified Armenian clay from Shahumyan. Air-dried (AD), ethylene-glycol (EG) saturated and thermal treatments at 350°C and 550°C. Minerals: (C) Chlorite, (I) Illite, (K) Kaolinite, (ML) Mixed-layer (C/S type), (P) Plagioclase, (Q) Quartz, (Sm) Dioctahedral smectite, (X) Non identified (zeolite or amphibole probably).

Table 9. Mineralogical composition of clay fraction of the raw Shahumyan sample

Clay mineral species	Position °2θ	d (001) Å	Area cts. °2θ	Ratio %
Smectite	5.295	16.68	975	49
Kaolinite	12.3709	7.15	389	19
Mixed-layer	5.842	15.12	273	14
Chlorite	6.183	14.28	181	9
Illite	8.855	9.98	176	9

3.3.5. Mineralogy of ceramic tablet fired at peak temperature 930°C (FP930)

The ceramic is mainly constituted (Figure 17) of quartz (3.34 Å), plagioclase (3.18 Å) (albite-bytownite sequence) associated with diopside (2.99 Å), gehlenite (2.86 Å), and hematite (2.69 Å). The formation of diopside and gehlenite is the result of the decomposition at about 800°C of the calcite present in the clay [66], [45], [67]. Moreover, by realizing CO₂, this decomposition also contributes the porosity formation. The presence of hematite in ceramics is noteworthy, as it is a source of iron. If Fe can move to the wine in its oxidized form (Fe³⁺), it can catalyze wine oxidation. The determination of these minerals is crucial for the rest of the study because they are constituents that may be in direct contact with the wine and form the source of migrating elements.

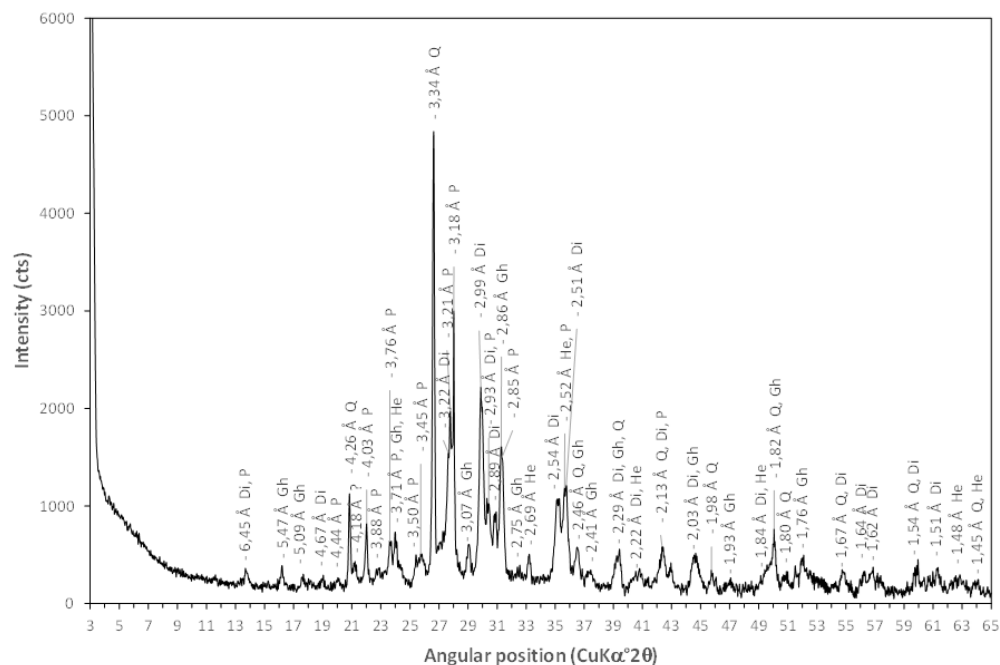


Figure 17. Diffractogram of the ceramic (FP930). Minerals: (Di) Diopside, (Gh) Gehlenite, (P) Plagioclase, (Q) Quartz, (He) Hematite

From Table 10, without entering into many details, it appears that the clay minerals (present in the clay) disappeared after being fired at 930°C. The only components present in both clay and ceramic are quartz and plagioclase. These chemical changes result from the transformation of clay minerals caused by heat treatment:

- It is well known that the clay mineral kaolinite transforms into metakaolin in the temperature range of 450–850°C [68], [69], which turns into gehlenite [66] at 850–900°C [44], [70].
- The firing of calcite- and dolomite-rich clays above 900°C yields the gehlenite and diopside [45], [71].
- Illite disappears in the temperature range of 950-1050°C [72].
- The carbonates (calcite and dolomite) present in clay are decomposed (800-1000°C) by heat treatment and not observed in ceramic (at least in a crystalline form) [67], [73].

Table 10. Minerals identified in Shahumyan row and purified clay materials and ceramic products (minerals for chlorite and smectite groups are reported as possible minerals in clay), Mmt stands for Montmorillonite.

Clay		Ceramic (FP930)	
Chlorite			
Clinocllore:	$(\text{Mg, Fe}^{2+})_5\text{Al}(\text{Si}_3\text{Al})\text{O}_{10}\text{OH}_8$	Diopside	$\text{CaMgSi}_2\text{O}_6$
Chamosite:	$(\text{Fe}^{2+}, \text{Mg, Fe}^{3+})_5\text{Al}(\text{Si}_3\text{Al})\text{O}_{10}\text{OH}_8$	Gehlenite	$\text{Ca}_2\text{Al}(\text{AlSi})\text{O}_7$
Calcite	CaCO_3	Hematite	Fe_2O_3
Dolomite (?) (only in non-purified clay)	$\text{MgCO}_3 \cdot \text{CaCO}_3$		
Gypsum	$\text{CaSO}_4 \cdot 2\text{H}_2\text{O}$		
Illite	$\text{K}(\text{Al, Mg, Fe})_2(\text{Si, Al})_4\text{O}_{10}(\text{OH})_2 \cdot \text{H}_2\text{O}$		
Kaolinite	$\text{Al}_2\text{O}_3 \cdot 2\text{SiO}_2 \cdot 2\text{H}_2\text{O}$		
		Plagioclase:	
Plagioclase (Albite-type)	$\text{NaAlSi}_3\text{O}_8$	Albite	$\text{NaAlSi}_3\text{O}_8$
		Labradorite	$\text{Ca}_{0.6}\text{Na}_{0.4}(\text{Al}_{1.6}\text{Si}_{2.4})\text{O}_8$
		Bytownite	$\text{Ca}_{0.8}\text{Na}_{0.2}(\text{Al}_{1.6}\text{Si}_{2.4})\text{O}_8$
		Anorthite	$\text{CaAl}_2\text{Si}_2\text{O}_8$
Dioctahedral Smectites:			
Ca-Mmt	$\text{Ca}_{0.2}\text{Al}_2\text{Si}_4\text{O}_{10}(\text{OH})_2 \cdot 10\text{H}_2\text{O}$		
Na-Beidellite	$\text{Na}_{0.5}\text{Al}_2.5\text{Si}_{3.5}\text{O}_{10}(\text{OH})_2 \cdot \text{H}_2\text{O}$		

3.3.6. Conclusion

Based on the results of the X-ray diffraction analysis, we can conclude that:

- The heat treatment necessary for the making of ceramic tablets entailed the total modification of the clay minerals forming the basic clay materials. The minerals we observed in raw clay powder, were not identified in ceramic tables fired at 930°C.
- The clay from the Shahumyan/Yuva deposit contains lots of quartz which acts as a degreaser, i.e. an element ensuring the structural cohesion of the clay paste during the manufacturing operations (drying and cooking) and playing a preponderant role in certain qualities (mechanical resistance and impermeability in particular) of the ceramic obtained.
- The deposit clay also contains a large amount of calcite (CaCO_3) that contributes to the formation of the principal calcium minerals in the ceramics (gehlenite ($\text{Ca}_2\text{Al}(\text{AlSi})\text{O}_7$), diopside ($\text{CaMgSi}_2\text{O}_6$), and plagioclases of the albite-bytownite sequence ($(\text{Ca}_{0.8}\text{Na}_{0.2}(\text{Al}_{1.6}\text{Si}_{2.4})\text{O}_8)$).
- Hematite is also present in the ceramic, this is of prime importance since it is a source of iron that can catalyze wine oxidation.

3.4. Determination of porosity of clay-based ceramic by He-pycnometry

Ceramics are well known for their porosity, which is a key point of their application. The porosity of ceramic materials varies from 20-95% [74]. It may contain closed pores (no access to the environment), as well as open pores (accessible from the outside). Porosity in natural ceramics depends on their genesis while in synthetic ceramics, it depends on their manufacturing. The porosity of ceramics is usually classified according to their pore size: microporous (< 2 nm), mesoporous (2-50 nm) and macroporous (> 50 nm) [75], [76]. In our study, porosity of ceramics obtained at two firing temperatures were investigated, but the goal is not to study the porosity in function of the heating protocol or going into details about the classification of pores and pores size distribution. It is clearly to measure the porosity and surface area, with a sufficient confidence because they are important characteristics impacting the dissolution of the ceramic in the wine.

3.4.1. Results

The results obtained from the pycnometry measurements reported in Figure 18 allow us to have an estimation of the porosity of ceramics. Tablets issued from FP800 and FP900 have similar porosity. There is a significant discrepancy between the big (63%) and small (80%) tablets. It is certainly due to the high uncertainty of the measurement on the small tablet.

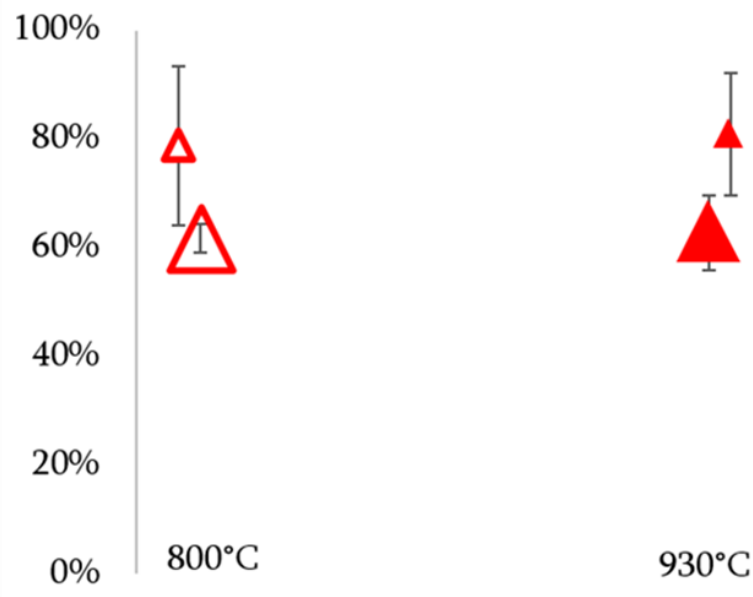


Figure 18. Porosity of big (big triangle) and small (small triangle) ceramic tablets fired at 800 °C (open triangle) or 930° C (filled triangles).

3.4.2. Discussion

There is rich reference data on the effect of temperature on the porosity of ceramics. It is well known that firing temperature [77]–[80], as well as the heating rate [76] have an influence on the porosity of the ceramics. The analysis of the above-mentioned literature data shows that the increase in temperature leads to a decrease in the porosity of ceramics but it becomes significant above 950°C [80]. Consistently in our case, no porosity variation is observed between the two firing protocol. The open porosity measured (63%, if we consider big tablets) allows to classify tablets as a high-porous ceramics.

However, to be able to analyze the interaction between ceramic tablet and model wine in point of view of the dissolution of minerals we need to know not only the porosity, but also specific surface area of the ceramic.

3.5. BET (Brunner-Emmett-Teller) characterization of ceramic tablets

BET theory is used to measure the surface area of solid or porous materials. This gives an important information about their physical structure, since the surface area of a material influences how that solid will interact with its environment [81]. BET method was used to determine the specific surface area (m^2/g) of FP 930 ceramic tablets as well as for a real fragment of Armenian pithos.

3.5.1. Results

The specific surface area of the ceramic tablets measured by the BET technique is $2 \text{ m}^2/\text{g}$. Remarkably, the same measurement on a fragment of an Armenian pithos (degassed at 600°C) give a close value of $2.2 \text{ m}^2/\text{g}$.

3.5.2. Conclusion

In this chapter we discuss the porosity of ceramic tablets as a function of temperature. Concluding the results from He-pycnometry measurements, we see that:

- the porosity of ceramic tablets is high (62%-81%) according to the classification of porous ceramics.
- no difference was observed between the two firing programs for either large (FP800 - 62%, FP930 - 63%) or small (FP800 - 79%, FP930 - 81%) tablets, probably due to the low sensitivity of the technique used.
- there is a difference in porosity between big and small tablets of about 20%, which may be related to the limit of measurements of the instrument for small tablets.
- The surface area of our ceramic made in the laboratory is comparable to the one measured on a fragment of an Armenian pithos: $2 \text{ m}^2/\text{g}$ for the tablets, $2.2 \text{ m}^2/\text{g}$ for the pithos.

3.6. Characterization and chemical analysis of ceramic by scanning electron microscopy (SEM)

Scanning electron microscopy may provide high-resolution imaging of the surface of materials. SEM images allow evaluating the differences on the surface of the sample as well as between different samples. When associated with energy-dispersive X-ray spectroscopy (EDX), SEM allows for a chemical analysis of the surface. For our study, SEM images (on a μm scale) and EDX analyses have been performed in the laboratory of the National Research Institute for Agriculture, Food, and Environment (INRAE) in Dijon.

Numerous images of the clays and ceramics have been recorded. We have selected very few of them to illustrate morphology, porosity and chemical composition aspects of the ceramics discussed in the three previous chapters.

Ceramic tablets made up of Shahumyan's clay deposit (Armenian) and fired up to 930°C were used. To obtain internal images of the ceramics, the tablets were simply cracked.

3.6.1. Results

3.6.1.1. SEM analyses of raw clay powder from Shahumyan's deposit

SEM images of raw clay powder illustrated in Figure 19 show that the sample is morphologically homogeneous [82] and consists of randomly oriented particles of different sizes. A simple morphological comparison with SEM images of the literature shows similitudes with images obtained on mixture of smectite, kaolinite and illite [83] which was previously revealed by XRD results (Table 9).

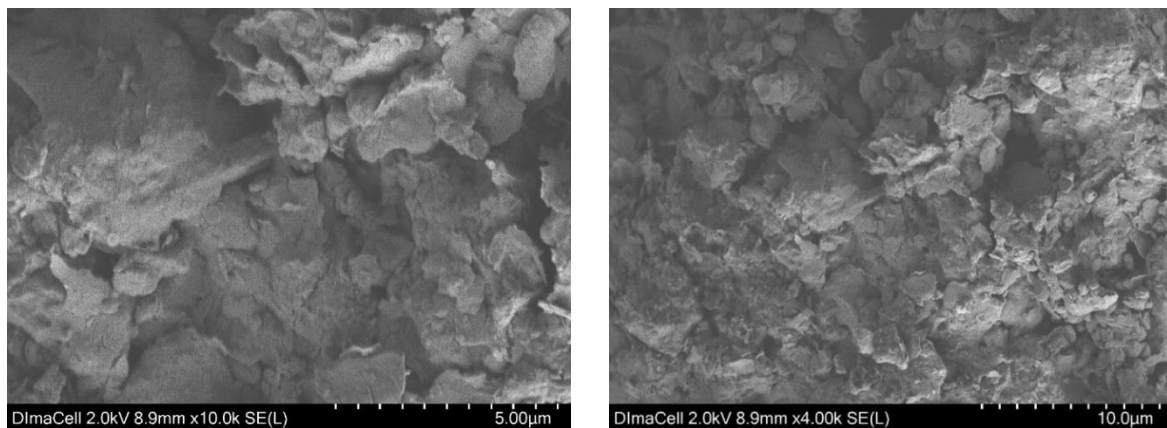


Figure 19. Microstructure of raw clay powder from Sh1 sample (Shahumyan deposit)

According to Armenian sources, the clay from Shahumyan's deposit contains a rich complex of marine fauna found during the excavations such as corals, foraminifers, gastropods etc. Most characteristic is the presence of microfaunal shells, fragments of crinoids, and algae, which are also mixed with hard and clayey matter and calcite, thus autogenous clay minerals develop on a clay base of rock fragments and minerals, as well as the remains of microorganisms [23].

Consistently, during SEM observations in the raw clay powder, phytoplankton (algae) fossils like diatoms (a) [84]–[86] and coccolithophores (b) [87], [88] were observed (Figure 20). Coccolithophores are distinguished by calcium carbonate scales (coccoliths). This may be of interest for the explanation of the high concentration (15-22%) of calcium containing in raw clay [89], [90]. Fossils are also used as a *biostratigraphic* and paleoecologic indicators [91]. From a geological perspective, the fossils found in raw clay indicate that the Shahumyan's clay deposit has marine/oceanic origin, since diatoms and coccolithophores are widespread in water ecosystem [92]. The fact that the deposit has a marine/oceanic origin, is also cited by Armenian scientists [23], [28].

It is not our task to determine the species affiliation of the discovered remains, but the literature data allow us to make a rough conclusion that this refers to the species *Coccolithus pelagicus* [87], [93]. This is the only extant species and belongs to cooler (up to 18°C) water form (arctic form and temperate form) [94].

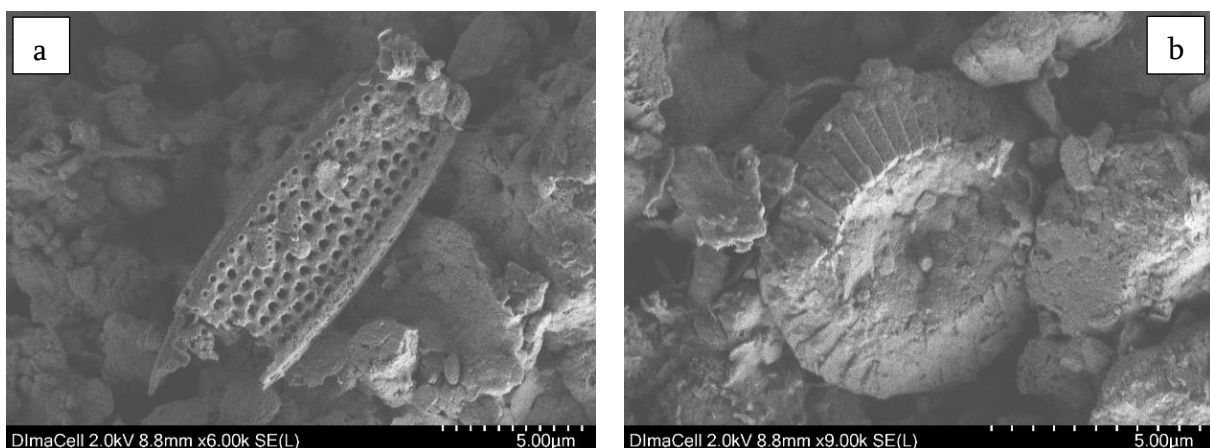


Figure 20. SEM images of clay powder from Shahumyan deposit (Armenia). Diatomite (Bacillariophyta) (a) ($\sim 5 \mu\text{m}$ in diameter, and $\sim 15 \mu\text{m}$ in length) Coccolithophore - *Coccolithus pelagicus* (b) remains ($\sim 8 \mu\text{m}$ in diameter).

Scanning electron microscopy also shows the presence of plant roots and porous stem-like remains (Figure 57, Annex III). The terroir is fundamentally and intimately a factor affecting the quality of wines and these images, maybe more suggestive when the presence remains of living organism is revealed, show that pithoi or other ceramic containers may also bring a contribution of the land to the wine.

3.6.1.2. SEM analyses of ceramic

The SEM images in Figure 21 show the morphological change of the sample after heat treatment. Tablets fired at 930°C were morphologically changed due to the phase transformation of clay minerals. It can be seen how the crude tablet with apparently no porosity is transformed into a highly porous ceramic material. The coarse texture of the microstructure of the ceramic is typically obtained when a calcareous clay (containing more than 6% of CaO [95] is used for the ceramic production. The calcareous nature of the clay was previously observed by XRF analysis (Table 7). From images obtained by SEM, the ceramics consist mainly of macropores (> 50 nm).

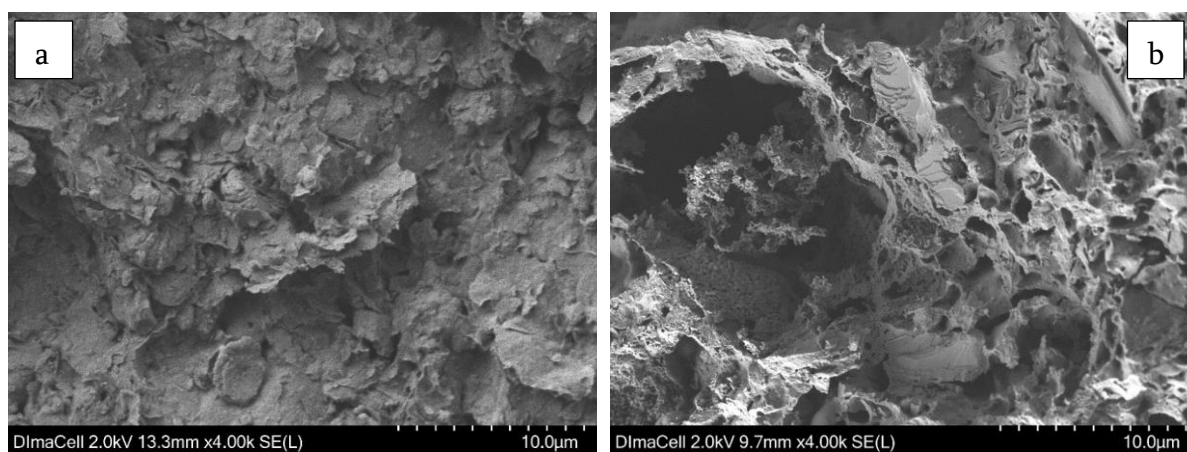


Figure 21. The change of the microstructure of tablet before (a) and after (b) firing at 930°C.

3.6.1.3. SEM/EDX elemental analysis of ceramic

During the EDX measurements, different areas were focused. Details of the measurements on seven areas in 26 points in atomic % are listed in Table 18 (Annex III).

Seventeen elements (O>>Si>Ca>Al>Mg>Fe>K>Mn>Na>Ti>S>Cr>F>P>Cl>Mo) were determined in ceramic. The mean values of the elemental composition of the ceramic acquired from 26 points is presented in Table 11. The EDX analysis indicated the presence of oxygen, silicon, calcium, and aluminum as the main element in the sample. Elemental mapping of ceramic is presented in Table 19 and Table 20 of Annex III.

Table 11. Mean of the SEM/EDX analysis of ceramic fired at 930°C. The observations have been performed at the point levels on a scale of 10 µm. The number of points analyzed is 26. The results are expressed in atom and weight (%).

Elements	Atomic %	Elements	Weight %
O	52.9	O	40.58
Si	14.6	Si	13.06
C	9.93	Ca	12.23
Ca	7.6	Al	11.51
Al	5.82	Fe	6.76
Mg	3.03	C	6.66
Fe	2.08	Mg	4.21
K	1.32	K	2.27
Mn	1.23	Na	1.14
Na	1.07	Ti	0.55
Ti	0.29	F	0.4
S	0.06	Mn	0.21
Cr	0.04	S	0.09
F	0.03	Cr	0.04
P	0.009	Mo	0.04
Cl	0.008	Cl	0.01
Mo	0.009	P	0.008
Total	100	Total	99.75

3.6.2. Discussion

3.6.2.1. Image analysis of ceramic tablets

A localized melting process is observed (Figure 22), which leads to the destruction of the minerals structure in ceramic. It can be related to the vitrification of the material (starting at $\sim 850^{\circ}\text{C}$ and higher) [96], [97].

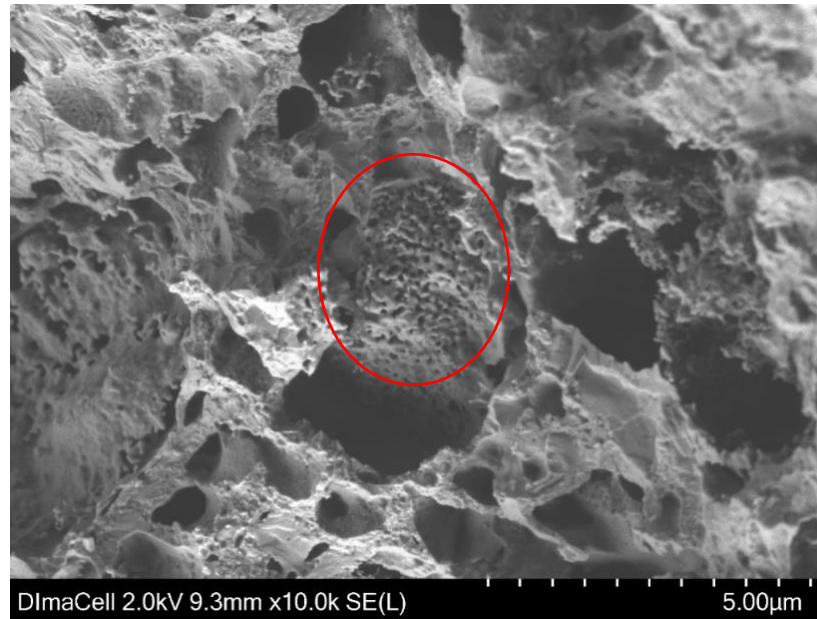


Figure 22. SEM image of ceramic tablet fired at 930°C showing the melting process.

Figure 23 compares the exterior and interior parts of the ceramic tablet under SEM. On its external surface, the ceramic is covered by an apparently homogeneous layer and the porosity of the ceramic is not directly open to the exterior.

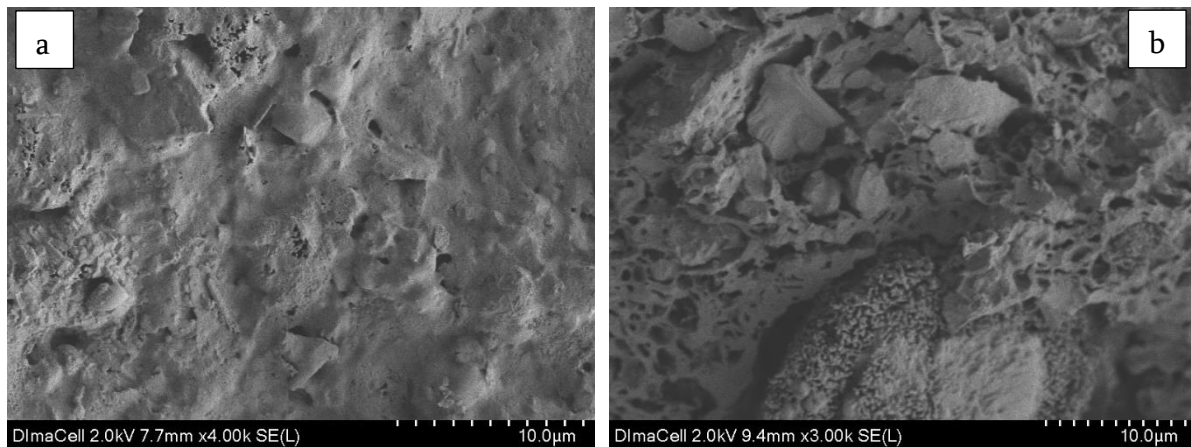


Figure 23. SEM images of ceramic tablet fired at 930°C . The surface of the tablet (a) and interior part (b).

3.6.2.2. Qualitative analyses

In agreement with previous XRD and XRF results on clay, and ceramic, EDX analyses exhibit the presence of silicon, calcium, aluminum, magnesium iron, potassium, manganese and sodium as the main cations (Figure 24). However, the dominant elements is oxygen (52.9%), which indicates that metal oxides are abundant (amorphous or crystalline phases) in the ceramic [97]. The clay (aluminosilicate) can be associated with the principal source of the high amount of Si and Al observed in the ceramic.

The abundance of calcium in ceramic is related to significant amount of calcite in the Shahumyan clay deposit (the XRF, Table 7, reports about 10% of CaO in the starting material (clay body)).

The presence of Fe, Mn, and Ti is an important point for relaxometric measurements. They are discussed in more detail in the next chapter.

Significant amounts of K, Mg and Na are detected (1-3%) and trace elements like S, Cr, F, P, Mo, Cl are also revealed (< 0.1%).

Results obtained by SEM/EDX analysis are in close agreement with the literature data [98]–[100].

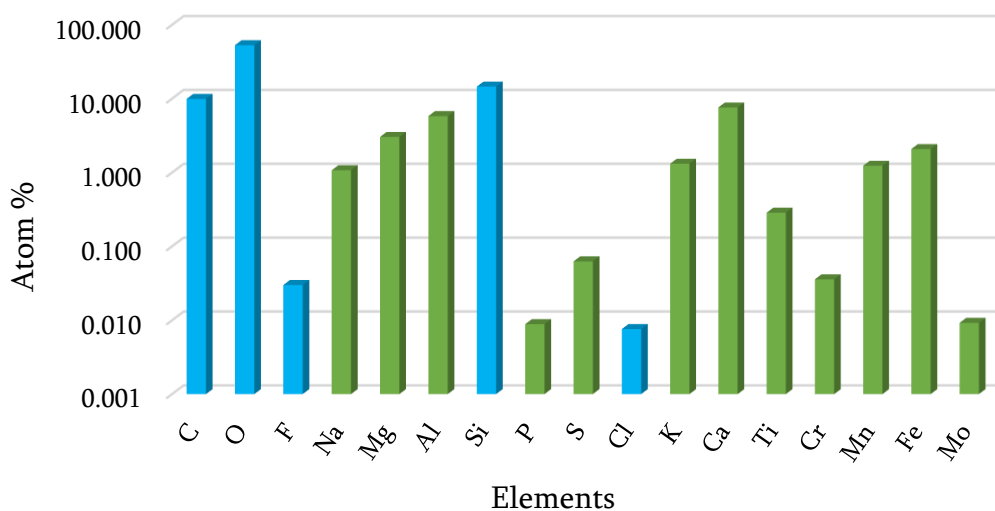


Figure 24. Elemental average concentration in ceramic, measured with 26 points from seven areas. Blue columns represent elements identified only by SEM/EDX. Green columns represent elements identified by both ICP-AES and SEM/EDX methods.

3.6.3. Conclusion

The microstructural and qualitative investigation in different areas of the ceramic fired at 930°C were performed. Based on the obtained results on the elemental composition and microstructure of ceramics, we conclude, that:

- (i) Ceramic tablets have a high porosity, which is not widely open to the exterior.
- (ii) Qualitative analysis identified the presence of 17 elements in ceramics, amongst most abundant are Si, Ca, Al, O in consistency with XRF results.

Chapter 4. Ion migrations from ceramic to wine

4.1. Ion migrations from ceramic to model wine followed by ICP-AES

From a general point of view, although earthen-ceramics are resistant to corrosion, it is not always possible to avoid negative environmental influences. In the construction domain, corrosion of bricks or tiles, due to acid rain ($\text{pH} < 5$) [101]. Over time, the ceramic substance decomposes which leads to the dissolution of minerals forming the ceramics. The dissolution of ceramic depends on the pH and temperature of the environment, but also on the specific surface area of the material [73]–[77]. Wines being relatively acidic (pH around 2.5) may dissolve the ceramic at the expense of its organoleptic properties. This chapter is devoted to the inductively coupled plasma atomic emission spectroscopy (ICP-AES) elemental analysis of model wines, which were in contact with a ceramic for various periods of time, from 1 hour to 16 months.

ICP-AES is a powerful multi-element analysis method used for the detection of chemical elements suited for the direct analysis of solutions. It uses the inductively coupled plasma to produce excited atoms and ions that emit electromagnetic radiation at wavelengths characteristic of a particular element [107]. The method is based on the principles of atomic spectroscopy being able to determine of more than 70 elements with detection limits in the ppb to ppm range [54]. Vaporization and atomization of the samples take place in an extremely high temperature ($\sim 7000\text{ }^\circ\text{C}$) argon plasma generated by radio frequency coupling [108].

4.1.1. Sample preparation

Twenty samples were prepared for the analysis. For each sample, one ceramic tablet was placed in a 10 mm NMR tube, then 2.8 ml of model wine was added, after which the tube was flame sealed. The ratio of the volume of the model wine to the volume of the headspace was around 1:3. In the sealed tubes, in a controlled environment, the model wine was left in contact with the ceramic from 1 hour up to 16 months. All samples were stored at $25\text{ }^\circ\text{C}$ (during the first day in a water bath, with moderate exposition to the natural light of the laboratory, then in regulated thermal ($25\text{ }^\circ\text{C}$) chamber, in darkness). After aging for

suitable period, the liquid phase was separated from ceramic and sediments formed during the aging. Supernatant was flame sealed (with a ratio of volume of the model wine to the volume of the headspace less than 1:2) and stored at 25 °C in darkness until the last aging period (16 months) has elapsed. Eventually all samples were chemically analyzed by ICP-AES at the same time.

4.1.2. Results

Amazingly, the elemental analysis of model wine reported in Figure 25 shows a large variety of elements. Even if most of them were below the limit of quantification few elements are present in significant amount, and it is legitimate to question the reliability of this measurement. Tartaric acid is probably the more contaminated component of the model wine and we suspect it is the main source of the quantified elements (Al, B, Ca, Na, P). Its purity is given as > 99.7 % meaning that the amount of impurity would be of the order of 0.3 % (i.e. 1.5 mg/L of impurities in the model wine containing 5 g/L of tartaric acid). A simple sum of the concentration of the quantified elements in Figure 25 gives a total of 3.1 mg/L. This amount, albeit above the impurities concentration that may be expected from tartaric acid, remains reasonable. Moreover, ethanol purity being > 99.9 %, could also be a source of an additional contamination of the order of 1mg/L. Overall, we assume that the elemental analysis of the model wine is sensible and from now these concentrations are systematically subtracted from the values of elements concentration measured in the model wines in contact with ceramic tablets.

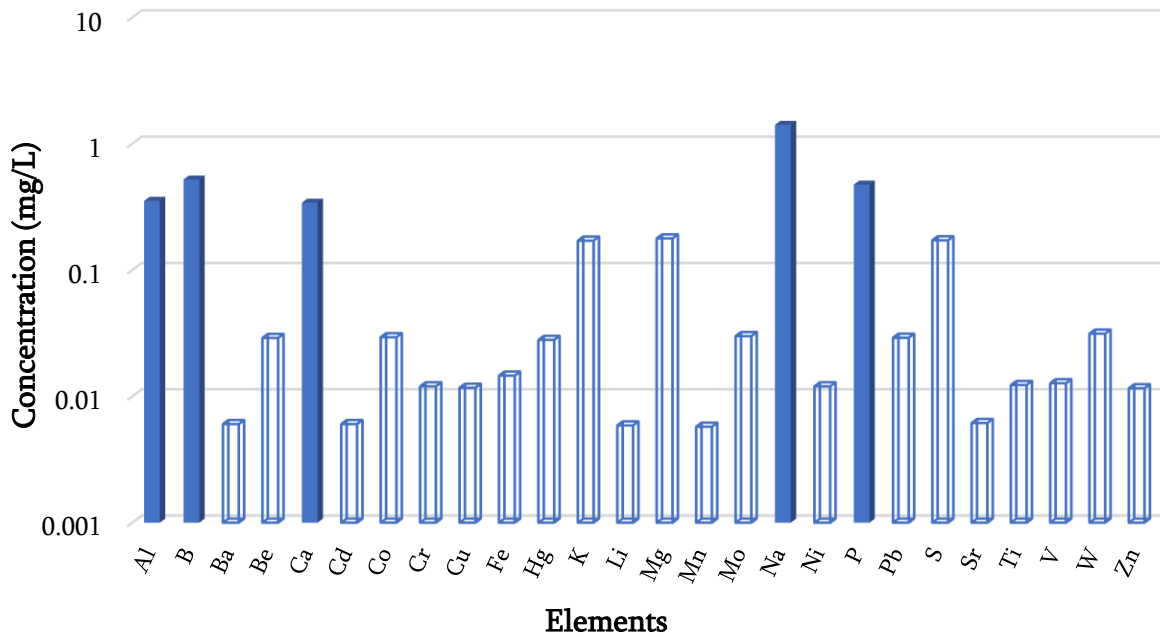


Figure 25. Elemental analysis of model wine alone (without contact with ceramic). Open columns correspond to elements below the limit of quantification (e.g. [Cu] < 11.7 $\mu\text{g/L}$).

Figure 26. shows the evolution of the elemental analyses of 19 model wines left in contact with ceramic from periods of time ranging from 1 hour to 16 months.

When the model wine is in contact with the ceramic, there is a significant migration of elements from the ceramic to the model wine (raw ICP-AES data are compiled in Table 23 of Annex VI). It should be noted that the migratory behavior of the element's changes over time, but if we try to class most abundant elements, a list could be ordered as follow: $\text{Ca} \gg \text{Na} > \text{Al} > \text{K} > \text{Fe} > \text{Mg} > \text{S} > \text{Sr}$. Compared to other elements, from the first instants, calcium stands out in an obviously high concentration. Overall, the concentrations seem to evolve with at least three-time scales: of the order of hours, days, and months (Figure 26).

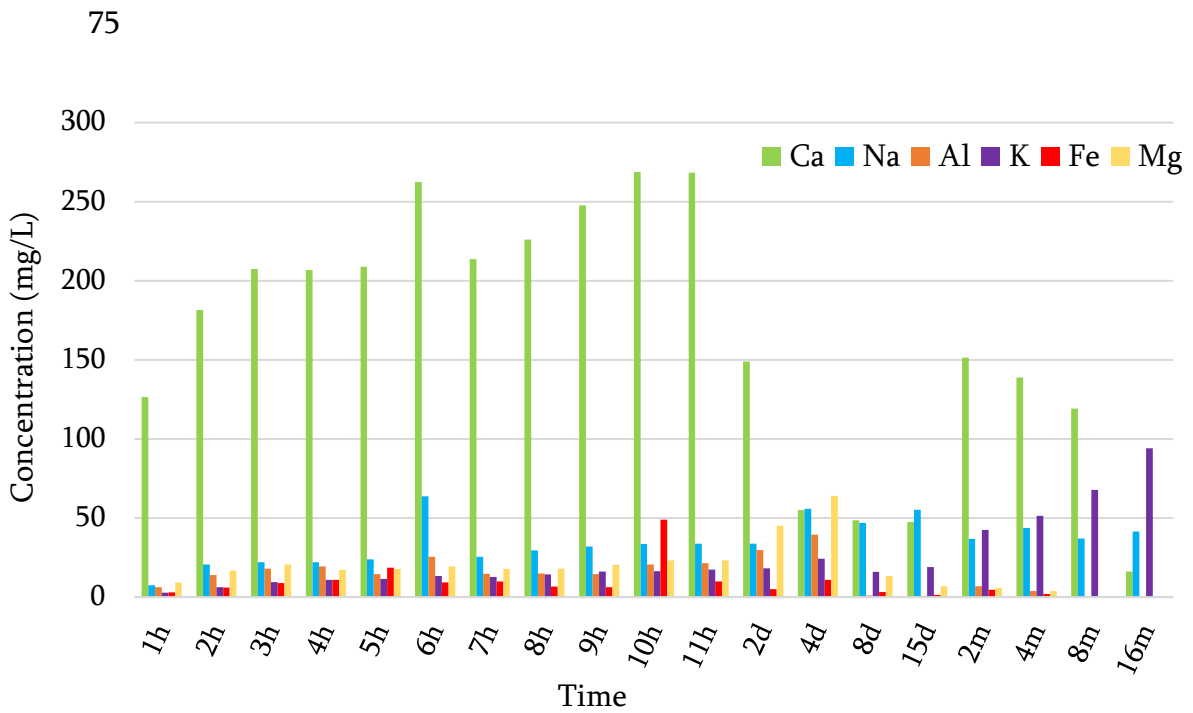


Figure 26. Concentrations of elements released from 1 g of ceramic tablet during aging from 1h (1 hour) up to 16m (16 months), d stands for days. Model wine elements concentration is subtracted.

For elements with concentration above 1mg/L, Table 12 reports the evolution of concentrations released from 1 g of the tablet to the model wine after contact with the ceramic (the migratory behavior of all elements is reported in Table 24 of Annex VI). Despite that in time each measurement is done on a different ceramic, on a logarithmic scale the evolutions are smooth except few accidents observed at 6 hours. This could be attributed to an experimental error or to a variability of the ceramic. For most elements there is a quick release during the first hours then the slope decreases. From there, three rough trends of evolution can be suspected (i) a decrease after 4 days (Al, Mg, Fe.), (ii) a rather steady state situation at a constant level over 16 months (Na, S), (iii) an increase at a long period of time (K, Cr). However, it is worth mentioning that a different time sampling of these experiments (in the presented results, it is linear during the 11th first hours and logarithmic from 2 days to 16 months, with a weak density of points) should very likely reveal more accurately (with a better resolution) details of these evolutions.

Finally, as an illustration, Figure 27 reports the elemental composition of the model wine after an 11 hour contact time with a ceramic (elemental composition of model wines for all contact times is reported in Table 25 of Annex VI).

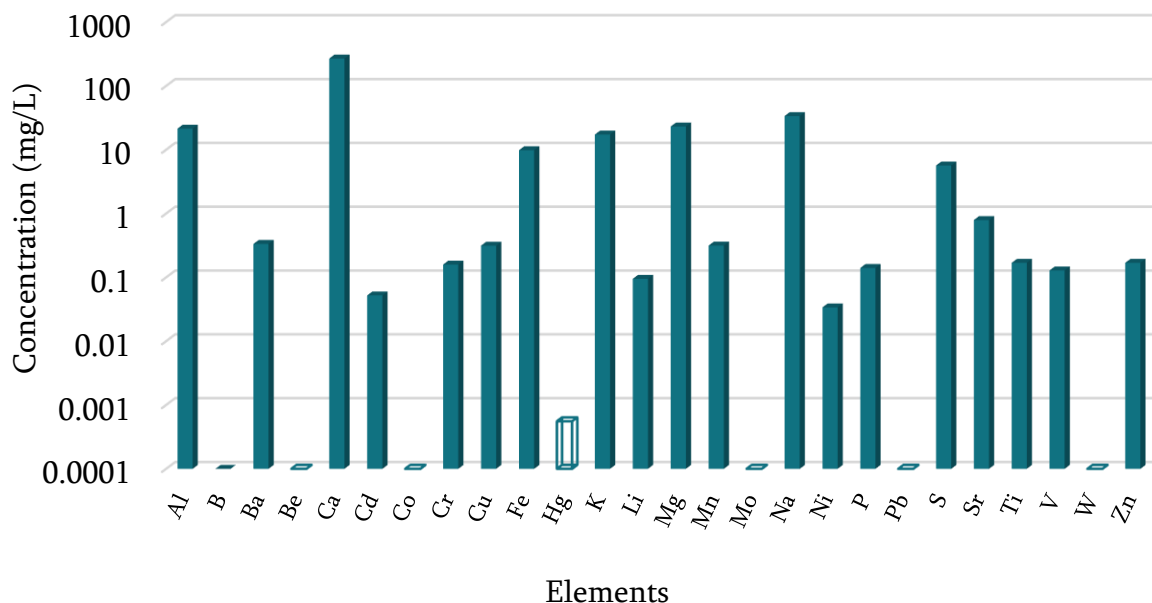


Figure 27. The concentration of elements released from 1 g of ceramic after 11 hours of contact with the model wine. Wine elements are subtracted. Elements with zero values were present in the model wine but their concentration did not increase after the contact with the ceramic. Open columns correspond to elements below the limit of quantification (e.g. [Hg] < 28.4 $\mu\text{g/L}$).

4.1.3. Discussion

We have not analyzed the evolution of all constituents and their interplays because of the tremendous underlying complexity. If necessary, the exploratory ICP-AES results reported in this section should be used as a base for the elaboration of model ceramics with targeted mineral(s) in order to simplify the analysis. However, we try to discuss mainly the concentration evolution of two dominant elements calcium and iron (Fe is further discussed in 4.2). Aluminum, potassium, and magnesium concentrations are also briefly evocated.

4.1.3.1. Evolution of calcium concentration

Simple liquid chemistry principles can be used to try to approach the evolution of the dominant element Ca, which concentration evolution is reported in Figure 28.

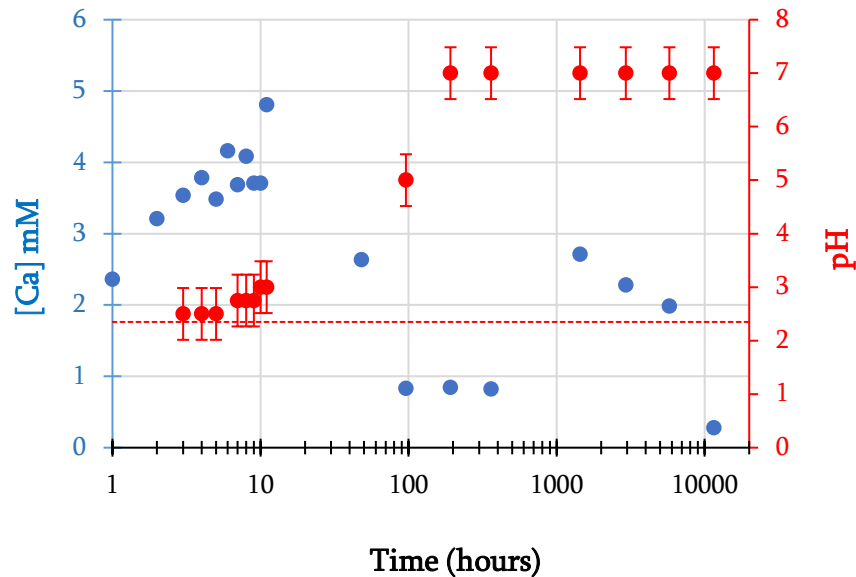
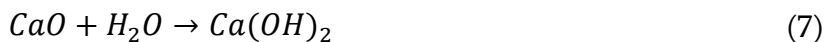


Figure 28. Blue: the evolution of calcium concentration in the model wine measured by ICP-AES (in mM) versus the contact time between the model wine and the ceramic (model wine subtracted). Red: evolution of pH. Because of few model wine was available the measurements were done by pouring a few drops of model wine onto some pH-paper, it is subject to significant uncertainties estimated as ± 0.5 and reported by error bars. The dotted line corresponds to the pH of the starting model wine (2.35).

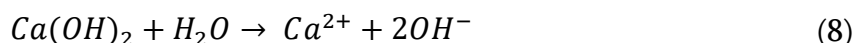
The raw materials contain lots of calcite (CaCO_3) (~15-20 % in the clay and ~10% in the mixture of clay and sand, Table 7) and in a first approach, we assume that calcite is the main raw source of calcium that migrates into the model wine. Upon firing, calcite forms calcium oxide (CaO) [76],[77], [111] which is expected to be also in a significant amount in the ceramic.



The calcium oxide reacts rapidly with liquid water (when exposed to wine and probably also to a lesser extent with atmospheric water during the storage of the ceramic) to form calcium hydroxide (Ca(OH)_2) [112], [113].



This hydroxide is known to be very slightly soluble in water (~ 1.65 g/L, 22 mM) [114], [115, pp. 4–49] but is considered as a strong base ($\text{p}K_{b1}=2.43$, $\text{p}K_{b2}=1.41$) [115, pp. 4–44]. All measured Ca concentrations are below 5mM, below the solubility of Ca(OH)_2 . It is difficult to estimate the kinetic of solvation, but one has to remember that the analyzed model wine should be at equilibrium, because after the separation from the ceramics the model wine was kept in a flame sealed tube at a controlled temperature for generally a very long period of time (from 16 months for the first samples to several weeks for the last ones). So, we may hypothesize that all available calcium hydroxide present in the model wine is dissolved and dissociated, in particular for the first experiments with small contact times (<10 hours) where no precipitation or solid phases are observed. According to Eq. (8), the dissociation of calcium hydroxide should produce an increase of the pH of the model wine as seen on Figure 28.



Assuming a total dissociation of the base, for the first samples, the pH shift from 2.35 to 2.5 would correspond to a consumption of 1.3 mM of H_3O^+ , that result of the dissociation of 0.65 mM of Ca(OH)_2 . When the pH reaches 7 the same calculation gives a dissociation of 2.2 mM of Ca(OH)_2 . It is reassuring to observe that despite the rough approximations, estimated values are of the same order as concentrations measured by ICP-AES. Albeit the estimations for the first samples (0.65 mM) presents the maximum discrepancy with the observed values (from 2 to 5 mM) it might be easier to discuss since no precipitation or solid phases are observed at initial contact times and the pH remains fairly stable. The simplest explanation of the underestimation of calcium concentration would be that more Ca is dissolved from other source of minerals. XRD have evidenced the

presence of other calcium-containing-minerals in the ceramic: diopside ($\text{CaMgSi}_2\text{O}_6$), gehlenite ($\text{Ca}_2\text{Al}(\text{AlSi})\text{O}_7$), but also plagioclase (labradorite ($\text{Ca}_{0.6}\text{Na}_{0.4}(\text{Al}_{1.6}\text{Si}_{2.4})\text{O}_8$), bytownite ($\text{Ca}_{0.8}\text{Na}_{0.2}(\text{Al}_{1.6}\text{Si}_{2.4})\text{O}_8$), and anorthite ($\text{CaAl}_2\text{Si}_2\text{O}_8$)).

The dissolution of ceramics and minerals such as diopside, hematite, magnetite, anorthite, albite... has been studied by several researchers [102]–[106], [116]. Most of these studies have focused on mineral dissolution mechanisms as a function of pH and temperature. It is worth mentioning, that literature results may reveal noticeable discrepancies of the constants of dissolution depending on the surface, size of particles [116], [117]. Some of these literature dissolution rates for few minerals are given in

Table 13. Figure 29 simulates the dissolution according to of a hypothetical tablet of mass 679 mg made of 100% of the mineral (porosity of the ceramic (section 3.5) has been considered in the calculation).

Table 13. Dissolution constant (K_d) of some minerals identified in the ceramic. The reported values are generally obtained by a flow experiment. Quartz is given for comparison. 1 stands for low (not measured) dissolutions constants in bold were used for the calculations of Figure 29.

Mineral	Formula	pH	K_d ($\text{Mol cm}^{-2} \text{s}^{-1}$)	Reference
Anorthite	$\text{CaAl}_2\text{Si}_2\text{O}_8$	3	2.7×10^{-12}	[104]
Bytownite	$\text{Ca}_{0.8}\text{Na}_{0.2}(\text{Al}_{1.6}\text{Si}_{2.4})\text{O}_8$	2-3	10^{-12}	[105]
		7	10^{-15}	
Diopside	$\text{CaMgSi}_2\text{O}_6$	2-3	2.9×10^{-14}	[103]
Albite	$\text{NaAlSi}_3\text{O}_8$	4	4.7×10^{-17}	[102]
		6	4.6×10^{-17}	
Hematite	Fe_2O_3	1	5.8×10^{-14}	[106]
Iron (III) hydroxide	$\text{Fe}(\text{OH})_3$	4-6	10^{-13}	[118]
Quartz	SiO_2	2-3	3.6×10^{-17}	[116]

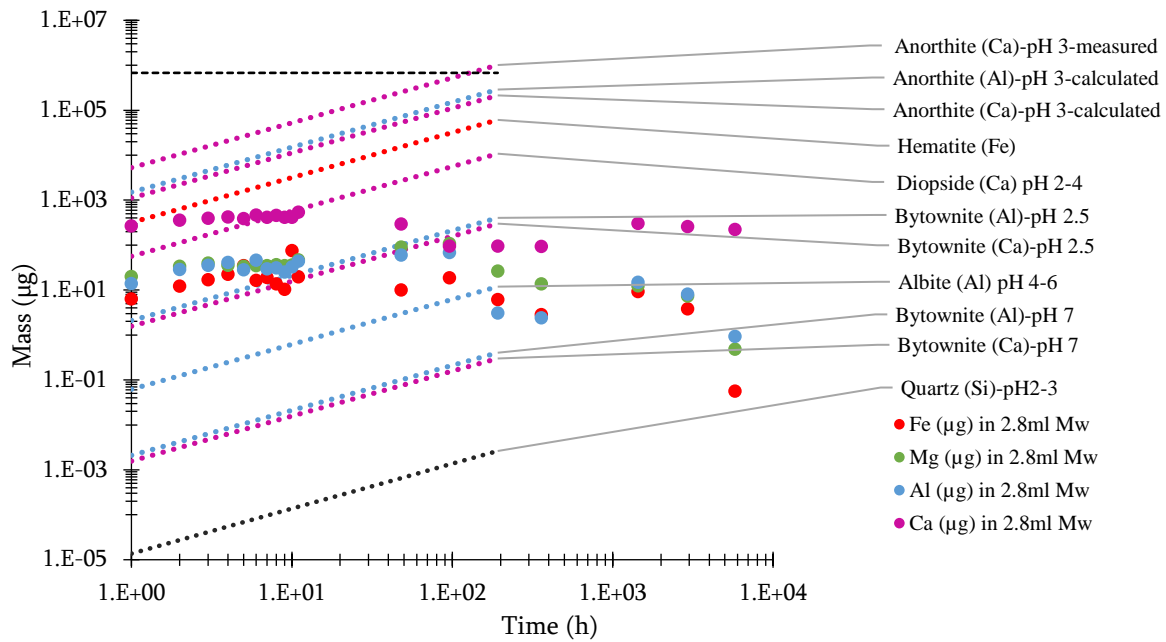


Figure 29. The mass of elements (μg) released from one tablet, measured in 2.8 ml of model wine by ICP-AES (full circles). Simulated dissolution from literature data of an equivalent tablet (same surface area, average mass of 679 mg) are reported with dotted lines. The upper horizontal dashed black line figures the level corresponding to a mass of 679 mg.

According to Figure 29, by example a tablet of anorthite at pH 3 would be able to dissolve in one hour 5.3 mg of calcium. In other words, a tablet containing 5% of anorthite (if the anorthite is homogeneous in the sample and on surface) would be sufficient to produce the amount of calcium observed by ICP-AES (266 μg) after one hour in 2.8 mL of model wine. More realistically of course, the tablets are not pure mineral, and the dissolution is not over a flow but these basic comparisons show a fairly reasonable consistency between the calculated quantities from dissolution coefficient of the literature and ICP-AES measurements. In addition, it is worth noting that Qin et al. [119] in a very similar material (ceramsites) have evidence that in conjunction of the calcium release from calcium hydroxide, minerals (like gehlenite and anorthite) are also important dissolution sources for calcium. The results of Qin et al [119] deserve to be further compare to our results and a detailed analysis of the calcium dissolution during the first hours may be

engaged. They have studied the Ca^{2+} and OH^- release of ceramsites containing anorthite and gehlenite prepared from waste lime mud.

Albeit the firing protocol of ceramsites is slightly different (*RT* room temperature):

- *Ceramsites*: $RT \xrightarrow{10^\circ\text{C}/\text{min}} (800^\circ\text{C} - 1\text{h}) \xrightarrow{15^\circ\text{C}/\text{min}} (1050^\circ\text{C} - 2\text{h}) \xrightarrow{\text{left to cool}} RT$
- *Ceramics (this work)*: $RT \xrightarrow{2.5^\circ\text{C}/\text{min}} (600^\circ\text{C} - 4\text{h}) \xrightarrow{20^\circ\text{C}/\text{min}} (930^\circ\text{C} - 2\text{h}) \xrightarrow{\text{left to cool}} RT,$

the ceramsites in the mentioned article present many similarities with our ceramic. Table 14 compares the materials and some results of Qin et al. with ours.

Table 14. Comparison of materials and some results obtained on ceramsites by Qin et al [119] and those of this work on ceramic.

	Ceramsites	Ceramic
Size	2-5 mm	4-5 mm / 7-8 mm
Density	1-1.4 g/cm ³	1.9 g/cm ³
Porosity	43-57 %	63-80%
Volume of solution	250 ml	0.6 ml / 2.8 ml <i>(it is below the limit of solubility of CaO)</i>
Masse of ceramsites/ceramics	2-10 g	0.1g / 0.8 g
Minerals contained	anorthite, gehlenite wollastonite, quartz	anorthite, gehlenite , diopside quartz plagioclase, hematite
Contact time	from 10 min to 12 h	from 1 h to 16 months

Qin et al have modeled (at initial pH 6.5) the dissolution of Ca^{2+} by an Avrami law (fixing the Avrami constant n to 0.9019):

$$\frac{C(t)}{C_{max}} = x = 1 - e^{-k t^n}, \quad (9)$$

Where k is the kinetic constant, n is characteristic constant of the solid (Avrami constant), t is the time, and x the fractional conversion ($C(t)$ is the concentration at time t and C_{max} is the maximal concentration).

They obtained kinetic coefficients from 0.0077 to 0.0125 min⁻ⁿ. In 12 hours, 30 or 90 (depending on the ceramsite) mg of calcium were released per liter of water. An identical fit to our data (Figure 30) give satisfying modeling, with the following numerical results: $C_{max}=153(7)$ mg/L , $k=0.025(7)$ min⁻ⁿ, and $n=0.9019$ (fixed).

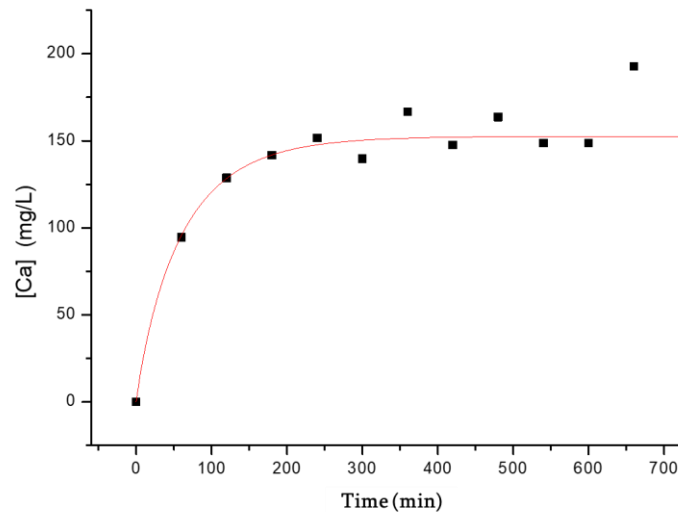
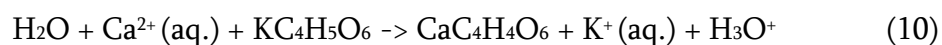


Figure 30. Refinement of the dissolution of calcium during the first 12 hours contacts with an Avrami law: $C(t) = C_{max} (1 - e^{-k t^n})$

Our ceramic has a kinetic constant twice the one obtained by Qin et al, this can be attributed to the lower initial pH in the wine (2.55) than in the water (6.5), but also to the higher porosity of the ceramic (63-80%) with respect to the ceramsite one (50%). Qin et al. have observed the same correlations; in particular, by varying the initial pH of the solution they observed very little difference in solutions with pH from 10.7 to 4.6. However, a drastic increase of solubility (x4) is obtained when the solution has an initial pH of 2.37.

The discussion for long contact time (time > 12 hours, reported in an adapted linear scale in Figure 31) is rather delicate. The calcium evolution is clearly not monotonous. There is a decrease of the calcium concentration after 10 h and it seems to stabilize from 100 to at least 350 hours (4 to 15 days). Then the measurement at 1500 hours (2 months) show that the concentration has increase by a factor of nearly 4, from there it decreases slowly and apparently linearly to ultimately reach its minimum. At this stage, we do not want to make hazardous hypotheses, but several point can be highlighted:

- (1) In front of the complex evolution of calcium concentration, the reliability of the measurement can be questioned. However, on regard of the previous discussion at low contact times, the measured concentration seems to be reliable up to 12 hours. Some other elements seem to have a smooth evolution (like potassium, sodium...) over the whole period of evolution. It seems unlikely that only the first measurements were correct and the other not, and we think that the concentration measured are sensible.
- (2) As mentioned previously, we think that the studied solutions were in equilibrium (the solution was separated from the ceramic and left in a controlled condition for several weeks or months before ICP-AES analyses). This would mean that the differences observed are due to longer contact with the ceramic and that even at very high pH and after a very long period the ceramic still impact the wine.
- (3) In the literature, the evolution (e.g. oxidation) of wine is generally analyzed in regard of organic molecules (catechin etc.) [120]–[123] over rather short period of time. These present results reveal that there can also exist a mineral chemistry that take place during aging of the wine over long periods of time.
- (4) From macroscopic observations, we know that there is a significant amount of solid phases (that seems containing some crystals) formed after a long contact. We think that some may be tartrate of several nature (potassium bitartrate are commonly encountered in wines but calcium, magnesium, and others may also be formed) [124]–[126]. And the mineral chemistry would produce formation of solid phases at some stage than can be later dissolved and release ions (that would explained the domain of low concentration of calcium (observe from ~ 90 to ~ 360 hours). One may naively imaging that above 400 hours (~ 17 days), as a consequence of the high pH potassium bitartrate ($\text{KC}_4\text{H}_5\text{O}_6$) is dissolved/dissociated in favor of calcium tartrate ($\text{CaC}_4\text{H}_4\text{O}_6$) that precipitates:



However, at this stage an analysis of these solid phases should be very informative but has not been done yet.

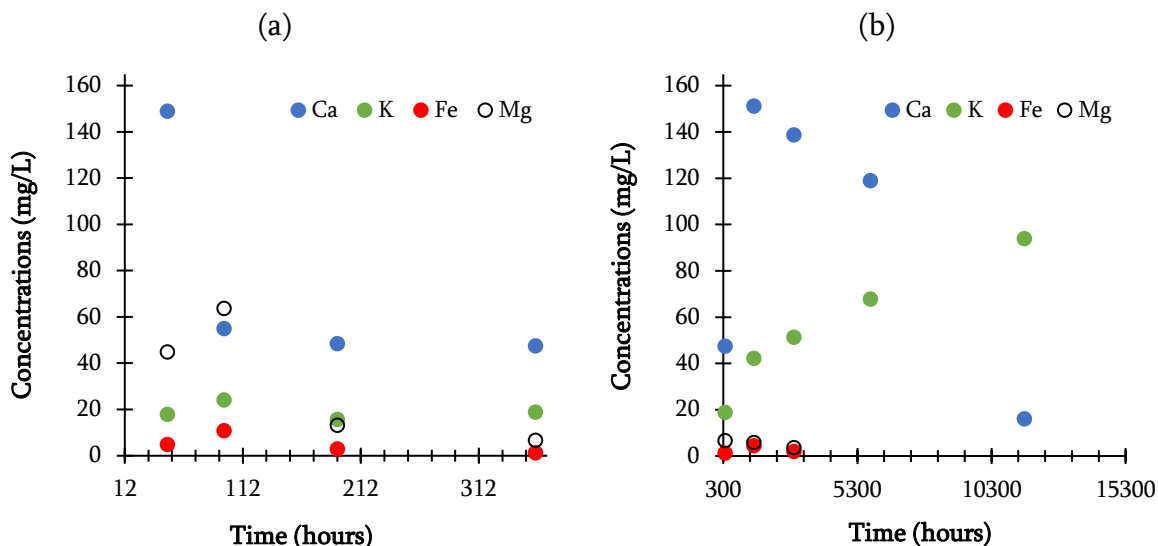


Figure 31. Evolution of calcium concentration (in linear scale) (a) from 12 to 350 hours and (b) from 300 to 15300 hours released from 1g of ceramic tablet. Potassium, magnesium, and iron concentrations are reported for comparison.

Before closing the discussion on calcium, we mention that some white spots appeared on the ceramics stored in the air. We think that it could reveal the formation of calcite (like efflorescence phenomena on brick walls, calcite can be one of the minerals formed by efflorescence, but other salts of sodium, potassium and calcium are usual).



If formed, this calcite would readily be dissolved in acid medium.

4.1.3.2. Evolution of iron and magnesium concentration

To complete the description of Figure 29, as far as iron is concerned for simplification, we based our discussion on the hypothesis that the main source of iron is hematite, which has been found in a significant amount in the ceramic (4% from XRF in the mixture (Table 7)). As previously mentioned, the dissolution is accelerated in acidic solutions. But it is important to mention that the dissolution rate of (minerals) hematite is

significantly faster in organic acids, mainly oxalic and citric, compared to inorganic acids [127], [128].

On Figure 29, during the first hours of dissolution, ICP-AES measures concentrations of iron that would be around 50 times less than what would be dissolved by an equivalent pure hematite tablet. A basic extrapolation would suggest that the ceramic tablets contain 2% of hematite which is reasonably close to the XRF data that gives 4% of Fe_2O_3 , (Table 7).

The concentration of iron in wines is naturally small ($\sim 1\text{-}10$ mg/L) [129], but when the iron concentration gets above 4-5 mg/L, some instability problems may occur [130]. The aeration of wine results in the oxidation of ferrous ions to ferric ions, leading to a risk of precipitation (ferric casse). This iron-induced precipitation is likely to appear when the iron concentration reaches 10 to 20 mg/L [129] and can alter sensory characteristics. Once iron concentration exceeds 20 mg/L, iron inhibits fermentation [131].

For aluminum reported in Figure 29, it is also satisfactory to observe that during the first hours of dissolution an equivalent tablet of androthite would produce far more Al than it has been observed by ICP-AES.

The concentration of aluminum can be a subject of discussion, considering the toxicity of this element. The toxic impact of aluminum on human health has been linked to the pathogenesis of several neurodegenerative disorders such as Parkinson's and Alzheimer's diseases. The European food safety authority defined in 2008 a daily acceptable adsorption of 10 mg for a 70 kg person reported by the black dotted line [132]. Of course, between our experiment and a real container there is a scaling factor, that has to be taken into account, but the amount of aluminum may be an issue for wine in ceramic.

The evolution of the magnesium concentration described in Figure 29, cannot be explained by the unique dissolution of the diopside, but it is of course very unlikely that the diopside is the only source of magnesium in the tablet.

4.1.4. Conclusion

In this section, we have focused on the measurement of the concentration of dissolved elements (or group of elements) of a ceramic immersed in a model wine versus

the time. The pH has been also roughly measured. As a safeguard, oversimplified considerations were performed in regard of the constant of dissolution of some of the minerals identified in the ceramic. The calcium dissolution is compared to the one measured in ceramsites [119]. We can conclude that:

- (iii) there is a wide range of elements migrating from the ceramic to the model wine by dissolution of the minerals constituting the ceramic.
- ii) the most abundant element is calcium. It can be explained by the high amount of calcite in clay.
- iii) the model wine pH increases with the contact time between the model wine and the ceramic, from 2.35 it reaches 5 in 4 days and 7 in 8 days.
- iv) for the few elements over flied (Ca, Fe, Al, Mg), the amount of minerals present in the ceramic and their dissolution rates are compatible with the elemental concentrations measured by ICP-AES.
- v) elements show different migratory behavior in function of time. This may be due to the quick and sharp increase of pH of the model wine, as well as to the chemical process occurring in the solution during aging (precipitation/crystallization, dissolution, re-precipitation/-crystallization).
- vi) the volume of the model wine over the surface of ceramic (R) is 0.186 m in Armenian amphorae and 0.009 m in IC-AES measurements. This means that there is relatively about 20 times more wine in amphorae, concentration measured in the 10 mm tubes are overestimated. In real conditions, one may reasonably assume that at least at the beginning of the contact of the wine with the ceramic in real condition, these concentrations should be 20 times inferior.

4.2. Ion migration from ceramic to wine followed by time domain nuclear magnetic resonance

The study of relaxation mechanisms observed in time domain nuclear magnetic resonance (TD-NMR) is an extremely wide and complex domain of physics that is investigated since the discovery of NMR in 1945. We briefly evocate in Annex VII the relaxation mechanisms occurring in our experiments that can, fortunately, be simply described. The main point to consider here is that the relaxation rate of an aqueous solution depends linearly on the concentrations of the paramagnetic ions in the solution. Obviously, the intercept being the relaxation rate of the pure solution (without the paramagnetic elements) and distinct paramagnetic ions or molecules (Fe^{3+} , Fe^{2+} , Mn^{2+} , O_2) may have a very different slope (relaxivity). Of course, this depends on the temperature, viscosity, and magnetic field. In our study all experiments were performed at the same magnetic field (20 MHz), and with great care at the same temperature (25°C). An increase of the viscosity of the solutions would produce an increase in the relaxation rate but this was not directly observed or quantified.

A point to consider is the formation of solid phases during these experiments. In NMR experiments, no solids were observed before 10 hours, first solids were sometimes observed after 24 h. However, the samples were not visible during T_1 measurements and the presence of solid was observed only at the end of the measurements. After one week of contact between the ceramic and model wine, white and/or yellow solid phases were generally observed. The precipitates have been saved, but not studied so far.

4.2.1. Sample preparation

Based on the experimental conditions distinct groups of samples were prepared:

Flame-sealed samples with small headspace – 7 mm NMR tubes with a small headspace containing model wine and a small ceramic tablets were flame sealed. The ratios of the volume of the headspace to the volume of wine ($V_{\text{air}}/V_{\text{wine}}$) was between 1 and 3. The 7 mm system was inserted in a 10 mm NMR tube, closed with an NMR cap, to run the experiment (Figure 39).

Large headspace samples – unlike flame sealed samples, the samples with a large headspace were prepared directly in a 10 mm NMR tubes and closed with an NMR cap. Required volume of model wine was firstly added in NMR tube, after ceramic tablet was gently dropped in model wine. Before dropping the tablet, T_1 of model wine alone was measured. The $V_{\text{air}}/V_{\text{wine}}$ ratio was 17.

Degassed environment – the sample was prepared under a degassed environment in a glove bag. In a 10 mm NMR tube was put a needed amount of model wine, the ceramic tablet was hung in the tube with a special sample holder, the tube was closed with an NMR cap and vacuum grease was put over the cap. After the T_1 measurement of model wine the tablet was dropped in model wine without opening the NMR tube. The sample had an $V_{\text{air}}/V_{\text{wine}}$ ratio of 17.

Beeswax coated samples - model wine and ceramic tablet coated with beeswax were placed in 10 mm NMR tube. Tube was closed with NMR cap. Ceramic tablets coated with one and two layers of beeswax were used for this set of experiments. A sample with model wine and beeswax alone was also prepared. The $V_{\text{air}}/V_{\text{wine}}$ ratio was 12.

The composition of the model wine is given in Table 1. The amount of model wine used for each experiment and details are reported next to each relaxogram.

4.2.2. The benefit of proton time domain nuclear magnetic resonance (TD NMR)

Despite its theoretical complexity, proton TD NMR is an easy experiment that allow to shed light on the complex physico-chemical evolution occurring when a ceramic is in presence of model wine. In particular, it allows performing experiments *in situ* without the need of recourse to any exterior probes. We have measured the relaxation times of protons, which are very abundant in the wine solution (mainly coming from water). The model wine used contains 12% in volume of ethanol (at 20°C), it correspond to a molar fraction of 96% of water molecules allowing to reasonably neglect the ethanol contribution [55]. At the first order, the relaxation rate of water molecules will be governed by paramagnetic

relaxation [133]–[135]. Figure 32 reports the elements concentration that can generate paramagnetic ions in solution: (Cd, Co, Cr, Cu, Fe, Mn, Mo, Ni, Ti, V).

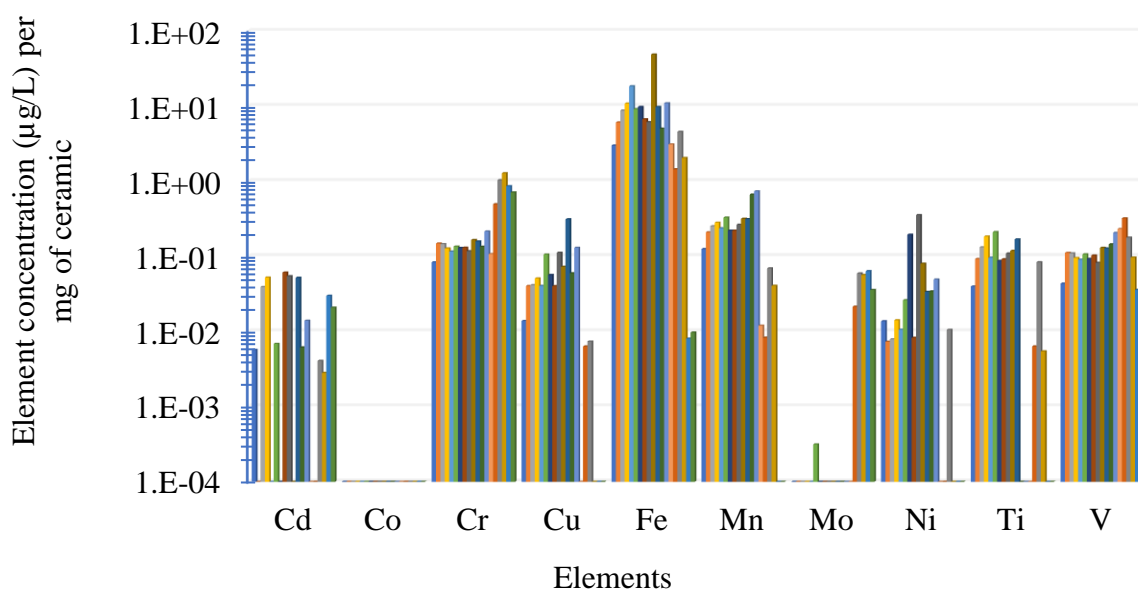


Figure 32. Metallic element concentration ($\mu\text{g/L}$) per mg of ceramic immersed in 2.8 mL of model wine in sealed glass 10-mm NMR tubes, measured during aging by ICP-AES. For each element, from left to right, one bar chronologically corresponds to a contact time (1 hour to 16 months).

Except for very long times (> 7 months), iron is the major paramagnetic aquaion presents in the solution. It may be present as ferric ions (particularly at low pH) as a result of decomposition of hematite identified in the ceramic (section 3.3.5). However, each paramagnetic ion does not have the same relaxivity ("power of relaxation"). Table 15 classes the various paramagnetic aquaions in function of their relaxivity [136].

Table 15. Relaxivity (r) of aquaions at 20 MHz, 25°C. Grey cells report non-majoritarian forms. It is worth noting that at a lower magnetic field (1 MHz or lower) or different temperature the relaxivity may strongly vary particularly for Mn^{2+} and V^{4+} .

Aquaion	Fe^{3+}	Mn^{3+}	Mn^{2+}	Cr^{3+}	Cu^{2+}	Ti^{3+}	V^{4+}	Ni^{2+}	Fe^{2+}	V, V^{2+} , V^{3+}	Cd^{3+}
Relaxivity ($\text{s}^{-1} \text{mM}^{-1}$)	15	15	10	5	1	1	0.8	0.7	0.38	-	-

By crossing the ICP-AES data and the relaxivities of Table 15, it is possible to picture what can be the major paramagnetic source of proton relaxation in the solution (Figure 33).

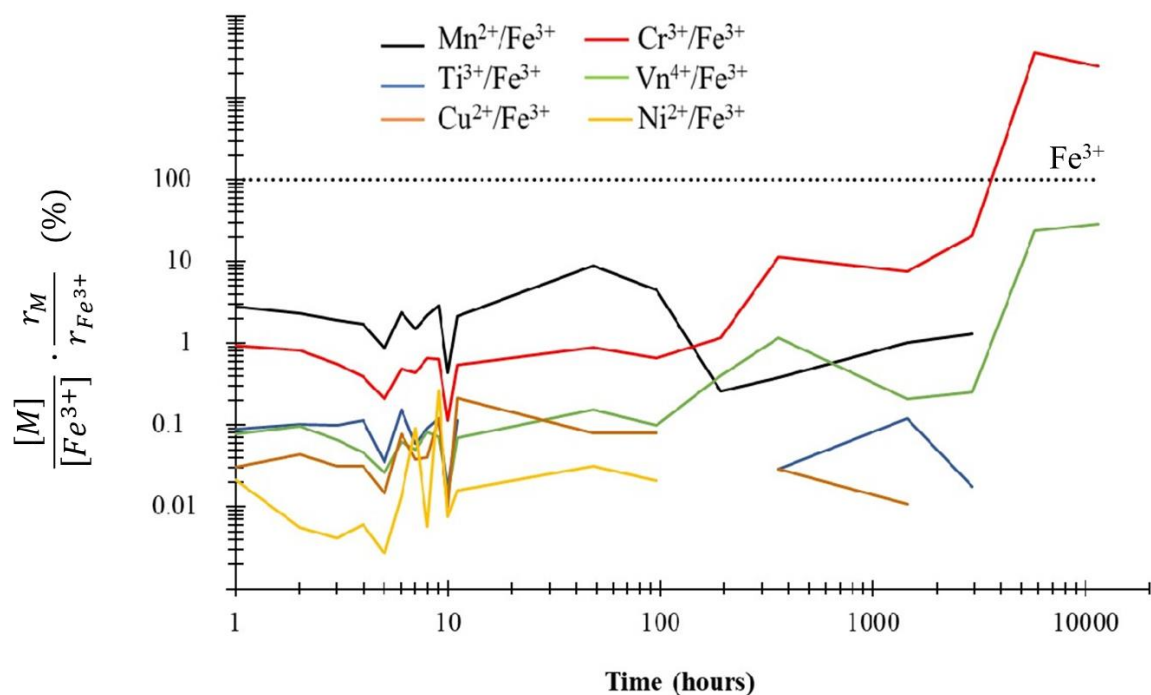


Figure 33. Ratios (in percent) of paramagnetic ions concentration with respect to the Fe concentration (extracted for ICP-AES data) versus aging time, with ponderations relative to their relaxivity (Table 15). Model wine elements concentrations are subtracted. It is assumed that all elements are in the reported oxidation states. The horizontal dotted black line represents the calculated quantity for iron (100 %).

Figure 33 can be read as follow, if we look at one hour after the contact of model wine and ceramic (first point), the quantity ($[Mn^{2+}]/[Fe^{3+}]$) ($R_{Mn^{2+}}/R_{Fe^{3+}}$) is 36, meaning that Fe^{3+} contributes 36 times more than the Mn^{2+} to the relaxation of the solution. Neglecting all other contributions Mn^{2+} would contribute for 3.2% of the relaxation of the solution. Fe^{3+} contributes 100 times more than Cr^{3+} . This is very likely and reasonable picture during the first hours of the contact of the ceramic with the wine. However, it should not be extrapolated for longer times since reduction of ions, crystallizations, and formation of solid phases occur and strongly modify the paramagnetic ions concentration in the solutions.

The lower ratio calculated for Cr^{3+} and V^{4+} at long contact time probably reflect less aptitude to crystallize or form solid materials.

At this stage, we retain that iron is probably the first source of relaxation of protons in the solution, followed by manganese. This is all the more true during the first hours of contact when the pH of the solution is low (2.6) and the amount of oxygen present in the environment is relatively high, a situation usually more favorable to Fe^{3+} than Fe^{2+} (Annex VIII). An additional paramagnetic element of importance must be considered in the experiment is the dissolved dioxygen in the solutions (Figure 34).

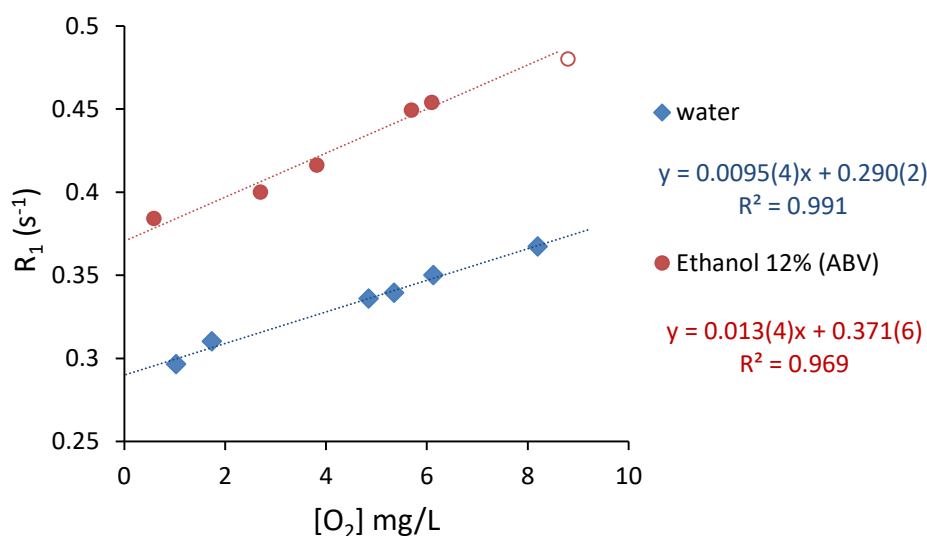


Figure 34. Titration of O_2 concentration in ultrapure water (blue) and 12 % (alcohol by volume - ABV) hydroalcoholic solution (red), at 25 °C. Abscise of open symbol has been calculated from [137], the open symbol is only reported and not used in the linear regression.

For both curves, the higher relaxation point corresponds to atmospheric equilibrium, while the intercept is associated to the relaxation rate corresponding to the solutions free of paramagnetic O_2 . The relaxation rate of fully degassed distilled deionized water is reported as 0.280 s^{-1} [138]. The different relaxivities for the two solutions are within fitting errors but the discrepancies are likely to be attributed to the dioxygen concentration

measurements performed with two different pastilles (sensors). Figure 34 allows to calculate a dioxygen relaxivity of $0.33 \text{ s}^{-1}/\text{mM}$ (expressed in the same units as Table 15).

4.2.3. Representation of relaxograms

A typical curve obtained by recording the ^1H relaxation time of model wine in contact with a ceramic versus time is shown in Figure 35. For the sake of simplicity let's call this curve a relaxogram according to the naive definition of "a diagram obtained by relaxometry".

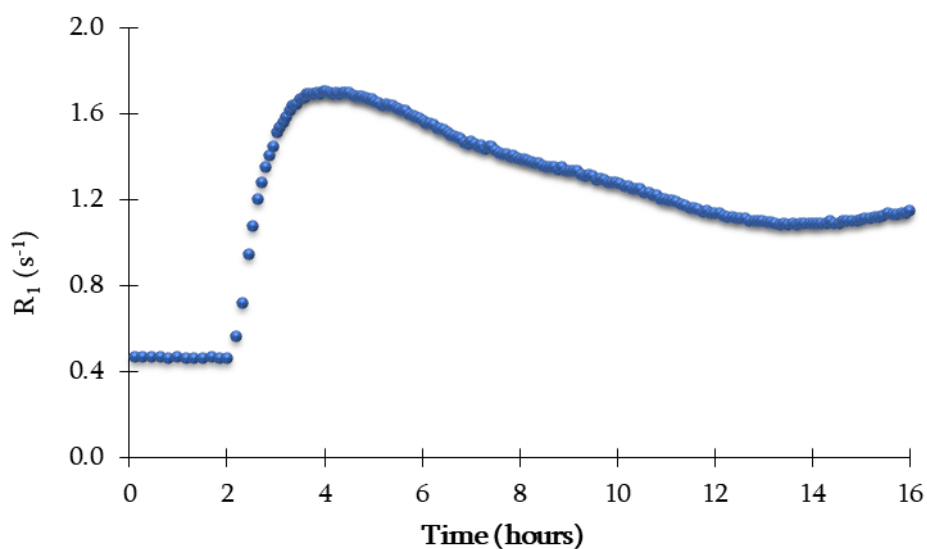


Figure 35. Typical proton relaxogram of a model wine in contact with a ceramic. The ceramic is dropped in the wine at ~ 2 hours and initiate the increase of the relaxation rate.

As presented in Annex VII, the proton relaxation rate of a solution containing paramagnetic aquaions has a remarkable properties of linearity with the paramagnetic aquaion concentration [139]. In the case of Fe^{3+} the linearity is illustrated in Figure 36.

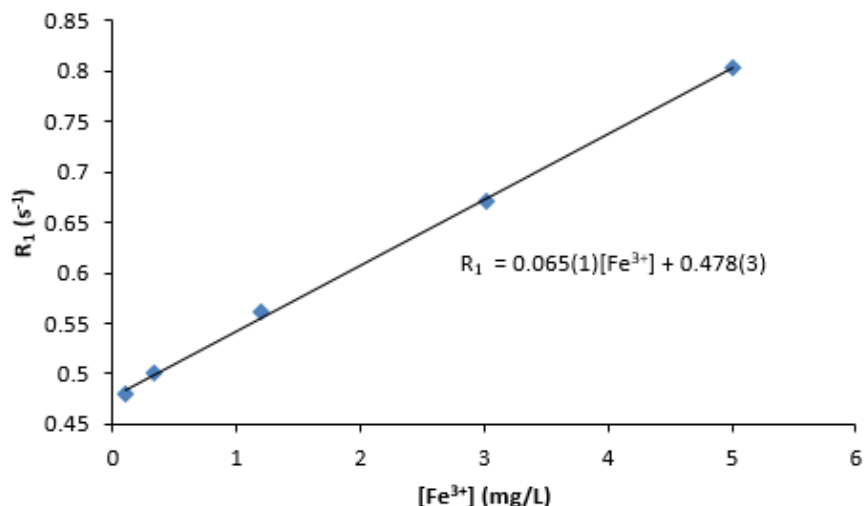


Figure 36. Titration of ferric ions concentration in a model wine. This curve has been obtained by individual synthesise, (no dilution of a stock solution was used). Number in brackets are the incertitude given by the linear regression on the previous digit.

It is interesting to note that for a naught concentration of iron we obtain the relaxation rate of the pure model wine solution (0.48 s^{-1}). This value corresponds to the cumulative relaxation rate of three mechanisms: rotational and translational isotropic diffusion of water and of the coupling of protons (from H_2O) with paramagnetic dissolved O_2 . This linearity allows reproducing the raw relaxogram in a different space where only the concentration effect of the dissolved paramagnetic ions is revealed. In a first step we subtract the model wine contribution (0.48 s^{-1}) to the relaxation rate and in a second step we use the inverse linearity relaxation to calculate the iron concentration:

$$[\text{Fe}^{3+}] = (R_1 - 0.478) / 0.0649 \quad (12)$$

The titration diagram is reported in Figure 37.

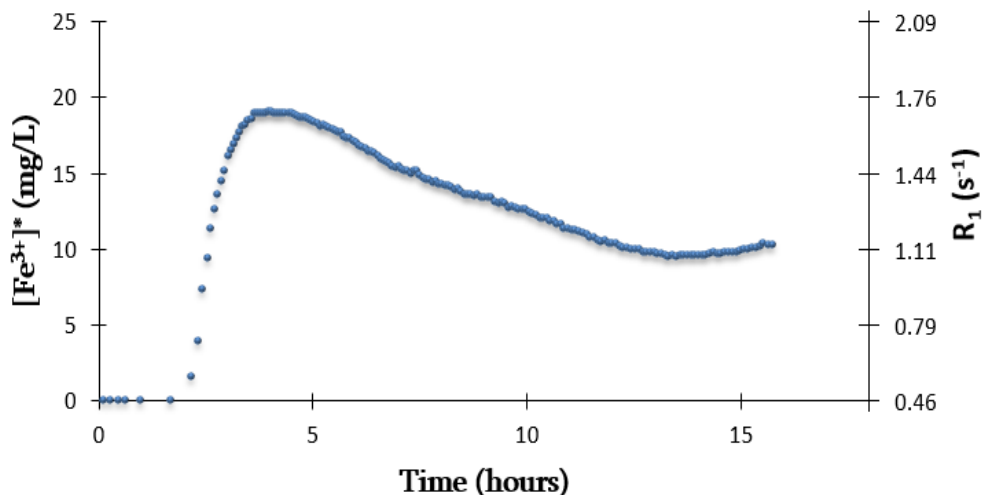


Figure 37. First hours of Fe^{3+} titration diagram of a model wine in contact with a ceramic. The concentration is labeled with an asterisk to recall that it is an apparent Fe^{3+} concentration. It considers a constant atmospheric level of dioxygen in the solution. Even if we have seen previously that iron should be the dominant source of relaxation in the solution, other possible contributions should not be completely forgotten.

4.2.4. Relaxation rate of solutions in contact with a ceramic

Figure 38 reports the relaxation rate of water, hydroalcoholic solution (12% ABV) and tartaric acid solution with and without contact with ceramic. The first four or five points are the relaxation rate of the solution, they are constant and the higher relaxation rate of the hydroalcoholic solution results from the higher viscosity of the solution in presence of ethanol. There is not impact of the pH i.e. of the tartaric acid (the first four points of water superpose the points of the tartaric acid solution) [55]⁸. In the solutions the

⁸P. R. Bodart, Aymerick Batlogg¹, Eric Ferret¹, Adam Rachocki², Magdalena Knapkiewicz², Syuzanna Esayan^{1,3}, Nelli Hovhannisyan⁴, Thomas Karbowski¹, Régis D. Gougeon⁵, “Analysis of the Proton Spin–Lattice Relaxation in Wine and Hydroalcoholic Solutions,” *Food Anal. Methods*, vol. 15, no. 2, pp. 266–275, Feb. 2022, doi: 10.1007/s12161-021-02118-w.

relaxation mechanism only results from rotational, translational diffusions and O_2 paramagnetic relaxation.

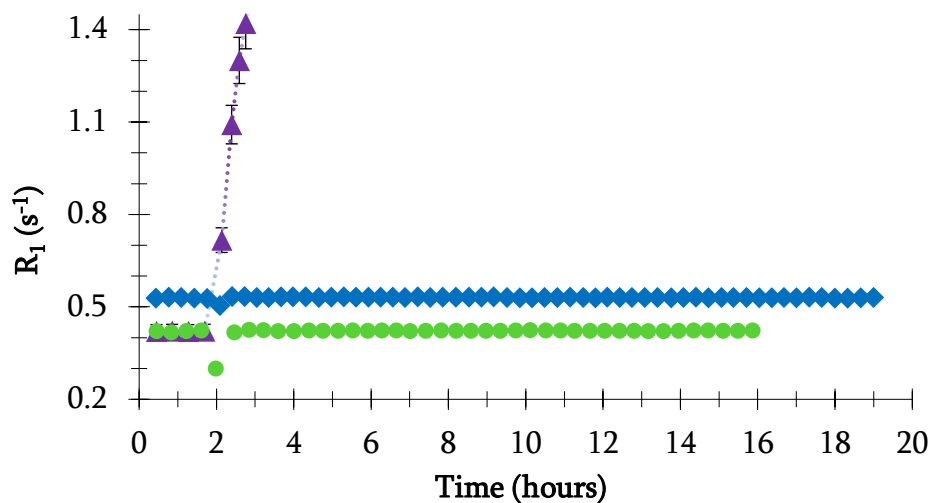


Figure 38. Relaxation rate of water (green ●), hydroalcoholic solution (blue ◆) (12% ABV), and tartaric acid solution (purple ▲) before (up to 2 hours) and after contact (after 2 hours) with ceramic.

The ceramic is dropped at 2 hours, it is seen on the solution when the point appears at a lower relaxation rate with a visible uncertainty on the measurement of the model wine relaxation rate. (Error bars are not visible when lower than the size of the points). After the ceramic is immersed in the water and hydroalcoholic solutions, the relaxation rates take a steady value barely superior to the one without the ceramic. This very slight increase of the relaxation rate can be attributed to the porous nature of the ceramic confined water molecules in the pore or in interaction at the surface have a higher relaxation rate that can increase by diffusion the overall relaxation rate of the solution [140], [141]. It worth noting that the porosity distribution of the ceramic could be evaluated by some dedicated TD NMR experiments [142], but this has not been investigated in this work. The situation is quite different in the case of the tartaric acid solution. There is an immediate acid attack of the ceramic that dissolve paramagnetic ions in the solution which induce an increase of the relaxation rate due to a dipolar paramagnetic relaxation mechanism. It is interesting to note that error bars are clearly visible indicating that upon the time required for the data

collection of one point (20 minutes) the solution is evolving. This is a neat illustration of acid corrosion observed on earthen ceramics (widely used for constructions) and mentioned in the precedent chapter.

4.2.5. Relaxogram of model wine in contact with a ceramic, small headspace in sealed environment



Figure 39. Experimental design of the flame sealed environment

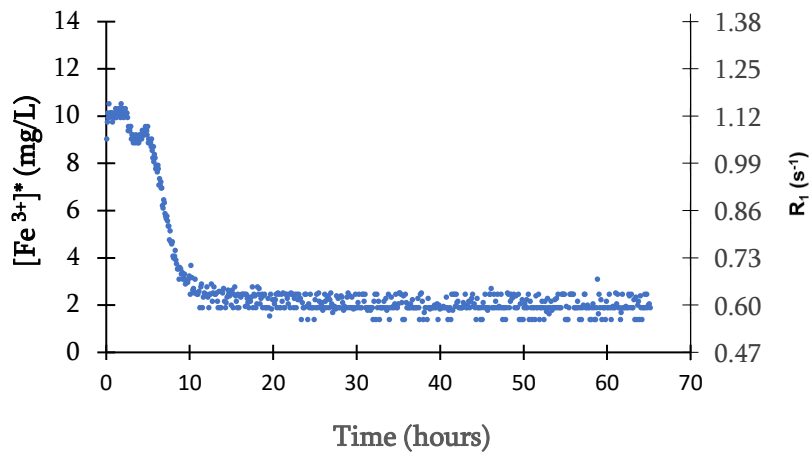
Figure 39 illustrates the experimental design used to follow the evolution of the relaxation rate in a sealed environment to approach the hermetic condition of bottle of wine in general. The ceramic is inserted in a 7 mm NMR tube, the tube is shaped with a flame to create a neck with a small orifice at the top (of the size of a small needle). When the glass is cold, the wine is injected with a syringe. Eventually, the thin glass neck tube is closed with a rapid exposure to a flame without heating the wine. The sealed system is weighted and transferred to the NMR apparatus in 10 mm NMR tube. Less than 30 minutes elapse between the ceramic contact with the wine and the

beginning of the TD NMR experiment. Once the experiment is finished the weight is checked and controlled several months latter to test the sealing (a loss of weight by evaporation would evidence a sealing default).

Figure 40 reports the evolution of the relaxograms (three repetitions) of some model wine in contact with a ceramic in a sealed environment. In (a) and (b) the error bars are higher than in (c) and at long times, the points oscillate between two values these are artefacts resulting of an inadequate setup of the gain (the conversion of the signal from analogic to digital was too crude). However, the relaxograms remains informative. In all experiments, there is a rapid and significant increase of the relaxation rate due to the dissolution of the ceramic upon acid attack and release of some paramagnetic ions. In less than roughly 10 hours two close, more or less resolved, maxima are observed then the

relaxation rate decreases for 10 or 20 hours and reach a steady value, which is for relaxograms (a) and (b), above the expected level of the model wine alone (it is also an artefact, further discussed in the last paragraph of this section). The overall, decrease of the relaxation rate can be due to only two reasons. (1) a decrease of the labile paramagnetic ions concentration in the solution. This could occur if there is formation of solids (crystallization, precipitation...). (2) An oxidation-reduction of the labile paramagnetic ions. Namely, the ferric ions in a closed environment where the oxygen concentration decrease (e.g., because of ethanol oxidation) and where the pH is increasing (as a result of the consumption of H_3O^+ during the acidic attack) are reduced to ferrous ions. Since ferrous ions are up to 36 times less effective relaxing agent than ferric ions (Table 15), the relaxation rate decreases significantly, down to a value close to the model wine relaxation rate.

(a)



$$W_{\text{tablet}} = 100.42 \text{ mg}$$

$$V_{\text{vine}} = 175 \mu\text{L}$$

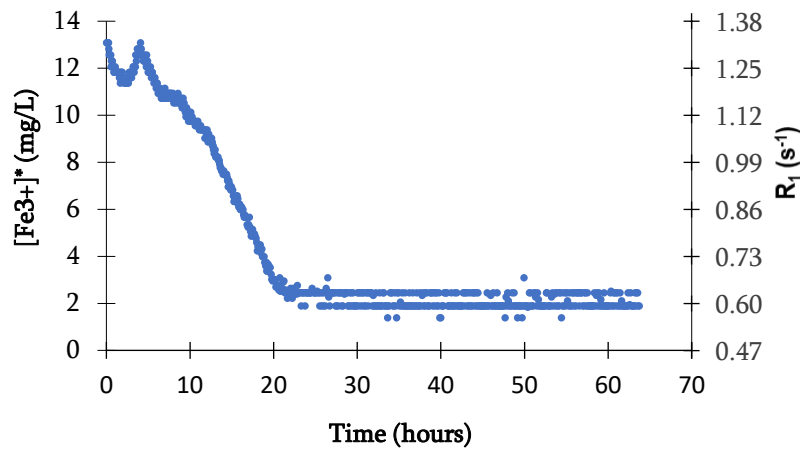
$$\frac{V_{\text{air}}}{V_{\text{Wine}}} = 2.3$$

$$\frac{V_{\text{Wine}}}{W_{\text{tablet}}} = 1.74 \frac{\mu\text{L}}{\text{mg}}$$

$$\rho = 2.15 \text{ mm}$$

$$\text{pH}(t=0) = 2.47$$

(b)



$$W_{\text{tablet}} = 89.7 \text{ mg}$$

$$V_{\text{vine}} = 200 \mu\text{L}$$

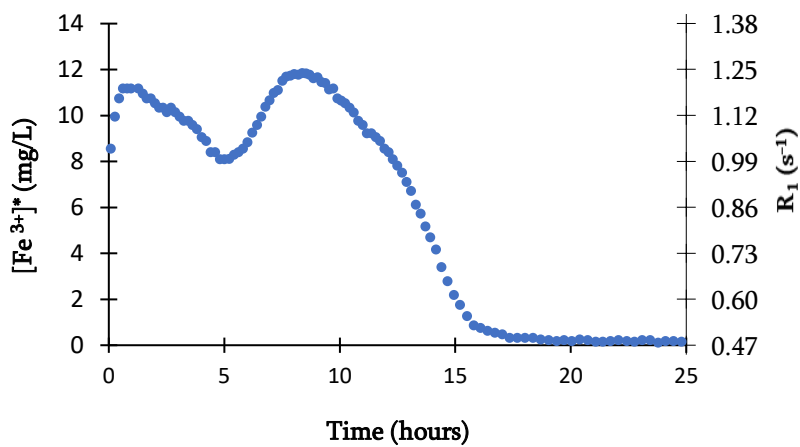
$$\frac{V_{\text{air}}}{V_{\text{Wine}}} = 1.2$$

$$\frac{V_{\text{Wine}}}{W_{\text{tablet}}} = 2.23 \frac{\mu\text{L}}{\text{mg}}$$

$$\rho = 2.44 \text{ mm}$$

$$\text{pH}(t=0) = 2.47$$

(c)



$$W_{\text{tablet}} = 110.63 \text{ mg}$$

$$V_{\text{wine}} = 200 \mu\text{L}$$

$$\frac{V_{\text{air}}}{V_{\text{Wine}}} = 2.25$$

$$\frac{V_{\text{Wine}}}{W_{\text{tablet}}} = 1.80 \frac{\mu\text{L}}{\text{mg}}$$

$$\rho = 2.28 \text{ mm}$$

$$\text{pH}(t=0) = 2.49$$

Figure 40. Three repetitions of the evolution of the relaxation rate of model wine solutions in contact with a ceramic. Samples are in a sealed 7mm-NMR tube with a

limited headspace. W_{tablet} is the weight of the ceramic tablet, V_{wine} is the volume of model wine added, $\frac{V_{air}}{V_{wine}}$ is an estimation of the ratio of the headspace over the volume of wine. ρ_S is the volume of the model wine to surface of the ceramic tablet. pH of the model wine is given at initial time.

During the first hours, relaxograms present at least two maxima. There is a simple hypothesis that may be envisaged: after firing, the ceramic contains small accessible particles (e.g. on surface, in big pores), that may dissolved more rapidly [116], [117] and could give rise to the first maximum, and the dissolution of the mass of the ceramic would occur at a slower rate and produce the second maximum. This seems supported by the relaxogram of a washed ceramic for which a single maximum is observed (Annex VII, Figure 71). Unfortunately, so far we did not do any complementary experiment to evaluate this assumption.

Noticeably, relaxogram (c) presents clearly resolved maxima, with a second peak around 10 hours (that may be associated with the broad shoulder observed in (b)). When compared to relaxogram (a) this becomes quite surprising because experiments (a) and (c) have close dimensions in terms of V_{air}/V_{wine} and V_{wine}/W_{tablet} ratios. The intensity and the position of this second peak becomes a major features of the experiments recorded with large headspace (see below). This peaks could be correlated with the amount of dioxygen present in the headspace which can here vary from one sample to another. The flame sealing may distinctively heat the air situated in the headspace (and change pressures) or consume more or less of its dioxygen. However, because of the constraints of the experimental preparation of the samples, we were unable to measure this quantity and we do not discuss in more detail this phenomenon in this section.

A comparison of the three curves seems to indicate that the delay to reach the steady state is proportional to the $\rho_S \left(\frac{V_{wine}}{S_{tablet}} \right)$ or equivalently $\rho_W \left(\frac{V_{wine}}{W_{tablet}} \right)$ ratio (Figure 41). This suggests that the evolution of the relaxation rate stop faster when the ρ_S or ρ_W ratio is smaller. This could be attributed to the fact that the acidic reservoir is smaller with respect to the size of the tablet when ρ is small. In other words the reaction would stop earlier

because the pH of the solution would increase faster and the acidic attack can no longer takes place.

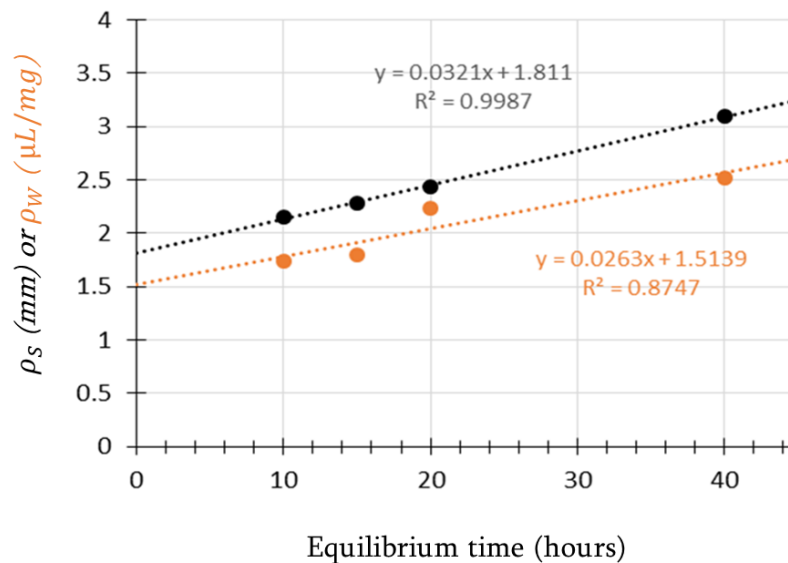


Figure 41. ρ_s (black) and ρ_w (orange) ratios versus the delay to reach the steady state. The point at 40 hours is obtained from Figure 71 of Annex VII.

As previously evocated, the equilibrium value of the relaxation rate is significantly higher than the expected value of the model wine for curves in Figure 40 (a) and (b). This is unexpected high value and has never been observed in subsequent experiments to such an extent. We attribute this overestimation to an insufficient number of points used to record the relaxation curves. 8 points were used in Figure 40 (a) and (b) whilst 16 points were used in all other experiments except in the relaxogram of Figure 71 of Annex VII (8 points). Control measurements of each of these two samples performed at 1000 hours gave more accurate (in a ratio from 2 to 4) relaxation rate values of 0.475 ± 0.01 and $0.419 \pm 0.008 \text{ s}^{-1}$ for Figure 40 (a) and (b) in agreement with the model wine level in (a) but lower in (b). Besides highlighting the questionable accuracy of the data in Figure 40 (a) and (b) a slow evolution of the relaxation time over long period of time could be supposed. Comparable observations have been made in Figure 71 of Annex VII.

4.2.6. Relaxograms of model wine in contact with a ceramic, large headspace

The relaxograms of some model wine in contact with a ceramic in a closed environment, with a large headspace, are reported in Figure 42. The headspace is qualified as large because the ceramic is immersed in 500 μL of solution in a 10 mm NMR tube closed with a cap. With respect to the previous sealed experiments (section 4.2.5), the ratio $\frac{V_{air}}{V_{wine}}$ is more than 10 times larger and the tube is not flame sealed but simply closed with an NMR cap to prevent strong evaporation. In Figure 42 (a), no significant variation of mass was observed after 8 or 18 days. These new relaxograms present similarities with the ones observed for the sealed experiment, in particular the presence of two clear maxima. However, the kinetic is one order of magnitude longer in presence of a large headspace. The curve in Figure 42 (a) ends with a long decrease toward the relaxation rate of the model wine. The main differences between experiments with small and large headspaces are the V_{air}/V_{wine} ratio and so the amount of disposable dioxygen in the headspace.

Relaxograms of Figure 42 result of identical experiments but in (a) the NMR tube was closed with an NMR cap and in (b) the NMR tube was left open (the cup was reversed on the top of the NMR tube to avoid major accidental particle or dust coming into the solution) so the amount of available dioxygen can be considered as infinite. Over a long period of time (10 days), the open experiment in Figure 42 (b) does not reach the relaxation level of pure model wine, meaning that the ferric ions are unable to be reduced to ferrous ions because dioxygen saturation in the solution. Of course, during this long period significant evaporation occurs: 33.7 % of the wine has evaporated. If we assume that no reduction occur in the solution, this evaporation would induce an equivalent increase of the equivalent Fe^{3+} concentration and an increase of the relaxation rate, which is not observed meaning that the reduction albeit not complete remains important. This being mentioned, a close look at the first hours of the experiments in Figure 42 (a) and (b) shows very comparable behaviors. In particular, the clear decrease at 60 hours in (a) is also present as a shoulder in (b). We attribute this inflection point at 60 hours to the combination of two mechanisms (i) the increase of pH significantly reduce the dissolution rate of iron. (ii) a reduction of iron ions that become discernable, that can be complete in the case of (a).

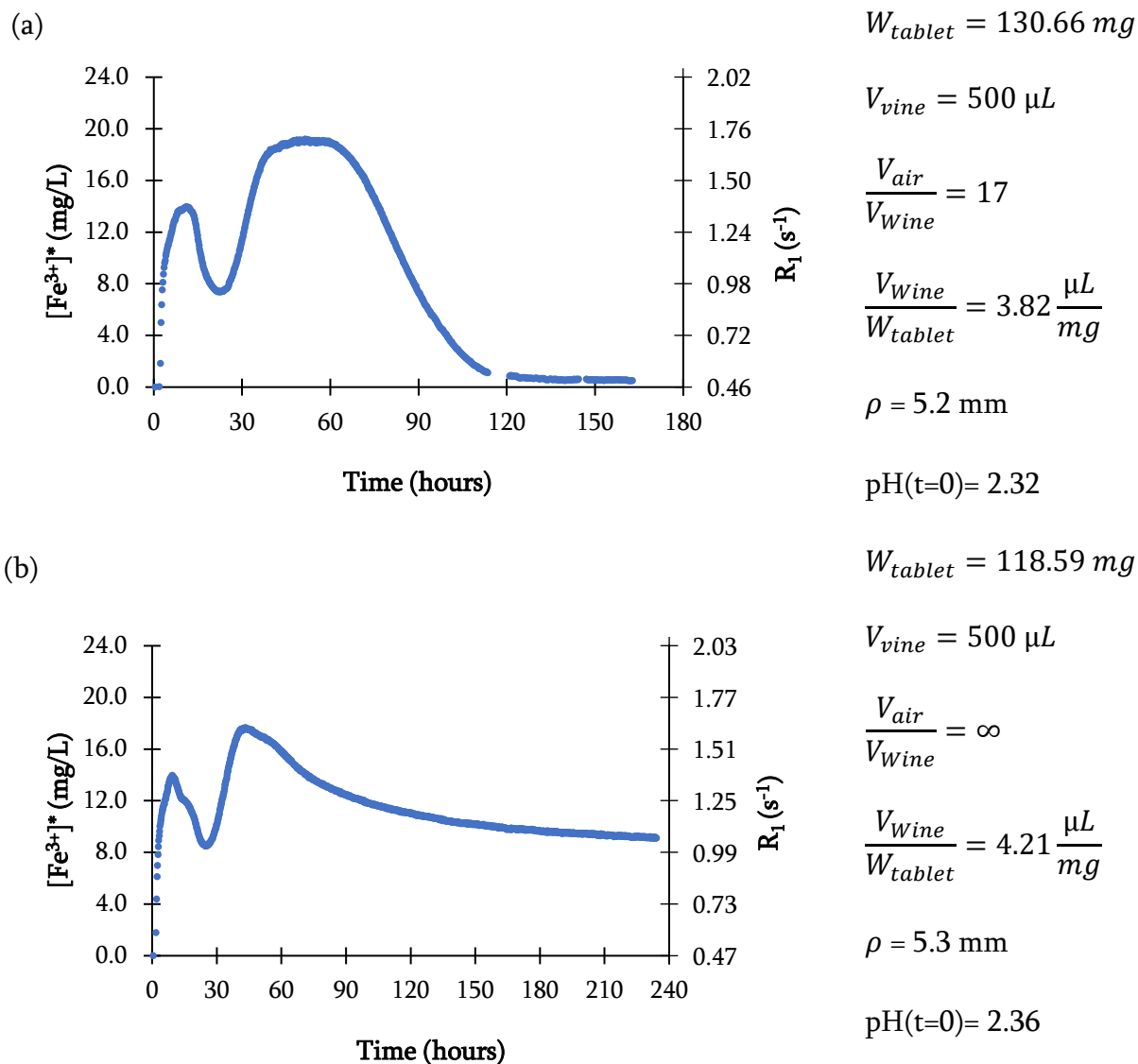
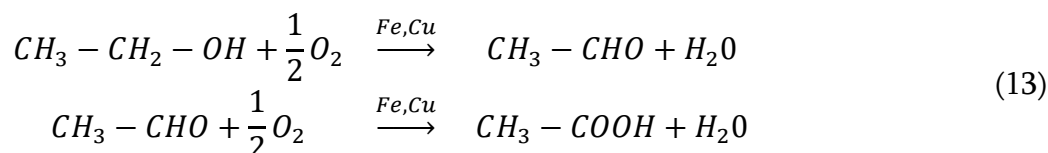


Figure 42. Evolution of the relaxation rate of model wine in contact with a ceramic. Samples are placed in 10mm-NMR tube with a large headspace. (a) in a closed tube (b) in an open tube (infinite headspace). Reported values on the right have the same meaning as in Figure 40.

An important point concerns the origin of the second maxima observed in the experiments performed with a large headspace (alternatively, the reason of the decrease observed around 20 hours). Figure 40 and Figure 42 indicate that dioxygen is certainly a key element of this compartment observed during the first hours of contact. We previously suggested that this could be due to the faster dissolution of small particles but here (in regard to the relaxogram of Figure 44, for which the solution does not contain ethanol, we

may propose an additional assumption. The second hypothesis is that during the first hours, there is a reaction that consumes dioxygen and around 20 hours there is a sufficient decrease of dioxygen amount in the solution leading to a reduction of Fe^{3+} resulting in the observed decrease of the relaxation rates. As an example the first oxidation mechanism that we can consider is the ethanol oxidation in ethanal and maybe ethanoic acid according to:



Initially at atmospheric equilibrium, the model wine contains around 9 mg/L ($2.8 \cdot 10^{-4}$ mol/L, Figure 34) of dioxygen. The molar fraction of ethanol in the model wine (12% ABV) is close to 4% (2.22 mol/L) [55]. Table 16 report the absolute amount of ethanol and dioxygen present during the large-headspace-closed experiment (Figure 42(a)).

Table 16: Amount (mmol) of ethanol and dioxygen (estimation) present in the 10 mm tube during the large-headspace-closed experiment (Figure 42(a)).

	wine	headspace
O ₂ (mmol)	$1.4 \cdot 10^{-4}$	0.08
Ethanol (mmol)	1.11	-

Of course, during the contact, dioxygen can also be introduced into the solution by the dissolution of minerals but in regard to Eq.(13) and Table 16, one may hypothesize that the ethanol oxidation can result in a significant consumption of dioxygen in the model wine (the metallic elements susceptible to catalyze this reaction are with no doubts present in the solution). The decrease of dioxygen in the solution is expected to reduce Fe^{3+} and this is the truer as the pH increase. But if the oxidation reactions slow down, the oxygen concentration in the wine may rise sufficiently (because of dissolution of oxygen from ceramic minerals and from the headspace into the solution) and limit the iron reduction, the ferric ions that continue to be dissolved cannot be readily reduced (and maybe some ferrous ions can be back oxidized to ferric ions) causing the second increase of relaxation

rates and this until the total amount (headspace included) of available oxygen become too low and iron reduction metals occurs again. In the sample with a small headspace (Figure 40) the amount of available dioxygen is probably not sufficient to observe the oxidation of the ferric ions occurring around 40 hours and the metals remain reduced. In this case, ethanol might be only partially reduced (as it may occur in bottled wine). In Figure 40, if the amount of dioxygen available in the headspace in relaxogram (c) is higher than in (a) and (b), the second maximum observed at 10 hours in (c) could be associated with a similar mechanism shifted to lower time. It is worth mentioning that the oxidation of ethanol can give rise to acetic acid (if ethanal does not evaporate, its boiling point being 25°C) but it has far less ability to dissolve hematite than tartaric acid [143].

Relaxogram (a) in Figure 40 allows for reporting a new point in Figure 41. It aligns amazingly very well (Figure 43). For the experiment performed with small and large headspace, this linear correlation suggests that the time to reach the relaxation rate of the pure model wine does not seem to depend on the dioxygen available but seems to depend primarily on the ρ ratio.

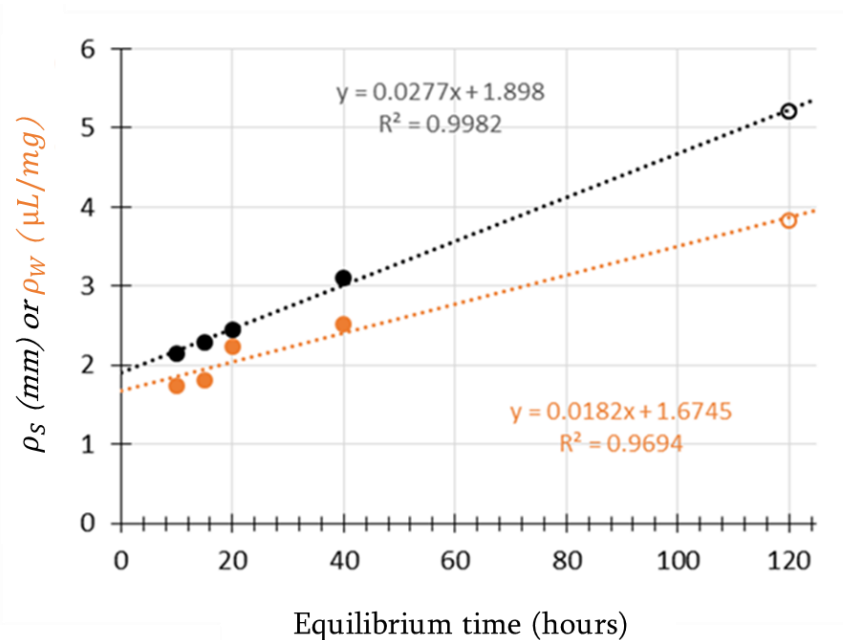


Figure 43. ρ_S (black) and ρ_W (orange) ratios versus the delay to reach the relaxation rate of pure model wine, open symbols correspond to experiment with a large headspace.

To check the hypothesis of the possible impact of ethanol oxidation, the relaxogram of a tartaric acid solution (corresponding to a model wine without ethanol) has been recorded and is presented in Figure 44. On this relaxogram, the valley is very weak, and the amount of dissolved equivalent Fe^{3+} is higher both suggesting that there is less consumption of dioxygen at the beginning of the kinetic, probably because of the absence of ethanol.

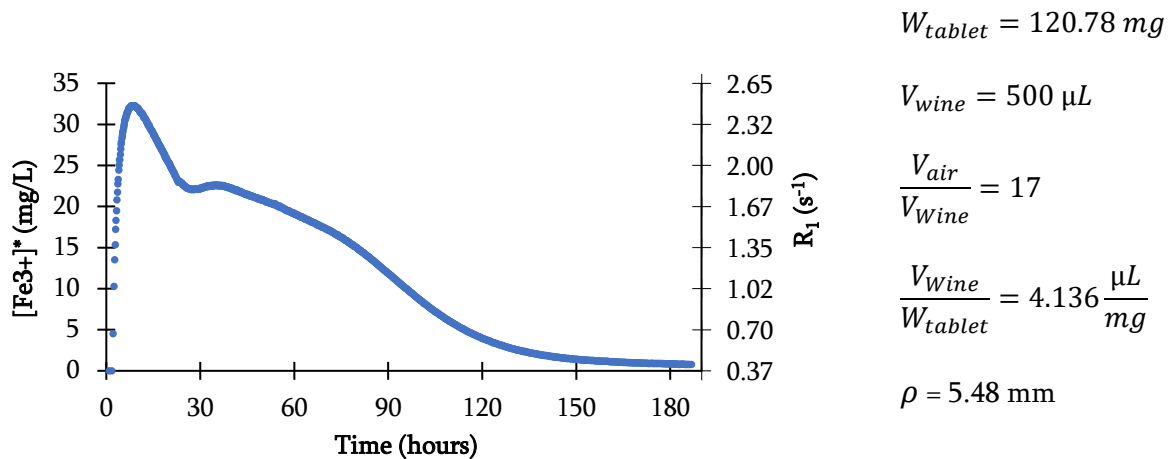


Figure 44. Relaxogram of a solution of tartaric acid (5g/L) in ultra-pure water.

The time necessary to reach the equilibrium relaxation rates reasonably respects the linear correlation with the ρ ratio (Figure 45).

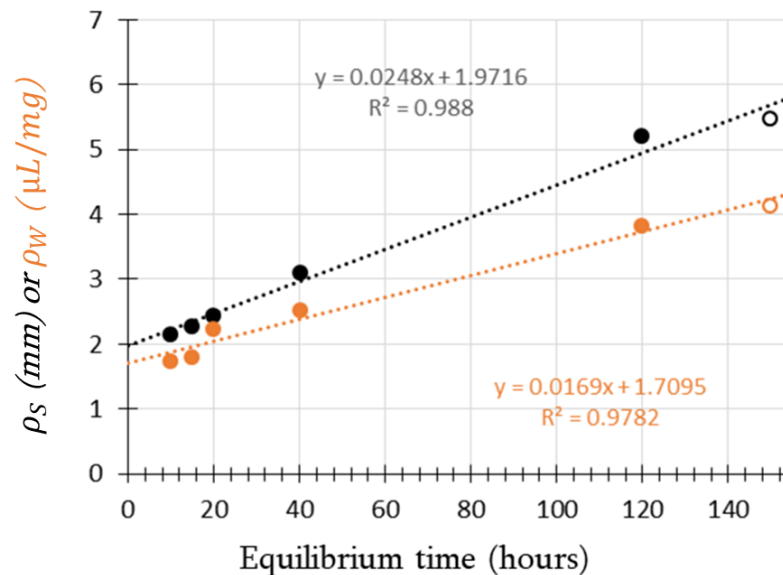


Figure 45. ρ_S (black) and ρ_W (orange) ratios versus the delay to reach the relaxation rate of pure model wine. The open symbols correspond to 5g/L of tartaric acid in ultra-pure water.

4.2.7. Relaxogram of model wine in contact with a ceramic, large headspace, second contact

To verify that the dissolution kinetics is determined by acidity, and to establish a relationship between the repeated use of ceramics and its effect on the dissolution of minerals, the following experiment was carried out. The relaxogram of Figure 46 (a) was obtained with the same ceramic tablet used in experiment of Figure 42 (a). At the end of experiment of Figure 42 (a) the ceramic tablet is removed, cleaned from solid phases deposited on the surface, rinsed, left for four/five hours in HPLC water then dried with paper and reintroduced as in experiment Figure 42 (a) in a fresh model wine. The relaxogram of the washed tablet in ultrapure water is reported in Figure 42 (c) with an expansion of Figure 38 for the ceramic immersed in ultrapure water. In Figure 42 (c), it is interesting to note that when the ceramic tablet is used directly after its production there is no significant dissolution. If it has previously been in contact with a model wine the tablet is able to release some paramagnetic ions, (of course not as easy as when immersed in the model wine). The first contact with model wine may be view in this context as a stripping of the ceramic. The relaxogram Figure 46 (a) present the same shape as in Figure 42 (a) but over a longer period of time and in addition the first maximum is significantly higher than in Figure 42 (a). This means that at the initial steps a larger amount of iron can dissolve, this could also result from a stripping after the first contact with the wine. We suspect that the ceramic may be partially covered (Figure 22 (a)), it is very speculative to propose the nature of this coverage but because of the large amount of calcite in the clay, the coverage could result from some formed (during the storage period of the ceramic) or remaining carbonates present in a glass form and not detected by XRD. Such a covering would strongly prevent the dissolution at high pH (in water) but would readily be dissolved in acidic conditions.

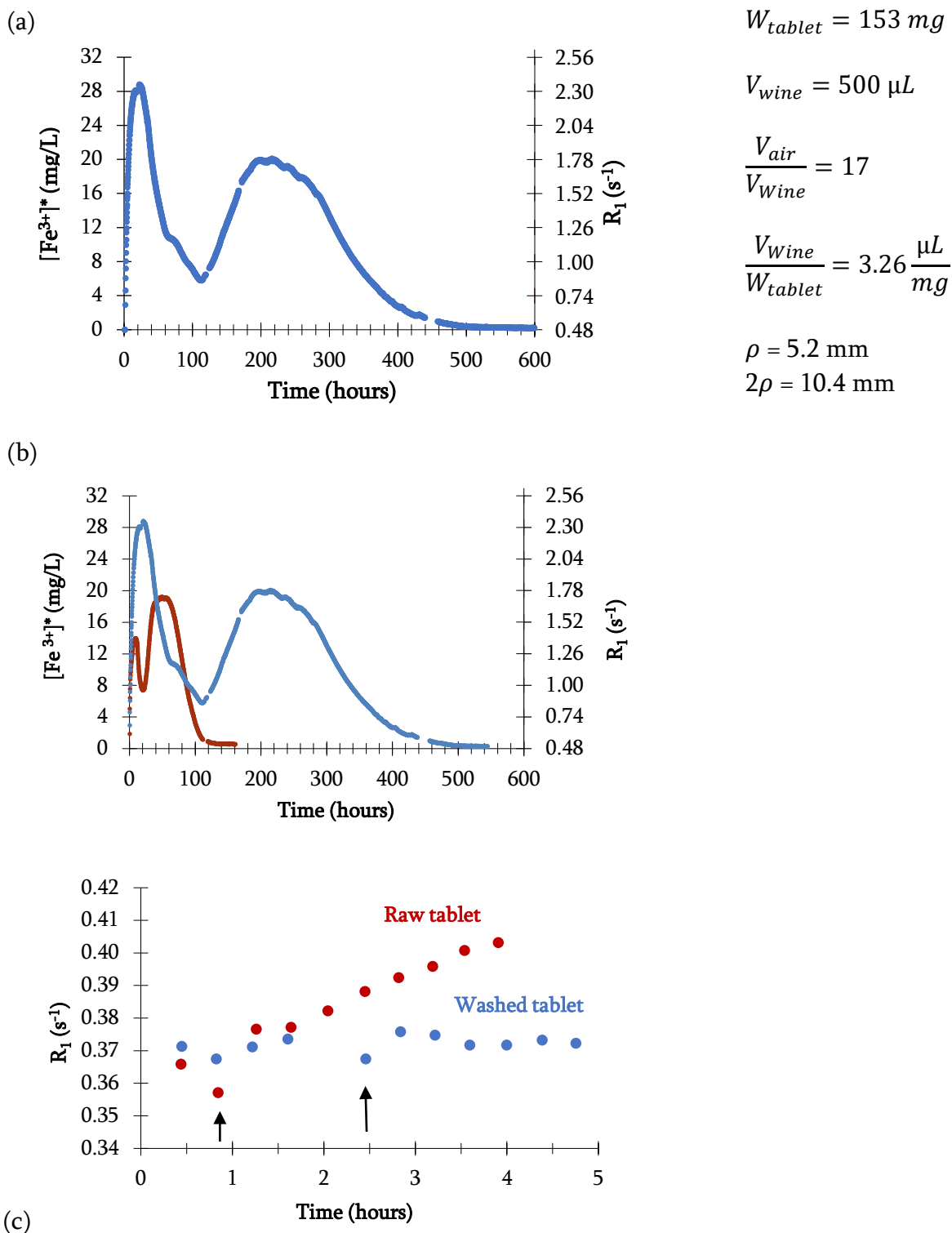


Figure 46. Relaxogram of model wine during first and second contact of ceramic with fresh model wine. The ceramic was washed between the two contacts. (a) second contact, (b) superposition of relaxogram recorded during the first contact (red from Figure 42 a) and relaxogram of the second contact (blue). (c) (●) raw tablet in contact with ultrapure water (extension from Figure 38), (●) washed tablet

(after the first contact of experiment (a) in Figure 42) in contact with ultrapure water. Arrows mark the insertion of the ceramic in the water.

One challenging point to address is the explanation of the shift in time of the humps between the first and second contact (corresponding relaxograms are compared in Figure 46 (b)). We could attribute it to a larger amount of tartaric acid available for directly dissolving the mineral without the initial step of stripping in the case of the second contact. This would result in more acidic condition over a longer period, less favorable to ethanol oxidation and slowing down the reactions.

Remarkably, by considering a double volume of wine (a double ρ ratio: 10.4) the time to reach the equilibrium after a second contact seems to satisfy the linear correlation (Figure 47).

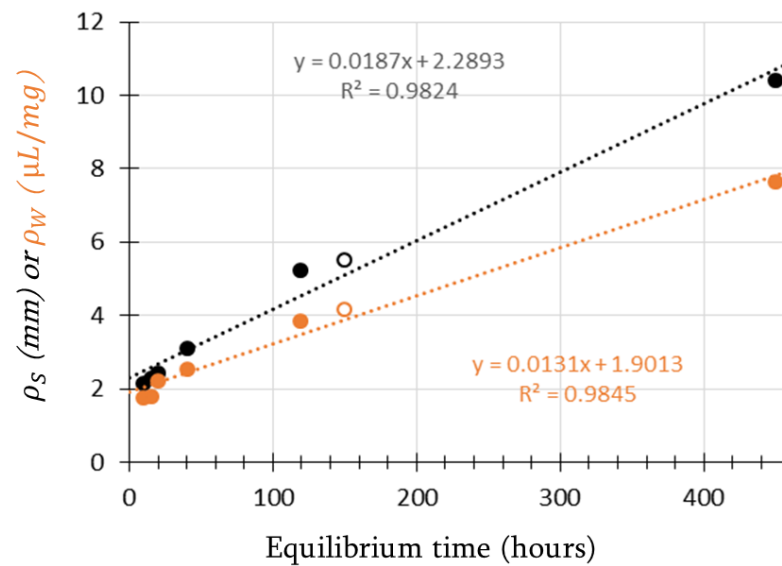


Figure 47. ρ_s (black) and ρ_w (orange) ratios versus the delay to reach the relaxation rate of pure model wine the open symbols correspond to 5g/L of tartaric acid in ultrapure water.

4.2.8. Evolution of the relaxation rate of model wine in contact with a ceramic in a low dioxygen environment

In order to further test the role of dioxygen, we slightly decreased the dioxygen concentration by nitrogen degassing the ceramic tablet, the wine and the headspace volume. Inside the glove bag (the dioxygen concentration in the glove bag was 13.7 mg/L (5%)), in the vial containing the model wine, the O₂ concentration in the model wine was measured as 0.23 mg/L. However, after 40 minutes once the NMR experiments started, the value of the relaxation rate of the pure model wine measured during 1.1 hours (4 points) was 0.4118(3) s⁻¹. According to Figure 34, it corresponds to a dioxygen concentration ($C_{O_2}^{wine}$) of 3.1 mg/L. The relaxation rate of the model wine was stable over the measurement time (1.1 h). This delay should be long enough to observe migration of dioxygen between the liquid and gas phases if they were far from equilibrium. In consequence, assuming an equilibrium system, the dioxygen concentration in the headspace ($C_{O_2}^{headspace}$) can be calculated with the Ostwald coefficient for dioxygen L (0.03255) for a 12% ABV hydroalcoholic solution according to Henry law [144]:

$$C_{O_2}^{wine} = L \cdot C_{O_2}^{headspace} \quad (14)$$

This equation would suggest a dioxygen concentration in the headspace of 95 mg/L. On overall we may conclude that, at the beginning of the experiment, the probable dioxygen concentrations were one third of the ones in atmospheric condition.

Once the model wine relaxation was measured, the ceramic initially placed in a special holder at the top of the closed NMR tube, was gently slid in the wine without opening the NMR tube. The relaxogram of the above-described sample is reported in Figure 48. It always presents the same singularities of two maxima but the valley between the two maxima is clearly less pronounced indicating that indeed this depression is likely correlated with the dioxygen available in the solution. The relaxation rate reaches the model wine solution slightly earlier than in comparable experiments (Figure 42, Figure 44) with a large atmospheric headspace. At 100 hours the NMR tube was opened and an immediate increase

of the relaxation rate is observed due to the incoming dioxygen. From Figure 34 it is clear that the increase of relaxation rate after opening cannot be only due to the paramagnetic effect of the dissolved O_2 (in a model wine, from a concentration of 0 mg/L to saturation the paramagnetic relaxation enhancement is of the order of 0.1 s^{-1}). In fact the paramagnetic enhancement is responsible for the stick step observed immediately after opening the NMR tube (it lasts 2 hours), the continuous increase observed from 100 to 115 hours is due to Fe^{2+} oxidation.

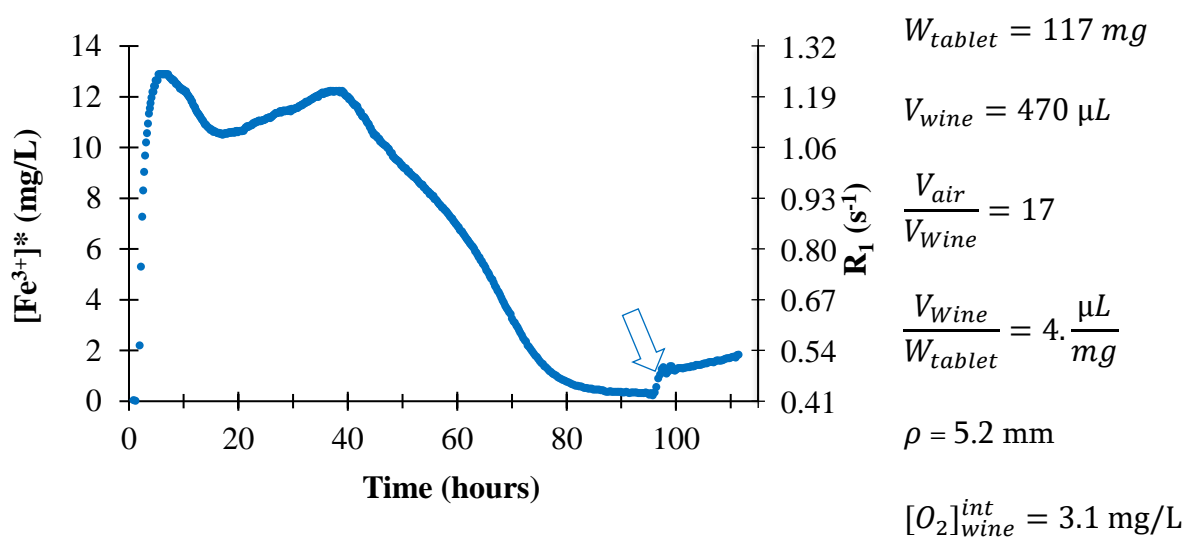


Figure 48. Relaxogram of a model wine in contact with a ceramic in an environment containing 1/3 of atmospheric dioxygen concentration. $[O_2]_{wine}^{int}$ is the initial dioxygen concentration in the model wine. Model wine pH=2.31 (at $t=0$)

In this experiment the relaxation rate seems to stabilize around 80 hours, but it does not align with the previous linear curve obtained for Figure 47. Figure 49 reports the previous correlation of ρ versus the time to reach the equilibrium but large and small headspace data are fitted separately. It appears that the correlation becomes very good suggestions that for a given headspace ρ is linearly correlated with the time to reach equilibrium but is not completely decorrelated to the amount of dioxygen available. Moreover, the experiment under nitrogen would suggest that the partial pressure of dioxygen may also be a variable to consider.

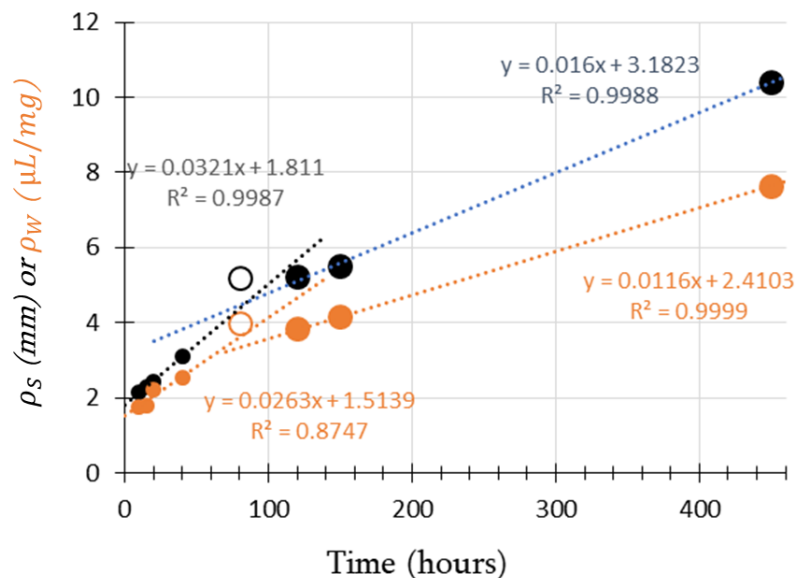


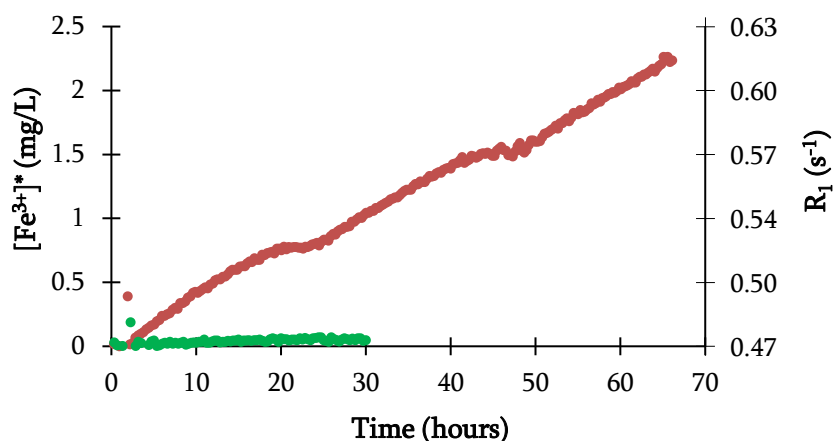
Figure 49. ρ_S (black) and ρ_W (orange) ratios versus the delay to reach the relaxation rate of pure model, big and small symbols correspond to the large and small headspace experiments respectively. Open symbols are N_2 degassed experiments.

4.2.9. Evolution of the relaxation rate of model wine in contact with a coated ceramic

The linear dependency between the time to reach the equilibrium (as represented in Figure 47) and the ρ ratio suggests that in a pithos as described in Table 3, the equilibrium would be reached in less than 14 months. At this state, the wine would be completely reduced and of course, it would have lost its qualities long before. To prevent this reduction, when earthenware containers are used for winemaking, their internal surface is coated. As mentioned in the introduction, the covering can take many forms: a glassing formed during the firing of the ceramic (at a higher temperature, sometimes with the preparation of the surface) or by a covering applied after the firing. Traditionally, in Armenia, ceramic pithoi are coated with beeswax to preserve the wines. Relaxograms of model wine containing a ceramic coated with one or two layers of natural beeswax issued from a fresh empty honeycomb and a ball of pure beeswax are reported in Figure 50. The coating has a strong effect on the release of ions from the ceramic into the solution. When well coated with two layers of beeswax, after 30 hours of contact, the release of equivalent Fe^{3+} is less than 1% of

the release of uncoated ceramic (e.g., Figure 42 (a)). But an insufficient or imperfect covering (one layer) can still allow a significant diffusion of metallic ions. This could be one of the reasons why Armenian winemakers (who are using ceramic jars) encounter more difficulties in winemaking white wines than red wines, the white wines being more sensible to oxidations.

(a)



$$W_{\text{tablet}} = 106.54 \text{ mg}$$

$$V_{\text{wine}} = 700 \text{ } \mu\text{L}$$

$$\frac{V_{\text{air}}}{V_{\text{Wine}}} = 12$$

$$\frac{V_{\text{Wine}}}{W_{\text{tablet}}} = 6.57 \frac{\mu\text{L}}{\text{mg}}$$

$$\rho = 10 \text{ mm}$$

(b)

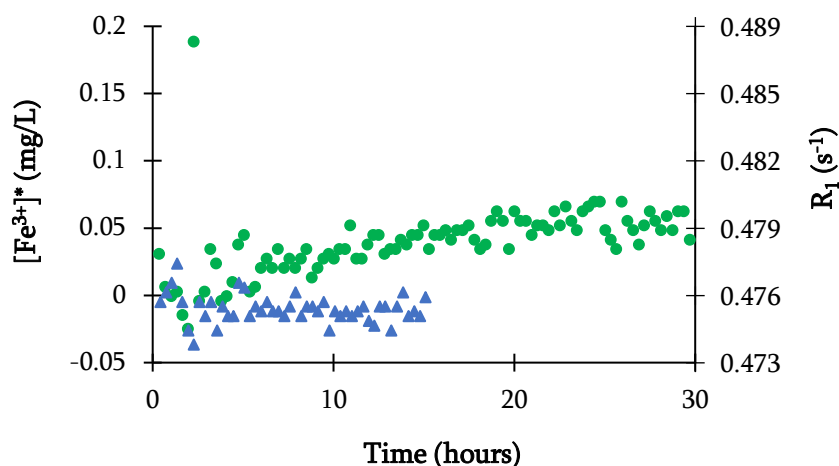


Figure 50. Relaxograms of model wine solution containing (a) a ceramic tablet coated with one (a, ●) and two (a & b, ●) layers of natural beeswax, or beeswax alone (b, ▲)

During the aging of the samples for one year, changes were observed related to both the color of the model wine and the texture of beeswax (Figure 51). After three months (Figure 51 (a)), the samples coated with one layer of beeswax turned yellow but remained transparent and the texture of beeswax was slightly damaged. It should also be noted that

no yellow or white precipitate or crystals were formed, which is typically observed with uncoated samples. A year later, the model wine in contact with one layer coated ceramic become hazy and the texture of beeswax continued to deteriorate (Figure 51 (b)). In samples coated with two layers of beeswax and beeswax alone in model wine none of these changes (crystallization, precipitation, haze formation, change in color) were observed. This allow to conclude that the changes occur in sample with one layer of beeswax are associated with the effect of ceramics, it means that, at least for the noted period of time, relatively big amount of beeswax limited the acidic attack of model wine on the ceramic.

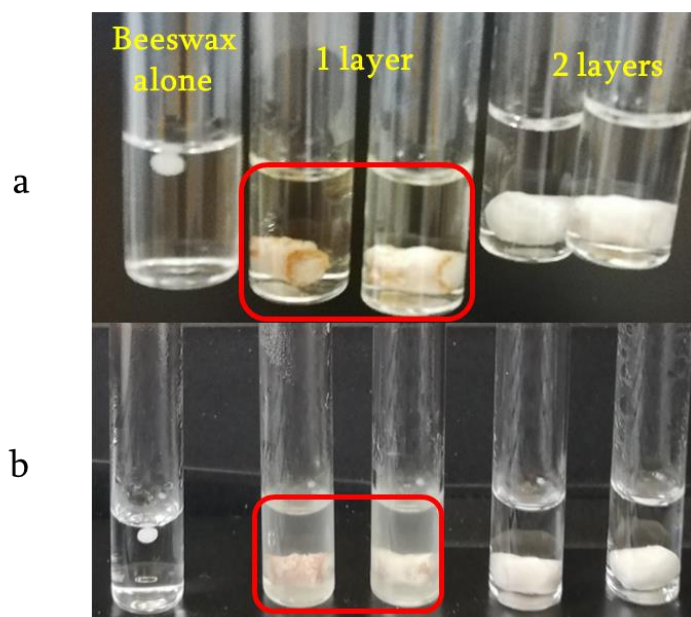


Figure 51. Model wine aged with ceramic coated beeswax. a) 3 months aged, b) 1 year aged.

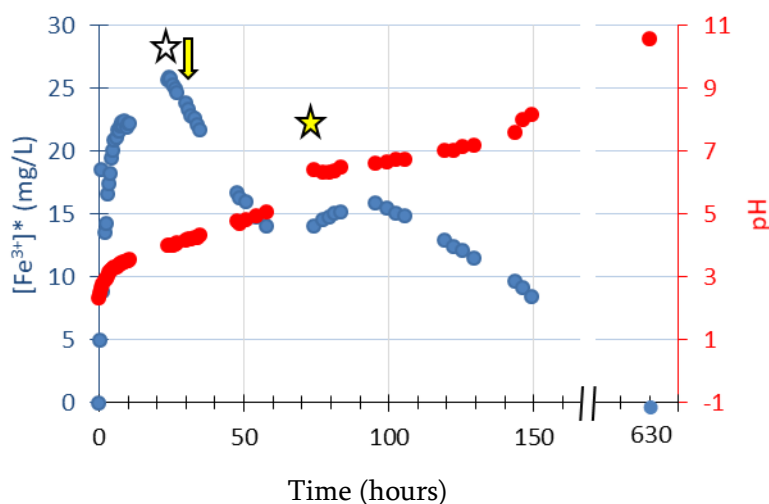
4.2.10. Evolution of pH during a contact period

In the previous discussions of the relaxograms, regular references to an acidic attack of the ceramic are used, to shed a more quantitative light, Figure 52 reports the evolution of the pH and the relaxogram (recorded simultaneously) of a model wine in contact with a ceramic.

For the monitoring of the pH of model wine as a function of time three repetitions have been performed. Ceramic tablets with similar parameters (mass, dimensions) were chosen to provide as similar conditions for replications as possible. Nine tablets were placed

in 27 ml of model wine, considering the volume-surface ratio. Samples were stored at 25°C. The pH of the samples was measured every 30 minutes (during first 10 hours), then the interval was adjusted up to 2 hours. Parallel to the pH measurements 600 µl of model wine was taken from repetition 1 to measure T_1 , after which it was put back. Not earlier than 10 hours and not later than 24 hours white precipitation was observed. In 29 hours after the beginning of the experiment model wine colored yellow. After 40 hours some yellow particles were observed in repetition 2 but not in repetition 1 and repetition 3.

The calculated standard deviations of pH values were within drawn points. The relaxogram (Figure 52) shows the typical previously observed evolution but a larger number of ions seems to be released at the early stage. This may be due to the different experimental conditions. The bottles were regularly opened and manipulated and therefore more or less shaken that foster gas dissolution in the liquid phase., probably because there is a regular opening of the bottles that saturate the headspace with oxygen (we are in a situation intermediate between a close and open environment see Figure 42). The pH evolution is impressive, particularly in regard to what wine can support. pH increases deeply at the very beginning in concomitance with the relaxation rate, but then seems to increase more regularly. A measurement at $t = 631$ hours (26 days) gives a pH value of 10.6.



$$W_{\text{tablet}} = 6063.2 \text{ mg} \\ (\text{9 tablets})$$

$$V_{\text{wine}} = 27 \text{ mL}$$

$$\frac{V_{\text{air}}}{V_{\text{wine}}} = -$$

$$\frac{V_{\text{wine}}}{W_{\text{tablet}}} = 4.45 \frac{\mu\text{L}}{\text{mg}}$$

$$\rho = 10.1 \text{ mm}$$

Figure 52. Relaxogram of model wine in contact with ceramic tablet (●) and pH of the solution (●). White star indicates the observation of white precipitation, the vertical yellow arrow, apparition of a yellowish color of one out of three

repetitions, the yellow start observation of yellowish crystals in one of three repetitions.

This pH increase strongly impacts the dissolution rate of minerals composing the ceramic. Miller et al. [145], have shown that tartaric acid was an effective dissolution agent of non-crystalline iron oxide. Forty ml of this acid can dissolve 80% (at pH 5.5) and nearly 90% (at pH 3.5) of 20 mg of Fe with 100 hours. However, tartaric acid was not able to dissolve 1% of crystalline hematite or goethite within 300 hours. In the case of oxalic and citric acids (that dissolve better iron oxides than tartaric acid) the dissolution rate drastically decrease at pH 6 [146]. We did not encounter equivalent data for tartaric acid, but such an effect seems also visible at pH around 6, where simultaneously the pH evolution seems less rapid and the relaxation time reach the second maximum (Figure 52). It must be noted that in some of the earlier experiments the ρ ratio can be significantly smaller from 1 to 5 mm. In such cases, the increase of pH is expected to be faster when the ρ ratio is smaller.

4.3. Comparison of TD NMR with ICP-AES

In order to check the consistency of the relaxogram, in particular the calculation of the equivalent ferric ion concentrations, with the ICP measurement, Figure 53 reports the iron concentration measured by ICP-AES (Chapter 4), the equivalent Fe^{3+} concentration calculated from a relaxogram recorded in a comparable experiment (closed 10 mm tube, $\frac{V_{air}}{V_{wine}} = 17$, $\frac{V_{wine}}{W_{tablet}} = 3.82 \frac{\mu\text{L}}{\text{mg}}$, $\rho = 5.2 \text{ mm}$) and the simulated iron concentration resulting from the dissolution of hematite [106]. For the first hours the ICP-AES and calculated apparent Fe^{3+} concentrations agree quite well. From 5 to 90 hours, the ICP concentration oscillates from 5 to 10 mg/L, above 90 hours up to 4 months the solution contains less than 5 mg/L to severely decreased to 30 $\mu\text{g/L}$ at very long times (more than 8 months see Figure 29). The relaxogram is an in situ and in tempore experiment which is not the case of the ICP-AES experiment (the wine has been separated from the ceramic at the reported time, flame sealed and reserved in obscurity, at 25°C). It is only after more than 16 months from the beginning of the experiment that the samples were altogether

analyzed by ICP-AES. This extend period of time could lead to some crystallization and only the supernatant was analyzed. As a safeguard, we roughly simulated the dissolution of hematite (assuming that 4% of the ceramic is composed of hematite according to the XRF data of section 3.2). The simulated concentrations are consistently always above the measured and calculated iron concentrations.

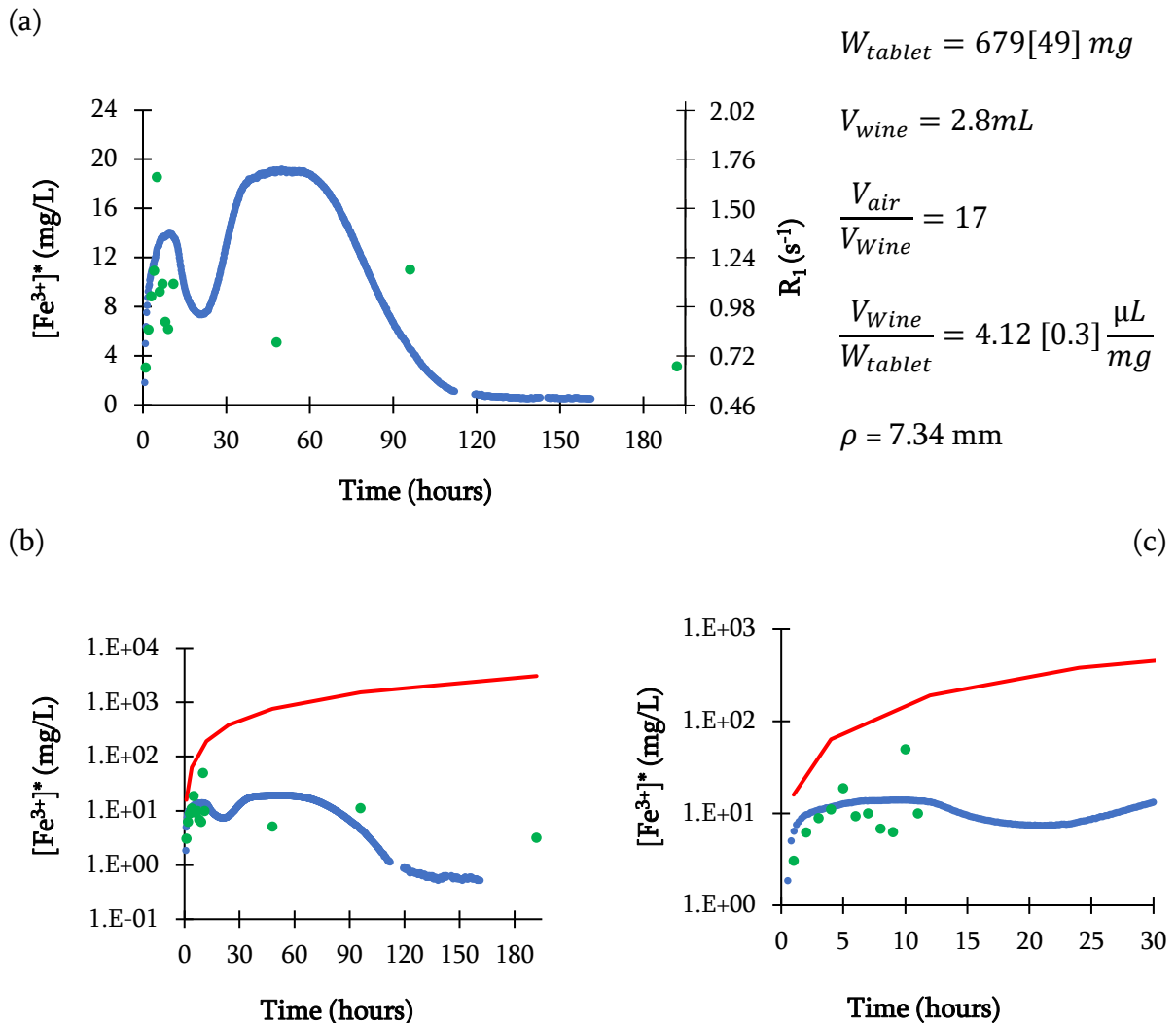


Figure 53. (a) Comparison of the equivalent ferric ion concentration calculated from a relaxogram (blue) and the ICP measurement (green) on the left numbers refer to the statistics performed on all the ceramic tablets used for the ICP experiment. The relaxogram correspond to the one displayed in Figure 42.b. Diagram in (b) additionally reports (continuous red line) the theoretical labile iron resulting of the dissolution of hematite (estimated as 5% of the mass of the ceramic) . (c) is an expansion of (b).

4.4. Conclusion.

Despite the underlined extremely complicated physico-chemical reaction, transformation, and transportation occurring during the contact of a ceramic with a model wine TD NMR allows, *in situ* and *in tempore* to qualify and quantify some essential aspects.

- (i) The migration of elements from ceramic in model wine is massive (on the scale of what the model wine could accept). Ceramic has to be coated minerally during the fabrication (by dedicated thermic treatment) or organically after the firing by covering the surface with beeswax, pine pitch... for proper use.
- (ii) In contact with the ceramic, model wine pH can rapidly and strongly increase.
- (iii) In Armenian ceramic iron is the most abundant paramagnetic element released and it is very likely the principal responsible for the relaxation observed.
- (iv) The oxygen plays an important role in various oxidation/reduction reaction occurring in the model wine and its concentration strongly affect the relaxograms.
- (v) A first contact with the model wine stripe the ceramic and during the forthcoming contact the element migration can be more pronounced.

Final conclusion

From time immemorial, Armenia has been one of the active winemaking centers in the world. This is evidenced by many winemaking complexes, which were excavated at different times by Armenian and foreign experts (archaeologists and historians). Vessels made of fired and/or unfired clay, in which wine was stored, were found in all the excavated complexes mentioned in the introduction of this dissertation. The technology of making wine using this traditional method is still up-to-date both in different countries of the world and in Armenia especially. However, despite the historical antiquity of the technology of making wine in ceramic pots and the increasing demand, limited scientific research has been done to study the nature of the interaction between the wine and the ceramic. These circumstances, as well as certain problematic points previously noticed during winemaking in ceramic vessels by our team in Armenia, such as the significant change in pH of real wine during aging, served as the basis for studying these relationships, choosing Armenian clay-based ceramics synthesized in laboratory and model wine as a simplified research model. The aim of this work was to look at the interaction between ceramics and model wine. Of course, it covers a very wide field, and we only opened a few doors. The chemical and mineralogical composition of raw clay and ceramic, the impact of two heat treatments on the porosity and micromorphology of ceramic, dissolution of ceramic in contact with model wine, and migration of elements from ceramic to model wine were studied. One of the first difficulties we faced, was the limited or almost non-existent scientific work related to the mineralogical composition of Armenian clay and ceramics. The existing Russian literature, apart from being old, contained conflicting data. And we had to start our investigation by a characterization of the clay and ceramics.

The starting material is extracted from Shahumyan deposit it contains calcareous clay (15-21% of calcium oxide) with high silicon content (~60%). The clay fraction is mainly composed of smectite, kaolinite, mixed-layer clay and illite. After firing, the ceramic is mainly formed of diopside, hematite, gehlenite and minerals from the plagioclase family. The obtained data on the porosity of ceramic tablets, prepared according to the method of Armenian potters, indicate that we are dealing with highly porous ceramics

(63%). Ceramic fired at 850 and 930 °C did not show variation of porosity and the surface area was comparable to what has been measured in a fragment of Armenian pithos. When in contact with model wine, the acidity of the solution (pH 2.55) favors the dissolution of the ceramic, in response the pH of the wine increases and the migration of all types of elements present in the ceramic occurs rapidly. ICP-AES made it possible to follow the migration of 26 elements over 16 months. Time Domain NMR is used to guide the approach to questions regarding the impact of headspace volume and oxygen concentration, ratio of the volume of wine/ surface of the ceramic on iron and ethanol redox processes in wine concomitant with the dissolution of the ceramic.

Summarize the research work, it: (i) updated the chemical and mineralogical composition of the Armenian clay of the Shahumyan deposit, (ii) recorded valuable results for winemakers working with ceramic pots, (iii) shed light on some of the processes that occur between ceramics and wine, in particular with respect to the oxidation/reduction processes occurring in the model wine in contact with the ceramic, and (iv) showed how coating is critical in limiting the mutual impacts of ceramic and model wine.

Perspectives

In this thesis, we have presented works that demonstrate the tremendous importance of studying the interaction between ceramic and wine. However, this work is just a first step. To complete the research on wine-ceramic interaction, various directions could be suggested:

- To analyze the solid phases performed during the contact of the model wine with the ceramic.
- To study the interaction between model tablet - model wine.
- To study the interaction between model tablet - real wine.
- To study the interaction between real ceramic and real wine.
- To continue to study the effect of coating of the ceramics.

The study of the above-mentioned points can have an important input in the improvement of winemaking in ceramic containers.

Lexicon

alluvial

Alluvium is loose clay, silt, sand, or gravel that has been deposited by running water in a stream bed, on a floodplain, in an alluvial fan or beach, or in similar settings [22], 26

biostratigraphy

Biostratigraphy determines the age of rocks through the use of fossils. Determining the environment in which the fossil species lived is inherent in this type of analysis., 66

ceramsites

Ceramsite is a lightweight porous material, and is used to, 81, 82, 87

chlorite

Chlorites have a 2-1 sandwich structure. The typical general formula is $(\text{Mg,Fe})_3(\text{Si,Al})_4\text{O}_{10}(\text{OH})_2 \cdot (\text{Mg,Fe})_3(\text{OH})_6$., 22

diluvial

A coarse surficial deposit formed by the glacial drift [23], 26

erosion

is the action of surface processes (such as water flow or wind) that removes soil, rock, or dissolved material from one location on the Earth's crust, and then transports it to another location where it is deposited, 21

fatty

Fat clays are cohesive and compressible clays of high plasticity, containing a high proportion of minerals that make it greasy to the feel., 27

feldspar

are a group of rock-forming aluminium tectosilicate minerals, containing sodium, calcium, potassium or barium, 21

illite

identifies a clay structure, which is of 2-1 type, dioctahedral, non-expanding, aluminous, and contains nonexchangeable K as the major interlayer cation, 22

kaolin

is a name given to a group of phyllosilicate minerals whose layers have a 1-1 structure with a composition of $\text{Al}_2\text{Si}_2\text{O}_5(\text{OH})_4$, 21

loss on ignition

Sequential loss on ignition (LOI) is a common and widely used method to estimate the organic and carbonate content of sediments [49]. The analogue of LOI is thermogravimetry., 51

*Minerals of the group of silicates built by stacking tetrahedral layers (, 44**palygorskite–sepiolite*

Like all ideal phyllosilicate minerals containing 2-1 layers where there is an octahedral sheet between two opposing tetrahedral sheets, the palygorskite–sepiolite minerals have continuous planes of tetrahedral basal oxygen atoms. However, unlike the ideal 2-1 phyllosilicates, the apical oxygen atoms point away from the basal oxygen atom plane in opposing directions to form ribbons of joined pyroxene-like chains, 22

pithos

(plural pithoi) is the Greek name of a large storage container used among the civilizations that bordered the Mediterranean Sea in the Neolithic, the Bronze Age and the

succeeding Iron Age. Pithoi were used for bulk storage, primarily for fluids and grains, 38

Riss-Würm period

Riss-Würm Interglacial Stage, a major division of Pleistocene time and deposits (2.6 million to 11,700 years ago) in Alpine Europe. [24], 25

smectite

also known as “swelling clay”, is a diverse group of clay minerals with a 2-1 layer silicate structure that can expand and contract upon wetting and drying. The smectite group (shows large chemical variability, 22

tandoor

Cylindrical clay oven used in cooking and baking, 26

volcanogenic-sedimentary

rock that consists of volcanic and sedimentary materials, 26

weathering

is the deterioration of rocks, soils and minerals as well as wood and artificial materials through contact with water, atmospheric gases, and biological organisms. Weathering occurs in situ (on site, with little or no movement), 21

References

- [1] D. Twede, “Commercial Amphoras: The Earliest Consumer Packages?,” *J. Macromarketing*, vol. 22, no. 1, pp. 98–108, Jun. 2002, doi: 10.1177/027467022001009.
- [2] N. A. Hovhannisyan, A. A. Yesayan, A. A. Bobokhyan, M. V. Dallakyan, S. G. Hobosyan, and B. Z. Gasparyan, *Armenian Vine and Wine*, Antares., 1 vols. Yerevan: Deutsche Gesellschaft für Internationale Zusammenarbeit (GIZ), 2017.
- [3] P. Weltman, “Why an Ancient Winemaking Technique is Making a Comeback,” May 16, 2018. <https://daily.seventy.com/why-an-ancient-technique-is-making-a-comeback/> (accessed Feb. 18, 2022).
- [4] F. F. Montalvo, J. L. García-Alcaraz, E. M. Cámara, E. Jiménez-Macías, and J. Blanco-Fernández, “Environmental impact of wine fermentation in steel and concrete tanks,” *J. Clean. Prod.*, vol. 278, p. 123602, Jan. 2021, doi: 10.1016/j.jclepro.2020.123602.
- [5] M. Gil i Cortiella, C. Ubeda, J. I. Covarrubias, V. F. Laurie, and Á. Peña-Neira, “Chemical and Physical Implications of the Use of Alternative Vessels to Oak Barrels during the Production of White Wines,” *Molecules*, vol. 26, no. 3, p. 554, Jan. 2021, doi: 10.3390/molecules26030554.
- [6] M. Nikolantonaki *et al.*, “Impact of Oak Wood Barrel Tannin Potential and Toasting on White Wine Antioxidant Stability,” *J. Agric. Food Chem.*, vol. 67, no. 30, pp. 8402–8410, Jul. 2019, doi: 10.1021/acs.jafc.9b00517.
- [7] A. Martínez-Gil, M. Del Alamo-Sanza, and I. Nevares, “Evolution of red wine in oak barrels with different oxygen transmission rates. Phenolic compounds and colour,” *LWT*, vol. 158, p. 113133, Mar. 2022, doi: 10.1016/j.lwt.2022.113133.
- [8] K. Chira, C. Gonzalez, and P. Teissedre, “Wine Ageing in Oak Barrel: Effect of Toasting Process,” *Agric. Res. Technol. Open Access J.*, vol. 12, no. 3, Nov. 2017, doi: 10.19080/ARTOAJ.2017.12.555847.
- [9] H. Work, *Wood, whiskey and wine: a history of barrels*. London: Reaktion Books, 2014.
- [10] L. Guerrini, F. Maioli, M. Picchi, B. Zanoni, A. Parenti, and V. Canuti, “Kinetic modeling of a Sangiovese wine’s chemical and physical parameters during one-year aging in different tank materials,” *Eur. Food Res. Technol.*, vol. 248, no. 6, pp. 1525–1539, Jun. 2022, doi: 10.1007/s00217-022-03982-4.
- [11] K. K. E. Neuendorf, J. P. Mehl, and J. A. Jackson, Eds., *Glossary of geology*. Alexandria, Virginia: American Geosciences Inst, 2011.
- [12] “Clay Types, Geology, Properties and Color Chart (GcCeramics) - Meeneecat.” <https://sites.google.com/site/meeneecat/educational-materials/clay-types-geological-origins-working-properties-gccceramics> (accessed Mar. 21, 2022).
- [13] H. H. Murray, “Applied clay mineralogy today and tomorrow,” *Clay Miner.*, vol. 34, no. 1, pp. 39–49, Mar. 1999, doi: 10.1180/000985599546055.
- [14] R. E. Grim, *Applied clay mineralogy*. New York: McGraw-Hill, 1962.
- [15] C. K. Wentworth, “A Scale of Grade and Class Terms for Clastic Sediments,” *J. Geol.*, vol. 30, no. 5, pp. 377–392, 1922.
- [16] R. E. Grim, *Clay mineralogy*. New York [NY: McGraw-Hill, 1968.

- [17] Yasuo Kitagawa, "AN ASPECT OF THE WATER IN CLAY MINERALS: AN APPLICATION OF NUCLEAR MAGNETIC RESONANCE SPECTROMETRY TO CLAY MINERALOGY," *Am. Mineral.*, vol. 57, pp. 751–764, 1972.
- [18] W. L. Pohl, *Economic Geology Principles and Practice: Metals, Minerals, Coal and Hydrocarbons - Introduction to Formation and Sustainable Exploitation of Mineral Deposits*. Oxford, UK: Wiley-Blackwell, 2011. doi: 10.1002/9781444394870.
- [19] R. E. Grim, *Clay mineralogy*. New York: McGraw-Hill, 1968.
- [20] Nadziakiewicz, Kehoe, and Micek, "Physico-Chemical Properties of Clay Minerals and Their Use as a Health Promoting Feed Additive," *Animals*, vol. 9, no. 10, p. 714, Sep. 2019, doi: 10.3390/ani9100714.
- [21] "Basics of Clay Minerals and Their Characteristic Properties | IntechOpen." <https://www.intechopen.com/online-first/76780> (accessed Nov. 14, 2021).
- [22] "Armenian Highlands - Alchetron, The Free Social Encyclopedia," *Alchetron.com*, Aug. 18, 2017. <https://alchetron.com/Armenian-Highlands> (accessed May 10, 2022).
- [23] I. Kh. Petrosov, *Clayey rocks of the Armenian SSR: Clay formation in the inner regions of geosynclines*, 500th ed. Yerevan: Academy of Science of Armenian SSR, 1983.
- [24] Ed. Kharazian and H. H. Sargsyan, "Geological map of Republic of Armenia," Ministry of Nature Protection, Geological Agency, Armenia, Yerevan, 2005. [Online]. Available: <https://www.geo-fund.am/filemanager/maps-02.pdf>
- [25] A. G. ISRAELYAN, H. H. SARGSYAN, T. K. LORSABYAN, and V. A. AGHAMALYAN, "Main Tectonic Units of Armenia," *I*, p. 10, 2012.
- [26] M. Nalbandyan, "MANAGEMENT AND PERSPECTIVES OF USING OF UNDERGROUND FRESHWATERS FROM TRANSBOUNDARY AQUIFERS IN ARMENIA," Jun. 2012, doi: 10.5593/SGEM2012/S13.V3034.
- [27] N. N. Tumanyan, E. A. Melikjanyan, A. A. Gevorkyan, and G. K. Gevorkyan, *Report on the results of preliminary exploration carried out in the northeastern part of the Shahumyan clay deposit in the Artashat region of Armenia for 1982-1983*. Yerevan: Geology of the Armenian SSR, 1983. [Online]. Available: file:///C:/Users/esoya/OneDrive/Desktop/PhD/About%20Armenian%20clay/Report_Armenian%20clay%20literature%20review/4027.pdf
- [28] M. M. Kazaryan, "The results of geological exploration work carried out at the Shahumyan (Yuva) clay deposit in the Artashat region of the Armenian USSR for 1960/reserve calculation.," Yerevan, 1414, 1961.
- [29] T. G. Bonney, *Volcanoes: Their Structure and Significance*. G. P. Putnam's sons, 1912.
- [30] S. S. Mkrtchyan, A. A. Gabrielyan, L. A. Vardanyants, I. G. Maghakyan, and K. N. Paffenholc, *Geology of Armenian SSR*, vol. VII. Yerevan: Academy of Science Armenian SSR, 1966.
- [31] G. M. Abramyan and A. O. Martirosyan, "A report on the results of exploration work carried out by the Shahumyan party at the Shahumyan clay deposit in the Artashat region of the Armenian SSR in 1969 with a calculation of reserves for 1970.," Armenia, Yerevan, 1970.

- [32] G. T. Saleiro and J. N. F. Holanda, "Processing of red ceramic using a fast-firing cycle," *Cerâmica*, vol. 58, no. 347, pp. 393–399, Sep. 2012, doi: 10.1590/S0366-69132012000300018.
- [33] P.-M. Nigay, T. Cutard, and A. Nzihou, "The impact of heat treatment on the microstructure of a clay ceramic and its thermal and mechanical properties," *Ceram. Int.*, vol. 43, no. 2, p. p.1747-1754, 2017, doi: 10.1016/j.ceramint.2016.10.084.
- [34] M. Pfeifer, "Material Properties and Materials Science," in *Materials Enabled Designs*, Elsevier, 2009, pp. 59–114. doi: 10.1016/B978-0-7506-8287-9.00004-5.
- [35] S. N. Monteiro and C. M. F. Vieira, "Activation Energy for the Sintering of Clay Based Ceramic Powder," *Mater. Sci. Forum*, vol. 660–661, pp. 813–818, Oct. 2010, doi: 10.4028/www.scientific.net/MSF.660-661.813.
- [36] M. A. Harech *et al.*, "Effect of temperature and clay addition on the thermal behavior of phosphate sludge," *Bol. Soc. Esp. Cerámica Vidr.*, vol. 60, no. 3, pp. 194–204, May 2021, doi: 10.1016/j.bsecv.2020.03.002.
- [37] A. Duzdabanyan, "In Armenia, Making Orange Wine is Personal," *Wine Enthusiast*, Feb. 09, 2022. <https://www.winemag.com/2022/02/09/orange-wine-armenia/> (accessed Feb. 21, 2022).
- [38] admin, "Ceramic Wine Egg for wine Fermentation and Storage," *Magnum 675*. <https://www.magnum675.com/> (accessed Feb. 18, 2022).
- [39] "5 Great Reasons to Explore Armenian Wines | Natalie MacLean." <https://www.nataliemaclean.com/blog/videos/5-great-reasons-to-explore-armenian-wines/> (accessed Feb. 21, 2022).
- [40] S. Ferrer, A. Mezquita, M. P. Gomez-Tena, C. Machi, and E. Monfort, "Estimation of the heat of reaction in traditional ceramic compositions," *Appl. Clay Sci.*, vol. 108, pp. 28–39, May 2015, doi: 10.1016/j.clay.2015.02.019.
- [41] A. Abdul Kadir and A. Mohajerani, "Effect of heating rate on gas emissions and properties of fired clay bricks and fired clay bricks incorporated with cigarette butts," *Appl. Clay Sci.*, vol. 104, pp. 269–276, Feb. 2015, doi: 10.1016/j.clay.2014.12.005.
- [42] "Ultra-high heating rate effects on the sintering of ceramic nanoparticles: an in situ TEM study." <https://www.tandfonline.com/doi/epub/10.1080/21663831.2021.1927878?needAccess=true> (accessed Mar. 28, 2022).
- [43] G. Cultrone, C. Rodriguez-Navarro, E. Sebastian, O. Cazalla, and M. J. De La Torre, "Carbonate and silicate phase reactions during ceramic firing," *Eur. J. Mineral.*, vol. 13, no. 3, pp. 621–634, May 2001, doi: 10.1127/0935-1221/2001/0013-0621.
- [44] M. F. Serra, M. S. Conconi, G. Suarez, E. F. Agietti, and N. M. Rendtorff, "Firing transformations of an argentinean calcareous commercial clay," *Cerâmica*, vol. 59, no. 350, pp. 254–261, Jun. 2013, doi: 10.1590/S0366-69132013000200010.
- [45] M. Trindade, M. Dias, J. Coroado, and F. Rocha, "Mineralogical transformations of calcareous rich clays with firing: A comparative study between calcite and dolomite rich clays from Algarve, Portugal," *Appl. Clay Sci.*, vol. 42, no. 3–4, pp. 345–355, Jan. 2009, doi: 10.1016/j.clay.2008.02.008.

- [46] contact@daquitaine.fr, “Tonnelierie d’Aquitaine - fabrication de fûts, tonneaux et barriques,” <http://www.daquitaine.fr/>. <http://www.daquitaine.fr/> (accessed Mar. 27, 2022).
- [47] “Bouteille Bordelaise PRESTIGIO - 75 cl - 560g - Bouteilles bordelaises spéciales - GOE SERVICE.” <http://www.goe-service.com/fr/produits/fournisseur-bouteille-vin/bordelaises/speciales/bouteille-bordelaise-prestigio-75-cl-560g/p-9-40.html> (accessed Mar. 27, 2022).
- [48] R. Parameshwaran, A. Sarı, N. Jalaiah, and R. Karunakaran, “Applications of Thermal Analysis to the Study of Phase-Change Materials,” in *Handbook of Thermal Analysis and Calorimetry*, vol. 6, Elsevier, 2018, pp. 519–572. doi: 10.1016/B978-0-444-64062-8.00005-X.
- [49] G. W. Brindley and G. Brown, Eds., *Crystal Structures of Clay Minerals and their X-Ray Identification*. Colchester and London: Mineralogical Society of Great Britain and Ireland, 1980, p. gswbk;9780903056373/1. doi: 10.1180/mono-5.
- [50] D. M. Moore and R. C. Reynolds, *X-ray diffraction and the identification and analysis of clay minerals*, 2nd ed. Oxford ; New York: Oxford University Press, 1997.
- [51] S. Tamari and A. Aguilar-Chávez, “Optimum Design of Gas Pycnometers for Determining the Volume of Solid Particles,” *J. Test. Eval.*, vol. 33, no. 2, p. 12674, 2005, doi: 10.1520/JTE12674.
- [52] F. J. Semel and D. A. Lados, “Porosity analysis of PM materials by helium pycnometry,” *Powder Metall.*, vol. 49, no. 2, pp. 173–182, Jun. 2006, doi: 10.1179/174329006X95347.
- [53] S. Ismajli, F. E. Soetaredjo, and A. Ayucitra, “The Characterization of Clay Minerals and Adsorption Mechanism onto Clays,” in *Clay Materials for Environmental Remediation*, Cham: Springer International Publishing, 2015, pp. 93–112. doi: 10.1007/978-3-319-16712-1_5.
- [54] O. D. Neikov and N. A. Yefimov, “Powder Characterization and Testing,” in *Handbook of Non-Ferrous Metal Powders*, Elsevier, 2019, pp. 3–62. doi: 10.1016/B978-0-08-100543-9.00001-4.
- [55] P. R. Bodart *et al.*, “Analysis of the Proton Spin–Lattice Relaxation in Wine and Hydroalcoholic Solutions,” *Food Anal. Methods*, vol. 15, no. 2, pp. 266–275, Feb. 2022, doi: 10.1007/s12161-021-02118-w.
- [56] J.-B. Diéval, S. Vidal, and O. Aagaard, “Measurement of the Oxygen Transmission Rate of Co-extruded Wine Bottle Closures Using a Luminescence-Based Technique: OXYGEN TRANSMISSION RATE MEASUREMENT OF CO-EXTRUDED CLOSURE,” *Packag. Technol. Sci.*, vol. 24, no. 7, pp. 375–385, Nov. 2011, doi: 10.1002/pts.945.
- [57] M. I. Bruno Tavares, “NMR Relaxometry Applied to Food Samples,” in *Applications of NMR Spectroscopy*, vol. 6, A. Rahman and M. I. Choudhary, Eds. UAE: Bentham Science Publishers Ltd., 2017, pp. 151–176. doi: 10.2174/9781681084398117060006.
- [58] J. Kowalewski, *Nuclear Spin Relaxation in Liquids*. London: CRC Press, 2017. Accessed: Mar. 26, 2022. [Online]. Available: <http://www.myilibrary.com?id=1056549>
- [59] R. Kimmich, *NMR Tomography, Diffusometry, Relaxometry*. 2019. doi: 10.1007/978-3-642-60582-6.

- [60] D. Kruk, *Understanding spin dynamics*. Pan Stanford Publishing Singapore, 2016.
- [61] P. R. Bodart *et al.*, “Quantification of manganese ions in wine by NMR relaxometry,” *Talanta*, vol. 209, p. 120561, Mar. 2020, doi: 10.1016/j.talanta.2019.120561.
- [62] M. G. Hamamchyan, O. V. Grigoryan, and G. H. Grigoryan, “INVESTIGATION OF THE CHEMICAL COMPOSITION OF THE CLAY DEPOSITS OF ARTASHAT, ARARAT, YEGHEGNADZOR REGIONS,” *Chem. J. Armen.*, vol. 1–2, no. 54, p. 5, 2001.
- [63] K. H. Navasardyan, “About some peculiarities of early Bronze Age pottery in Armenia,” *Banber”- Bull. Yerevan Univ.*, vol. 3, pp. 126–131, 1991.
- [64] R. V. Hakobyan and H. G. Banayan, “Formation of high-temperature phases during the process of firing clay from Ijevan and Shahumyan deposits,” *Proc. Yerevan State Univ.*, no. 1, p. 4, 2000.
- [65] E. Kh. Gulyan, N. S. Khachatryan, L. G. Ter-Abramyan, and V. E. Goginyan, “Feasibility study for the expediency of developing the Shahumyan clay deposit,” Yerevan, 1970.
- [66] K. Traoré, T. S. Kabré, and P. Blanchart, “Gehlenite and anorthite crystallisation from kaolinite and calcite mix,” *Ceram. Int.*, vol. 29, no. 4, pp. 377–383, Jan. 2003, doi: 10.1016/S0272-8842(02)00148-7.
- [67] C. Rodriguez-Navarro, E. Ruiz-Agudo, A. Luque, A. B. Rodriguez-Navarro, and M. Ortega-Huertas, “Thermal decomposition of calcite: Mechanisms of formation and textural evolution of CaO nanocrystals,” *Am. Mineral.*, vol. 94, no. 4, pp. 578–593, Apr. 2009, doi: 10.2138/am.2009.3021.
- [68] F. Moodi, A. A. Ramezani-pour, and A. Sh. Safavizadeh, “Evaluation of the optimal process of thermal activation of kaolins,” *Sci. Iran.*, vol. 18, no. 4, pp. 906–912, Aug. 2011, doi: 10.1016/j.scient.2011.07.011.
- [69] S. Astutiningsih, I. M. Banjarnahor, and A. Zakiyuddin, “Characterization and Fabrication of Metakaolin using Pulau Bangka Kaolin,” *E3S Web Conf.*, vol. 67, p. 03021, 2018, doi: 10.1051/e3sconf/20186703021.
- [70] C. Rathossi and Y. Pontikes, “Effect of firing temperature and atmosphere on ceramics made of NW Peloponnese clay sediments: Part II. Chemistry of pyrometamorphic minerals and comparison with ancient ceramics,” *J. Eur. Ceram. Soc.*, vol. 30, pp. 1853–1866, Jul. 2010, doi: 10.1016/j.jeurceramsoc.2010.02.003.
- [71] M. J. Trindade, M. I. Dias, J. Coroado, and F. Rocha, “Firing Tests on Clay-Rich Raw Materials from the Algarve Basin (Southern Portugal): Study of Mineral Transformations with Temperature,” *Clays Clay Miner.*, vol. 58, no. 2, p. 188, 2010.
- [72] E. Escalera, M.-L. Antti, and M. Odén, “Thermal treatment and phase formation in kaolinite and illite based clays from tropical regions of Bolivia,” *Mater. Sci. Eng. Conf. Ser.*, vol. 31, p. 2017, Feb. 2012, doi: 10.1088/1757-899X/31/1/012017.
- [73] K. S. P. Karunadasa, C. H. Manoratne, H. M. T. G. A. Pitawala, and R. M. G. Rajapakse, “Thermal decomposition of calcium carbonate (calcite polymorph) as examined by in-situ high-temperature X-ray powder diffraction,” *J. Phys. Chem. Solids*, vol. 134, pp. 21–28, Nov. 2019, doi: 10.1016/j.jpcs.2019.05.023.

- [74] U. M. B. Al-Naib, "Introductory Chapter: A Brief Introduction to Porous Ceramic," in *Recent Advances in Porous Ceramics*, U. M. B. Al-Naib, Ed. InTech, 2018. doi: 10.5772/intechopen.74747.
- [75] T. Ohji and M. Fukushima, "Macro-porous ceramics: processing and properties," *Int. Mater. Rev.*, vol. 57, no. 2, pp. 115–131, Mar. 2012, doi: 10.1179/1743280411Y.0000000006.
- [76] Y. Chen, N. Wang, O. Ola, Y. Xia, and Y. Zhu, "Porous ceramics: Light in weight but heavy in energy and environment technologies," *Mater. Sci. Eng. R Rep.*, vol. 143, p. 100589, Jan. 2021, doi: 10.1016/j.mser.2020.100589.
- [77] O. Delbrouck, J. Janssen, R. Ottenburgs, P. Van Oyen, and W. Viaene, "Evolution of porosity in extruded stoneware as a function of firing temperature," *Appl. Clay Sci.*, vol. 8, no. 2–3, pp. 187–192, Aug. 1993, doi: 10.1016/0169-1317(93)90036-Z.
- [78] M. F. Serra, M. F. Acebedo, M. S. Conconi, G. Suarez, E. F. Aglietti, and N. M. Rendtorff, "Thermal evolution of the mechanical properties of calcareous earthenware," *Ceram. Int.*, vol. 40, no. 1, pp. 1709–1716, Jan. 2014, doi: 10.1016/j.ceramint.2013.07.067.
- [79] R. Vijayaragavan and S. Mullainathan, "Effect of Sintering Temperature on the Properties and Microstructure of a Ceramic Product," vol. 8, p. 5, 2011.
- [80] M. M. Jordan, M. A. Montero, S. Meseguer, and T. Sanfeliu, "Influence of firing temperature and mineralogical composition on bending strength and porosity of ceramic tile bodies," *Appl. Clay Sci.*, vol. 42, no. 1–2, pp. 266–271, Dec. 2008, doi: 10.1016/j.clay.2008.01.005.
- [81] M. Jaroniec, M. Kruk, and A. Sayari, "Adsorption methods for characterization of surface and structural properties of mesoporous molecular sieves," in *Studies in Surface Science and Catalysis*, vol. 117, Elsevier, 1998, pp. 325–332. doi: 10.1016/S0167-2991(98)81008-2.
- [82] V. Cotiuga, A. V. Sandu, A. Ciocan, G. Olteanu, and V. Vasilache, "New Archaeometric Characteristics for Ancient Pottery Identification," *Int. J. Conserv. Sci.*, vol. 1, Jun. 2010.
- [83] B. F. Bohor, "Scanning Electron Microscopy of Clays and Clay Minerals," *Clays Clay Miner.*, vol. 19, no. 1, pp. 49–54, 1971, doi: 10.1346/CCMN.1971.0190105.
- [84] A. I. Salimon *et al.*, "A Mini-Atlas of diatom frustule electron microscopy images at different magnifications," *Mater. Today Proc.*, vol. 33, pp. 1924–1933, 2020, doi: 10.1016/j.matpr.2020.05.602.
- [85] M. Park, S. D. Lee, H. Lee, J.-Y. Lee, D. Kwon, and J.-M. Choi, "Identification of New Sub-Fossil Diatoms Flora in the Sediments of Suncheonman Bay, Korea," *J. Mar. Sci. Eng.*, vol. 9, no. 6, p. 591, May 2021, doi: 10.3390/jmse9060591.
- [86] M. Rybak *et al.*, "Marine and brackish Luticola D.G.Mann (Bacillariophyta) species from the Java Sea and South China Sea coasts with the description of three new species," *PhytoKeys*, vol. 183, pp. 115–142, Oct. 2021, doi: 10.3897/phytokeys.183.71049.
- [87] P. Holligan and W. Balch, "From the Ocean to Cells: Coccolithophore Optics and Biogeochemistry," 1991, pp. 301–324. doi: 10.1007/978-3-642-75121-9_12.

- [88] J. R. Young, M. Geisen, and I. Probert, "A review of selected aspects of coccolithophore biology with implications for paleobiodiversity estimation," *Micropaleontology*, vol. 51, no. 4, pp. 267–288, Oct. 2005, doi: 10.2113/gsmicropal.51.4.267.
- [89] S. Gardin, L. Krystyn, S. Richoz, A. Bartolini, and B. Galbrun, "Where and when the earliest coccolithophores?: *Where and when the earliest coccolithophores?*," *Lethaia*, vol. 45, no. 4, pp. 507–523, Oct. 2012, doi: 10.1111/j.1502-3931.2012.00311.x.
- [90] C. J. Daniels *et al.*, "A global compilation of coccolithophore calcification rates," *Earth Syst. Sci. Data*, vol. 10, no. 4, pp. 1859–1876, Oct. 2018, doi: 10.5194/essd-10-1859-2018.
- [91] A. M. Gombos, "Fossil Diatoms from Leg 7, Deep Sea Drilling Project," *Micropaleontology*, vol. 21, no. 3, p. 306, Jul. 1975, doi: 10.2307/1485198.
- [92] F. M. Monteiro *et al.*, "Why marine phytoplankton calcify," *Sci. Adv.*, vol. 2, no. 7, p. e1501822, Jul. 2016, doi: 10.1126/sciadv.1501822.
- [93] A. Parente, M. Cachão, K.-H. Baumann, L. Abreu, and J. Ferreira, "Morphometry of *Coccolithus pelagicus* s.l. (Coccolithophore, Haptophyta) from offshore Portugal, during the last 200 kyr," *Micropaleontology*, vol. 50, pp. 107–120, Jan. 2004.
- [94] J. R. Young, M. Geisen, L. Cros, A. Kleijne, C. Sprengel, and I. Probert, "A GUIDE TO EXTANT COCCOLITHOPHORE TAXONOMY," p. 132.
- [95] Y. Maniatis and M. S. Tite, "Technological examination of Neolithic-Bronze Age pottery from central and southeast Europe and from the Near East," *J. Archaeol. Sci.*, vol. 8, no. 1, pp. 59–76, Mar. 1981, doi: 10.1016/0305-4403(81)90012-1.
- [96] I. C. Freestone and A. P. Middleton, "Mineralogical applications of the analytical SEM in archaeology," *Mineral. Mag.*, vol. 51, no. 359, pp. 21–31, Mar. 1987, doi: 10.1180/minmag.1987.051.359.03.
- [97] A. Krapukaitytė, "SEM and EDX characterization of ancient pottery," *Lith. J. Phys.*, vol. 46, no. 3, pp. 383–388, 2006, doi: 10.3952/lithjphys.46310.
- [98] D. E. González-Santamaría *et al.*, "SEM-EDX study of bentonite alteration under the influence of cement alkaline solutions," *Appl. Clay Sci.*, vol. 212, p. 106223, Oct. 2021, doi: 10.1016/j.clay.2021.106223.
- [99] M. Zawrah, R. Gado, N. Feltin, S. Ducourtieux, and L. Devuille, "Recycling and utilization assessment of waste fired clay bricks (Grog) with granulated blast-furnace slag for geopolymer production," *Process Saf. Environ. Prot.*, vol. 103, Aug. 2016, doi: 10.1016/j.psep.2016.08.001.
- [100] B. Alina, M. Gligor, I. Dulama, S. Teodorescu, R.-M. Știrbescu, and C. Radulescu, "ATR-FTIR and SEM-EDS Analyses of Lumea Nouă Painted Pottery from Alba Iulia-Lumea Nouă Neolithic Site," *Rev. Chim. -Buchar. - Orig. Ed.*, vol. 68, Apr. 2017.
- [101] S. Zheng, L. Niu, P. Pei, and J. Dong, "Mechanical Behavior of Brick Masonry in an Acidic Atmospheric Environment," *Materials*, vol. 12, p. 2694, Aug. 2019, doi: 10.3390/ma12172694.
- [102] K. G. Knauss and T. J. Wolery, "Dependence of albite dissolution kinetics on pH and time at 25°C and 70°C," *Geochim. Cosmochim. Acta*, vol. 50, no. 11, pp. 2481–2497, Nov. 1986, doi: 10.1016/0016-7037(86)90031-1.

- [103] K. G. Knauss, S. N. Nguyen, and H. C. Weed, "Diopside dissolution kinetics as a function of pH, CO₂, temperature, and time," *Geochim. Cosmochim. Acta*, vol. 57, pp. 285–294, 1992, doi: 10.1016/0016-7037(93)90431-U.
- [104] A. Luetge, BOLTON, E. W., and LASAGA, A. C., "An interferometric study of the dissolution kinetics of anorthite; the role of reactive surface area," *Am. J. Sci.*, vol. 299, no. 7–9, pp. 652–678, Nov. 1999, doi: 10.2475/ajs.299.7-9.652.
- [105] S. A. Welch and W. J. Ullman, "The effect of organic acids on plagioclase dissolution rates and stoichiometry," *Geochim. Cosmochim. Acta*, vol. 57, no. 12, pp. 2725–2736, Jun. 1993, doi: 10.1016/0016-7037(93)90386-B.
- [106] J. Torrent, "The Reductive Dissolution of Synthetic Goethite and Hematite in Dithionite," *Clay Miner. - CLAY Min.*, vol. 22, pp. 329–337, Sep. 1987, doi: 10.1180/claymin.1987.022.3.07.
- [107] R. Sturza, C. Bilici, I. Zinicovscaia, O. A. Culicov, S. Gundorina, and G. Duca, "MOLDAVIAN WINE ANALYSIS BY ICP-AES AND NAA TECHNIQUES: COMPARISON STUDY," p. 8.
- [108] N. P. Cheremisinoff, "ELEMENTAL AND STRUCTURAL CHARACTERIZATION TESTS," in *Polymer Characterization*, Elsevier, 1996, pp. 43–81. doi: 10.1016/B978-081551403-9.50006-6.
- [109] B. R. Stanmore and P. Gilot, "Review—calcination and carbonation of limestone during thermal cycling for CO₂ sequestration," *Fuel Process. Technol.*, vol. 86, no. 16, pp. 1707–1743, Nov. 2005, doi: 10.1016/j.fuproc.2005.01.023.
- [110] V. Nikulshina, M. E. Galvez, and A. Steinfeld, "Kinetic analysis of the carbonation reactions for the capture of CO₂ from air via the Ca(OH)₂–CaCO₃–CaO solar thermochemical cycle," *Chem. Eng. J.*, p. 9, 2007, doi: 10.1016/j.cej.2006.11.003.
- [111] U. Sanchez-Garmendia, J. G. Iñáñez, and G. Arana, "Alterations and Contaminations in Ceramics Deposited in Underwater Environments: An Experimental Approach," *Minerals*, vol. 11, no. 7, p. 766, Jul. 2021, doi: 10.3390/min11070766.
- [112] E. Serris *et al.*, "Study of the hydration of CaO powder by gas–solid reaction," *Cem. Concr. Res.*, vol. 41, no. 10, pp. 1078–1084, Oct. 2011, doi: 10.1016/j.cemconres.2011.06.014.
- [113] Y. A. Criado, M. Alonso, and J. C. Abanades, "Kinetics of the CaO/Ca(OH)₂ hydration/dehydration reaction for thermochemical energy storage applications," p. 33.
- [114] L. B. Miller and J. C. Witt, "Solubility of Calcium Hydroxide," *J. Phys. Chem.*, vol. 33, no. 2, pp. 285–289, Feb. 1929, doi: 10.1021/j150296a010.
- [115] D. R. Lide, G. Baysinger, S. Chemistry, L. I. Berger, R. N. Goldberg, and H. V. Kehiaian, "CRC Handbook of Chemistry and Physics," p. 2661, 2005.
- [116] P. C. Bennett, M. E. Melcer, D. I. Siegel, and J. P. Hasset, "The dissolution of quartz in diluted aqueous solutions of organic acids at 25°C," *Geochim. Cosmochim. Acta*, vol. 52, pp. 1521–1530, 1988, doi: 10.1016/0016-7037(88)90222-0.
- [117] S. R. Bragança and C. P. Bergmann, "Effect of Quartz of Fine Particle Size on Porcelain Properties," *Mater. Sci. Forum*, vol. 530–531, pp. 493–498, Nov. 2006, doi: 10.4028/www.scientific.net/MSF.530-531.493.

- [118] Y. Deng, "Effect of pH on the Reductive Dissolution Rates of Iron(III) Hydroxide by Ascorbate," *Langmuir*, vol. 13, no. 6, pp. 1835–1839, Mar. 1997, doi: 10.1021/la9607013.
- [119] J. Qin, C. Yang, C. Cui, J. Huang, A. Hussain, and H. Ma, "Ca²⁺ and OH⁻ release of ceramsites containing anorthite and gehlenite prepared from waste lime mud," *J. Environ. Sci.*, vol. 47, pp. 91–99, Sep. 2016, doi: 10.1016/j.jes.2016.03.013.
- [120] C. Coelho *et al.*, "Molecular and Macromolecular Changes in Bottle-Aged White Wines Reflect Oxidative Evolution—Impact of Must Clarification and Bottle Closure," *Front. Chem.*, vol. 6, Apr. 2018, doi: 10.3389/fchem.2018.00095.
- [121] M. Nikolantonaki *et al.*, "Impact of Glutathione on Wines Oxidative Stability: A Combined Sensory and Metabolomic Study," *Front. Chem.*, vol. 6, Jun. 2018, doi: 10.3389/fchem.2018.00182.
- [122] J. C. Danilewicz, "Review of Oxidative Processes in Wine and Value of Reduction Potentials in Enology," *Am. J. Enol. Vitic.*, vol. 63, no. 1, pp. 1–10, Mar. 2012, doi: 10.5344/ajev.2011.11046.
- [123] J. C. Danilewicz, "Role of Tartaric and Malic Acids in Wine Oxidation," *J. Agric. Food Chem.*, vol. 62, no. 22, pp. 5149–5155, Jun. 2014, doi: 10.1021/jf5007402.
- [124] M. Aceto, O. Abollino, M. C. Bruzzone, E. Mentasti, C. Sarzanini, and M. Malandrino, "Determination of metals in wine with atomic spectroscopy (flame-AAS, GF-AAS and ICP-AES); a review," *Food Addit. Contam.*, vol. 19, no. 2, pp. 126–133, Feb. 2002, doi: 10.1080/02652030110071336.
- [125] P. Pellerin, T. Doco, and G. R. Scollary, "The influence of wine polymers on the spontaneous precipitation of calcium tartrate in a model wine solution," *Int. J. Food Sci. Technol.*, vol. 48, no. 12, pp. 2676–2682, Dec. 2013, doi: 10.1111/ijfs.12264.
- [126] A. J. McKinnon, G. R. Scollary, D. H. Solomon, and P. J. Williams, "The mechanism of precipitation of calcium L(+)-tartrate in a model wine solution," *Colloids Surf. Physicochem. Eng. Asp.*, vol. 82, no. 3, pp. 225–235, Feb. 1994, doi: 10.1016/0927-7757(93)02636-S.
- [127] M. Taxiarchou, D. Panias, I. Douni, I. Paspaliaris, and A. Kontopoulos, "Dissolution of hematite in acidic oxalate solutions," *Hydrometallurgy*, vol. 44, no. 3, pp. 287–299, Mar. 1997, doi: 10.1016/S0304-386X(96)00075-8.
- [128] D. Panias, M. Taxiarchou, I. Douni, I. Paspaliaris, and A. Kontopoulos, "Dissolution of hematite in acidic oxalate solutions: the effect of ferrous ions addition," *Hydrometallurgy*, vol. 43, no. 1–3, pp. 219–230, Nov. 1996, doi: 10.1016/0304-386X(96)00004-7.
- [129] S. Vallejos, A. Muñoz, S. Ibeas, F. Serna, F. C. García, and J. M. García, "Solid sensory polymer substrates for the quantification of iron in blood, wine and water by a scalable RGB technique," *J. Mater. Chem. A*, vol. 1, no. 48, p. 15435, 2013, doi: 10.1039/c3ta12703f.
- [130] Y. Margalit and J. Crum, *Concepts in wine chemistry*. San Francisco: Wine Appreciation Guild, 1997.
- [131] R. E. Coleman, R. B. Boulton, and A. A. Stuchebrukhov, "Kinetics of autoxidation of tartaric acid in presence of iron," *J. Chem. Phys.*, vol. 153, no. 6, p. 064503, Aug. 2020, doi: 10.1063/5.0013727.

- [132] E. F. S. Authority (EFSA), "Safety of aluminium from dietary intake - Scientific Opinion of the Panel on Food Additives, Flavourings, Processing Aids and Food Contact Materials (AFC)," *EFSA J.*, vol. 6, no. 7, p. 754, 2008, doi: 10.2903/j.efsa.2008.754.
- [133] N. Bloembergen, "Proton Relaxation Times in Paramagnetic Solutions," *J. Chem. Phys.*, vol. 27, no. 2, pp. 572–573, Aug. 1957, doi: 10.1063/1.1743771.
- [134] S. H. Koenig and R. D. Brown, "Relaxation of solvent protons by paramagnetic ions and its dependence on magnetic field and chemical environment: implications for NMR imaging," *Magn. Reson. Med.*, vol. 1, no. 4, pp. 478–495, Dec. 1984, doi: 10.1002/mrm.1910010407.
- [135] A. J. Pell, G. Pintacuda, and C. P. Grey, "Paramagnetic NMR in solution and the solid state," *Prog. Nucl. Magn. Reson. Spectrosc.*, vol. 111, pp. 1–271, Apr. 2019, doi: 10.1016/j.pnmrs.2018.05.001.
- [136] I. Bertini, C. Luchinat, G. Parigi, and E. Ravera, *NMR of paramagnetic molecules: applications to metalloproteins and models*. 2017. Accessed: Apr. 22, 2019. [Online]. Available: <http://search.ebscohost.com/login.aspx?direct=true&scope=site&db=nlebk&db=nlabk&AN=1145286>
- [137] R. M. Cornell and U. Schwertmann, *The iron oxides: structure, properties, reactions, occurrences, and uses*, 2nd, completely rev. and extended ed ed. Weinheim: Wiley-VCH, 2003.
- [138] F. Franks, Ed., *The Physics and Physical Chemistry of Water*. Boston, MA: Springer New York, 1972. doi: 10.1007/978-1-4684-8334-5.
- [139] A. Schlüter and A. Weiss, "Nuclear magnetic resonance relaxation titration," *Fresenius Z. Für Anal. Chem.*, vol. 266, no. 3, pp. 177–186, 1973.
- [140] P. R. Bodart *et al.*, "Access to water dynamic into the fibers of polygalacturonate gels by NMR relaxometry," *Carbohydr. Polym.*, vol. Submitted, 2021.
- [141] P. Bodart, P. Fouilloux, A. Rachocki, J. Tritt-Goc, T. Karbowski, and A. Assifaoui, "Mesh size determination in polycalacturonate gels by NMR relaxometry," *Be Submit 2022*.
- [142] P. Foulioux, "Etude d'hydrogel polysaccharidique par relaxométrie RMN.," bourgogne franche comté, Dijon, 2022.
- [143] W. P. Miller, L. W. Zelazny, and D. C. Martens, "Dissolution of synthetic crystalline and noncrystalline iron oxides by organic acids," *Geoderma*, vol. 37, no. 1, pp. 1–13, Feb. 1986, doi: 10.1016/0016-7061(86)90039-X.
- [144] S. A. Shchukarev and T. A. Tolmacheva, "Solubility of oxygen in ethanol ? Water mixtures," *J. Struct. Chem.*, vol. 9, no. 1, pp. 16–21, 1968, doi: 10.1007/BF00744018.
- [145] W. P. Miller, L. W. Zelazny, and D. C. Martens, "Dissolution of synthetic crystalline and noncrystalline iron oxides by organic acids," *Geoderma*, vol. 37, no. 1, pp. 1–13, Feb. 1986, doi: 10.1016/0016-7061(86)90039-X.
- [146] Y. Zhang, S. N. Kallay, and E. Matijević, "Interactions of Metal Hydrated Oxides with Chelating Agents. 7. Hematite-Oxalic Acid and -Citric Acid Systems?," p. 6.

- [147] “XRF Analysis.” <https://www.horiba.com/int/technology/elemental-analysis/energy-dispersive-x-rayfluorescence-ed-xrf/xrf-analysis/> (accessed Mar. 03, 2022).
- [148] C. Streli, P. Wobrauschek, and P. Kregsamer, “X-ray Fluorescence Spectroscopy, Applications,” in *Encyclopedia of Spectroscopy and Spectrometry*, Elsevier, 1999, pp. 2478–2487. doi: 10.1006/rwsp.2000.0337.
- [149] “What is X-ray Fluorescence (XRF).” <https://www.horiba.com/int/x-ray-fluorescence-spectroscopy-xrf/> (accessed Mar. 03, 2022).
- [150] V. Vishwakarma and S. Uthaman, “Environmental impact of sustainable green concrete,” in *Smart Nanoconcretes and Cement-Based Materials*, Elsevier, 2020, pp. 241–255. doi: 10.1016/B978-0-12-817854-6.00009-X.
- [151] M. Bimson, “The Examination of Ceramics by X-Ray Powder Diffraction,” *Stud. Conserv.*, vol. 14, no. 2, p. 83, May 1969, doi: 10.2307/1505350.
- [152] “Clay Shrinkage During Drying and Firing | Preventing Defects.” <https://www.lakesidepottery.com/HTML%20Text/Tips/Clay%20drying%20and%20firing%20process.htm> (accessed Nov. 17, 2021).
- [153] S. Oummadi, “Drying behaviour of ceramic green bodies: experimental characterization and numerical modeling,” UNIVERSITÉ DE LIMOGES, Dec. 16, 2019. [Online]. Available: <https://tel.archives-ouvertes.fr/tel-02495750/document>
- [154] S. OUMMADI, B. Nait-Ali, A. ALZINA, P. A. Y. A. Marie-Clotilde, G. A. I. L. L. A. R. D. Jean-Marie, and D. Smith, “Optical method for evaluation of shrinkage in two dimensions during drying of ceramic green bodies,” *Open Ceram.*, vol. 2, p. 100016, Aug. 2020, doi: 10.1016/j.oceram.2020.100016.
- [155] S. de Miranda, L. Patrino, M. Ricci, R. Saponelli, and F. Ubertini, “Ceramic sanitary wares: Prediction of the deformed shape after the production process,” *J. Mater. Process. Technol.*, vol. 215, pp. 309–319, Jan. 2015, doi: 10.1016/j.jmatprotec.2014.07.025.
- [156] D. Kruk, *Understanding spin dynamics*. Singapore: Pan Stanford Publishing, 2016.
- [157] Y. Ayant, E. Belorizky, J. Aluzon, and J. Gallice, “Calcul des densités spectrales résultant d’un mouvement aléatoire de translation en relaxation par interaction dipolaire magnétique dans les liquides,” *J. Phys.*, vol. 36, no. 10, pp. 991–1004, 1975, doi: 10.1051/jphys:019750036010099100.
- [158] I. Solomon, “Relaxation Processes in a System of Two Spins,” *Phys. Rev.*, vol. 99, no. 2, pp. 559–565, Jul. 1955, doi: 10.1103/PhysRev.99.559.
- [159] N. Bloembergen and L. O. Morgan, “Proton Relaxation Times in Paramagnetic Solutions. Effects of Electron Spin Relaxation,” *J. Chem. Phys.*, vol. 34, no. 3, pp. 842–850, Mar. 1961, doi: 10.1063/1.1731684.
- [160] I. Bertini, C. Luchinat, and G. Parigi, “¹H NMRD profiles of paramagnetic complexes and metalloproteins,” in *Advances in Inorganic Chemistry*, vol. 57, Elsevier, 2005, pp. 105–172. doi: 10.1016/S0898-8838(05)57003-X.
- [161] A. J. Pell, G. Pintacuda, and C. P. Grey, “Paramagnetic NMR in solution and the solid state,” *Prog. Nucl. Magn. Reson. Spectrosc.*, May 2018, doi: 10.1016/j.pnmrs.2018.05.001.

- [162] I. Bertini, M. Fragai, C. Luchinat, and G. Parigi, "Solvent ^1H NMRD Study of Hexaaquochromium(III): Inferences on Hydration and Electron Relaxation," *Inorg. Chem.*, vol. 40, pp. 4030–4035, 2001.
- [163] I. Bertini, F. Capozzi, C. Luchinat, and Z. Xia, "Nuclear and Electron Relaxation of $\text{Fe}(\text{OH}_2)_6^{3+}$," *J. Phys. Chem.*, vol. 97, no. 6, pp. 1134–1137, 1993.
- [164] C. Luchinat, G. Parigi, and E. Ravera, "Can metal ion complexes be used as polarizing agents for solution DNP? A theoretical discussion," *J. Biomol. NMR*, vol. 58, no. 4, pp. 239–249, Apr. 2014, doi: 10.1007/s10858-013-9728-8.
- [165] S. Aime, M. Botta, and E. Terreno, "Gd(III)-based contrast agent for MRI," in *Advances in Inorganic Chemistry*, vol. 57, Elsevier, 2005, pp. 173–237. doi: 10.1016/S0898-8838(05)57004-1.
- [166] "Atlas of Eh-pH diagrams Intercomparison of thermodynamic databases," Geological Survey of Japan Open File Report No.419 National Institute of Advanced Industrial Science and Technology Research Center for Deep Geological Environments Naoto TAKENO, May 2005.

Annex I. Mathematical code for calculating the ratio ρ for an axial symmetrical container

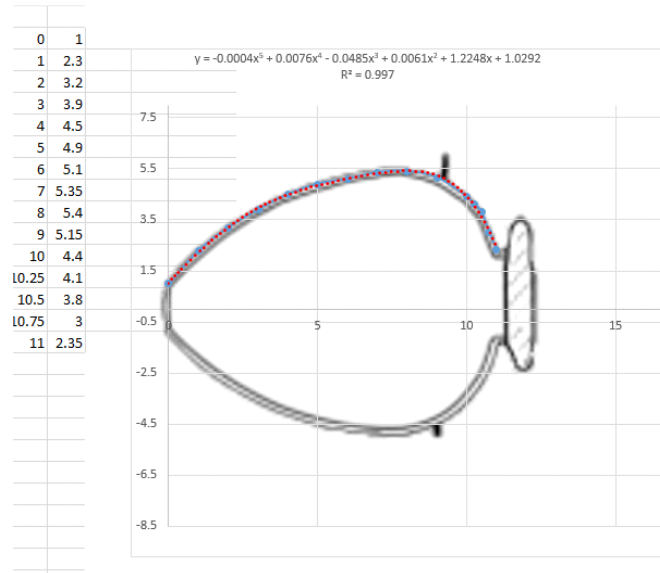
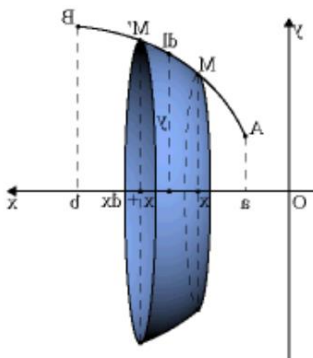


Figure 54. Original drawing from [1], fig 139, p 102 (Figure 10) and the revolution curve (red dots) with its digitalization reported in the two columns on the left.

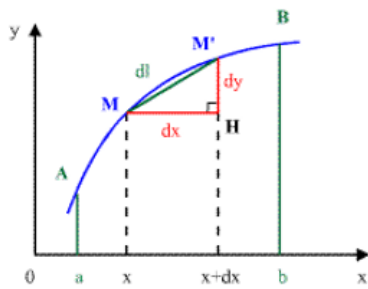
1. Area of a surface of revolution



A surface of revolution is generated by the rotation of a curve around an (Ox) axis. The elementary area $dS = 2\pi y dl$ produced by rotation of the arc $\widehat{MM'}$ corresponds to a truncated cone. In Cartesian coordinates dl is given by:

$$dl = \sqrt{1 + \left(\frac{dy}{dx}\right)^2} dx$$

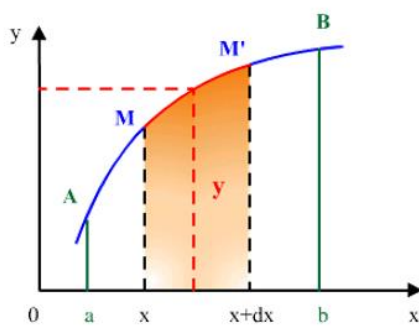
Hence, the surface of revolution of $y(x)$ in rotation around the axis Ox is obtained



with:

$$S = \int_A^B 2\pi y dl = 2\pi \int_{x_1}^{x_2} y \sqrt{1 + \left(\frac{dy}{dx}\right)^2} dx$$

2. Volume of a surface of revolution



In general, the calculation of volumes requires the use of triple integrals, but shapes with simple geometry or of revolution allow the use of a simple integral. The elementary volume dV generated by the colored area during rotation around the (Ox) axis is therefore:

$$dV = \pi y^2 dx$$

The volume generated by the area delimited by the arc \widehat{AB} , the axis (Ox) , and the lines of equations $x = a$ and $x = b$ is:

$$V = \int_a^b \pi y^2 dx$$

Annex II. XRF spectroscopy

XRF (X-ray fluorescence) is a non-destructive analytical technique that uses the interaction of x-rays with a material to determine the elemental composition. XRF is suitable for solids, liquids, and powders. There are two main XRF methodologies - energy dispersive (EDXRF) and wavelength dispersive (WDXRF). Each method has its own advantages and disadvantages. An energy dispersive detection system directly measures the different energies of the emitted X-rays from the sample. A wavelength-dispersive detection system physically separates the X-rays according to their wavelengths. The X-rays are directed to a crystal, which diffracts the X-rays in different directions according to their wavelengths (energies).

The range of detectable elements varies according to instrument configuration and setup, but typically EDXRF covers all elements from sodium (Na) to uranium (U), whilst WDXRF can extend this down to beryllium (Be). Concentrations can range from 100% down to ppm and in some cases sub-ppm levels. Limits of detection depend upon the specific element and the sample matrix, but as a general rule, heavier elements will have better detection limits. XRF is widely used as a fast characterization tool for applications as diverse as metallurgy, forensics, archaeology, environmental analysis, geology and mining. X-rays form part of the electromagnetic spectrum, and are characterized by energies lying between ultra-violet and gamma radiation. Wavelengths are typically in the range 0.01 to 10 nm, which is equivalent to energies of 125 keV to 0.125 keV. The interaction of X-rays with matter is more complex than simply 'passing through'. On reaching a material, some of the x-rays will be absorbed, and some scattered – if neither process occurs, the X-rays will be transmitted through the material. When absorption occurs, the X-rays interact with the material at the atomic level, and can cause subsequent fluorescence – it is this X-ray Fluorescence which forms the basis of XRF spectroscopy. The X-rays can also be scattered from the material. This scattering can occur both with and without loss of energy, called Compton and Rayleigh scattering respectively.

The ratio of absorption/fluorescence, scatter and transmission depends on the sample thickness, density and composition, and the X-ray energy. The absorption of X-rays

by a particular material varies according to the energy of the X-rays. As a rule of thumb, low-energy X-rays are absorbed more than high-energy photons.

To expel an electron from one of the orbitals, the X-ray energy must exceed the binding energy of that electron – however, if the X-ray energy is too high, then the coupling between X-ray and electron is inefficient, and only a few electrons will be knocked out. As the X-ray energy reduces, and approaches the electron binding energy, so the yield of expelled electrons increases. Just below this binding energy, a drop in absorption is observed, since the energy is not sufficient to emit electrons from that shell, and is too high in energy to emit electrons from the lower energy shells. Not all the incident X-rays result in fluorescence. The fluorescence yield is the ratio of fluorescence X-rays to incident X-rays. The diagram below illustrates the K and L fluorescence yield as a function of atomic number, Z. Detection limits depend very much on sample preparation and are in the range 20 -1000 $\mu\text{g/g}$ for low-Z elements, from 5 -10 $\mu\text{g/g}$ for medium-Z elements and from 1-20 $\mu\text{g/g}$ for high-Z elements. It is clear that the yield for the light elements is very low, and this is reflected in achievable sensitivity for these elements [147], [148].

XRF analyzers determine the chemistry of a sample by measuring the fluorescent (or secondary) X-ray energy of wavelength emitted from a sample when it is excited by a primary X-ray source. Each of the elements present in a sample produces a set of characteristic fluorescent X-rays (“a fingerprint”) that is unique for that specific element (Figure 55), which is why XRF spectroscopy is an excellent technology for qualitative and quantitative analysis of material composition.

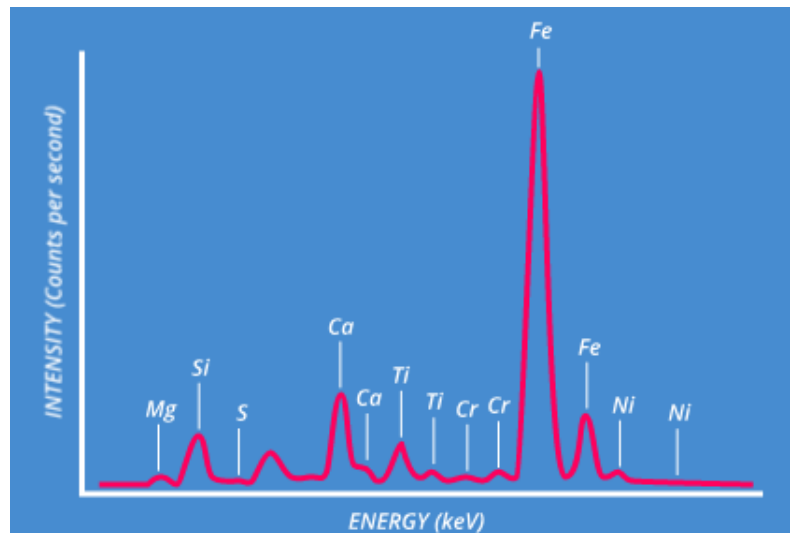


Figure 55. XRF spectrum of elements [147]

The X-ray fluorescence process: A sample (solid or a liquid) is irradiated with high-energy X-rays from a controlled X-ray tube. When an atom in the sample is struck with an X-ray of sufficient energy, an electron from one of the atom's inner orbital shells is dislodged. The atom regains stability, filling the vacancy left in the inner orbital shell with an electron from one of the atom's higher energy orbital shells. The electron drops to the lower energy state by releasing a fluorescent X-ray (Figure 56). The energy of this X-ray is equal to the specific difference in energy between two quantum states of the electron. The measurement of this energy is the basis of XRF analysis. When X-ray energy causes electrons to transfer in and out of these shell levels, XRF peaks with varying intensities are created and will be present in the spectrum, a graphical representation of X-ray intensity peaks as a function of energy peaks. The peak energy identifies the element, and the peak height/intensity is generally indicative of its concentration [149].

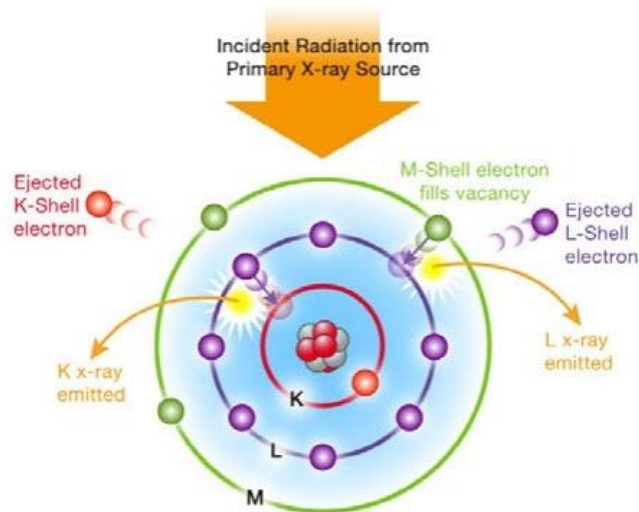


Figure 56. Emission of X-rays [149]

Table 17. Mechanical composition of the clay

Fraction - > 0,25 mm	0,2%
Fraction - 0,25 – 0,05 mm	9,0%
Fraction - 0,05 – 0,01 mm	41,1%
Fraction - 0,01 – 0,005 mm	21,7%
Fraction 0,005 – 0,001 mm	16,0%
Fraction - 0,001 mm	12,0%

According to X-ray diffraction and thermal analyzes, it has been proven that the clays of the Shahumyan deposit are represented by Illite (hydromica) - 17.2-23.5%, kaolinite - 6.2-13.9%, and very rarely montmorillonite. Clays of the Shahumyan deposit, depending on the mineral composition, belong to the kaolin-hydromica type, where the minerals of the kaolinite group are hydromica or both groups without the predominance of minerals of one group [27]. There is a contradictory between the reports about the mineralogical composition of Shahumyan clay. Reported in 1960 the results show that is mainly montmorillonite and contains less amount of Illite.

Annex III. Scanning electron microscopy (SEM)

Figure 57. Plant remains in clay powder from Armenian clay deposit Shahumyan.

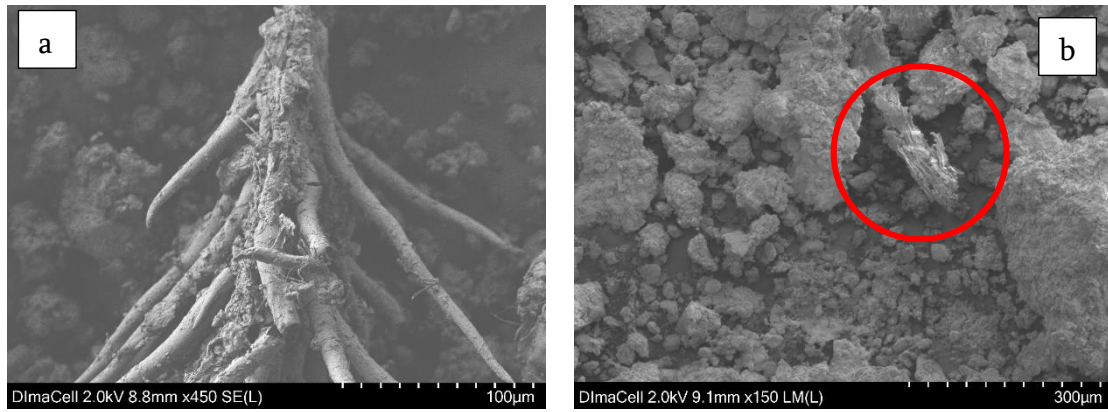
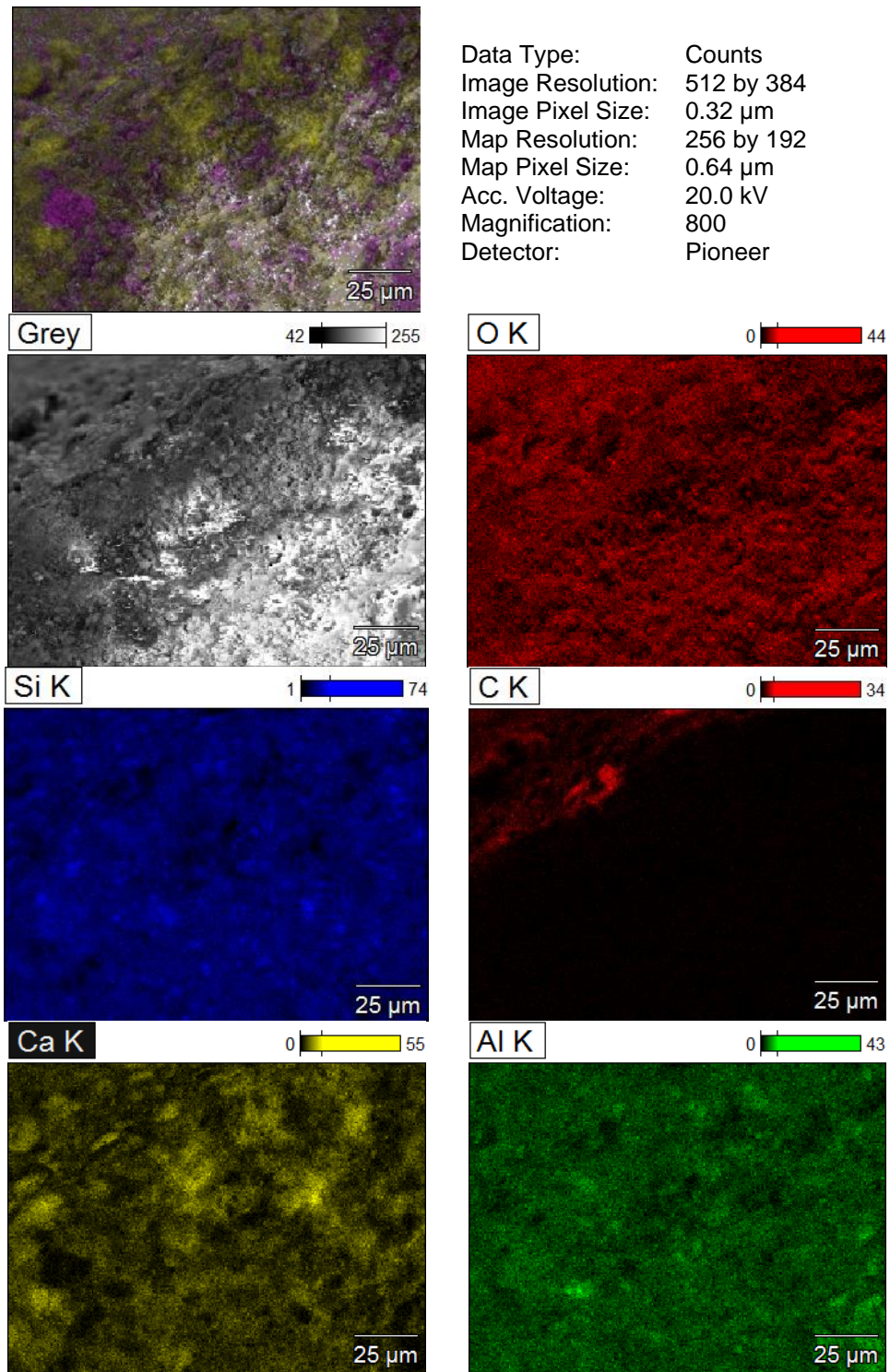


Table 18. SEM/EDX semiquantitative analysis of ceramic fired at 930°C measured for seven different areas at 26 points (pt1, pt2 ...). The results are presented in atomic %. Numbers in brackets [(1), (2),...] represent areas.

Elements Areas/Points	C	O	F	Na	Mg	Al	Si	P	S	Cl	K	Ca	Ti	Cr	Mn	Fe	Mo
(1)_pt1	52.53	37.04	0	0	0	7.81	1.89	0	0	0	0	0.73	0	0	0	0	0
(1)_pt2	52.77	37.94	0	0	0	6.54	1.66	0	0	0	0	1.09	0	0	0	0	0
(2)_pt1	42.13	41.72	0	0	0.71	7.87	3.97	0	0	0	0.29	1.68	0	0	0	1.64	0
(2)_pt2	6.74	51.93	0	1.12	2.88	5.77	16.16	0	0	0.03	0.52	11.57	0.25	0.29	0.05	2.7	0
(3)_pt1	4.4	60.25	0	2.89	0.11	7.9	19.45	0.13	0.02	0	2.39	1.61	0.14	0	0.06	0.65	0
(3)_pt2	5.22	52.51	0.78	0.27	2.48	3.67	12.29	0	1.53	0.16	0.19	17.62	0.87	0.13	0.18	2.1	0
(4)_pt1	3.74	58.34	0	1.37	2.62	6.49	17.7	0	0	0	0.43	7.16	0.16	0.07	1.93	0	0
(4)_pt2	4.55	59.89	0	1.08	3.88	6.2	14.28	0	0	0	0.52	6.73	0.24	0.05	2.58	0	0
(4)_pt3	6.05	13.18	0	0.5	2.92	7.43	29.13	0	0	0	6.07	16.9	1.83	0	16	0	0
(4)_pt4	5.07	31.79	0	1.05	3.08	8.22	31.89	0	0	0	2.93	8.92	0.78	0.18	6.09	0	0
(4)_pt5	6.81	62.46	0	1.19	2.17	3.72	8.7	0	0	0	0.46	10.72	0.22	0.18	3.36	0	0.02
(5)_pt1	5.35	58.08	0	0	21.49	1.27	3.27	0	0.08	0	0.03	8.3	0.08	0.03	0.12	1.9	0
(5)_pt2	5.52	62.59	0	0.29	2.15	2.07	11.9	0	0	0	0.13	14.22	0.1	0	0.03	1	0
(5)_pt3	4.66	62.35	0	3.09	0.56	11.4	14.03	0	0	0	1.39	2.05	0.05	0	0	0.41	0
(5)_pt4	5.01	31.45	0	0	10.89	3.03	5.57	0	0	0	0.1	24.28	0.33	0	0.8	18.55	0
(5)_pt5	4.44	31.83	0	0	6.07	2.1	3.68	0	0	0	0.2	36.88	0.46	0	0.57	13.61	0.15
(10)_pt1	3.52	64.9	0	2.08	1	5.66	19.32	0	0	0	1.95	1.08	0.04	0	0	0.42	0.02
(10)_pt2	2.88	64.09	0	2	1.3	5.78	19.97	0	0	0	1.77	1.51	0.06	0	0	0.61	0.03
(10)_pt3	4.15	65.87	0	2.06	1.36	5.22	17.94	0.1	0	0	1.49	1.29	0.05	0	0	0.48	0
(10)_pt4	2.65	60.73	0	1.49	2.28	7.07	18.19	0	0	0	0.69	5.23	0.16	0	0	1.51	0
(10)_pt5	2.28	64.56	0	0.95	1.43	3.25	24.34	0	0	0	0.61	1.78	0.1	0	0	0.7	0
(11)_pt1	5.57	60.61	0	1.43	1.58	6.62	16.63	0	0	0	2.76	2.27	0.24	0	0.15	2.12	0.02
(11)_pt2	5.83	56.62	0	1.39	2.21	7.04	18.42	0	0	0	2.59	3.72	0.31	0	0.06	1.8	0
(11)_pt3	5.57	62.92	0	1.31	1.8	6.43	15.61	0	0	0	2.08	2.58	0.34	0	0.05	1.31	0
(11)_pt4	6.25	62.84	0	1.23	2.24	5.53	13.36	0	0	0	1.28	5.16	0.4	0	0.07	1.65	0
(11)_pt5	4.58	59.25	0	1.15	1.64	7.1	19.45	0	0	0	3.32	2.4	0.23	0	0	0.88	0
Average	9.933	52.913	0.030	1.075	3.033	5.815	14.569	0.009	0.063	0.007	1.315	7.595	0.286	0.036	1.235	2.078	0.009

Table 19. Elemental mapping of ceramic fired at 930°C. Magnification: 800x



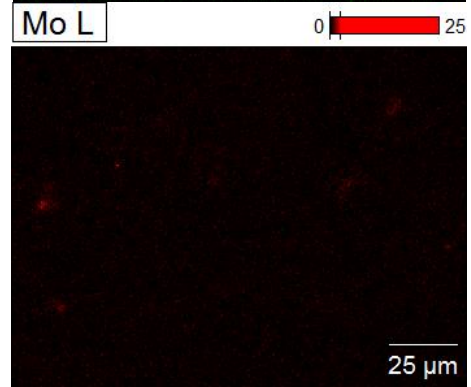
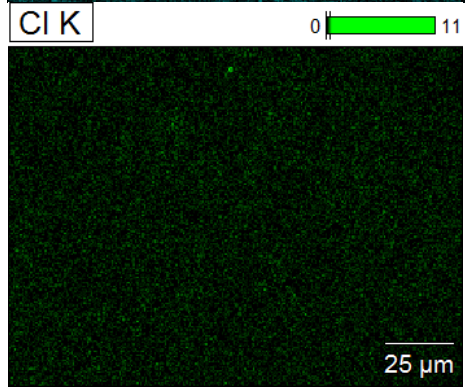
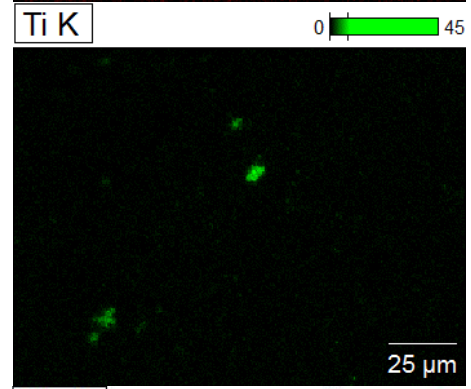
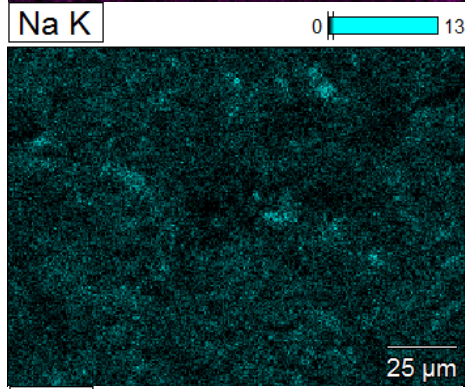
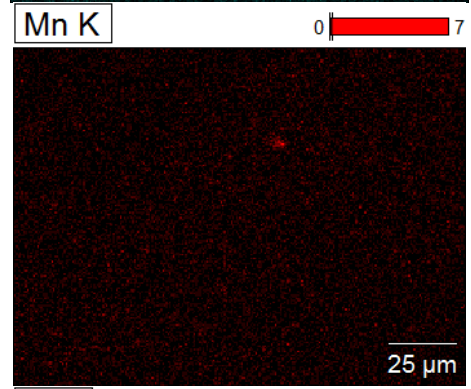
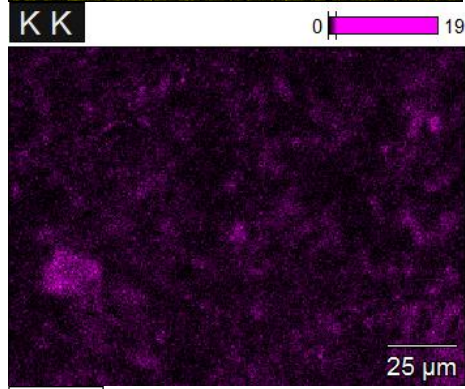
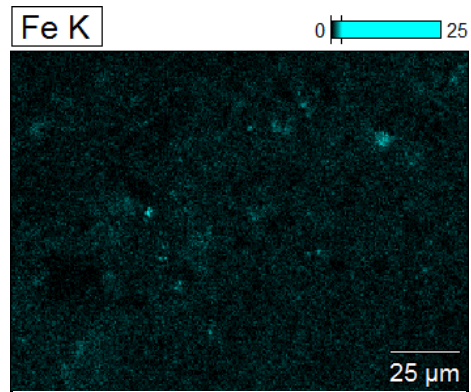
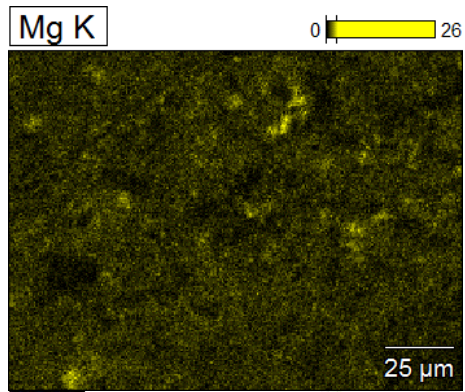
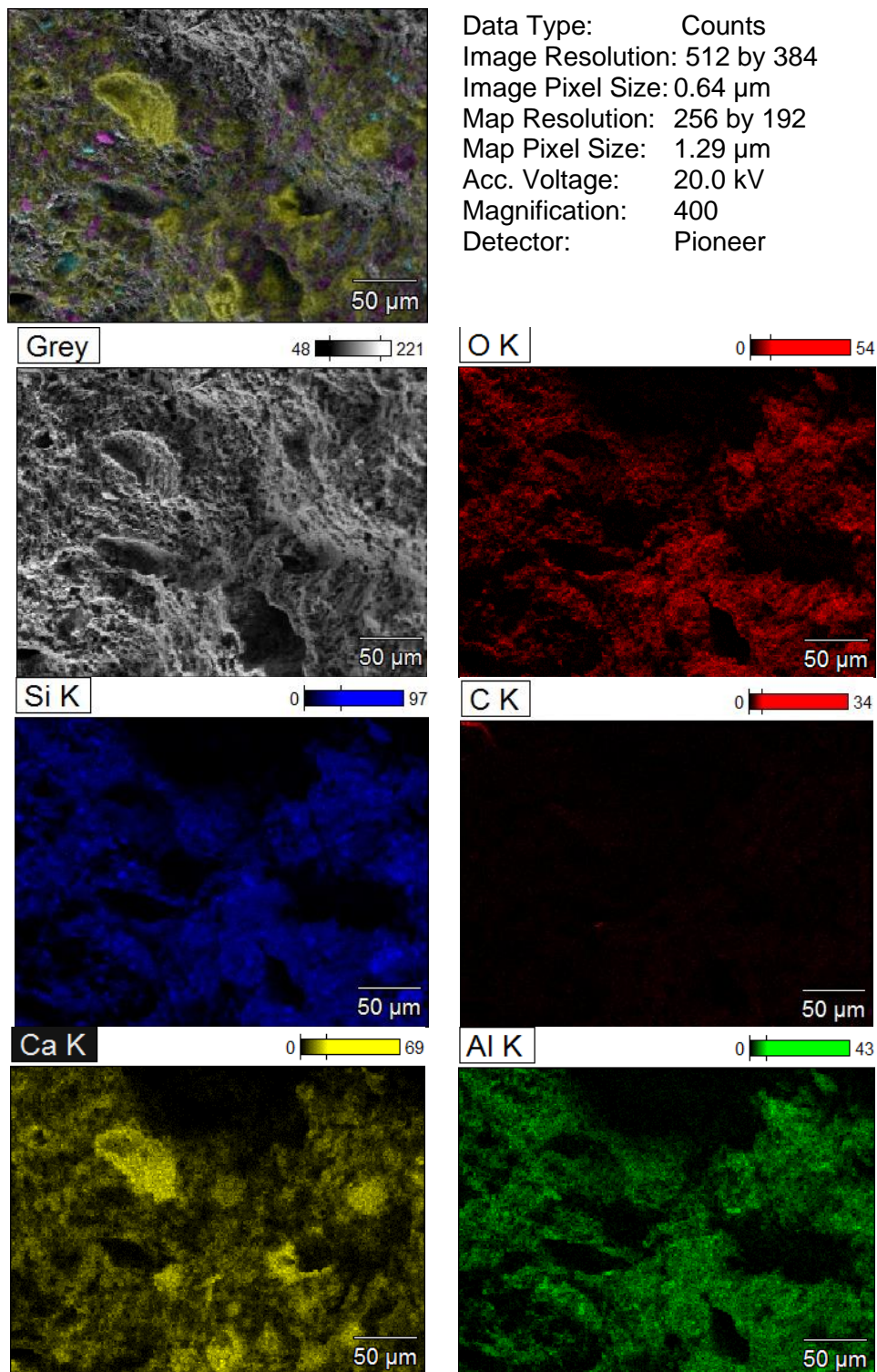
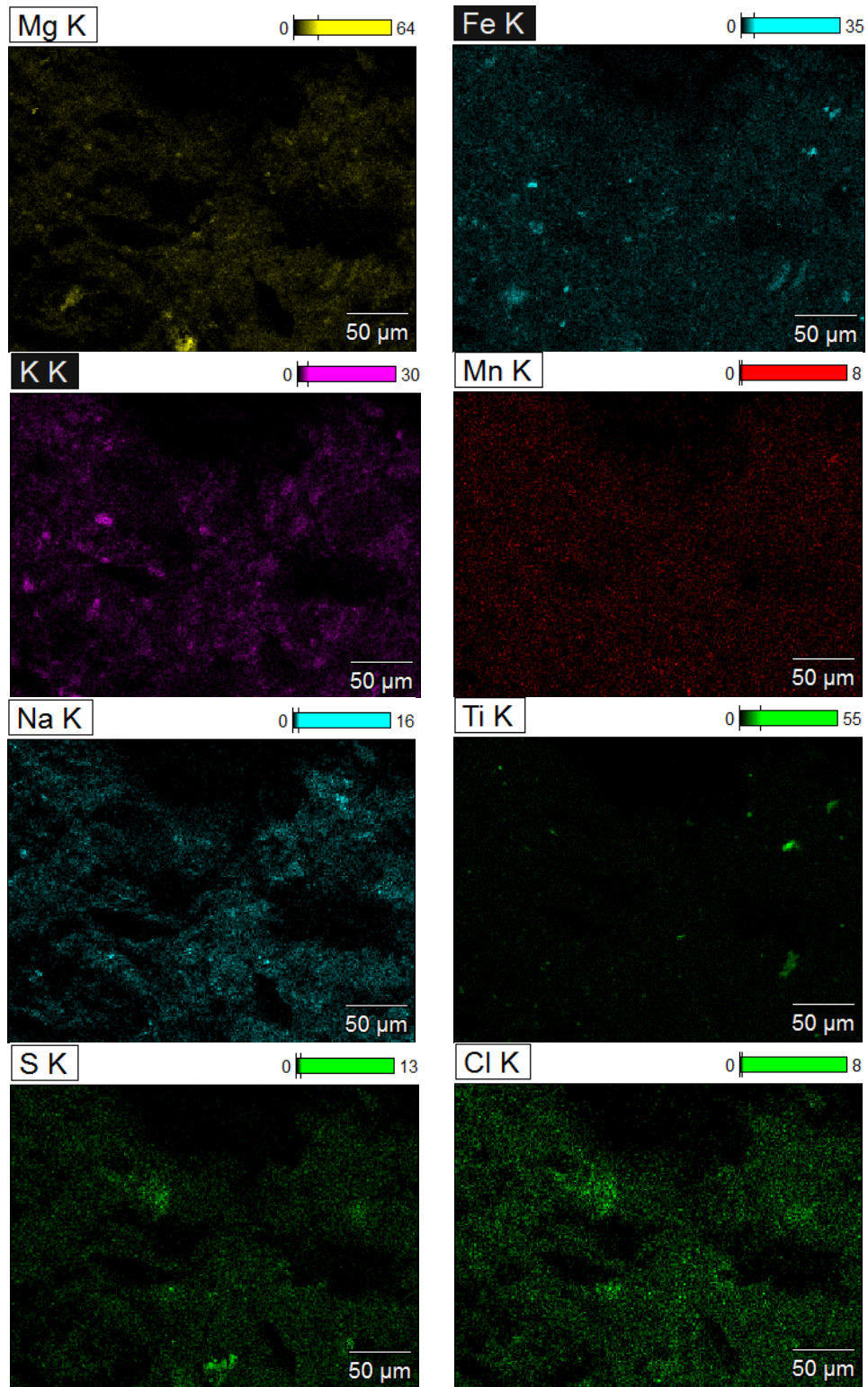


Table 20. Elemental mapping of ceramic fired at 930°C. Magnification: 400x





Annex IV. X –ray diffraction

The X-ray powder diffraction method has been applied for identification of clay minerals since 1920s. For determination and classification of the type of clay minerals very often it is quite sufficient to identify the minerals present in the ceramic body by X-ray powder diffraction. XRD is a technique used to find out the nature of the materials as crystalline or amorphous. XRD works by irradiating a material with incident X-rays and then measuring the intensities and scattering angles of the X-rays that leave the material.

Crystals are regular arrays of atoms, whilst X-rays can be considered as waves of electromagnetic radiation. Crystal atoms scatter incident X-rays, primarily through interaction with the atoms' electrons. This phenomenon is known as elastic scattering; the electron is known as the scatterer. A regular array of scatterers produces a regular array of spherical waves. In many directions, these waves cancel each other out through destructive interference, however, they add constructively in a few specific directions, as determined by Bragg's law (Figure 58). The position of characteristic XRD peaks of clay-minerals allow to access to the interlayer distance (d) thanks to the Bragg's equation

$$n\lambda = 2d\sin\theta \quad (15)$$

where λ is the length wave of the irradiating X-ray , n is the diffraction order, and θ is the diffraction angle.

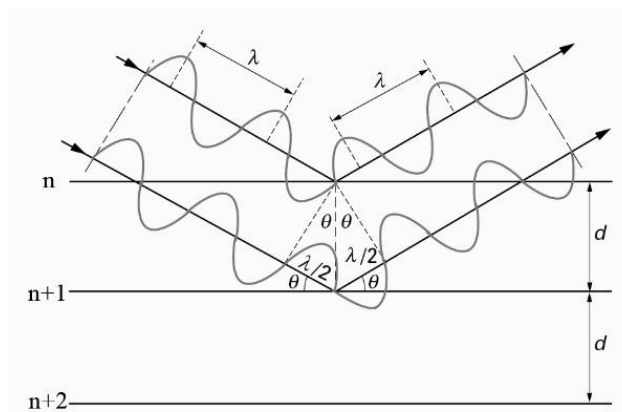


Figure 58. Illustration of the Bragg Law

XRD analysis is based on constructive interference of monochromatic X-rays and a crystalline sample and the XRD pattern analysis provides a unique fingerprint (Figure 59) of the crystals present in the sample. The identification of clay minerals using XRD definitions is based on the positions of *00l* reflections of samples [53].

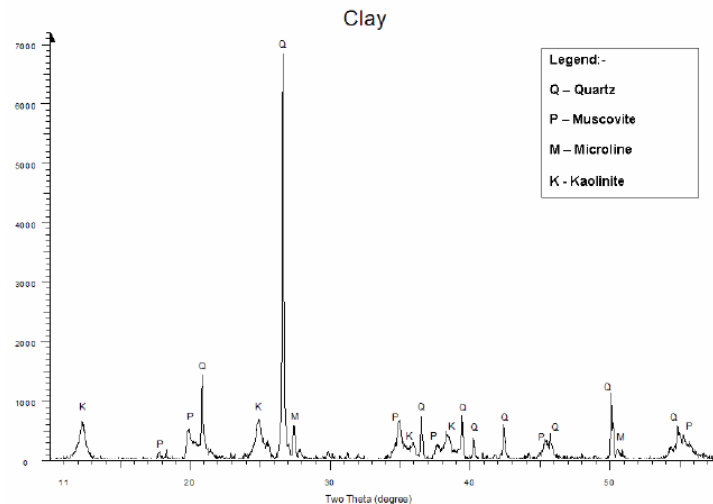


Figure 59. XRD Diffractogram of a clay

The analyses have been performed at University of Poitiers (ENSIP/IC2MP). The XRD analysis has been done with an X-ray source of Cu $K\alpha$ radiation ($\lambda = 1.5406 \text{ \AA}$). It analyzes and identifies the unknown crystalline compounds by Bragg Brentano method. The different parameters such as scan step size, collection time, range, X-ray tube voltage and current should be fixed based on the specimen's requirement analysis. The standard database (JCPDS database) for XRD pattern is used for phase identification for a large variety of crystalline phases in the concrete specimens [150]. This technique not only provides information on the crystalline structure of ceramics, which is not obtainable by any other method, but it also requires such a small amount of material that it can virtually be classed as a non-destructive technique. An adequate sample may weigh less than $50 \mu\text{g}$ and be hardly visible to the naked eye. This is particularly important in the case of rare and valuable objects. The method consists of mounting a few grains of powder on the tip of a gelatin filament* and placing it in a special camera where it is rotated in a very fine beam of X-rays; this radiation is diffracted by the crystals of the sample to form a series of concentric cones which intercept a curved strip of the film within the camera. The pattern

so formed is characteristic of the particular substance and can be regarded as a type of fingerprint. Many thousands of these patterns have been collected and filed by the American Society for Testing Materials (A.S.T.M.)*. The cristobalite occurs as a product of the devitrification of the glassy phase. In earthenware with a high lime content a calcium aluminum silicate may be formed, though this is relatively uncommon in the material we have examined, e.g. anorthite ($\text{CaO} \cdot \text{Al}_2\text{O}_3 \cdot 2\text{SiO}_2$, A.S.T.M. 10-379) and gehlenite ($2\text{CaO} \cdot \text{Al}_2\text{O}_3 \cdot 2\text{SiO}_2$ A.S.T.M. 9-216) [151].

Annex V. Shrinking measurement on Shahumyan ceramics and Kaolin-based ceramics

Having an idea about the physical and chemical process clay goes through during drying and kiln firing will help in avoiding with problems such as cracking, breaking, exploding of ceramic products. During fabrication, the ceramic product is exposed to thermal and mechanical stress. Due to thermal stress, Shahumyan clay is mainly used as a raw material for making ceramic jars (arm. [karases]) for winemaking in Armenia, as it does not crack when heat-treated at the temperature (930°C) chosen by the pottery makers. During drying and firing clay bodies change their size which leads to shrinkage of the product. Product sizes also matter. The larger the product is, the more movement of shrinkage will take place. When clay starts to dry, water evaporates from it. As this happens, the particles of clay are drawn closer together resulting in shrinkage.

Clay shrinks both in drying and in firing. Different clay bodies shrink at different rates which can be as little as 4% or as much as 15% for some clay bodies. Even one percentage point can make a difference in the final product depending on the need for precision [152].

In the ceramic industry, the drying step is necessary before firing ceramic bodies at high temperature. Drying process includes the extraction of water from clay/ceramic body. One of the methods for the description of the drying process is the weight loss over time as shown in Figure 60.

Weight loss during drying

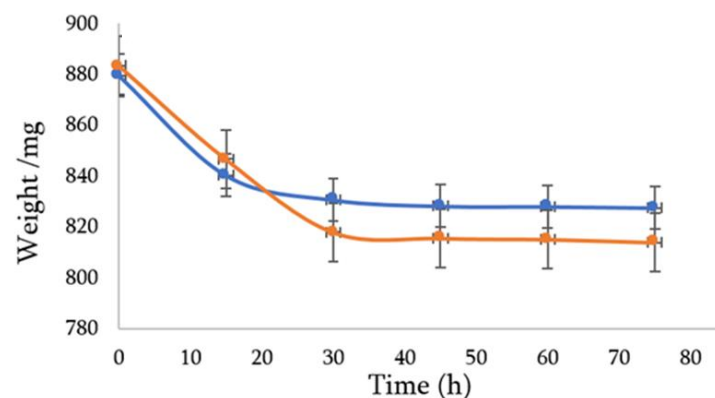


Figure 60. Typical weight loss of two big tablets as function of the time

Ceramic tablets have been dried at room under constant conditions (temperature, relative humidity, airflow). As the curve shows in the initial stage the weight loss has a linear appearance. Drying process goes through various stages. First, the moisture content decreases linearly at the beginning of drying. Then the drying rate decreases. These two phases lead to the shrinking of the ceramic tablets.

In the literature, drying shrinkage has mostly been expressed as change in length [153], mass [154] or the volume [155] over time. Removing the time dependence by plotting the water content as a function of the linear shrinkage gives the well-known Bigot curve (Figure 61). Bigot curves are used today to study drying behavior which can vary depending on raw materials, component proportions in the paste mixture, additives or drying conditions [154].

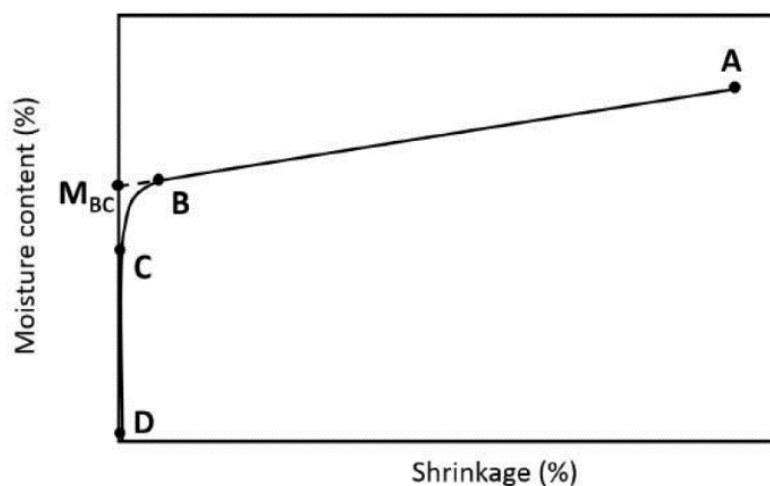


Figure 61. Schematic representation of a typical Bigot's curve [153]

Three characteristics of the tablets were measured, weight (± 0.01 mg), diameter and height (± 0.1 mm) upon the process of tablet elaboration.

Figure 62 reports the total shrinking of the samples; measurements were performed after the shaping and after firing stages. This first batch correspond to a traditional work of the paste, the second corresponds to a more controlled process. At first glance, there is a big difference between the first batch (yellow) and the second (green) i.e., if the weight lost is comparable for the two batches, the other dimensions do not agree. This noticeable

result come from the operation chain during the elaboration process of the samples. For batch 1, each time about 100 samples (from a new paste) were extruded, then measured and finally weighted. During this chain the samples have dried, and the last measurements reveal more shrinking (in length or weight) than the initial records. During the process (as in real pottery situation) the paste dries also, and small amount of water are added when necessary to obtain a paste with the desired plasticity to be shaped.

In the second batch, a total of 140 tablets was extruded from the same paste, the total process last less time and the drying does not show a strong effect. The green columns show little dispersion.

When compared to the Kaolin tablet (used as a reference for its non-swelling property), a stronger shrinking is revealed in the Armenian tablet suggesting the likely presence of smectic clays.

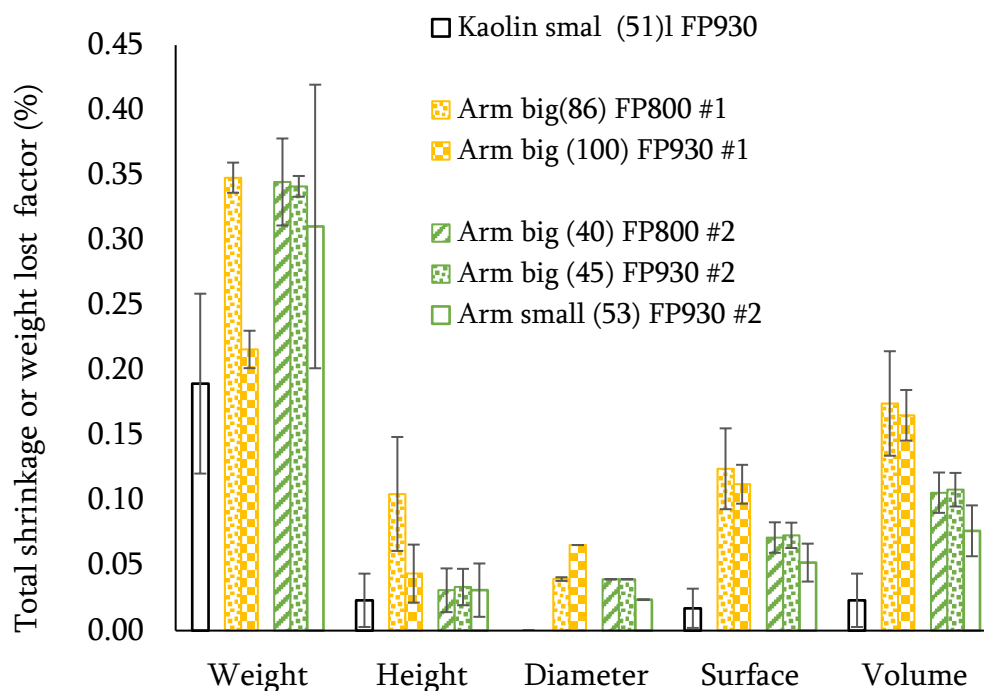


Figure 62. Total shrinkage and weight loss on big and small Armenian and kaolin tablets.

Number in brackets correspond to the tablet population, FP correspond to the firing protocol (800 or 930 °C), the number preceded by a # is the batch number. Error bars correspond to standard deviation.

Batch 1 samples. Dried samples were measured xx days after shaping, fired occurred xxx days after shaping. Batch 2 samples:

Small Arm #2	shaped 19/03/2021	dried	fired 09/04/2021
Big Arm HP3 #2	shaped 22/03/2021	dried 24/03/2021	fired 09/04/2021
Big Arm HP4 #2	shaped 22/03/2021	dried 24/03/2021	fired 09/04/2021
model big HP3	shaped 26/03/2021	dried 29/03/2021	fired 09/04/2021
model big HP4	shaped 26/03/2021	dried 29/03/2021	fired 09/04/2021

Figure 63 reports the shrinking and weight loss between the drying and firings stages. There is far less variation between the samples. The Kaolin tablets keep showing a weak shrinking, but interestingly, the shrinking upon firing of the two batches of Armenian tablets is fairly reproducible. This is likely to be a valued property of Armenian clay for traditional potters and may contribute to the high quality reputation of the Shahumyan deposit.

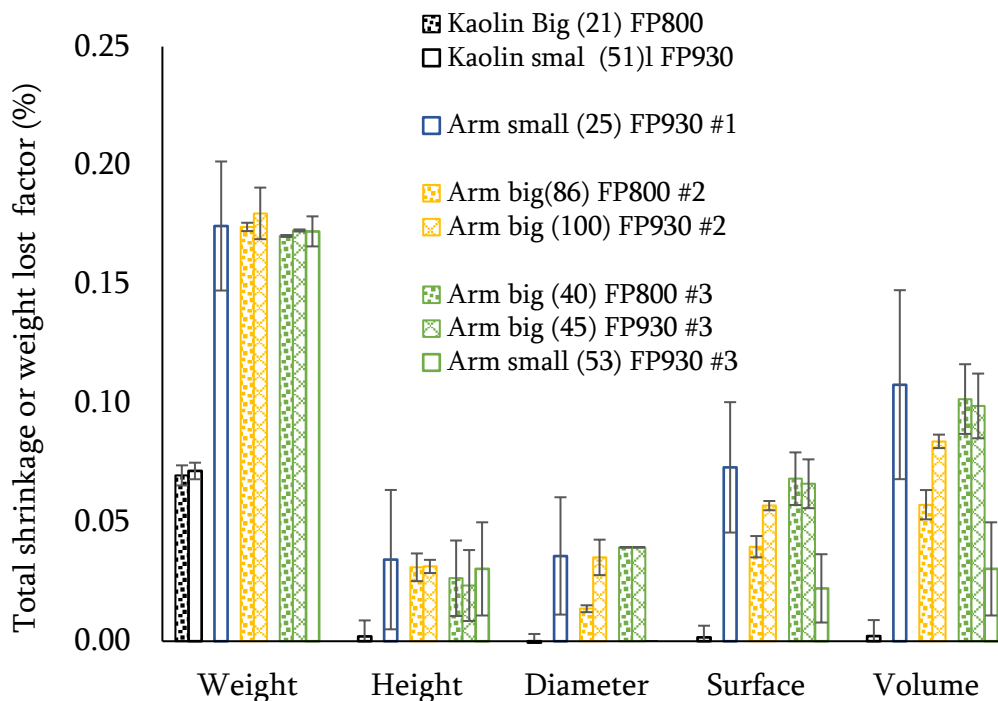


Figure 63. Shrinkage and weight lost on big and small Armenian and kaolin tablets between drying and firing stages. Symbolism is as described in Figure 62.

Figure 64. draws the weight versus the volume of ceramic tables of various batches, a fairly constant density of 1.8 -1.7 is observed the tablets fired at 800 °C could be slightly less dense that would indicate a slightly higher porosity

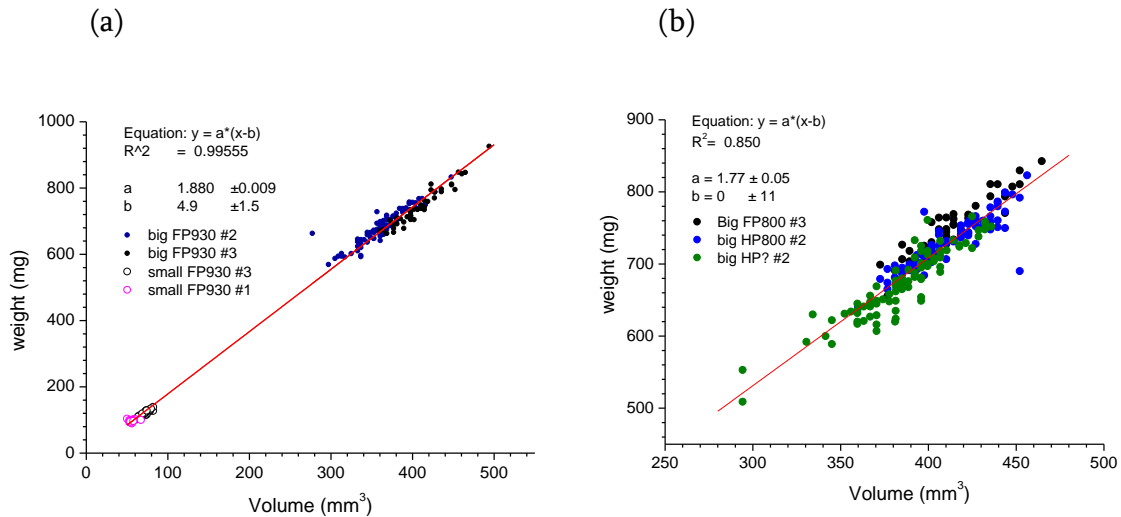


Figure 64. Weight in function of volume of tablets for various batches. FP correspond to the firing protocol (800 or 930 °C), the number preceded by a # is the batch number

Table 21. Tablets dimensions (in mg, mm; mm² and mm³ for the weight, length, surface, and volume respectively) and shrinkage between the dried and fired stages of the firing protocols.

tablet	Dimensio n	after drying	+/-	final	+/-	shrinkage (%)	+/-
Kaolin small (51) FP930	Weight	143.80	8.15	133.42	7.40	0.07	0.00
	Height	6.04	0.39	5.99	0.34	0.00	0.01
	Diameter	4.40	0.00	4.40	0.00	0.00	0.00
	Surface	113.83	5.45	113.14	4.66	0.00	0.00
	Volume	91.75	6.01	91.00	5.13	0.00	0.01

	weight	858.18	50.22	790.61	43.80	0.07	0.00
Kaolin	Height	10.17	0.55	10.04	0.50		
Big (21)	Diameter	8.20	0.00	8.10	0.00		
FP800	Surface	367.26	14.48	359.62	12.29		
	Volume	536.28	0.00	441.61	186.93		

Arm	weight	886.4	43.2	732.0	34.9	0.2	0.0
big(86)	Height	10.2	0.5	9.9	0.5	0.0	0.0
FP800	Diameter	7.4	0.0	7.3	0.0	0.0	0.0
#2	Surface	322.7	12.0	309.9	11.6	0.0	0.0
	Volume	437.8	22.2	412.7	21.2	0.1	0.0

Arm big	weight	837.3	62.8	683.79	52.34	0.18	0.01
(100)	Height	9.5	0.7	9.20	0.72	0.03	0.00
FP930	Diameter	7.3	0.0	7.10	0.00	0.04	0.01
#2	Surface	301.5	16.5	284.30	16.01	0.06	0.00
	Volume	397.4	0.0	364.09	28.41	0.08	0.00

Arm	weight	117.4	4.9	96.55	4.08	0.17	0.03
small	Height	5.9	0.2	5.67	0.27	0.03	0.03
(25)	Diameter	3.7	0.0	3.52	0.07	0.04	0.02
FP930	Surface	88.8	3.0	82.15	2.15	0.07	0.03
#1	Volume	61.97	3.01	55.14	1.88	0.11	0.04

Arm big	weight	911.91	51.07	753.29	41.01	0.17	0.00
(40)	Height	10.21	0.58	9.88	0.54	0.03	0.02
FP800	Diameter	7.60	0.00	7.30	0.00	0.04	0.00
#3	Surface	334.44	13.96	310.38	12.45	0.07	0.01
	Volume	463.06	0.00	413.67	22.73	0.10	0.01

	weight	899.64	68.91	744.97	58.07	0.17	0.00
--	--------	--------	-------	--------	-------	------	------

Arm big	Height	10.00	0.73	9.77	0.71	0.02	0.01
(45)	Diameter	7.60	0.00	7.30	0.00	0.04	0.00
FP930	Surface	329.49	17.52	307.86	16.34	0.07	0.01
#3	Volume	453.65	0.00	409.07	29.82	0.10	0.01

Arm	weight	142.10	9.58	119.30	8.46	0.17	0.01
small	Height	5.52	0.37	5.38	0.38	0.03	0.02
(53)	Diameter	4.10	0.00	4.10	0.00	0.00	0.00
FP930	Surface	97.54	4.73	95.75	4.91	0.02	0.01
#3	Volume	72.91	0.00	71.08	5.04	0.03	0.02

Table 22. Tablets dimensions (in mg, mm; mm² and mm³ for the weight, length, surface and volume respectively) and shrinkage between the shaped and fired stages of the firing protocols

tablet	Dimension	after shaping	+/-	final	+/-	shrinkage (%)	+/-
Kaolin small (51) FP930	Weight	164.86	14.72	133.42	7.40	0.19	0.07
	Height	6.16	0.37	5.99	0.34	0.02	0.02
	Diameter	4.40	0.00	4.40	0.00	0.00	0.00
	Surface	115.60	5.15	113.14	4.66	0.02	0.02
	Volume	93.71	5.67	91.00	5.13	0.02	0.02
Arm big(86) FP800 #1	weight	1123.16	56.94	731.96	34.91	0.35	0.01
	Height	11.02	0.11	9.89	0.54	0.10	0.05
	Diameter	8.30	0.00	7.30	0.01	0.12	0.00
	Surface	395.59	2.90	310.39	12.34	0.22	0.03
	Volume	596.30	6.01	413.68	22.51	0.31	0.04
	weight	878.08	68.33	683.79	52.34	0.22	0.01
	Height	9.62	0.68	9.20	0.72	0.04	0.02

Arm big	Diameter	8.30	0.00	7.10	0.00	0.14	0.00
(100)	Surface	358.93	17.80	284.30	16.01	0.21	0.01
FP930 #1	Volume	520.23	36.93	364.09	28.41	0.30	0.02

Arm big (40) FP800 #2	weight	1159.21	115.71	753.29	41.01	0.34	0.03
	Height	10.26	0.61	9.88	0.54	0.03	0.02
	Diameter	7.60	0.00	7.30	0.00	0.04	0.00
	Surface	335.70	14.45	310.38	12.45	0.07	0.01
	Volume	465.44	27.46	413.67	22.73	0.11	0.02

Arm small (25) FP930 #1	weight	170.75	7.57	97.35	3.20	0.43	0.03
	Height	7.00	0.00	5.71	0.22	0.18	0.03
	Diameter	4.50	0.00	3.52	0.07	0.22	0.02
	Surface	130.77	0.00	82.63	3.03	0.37	0.02
	Volume	111.33	0.00	55.60	2.98	0.50	0.03

Arm big (45) FP930 #2	weight	1130.19	84.32	744.97	58.07	0.34	0.01
	Height	10.11	0.71	9.77	0.71	0.03	0.01
	Diameter	7.60	0.00	7.30	0.00	0.04	0.00
	Surface	332.04	16.98	307.86	16.34	0.07	0.01
	Volume	458.48	32.25	409.07	29.82	0.11	0.01

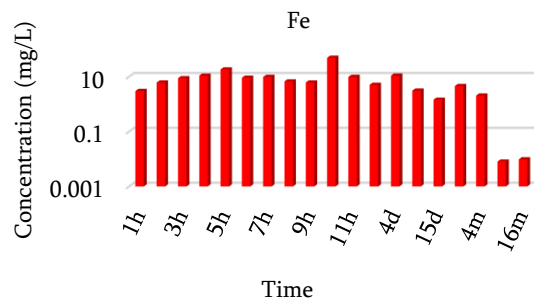
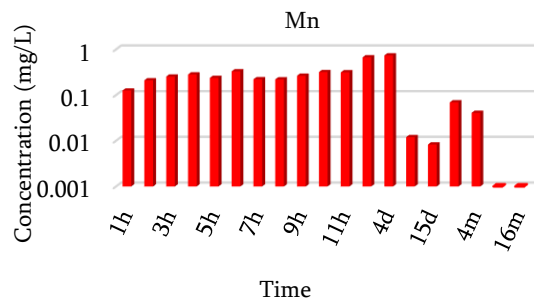
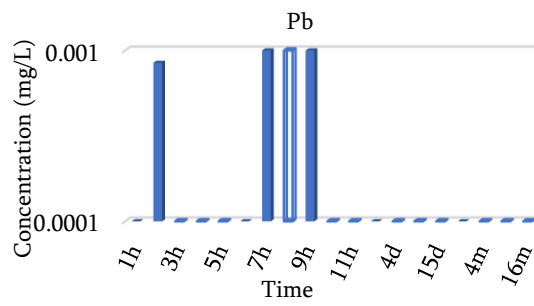
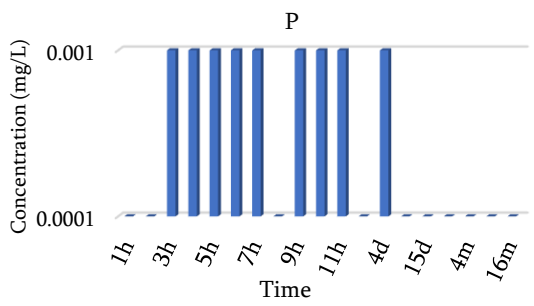
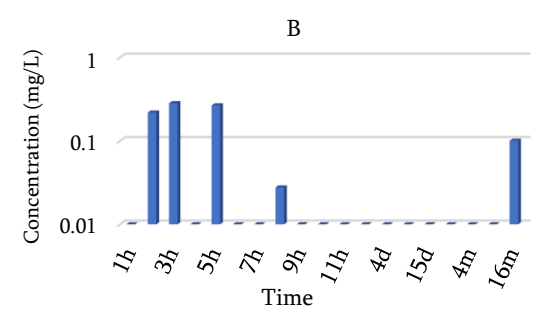
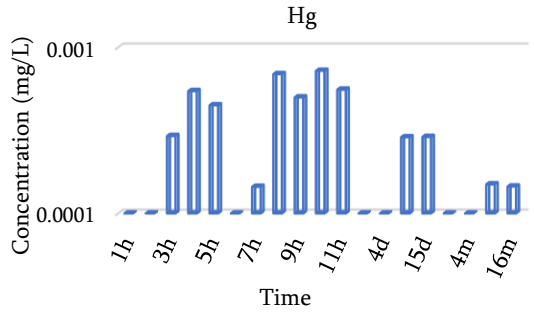
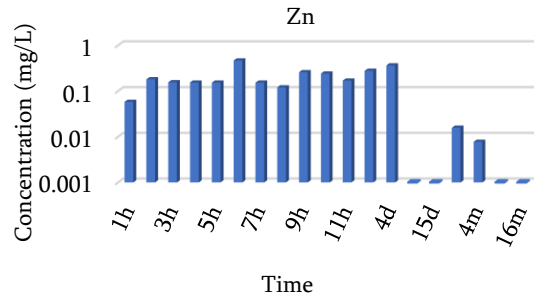
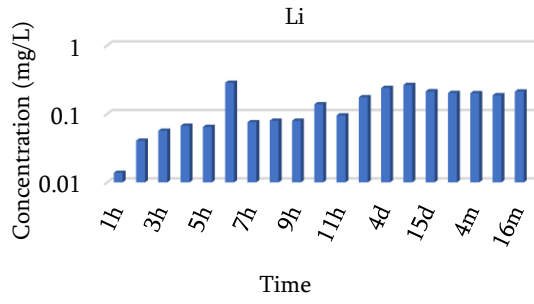
Arm small (53) FP930 #2	weight	167.53	13.17	119.30	8.46	0.31	0.11
	Height	5.53	0.37	5.38	0.38	0.03	0.02
	Diameter	4.20	0.00	4.10	0.00	0.02	0.00
	Surface	100.70	4.90	95.75	4.91	0.05	0.01
	Volume	76.64	5.14	71.08	5.04	0.08	0.02

Annex VI. ICP-AES

Table 23. Concentrations (mg/L) of elements released from ceramic to model wine determined by ICP-AES. Samples are aged from 1 hour (1h) up to 16 months (16m), h, d, m stand for hour, day month respectively. Sample 0 corresponds to model wine alone (without contact with the ceramic). The ratio ρ corresponds to the ratio of the volume of model wine (V_w) to the surface of the tablet (S). The colormap highlights the concentration of elements from lowest value (red) to the highest value (green).

Samples	0	1h	2h	3h	4h	5h	6h	7h	8h	9h	10h	11h	2d	4d	8d	15d	2m	4m	8m	16m
Mass of the tablets (mg)	-	748	709	683	733	669	635	691	724	600	553	718	709	606	695	692	718	658	668	668
ρ (m)	-	0.0086	0.0090	0.0087	0.0102	-	0.0096	0.0094	0.0090	0.0086	0.0092	0.0088	0.0092	0.0091	0.0098	0.0091	0.0087	0.0093	0.0094	0.0088
Al	0.35	4.96	10.20	12.60	14.60	10.10	16.50	10.60	11.20	9.05	11.70	15.70	21.40	24.30	1.10	0.86	5.32	2.89	0.33	0.52
B	0.52	0.16	0.68	0.71	0.37	0.70	0.17	0.25	0.54	0.32	0.36	0.41	0.36	0.52	0.40	0.48	0.00	0.44	0.30	0.59
Ba	0.01	0.23	0.24	0.20	0.24	0.15	0.14	0.18	0.19	0.24	0.20	0.25	0.31	0.19	0.07	0.13	0.15	0.15	0.21	0.03
Be	0.03	0.06	0.03	0.03	0.03	0.03	0.06	0.03	0.03	0.03	0.03	0.03	0.06	0.03	0.03	0.03	0.05	0.03	0.03	0.03
Ca	0.34	95	129	142	152	140	167	148	164	149	149	193	106	33.7	34.1	33.3	109	91.7	79.9	11.5
Cd	0.01	0.01	0.01	0.03	0.04	0.01	0.01	0.01	0.05	0.04	0.01	0.04	0.01	0.01	0.01	0.01	0.01	0.01	0.03	0.02
Co	0.03	0.02	0.03	0.03	0.03	0.03	0.02	0.03	0.03	0.03	0.03	0.03	0.02	0.03	0.03	0.03	0.02	0.03	0.03	0.03
Cr	0.01	0.07	0.12	0.11	0.11	0.09	0.10	0.10	0.11	0.08	0.10	0.13	0.11	0.14	0.09	0.36	0.76	0.86	0.59	0.50
Cu	0.01	0.02	0.04	0.04	0.05	0.04	0.08	0.05	0.04	0.08	0.05	0.24	0.05	0.09	0.01	0.02	0.02	0.01	0.01	0.01
Fe	0.01	2.27	4.35	6.03	8.01	12.40	5.86	6.81	4.89	3.71	27.10	7.08	3.60	6.68	2.18	1.02	3.31	1.37	0.02	0.02
Hg	0.03	0.01	0.03	0.03	0.03	0.03	0.01	0.03	0.03	0.03	0.03	0.03	0.01	0.03	0.03	0.03	0.01	0.03	0.03	0.03
K	0.17	2.20	4.65	6.67	8.17	7.84	8.66	8.95	10.60	9.91	9.20	12.60	13.00	14.90	11.20	13.30	30.60	34.00	45.50	64.90
Li	0.01	0.02	0.03	0.04	0.06	0.05	0.19	0.06	0.06	0.05	0.08	0.07	0.13	0.15	0.19	0.15	0.15	0.14	0.13	0.15
Mg	0.18	7.09	12.00	14.30	12.70	12.10	12.50	12.40	13.20	12.40	13.00	16.80	32.10	38.90	9.41	4.88	4.44	2.63	0.17	0.17
Mn	0.01	0.10	0.16	0.18	0.21	0.17	0.22	0.16	0.17	0.17	0.18	0.23	0.48	0.45	0.01	0.01	0.06	0.03	0.01	0.01

Mo	0.03	0.02	0.03	0.03	0.03	0.03	0.03	0.03	0.03	0.03	0.03	0.03	0.02	0.03	0.03	0.04	0.07	0.07	0.07	0.05
Na	1.41	7.03	16.10	16.40	17.50	17.40	41.90	19.00	22.80	20.60	20.00	25.60	25.30	35.20	34.00	39.60	27.90	30.20	26.20	30.00
Ni	0.01	0.02	0.02	0.02	0.02	0.02	0.03	0.15	0.02	0.23	0.06	0.04	0.04	0.04	0.01	0.01	0.02	0.01	0.01	0.01
P	0.47	0.14	0.38	0.49	0.56	0.55	0.62	0.51	0.46	0.70	0.54	0.58	0.27	0.67	0.47	0.46	0.24	0.46	0.41	0.42
Pb	0.03	0.03	0.03	0.03	0.03	0.03	0.02	0.03	0.03	0.03	0.03	0.03	0.02	0.03	0.03	0.03	0.02	0.03	0.03	0.03
S	0.17	1.58	2.94	3.18	3.15	2.81	14.50	3.12	3.49	2.87	3.20	4.23	2.75	2.91	2.53	2.91	3.22	4.95	4.22	3.05
Sr	0.01	0.25	0.38	0.42	0.44	0.42	0.45	0.44	0.47	0.43	0.44	0.57	0.63	0.62	0.28	0.25	0.37	0.36	0.34	0.09
Ti	0.01	0.04	0.08	0.10	0.15	0.08	0.15	0.07	0.08	0.08	0.08	0.13	0.01	0.01	0.01	0.02	0.07	0.02	0.01	0.01
V	0.01	0.05	0.09	0.09	0.08	0.07	0.08	0.08	0.09	0.06	0.09	0.11	0.12	0.14	0.18	0.24	0.14	0.08	0.04	0.05
W	0.03	0.00	0.03	0.03	0.03	0.03	0.00	0.03	0.03	0.03	0.03	0.03	0.00	0.03	0.03	0.03	0.00	0.03	0.03	0.03
Zn	0.01	0.05	0.14	0.12	0.12	0.11	0.31	0.12	0.10	0.17	0.15	0.13	0.21	0.23	0.01	0.01	0.02	0.02	0.01	0.01



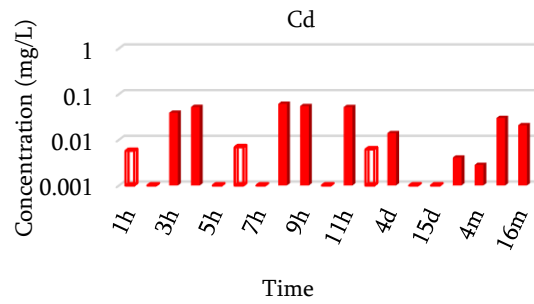
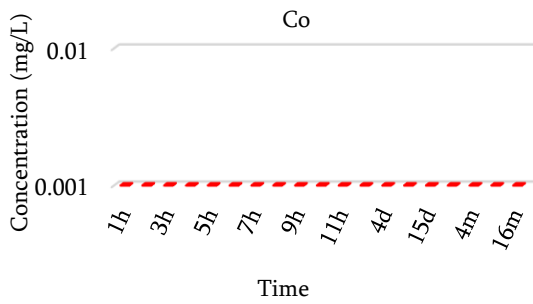
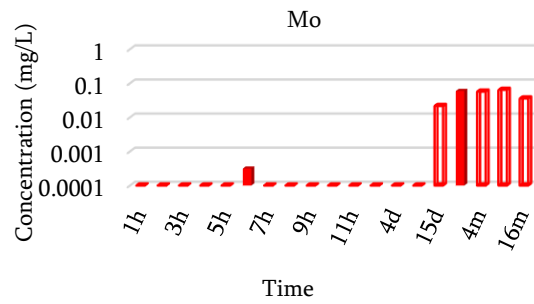
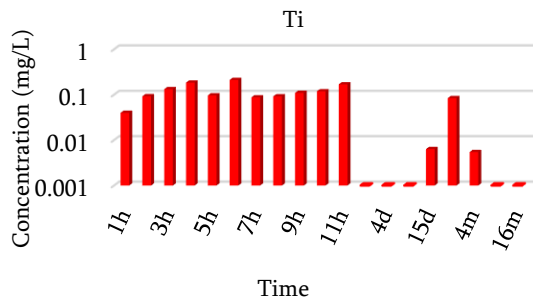
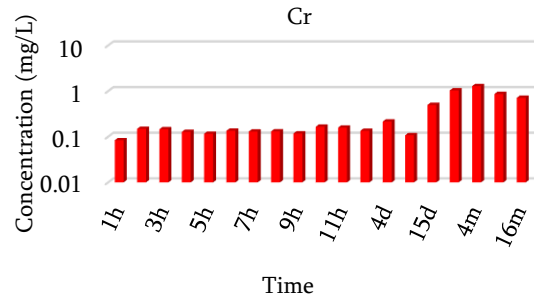
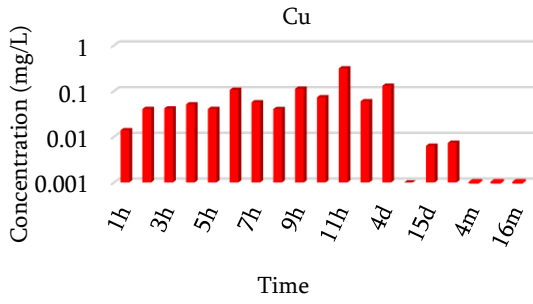
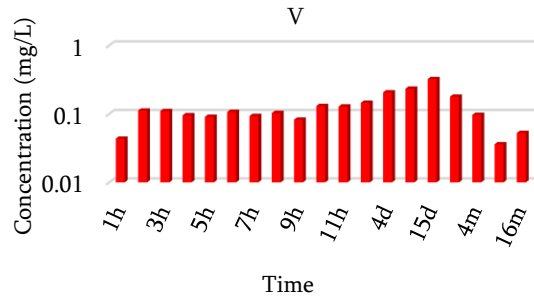
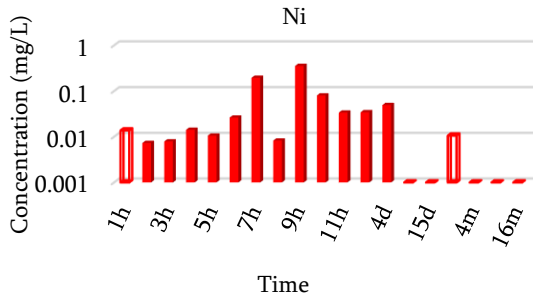
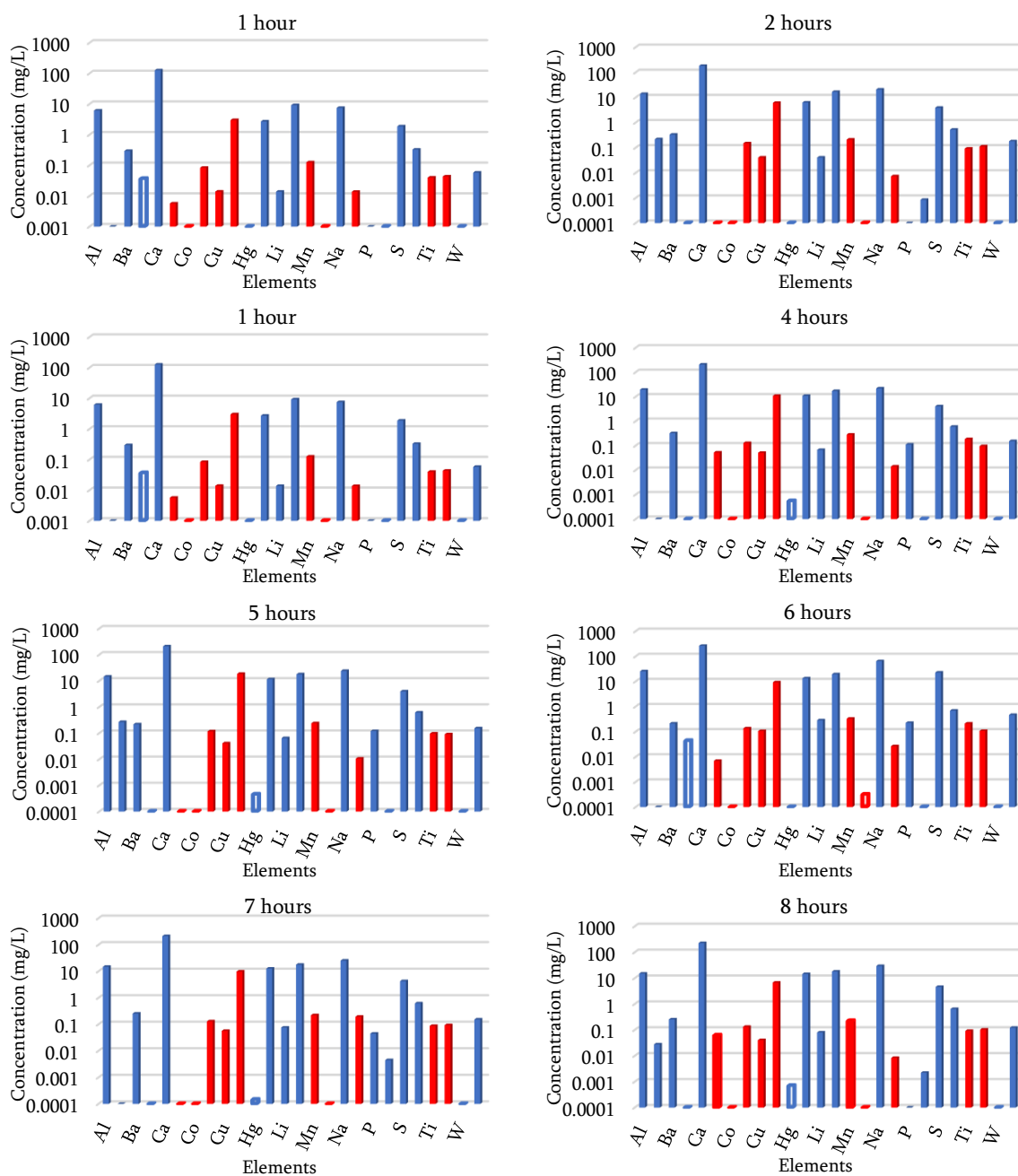
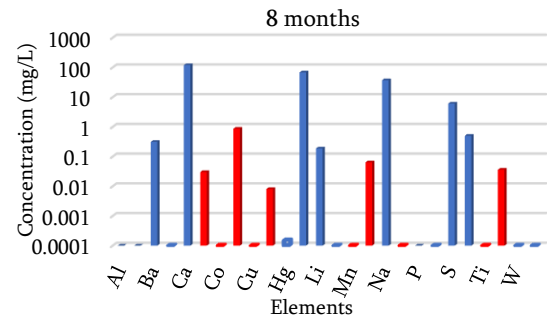
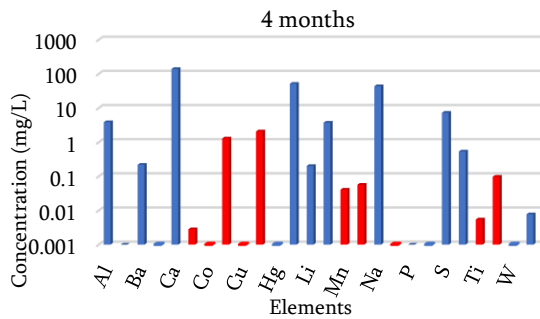
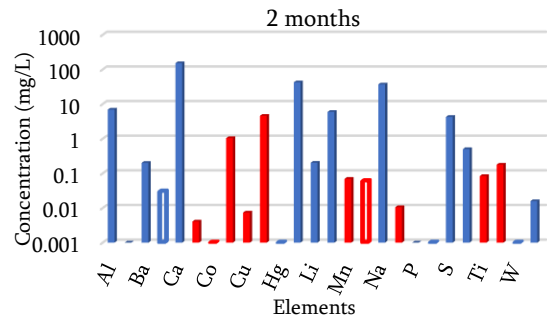
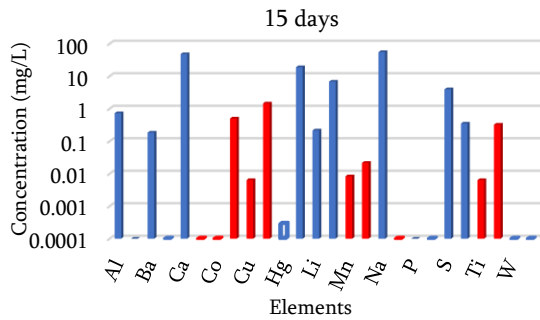
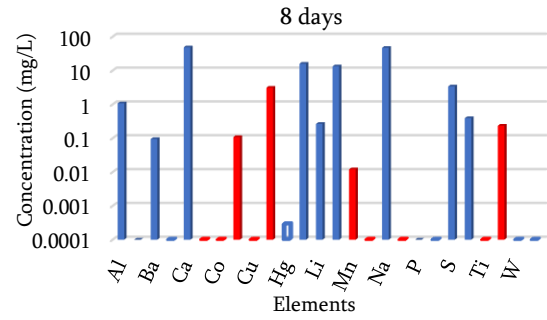
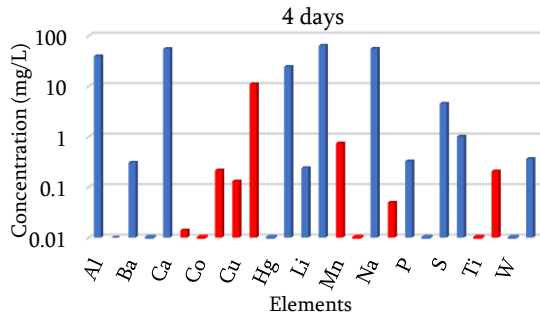
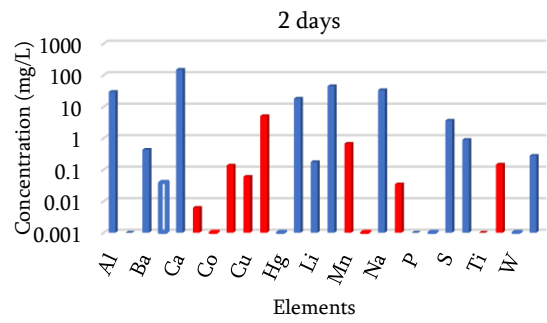
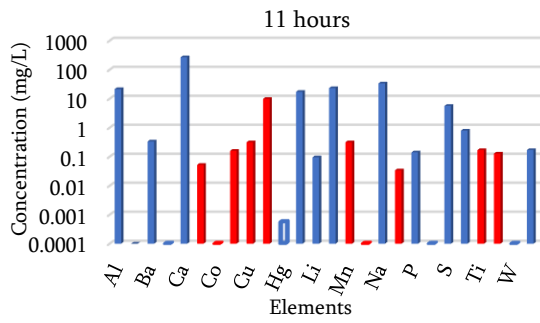
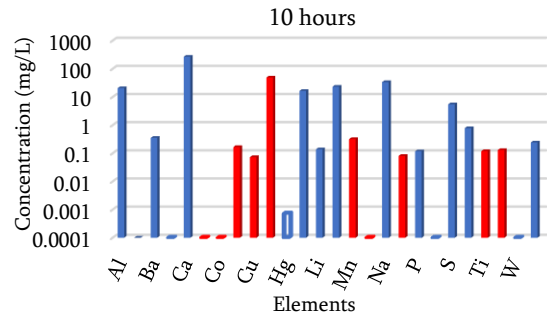
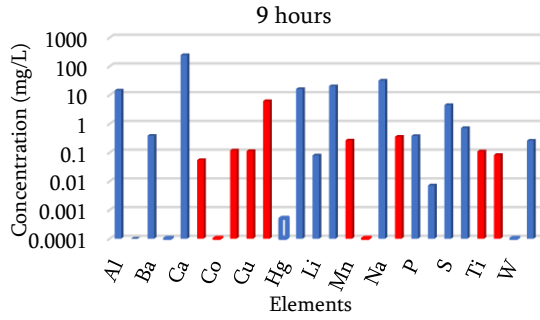
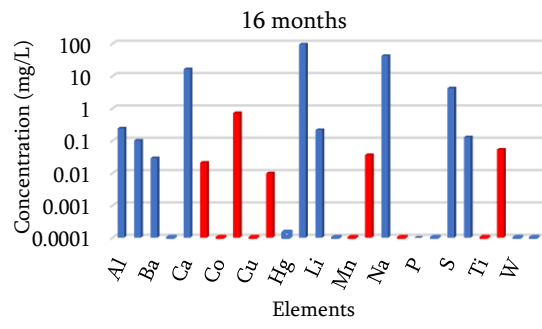


Table 25. The concentration (mg/L) of elements released from 1 g of ceramic to the model wine (wine elements subtracted), sample by sample. Open columns correspond to elements below the limit of quantification (e.g. [Hg]). Red columns correspond to paramagnetic elements. Elements are ordered as follow: {Al, B, Ba, Be, Ca, Cd, Co, Cr, Cu, Fe, Hg, K, Li, Mg, Mn, Mo, Na, Ni, P, Pb, S, Sr, Ti, V, W, Zn} but for the sake of visibility only one over two is reported in the label of abscise axis.







Annex VII. TD NMR relaxometry

Relaxation mechanisms in water

The relaxation is the mechanism that allows to the spin system to release the energy it has accumulated during the excitation step of an NMR experiment. This relaxation is due to the molecular dynamic of the molecule's rotation and translation of water molecule due to Brownian motions. In most isolated water molecule there can exist only one NMR interaction: the dipolar interaction between the two protons. The oxygen atom can be neglected because the only NMR active isotope of oxygen is ^{17}O with a natural abundance of 0.04%. The dipolar interaction between two protons depends on the angle between the internuclear vector and the direction of the static magnetic field (Figure 65)

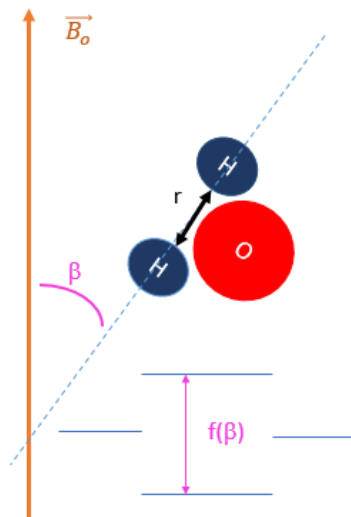


Figure 65. Schematic representation of a water molecule with the internuclear vector r and the energy levels of the coupled system that depend on the angle β between r and the direction of the static magnetic field \vec{B}_0 .

If the water molecule is not isolated, the dipolar interaction can also occur between two distinct water molecules. In this case the movement rotation and translation of each individual molecules modulate the dipolar interaction but the rotations are generally neglected with respect to the translation motions Figure 66.

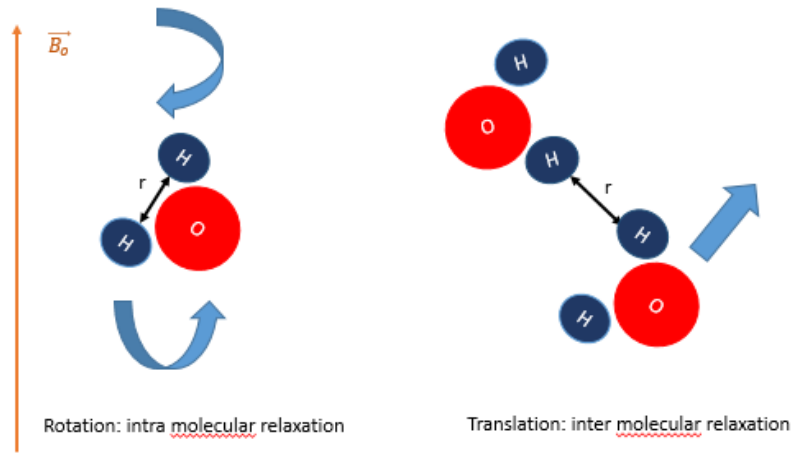


Figure 66. The two types of dynamics modulating the dipolar interactions

Intra molecular relaxation (rotational diffusion)

The relaxation rate of the intra molecular rotation is described as:[156]

$$R_1^{rot}(\nu) = C_r \left[\frac{\tau_r}{1 + (2\pi\nu\tau_r)^2} + \frac{4\tau_r}{1 + 4(2\pi\nu\tau_r)^2} \right], \quad (16)$$

where the correlation time τ_r is expressed as the combination of the correlation time of the rotation of the hydrated ions (τ_{rot}) and of the exchange time corresponding to the residence time (τ_{ex}) of the water molecule in the hydration sphere of the ions:

$$\frac{1}{\tau_r} = \frac{1}{\tau_{rot}} + \frac{1}{\tau_{ex}}. \quad (17)$$

When only two protons are interacting, the dipolar coupling constant C_r is given by:

$$C_r = \frac{3}{10} \left(\frac{\mu_0}{4\pi} \frac{\gamma^2 \hbar}{r^3} \right)^2, \quad (18)$$

where γ denotes the proton gyromagnetic ratio, r is the internuclear proton distance, while the other symbols designate usual physical constants.

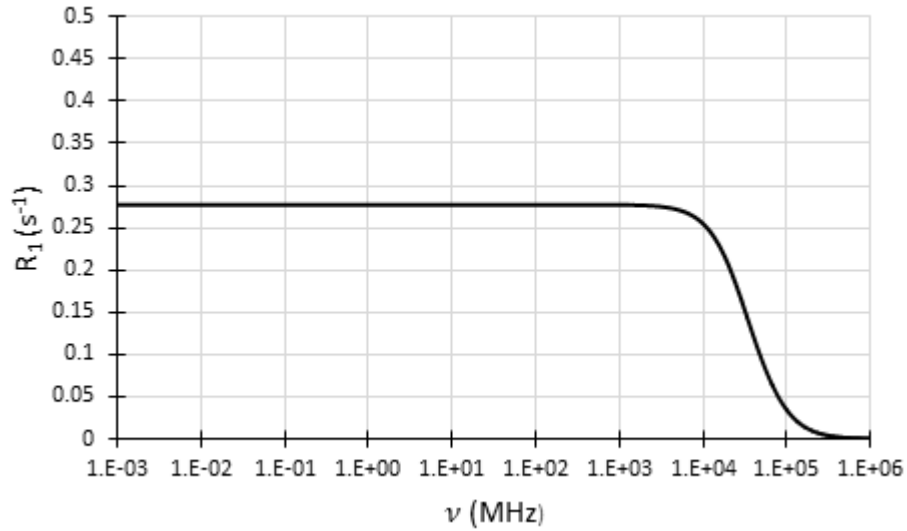


Figure 67. Simulation of the isotropic rotational diffusion relaxation rate for water molecules ($\tau_r = 2.6 \cdot 10^{-12}$ s) versus the proton Larmor frequency of the magnetic field.

Inter molecular relaxation (translational diffusion)

In the case of an isotropic diffusion, the relaxation contribution issued from the translational molecular process can be expressed as:[156], [157]:

$$R_1^{trans}(\nu) = C_t \int_0^{\infty} \frac{u^4}{81 + 9u^2 - 2u^4 + u^6} \left(\frac{\tau_t}{u^4 + (2\pi\nu\tau_t)^2} + \frac{4\tau_t}{u^4 + (4\pi\nu\tau_t)^2} \right) du, \quad (19)$$

with

$$C_t = \frac{108}{5} \left(\frac{\mu_0}{4\pi} \gamma^2 \hbar \right)^2 \frac{N_H}{d^3}, \quad (20)$$

where N_H is the number of protons per m^3 and d is the closest approach distance of the interacting water molecules, assumed to correspond to the diameter of a water molecule (2.75 Å).

The translational correlation time, τ_t is defined as:

$$\tau_t = \frac{d^2}{D_t}, \quad (21)$$

where D_t is the relative translational diffusion (not self-diffusion) coefficient of the water molecules.

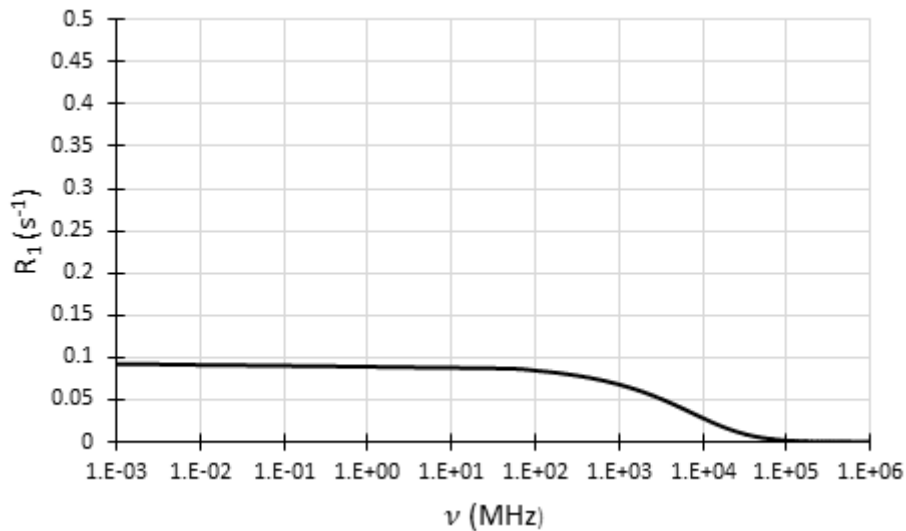


Figure 68. Simulation of the isotropic translational diffusion relaxation rate for water molecules ($\tau_t = 9 * 2.6 * 10^{-12} s$) versus the proton Larmor frequency of the magnetic field.

The complete relaxation profile of water is obtained by the sum of the two contributions (Figure 69).

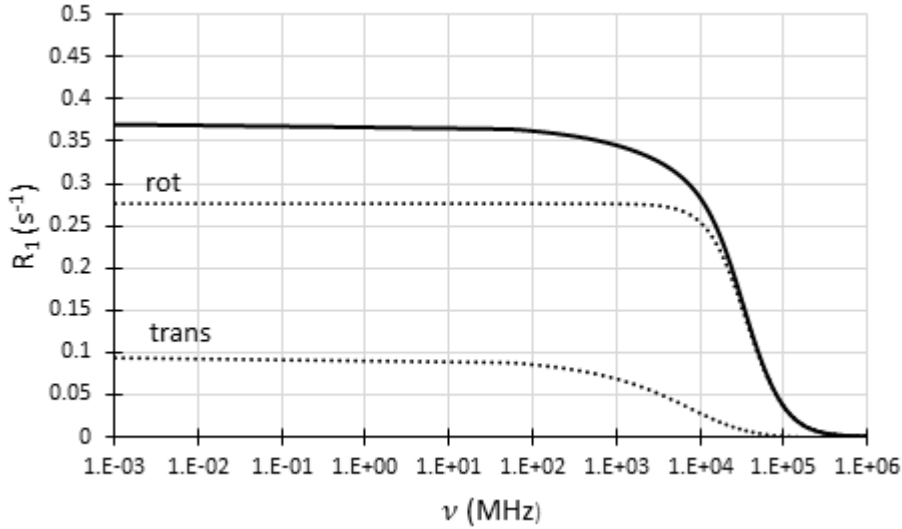


Figure 69. Simulation of the relaxation profile of water with translational and rotational contribution

Relaxation mechanisms of solution in presence of paramagnetic ions

Dipolar paramagnetic relaxation Solomon mechanism

Paramagnetic interactions are described by several mechanisms. The simplest one considers that the unpaired electrons are localized at the paramagnetic ion. The relaxation is described by an interaction between an electronic point dipole and a nuclear point dipole (Solomon mechanism).

The associated dipolar paramagnetic relaxation rate can be written in the case of two spins as [158]–[161], [134]:

$$\tilde{R}_D(\omega_I, \tau_{d1}, \omega_S, \tau_{d2}) = \tilde{C}_D \left[\frac{7\tau_{d2}}{1 + (\omega_S\tau_{d2})^2} + \frac{3\tau_{d1}}{1 + (\omega_I\tau_{d1})^2} \right] \quad (22)$$

With

$$\tilde{C}_D = \frac{2}{15} \left(\frac{\mu_0}{4\pi} \right)^2 \frac{S(S+1)(\gamma_I \gamma_S \hbar)^2}{r_{IS}^6} \quad (23)$$

Where S is the electron spin number of the paramagnetic ion, and S -subscript refers to paramagnetic ion. Correlation time τ_{di} is a composition of the reorientational correlation time of the paramagnetic ion (τ_R) due to Brownian rotational motion, longitudinal ($i=1$) or transverse ($i=2$) electron relaxation time (τ_{Si}), and of the lifetime of the nuclei on the paramagnetic ion (τ_M):

$$\frac{1}{\tau_{di}} = \frac{1}{\tau_R} + \frac{1}{\tau_M} + \frac{1}{\tau_{Si}} \quad (24)$$

In practice, at low magnetic field, $\tau_{d1} = \tau_{d2} = \tau_d$ [162].

Equation (22) evidences two dispersions that can be observed at different frequencies (Figure 70).

Paramagnetic contact relaxation (Bloembergen mechanism)

The Solomon mechanism is not always sufficient to reproduce the NMRD profiles. In particular, in the case of the paramagnetic nuclei present in wines, an additional fermi-contact interaction (Bloembergen mechanism) must be considered. This interaction arises from a delocalization of the electronic wave function of the paramagnetic nuclei to the physical location of I-nuclei.

The relaxation rate in the case of two spins experiencing a contact interaction (scalar or hyperfine interaction) is given by [134], [159]–[161]:

$$\tilde{R}_C(\omega_s, \tau_c) = \tilde{C}_C \left[\frac{\tau_c}{1 + (\omega_s \tau_c)^2} \right] \quad (25)$$

With:

$$\tilde{C}_C = \frac{2A^2 S(S+1)}{3\hbar^2} \quad (26)$$

Where A is the scalar coupling constant of the spin exchange interaction between nucleus and electron, and τ_c is given by:

$$\frac{1}{\tau_c} = \frac{1}{\tau_M} + \frac{1}{\tau_{S2}} \quad (27)$$

Several aquaions, (e.g. Mn^{2+} [61], [134] Fe^{3+} [160], [163], Cr^{3+} [160], [162], VO^{2+} [160], [164]) may experience this contact interaction, In wines, Mn^{2+} has been shown to govern the relaxation profile [61] and a representation of the relaxation profile is given in Figure 70.

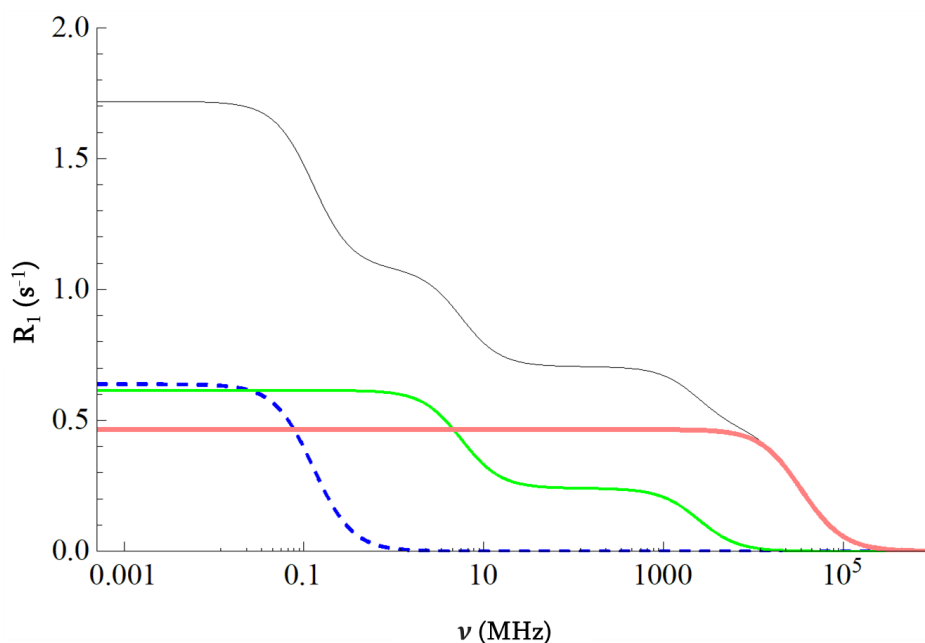


Figure 70. Simulation of the proton profile of a model wine solution containing 1.28 mg of Mn^{2+} (black). In red model wine contribution rotation and translation, green dipolar contribution (with its two dispersions) blue contact interaction.

It must be pointed out that if the above simulations have been performed with realistic parameter for the water, model wine or Mn concentration encountered in real wines, but in other conditions (viscosity, temperature) or systems, the paramagnetic relaxation may be present dispersions at very different frequencies.

We conclude this rapid theoretical description by emphasizing two properties that are of prime importance in this study.

Linearity

Importantly, the linearity of the relaxation rate of the solution with the paramagnetic ion concentration is evidenced as follows: the paramagnetic longitudinal relaxivity of the water protons (R_1^p) is given by [134], [165]

$$\frac{pq}{R_1^p} = \frac{1}{\tilde{R}_D + \tilde{R}_C} + \tau_M \quad (28)$$

where p is the concentration of the ions compared to the concentration of the solvent molecules (water) and q the number of metal-bound water molecules. Assuming a fast chemical exchange of the water molecules ($\tau_M \ll 1/(R_D + R_C)$) the relaxation of the water proton can be written:

$$R_1 = R + R_1^p = R + pq(\tilde{R}_C + \tilde{R}_D) = R + R_D + R_C, \quad (29)$$

where R can be associated to the background or solvent rate in the absence of paramagnetic ions, R_D and R_C are the dipolar and contact paramagnetic contribution from the exchange of solvent nuclei with the hydrated paramagnetic ions (first sphere of coordination). \tilde{R}_C and \tilde{R}_D refer to two-spin systems as presented in the equations, but R_D and R_C refer to macroscopic paramagnetic contribution to relaxation.

Additivity

We may also recall the remarkable additive property (used implicitly above) of the relaxation rate induced by the different mechanisms or by different paramagnetic ions present in the solutions. The relaxation rates R_S of a solution containing a number n of various paramagnetic ions at concentration C_i is the sum of the relaxation rates of the pure solution ρ and of the relaxation rates R_i of individual solutions at the same concentration

C_i . Because of the linearity of the relaxation rate the relaxation rate of the solution can be expressed in function of the paramagnetic ions concentration:

$$R_S = R_1^{rot} + R_1^{trans} + \sum_{i=1}^n R_i = R + \sum_{i=1}^n R_i = R + \sum_{i=1}^n a_i C_i + b_i = \sum_{i=1}^n a_i C_i + B_i \quad (30)$$

Additional relaxograms

Relaxogram of a washed tablet small headspace

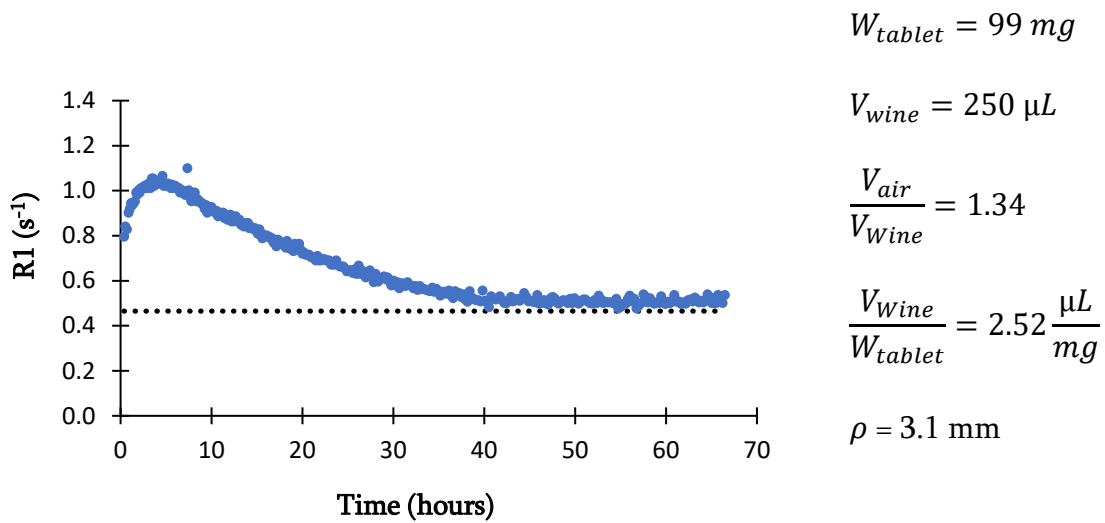


Figure 71. Relaxogram of a flame sealed sample, the ceramic has been washed with HPLC water and Na exchanged before contact with the model wine.

Figure 71 reports the relaxogram of a ceramic washed with HPLC water and Na-exchanged (experiment in flame sealed 7 mm tube). The purpose of the experiment was to remove any tiny particles that could be present on the surface of the tablet or in accessible pores. In order to limit a rapid dissolution of particles as it is known that the dissolution rate may strongly increase as the size of the particles decreases (particularly in the nanoscale range) [116], [117]. The sodium exchange was used to exchange potentially some exchangeable ions at the surface of the ceramic. This exchange that should more realistically named as a washing with an ionic solution has probably little effect, but we have not further analyzed it. However, after washing the ceramic the relaxation rate curved is far smother, a single

broader maximum is observed at the same time and the relaxation rate decreases to a level just above the pure model wine relaxation rate.

By comparison with curves (a-c) of Figure 40 we may attribute the multiple maxima observed in the range 0-8 hours, the more visible in relaxograms (a) and (b) of Figure 40 to the more rapid dissolution of small particles than can easily diffuse into the wine (or be easily washed) and be rapidly dissolved producing a rapid increase of relaxation.

This experiment is also subject to artefact since it has been recorded with only 8 points. A control experiment performed at time $t = 790$ hours give a relaxation rates of $0.446 \pm 0.006 \text{ s}^{-1}$, possibly slightly lower than the expected model wine level (0.465 s^{-1}) this within incertitude, this decrease ($\sim 0.1 \text{ s}^{-1}$) is compatible with a total consumption of dissolved dioxygen.

Relaxogram in low oxygen environment and large headspace

Figure 72 reports the relaxogram of an attempt to follow the evolution of model wine in contact with a ceramic a closed (with an NMR cap and vacuum grease) 10 mm NMR tube. It is a large headspace experiment. This experiment did not reach its goal (because the degassing of the wine was performed for a too extend period of time through an exchange with a big N_2 reservoir. It results in a vaporization of the ethanol this is clearly visible on the relaxogram where the relaxation time of the pure "model wine" was 0.30 a value that cannot be reached by a 12% ABV model wine but is very close to what a water solution would give in a low dioxygen environment (Figure 35). If we assume that the evolution of the relaxation time with ABV (the slope at low ABV) does not vary with the amount of dissolved dioxygen, it is possible to have an estimation of the ABV of the solution (Figure 73). A rough calculation gives a value of 1% ABV. The relaxogram is very similar to the one observed in water (Figure 44) with a smaller second hump and with also an initial higher relaxation rate when compare to a contact in a model wine (Figure 42). An interesting aspect of this experiment is that we followed the evolution of the dioxygen content in the large headspace (diagrams b) this record highlight a linear correlation with time with no observed departure at the early stage (time < 200 hours). This would mean

that no evidence of important consumption of dioxygen can be observed at this scale in water. The persistence of the same rate of diffusion at very long time clearly indicates that it is a diffusion from the exterior into the headspace through the vacuum-greased interface of the NMR cap and the glass tube. This allows to estimate that the uptake of exterior dioxygen is of 150 $\mu\text{g/L}$ within 200 hours.

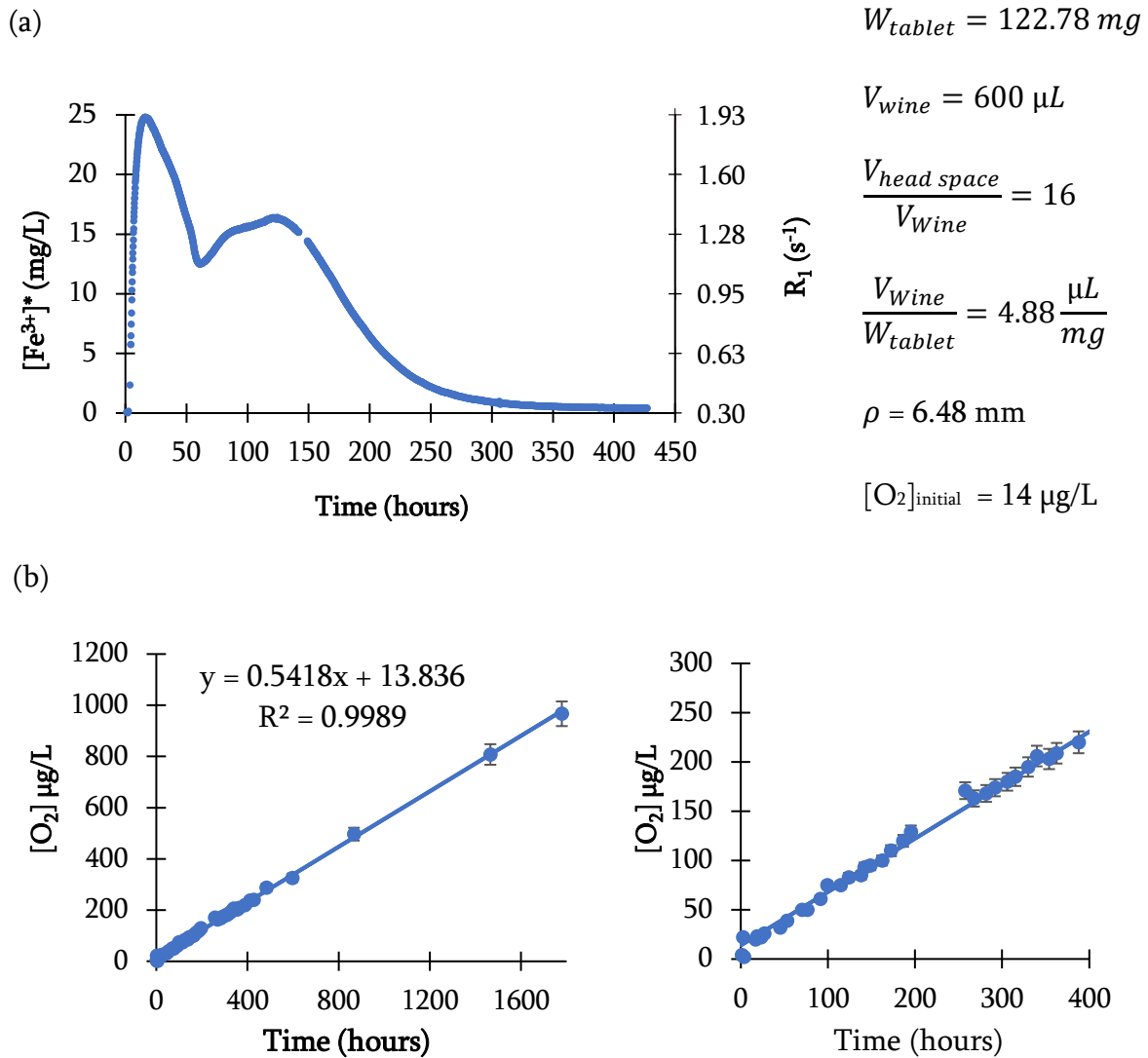


Figure 72. (a) Relaxogram of a model wine with a weak ethanol concentration (estimated around 1 % ABV) in a low oxygen content (initial dioxygen content in the headspace 14 $\mu\text{g/L}$). (b) Evolution with time of the dioxygen content in the headspace.

Fig. 1 **a** Open circles (○) represent the proton spin–lattice relaxation rate at 19.65 MHz and 25 °C of hydroalcoholic solutions versus ABV and X_{water} . Filled circles (●) correspond to the ratio of the relaxation rate of the hydroalcoholic solution corrected by the dioxygen contribution over the viscosity (i.e. R_1^* ratio, see below in the text); **b** open circles (○) represent the dynamic viscosity of the hydroalcoholic solution, measured at 25 °C, versus ABV and X_{water} .

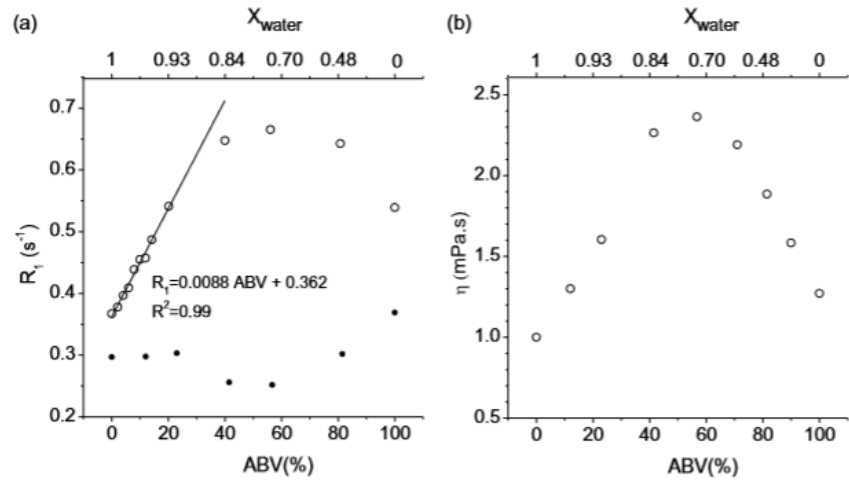
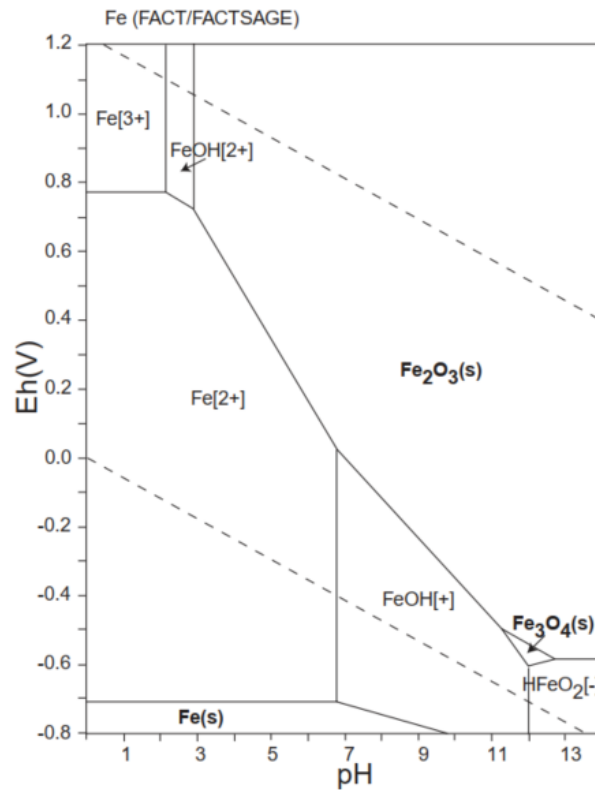


Figure 73. Evolution of relaxation time of hydroalcoholic solution with ABV, from [55].

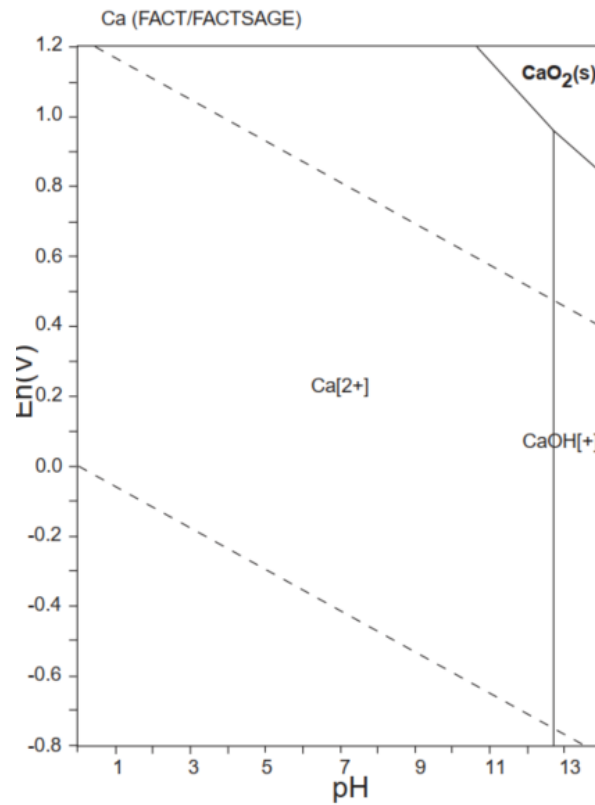
Annex VIII. Pourbaix diagrams (Fe, Ca, Mn)

The stability field of water is delimited by dashed lines, solid phases are in bold.

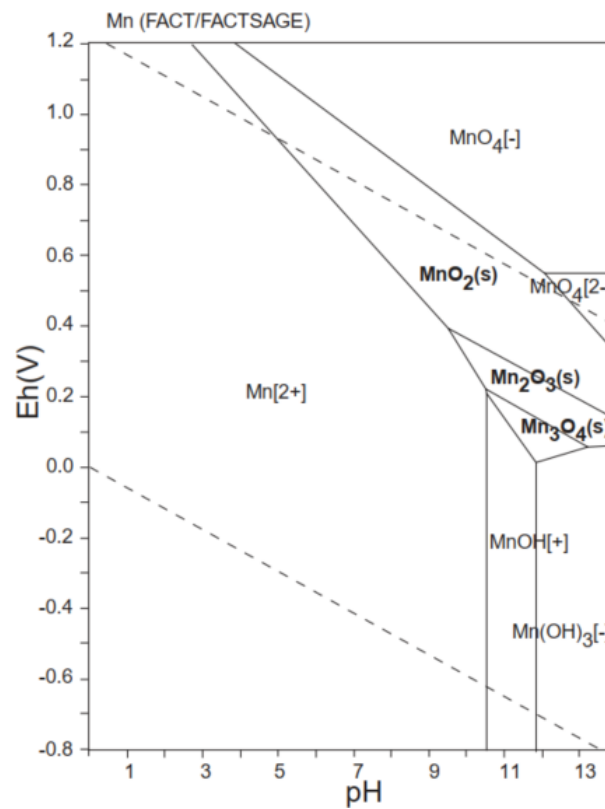
These Eh-pH diagrams reported are strictly valid for a single redox couple, at low concentration (when activity can be identified to concentration). In the case of wine, they should be considered with lots of caution.



E-pH diagram of the system Fe-O-H, $\Sigma\text{Fe } 10^{-10} \text{ mol/kg}$, 298.15 °K, 10^5 Pa [166],



E-pH diagram of the system Ca-O-H, $\Sigma\text{Ca } 10^{-10} \text{ mol/kg}$, 298.15 °K, 10^5 Pa [166],



E-pH diagram of the system Ca-O-H, $\Sigma\text{Ca } 10^{-10} \text{ mol/kg}$, 298.15 °K, 10^5 Pa [166]

Annex IX. Publications

Oral Presentation - A traditional Armenian vinification: clay-based ceramic and wine interaction followed by relaxometry

Conference on achievements and perspectives of NMR relaxometry CA-15209

15-17/03/2021

Ph.D. student - Syuzanna ESOYAN

Supervisors - Philippe Bodart, Camille Loupiac, Nelli Hovhannisyan

EURELAX COST ACTION CA15209

COST Action CA15209: "European Network on NMR Relaxometry"

http://www.cost.eu/COST_Actions/ca/CA15209

<http://eurelax.uwm.edu.pl/>

[conference_programme_conference_on_achievements_and_perspectives_of_nmr_relaxometry.pdf\(uwm.edu.pl\)](#)

Forum Des Jeunes Chercheurs (FJC , 16-17/06/2022)**Migration of chemical elements from ceramics into model wine**

Syuzanna Esoyan^{1,2}, Camille Loupiac¹, Thomas Karbowski¹, Bernhard Michalke³, Philippe Schmitt-Kopplin^{3,4}, Régis D. Gougeon⁵, Nelli Hovhannisyan⁶, Philippe R. Bodart¹

¹ Université Bourgogne Franche-Comté, L'Institut Agro Dijon, UMR PAM A02.102, 1 Esplanade Erasme, 21000, Dijon, France

² Institute of Biology, Yerevan State University, 1 Alex Manoogian Str., 0025, Yerevan, Armenia

³ Research Unit Analytical BioGeoChemistry, Helmholtz Zentrum München, Ingolstaedter Landstrasse 1, Neuherberg, 85764, Germany

⁴ Chair of Analytical Food Chemistry, Technische Universität München, Alte Akademie 10, 85354, Freising-Weihenstephan, Germany

⁵ Institut Universitaire de la Vigne et du Vin, UMR PAM A02.102, Université Bourgogne Franche-Comté, Esplanade Erasme, 21000, Dijon, France

⁶ E. & J. Gallo Winery, 600 Yosemite Blvd, Modesto, CA 95354, USA

Clay-based ceramic vessels (jars, pythoi, etc.) for wine fermentation and aging processes have been used in several cultures for millennia. This know-how still in practice in several countries of the Armenian highland is gaining worldwide in curiosity, popularity, and interest. Ceramic pots are famous among traditional winemakers for their benefits such as temperature regulation, natural cooling system, favorable oxygen exchange, and impact on pH, which are different from those of stainless steel, wood barrels, or concrete. Despite a 5000-years-old history of the use of clay-ceramic vessels (amongst other in Armenia), there is only few scientific regard on the impact on wine quality. To approach this subject, it is necessary to recourse to many analytical techniques and we only report some results obtained by ICP-AES and proton NMR relaxometry on a model wine. ICP-AES is used to identify the migration of elements from the ceramic to the model wine. The results of the elemental analysis of the model wine in contact with ceramics over time, showed that a large number of elements, were transferred from the ceramic to the model wine with different migration behaviors. The noticeable amount of migrating iron attracted attention. NMR relaxometry is used to follow in situ, the migration of paramagnetic elements (like iron), reduction of iron, but also the consumption of dioxygen in the model wine in contact with the ceramic. It is also shown that coated ceramic (e. g. with beeswax; a traditional Armenian method) can drastically limit chemical exchange.

Keywords: Ceramics, Model wine, beeswax, ICP-AES, NMR relaxometry

Format: Poster

Wine active compounds (WAC, 29/06-01/07/2022)

Interaction Between Armenian Clay-based Ceramic and Model Wine

Authors: **Syuzanna Esoyan**^{a, b}, Camille Loupiac^a, Thomas Karbowiak^a, Bernhard Michalke^c, Philippe Schmitt-Kopplin^{c, d}, Régis D. Gougeon^e, Nelli Hovhannisyan^f, Philippe R. Bodart^a

^a Université Bourgogne Franche-Comté, Agropur Dijon, UMR PAM A02.102, 1 Esplanade Erasme, 21000, Dijon, France

^b Yerevan State University, Institute of Biology, 1 Alex Manoogian Str., 0025, Yerevan, Armenia

^c Research Unit Analytical BioGeoChemistry, Helmholtz Zentrum München, Ingolstaedter Landstrasse 1, Neuherberg, 85764, Germany

^d Chair of Analytical Food Chemistry, Technische Universität München, Alte Akademie 10, 85354, Freising-Weihenstephan, Germany

^e Université Bourgogne Franche-Comté, Institut Universitaire de la Vigne et du Vin, UMR PAM A02.102, Esplanade Erasme, 21000, Dijon, France

^f E. & J. Gallo Winery, 600 Yosemite Blvd, Modesto, CA 95354, USA

Key words: Ceramics, Model wine, beeswax, ICP-AES, NMR relaxometry

Clay-based ceramic vessels (jars, pithoi, etc.) for wine fermentation and aging processes have been used in several cultures for millennia. This know-how still in practice in several countries of the Armenian highland is gaining worldwide in curiosity, popularity, and interest. Ceramic pots are famous among traditional winemakers for their benefits such as temperature regulation, natural cooling system, favorable oxygen exchange, and impact on pH, which are different from those of stainless steel, wood barrels, or concrete.

Despite a 5000-years-old history of the use of clay-ceramic vessels (amongst other in Armenia), there is only few scientific regard on the impact on wine quality. To approach this subject, it is necessary to recourse to many analytical techniques and we only report some results obtained by ICP-AES and proton NMR relaxometry on a model wine.

ICP-AES is used to identify the migration of elements from the ceramic to the model wine. The results of the elemental analysis of the model wine in contact with ceramics over time, showed that a large number of elements, were transferred from the ceramic to the model wine with different migration behaviors. The noticeable amount of migrating iron attracted attention.

NMR relaxometry is used to follow in situ, the migration of paramagnetic elements (like iron), reduction of iron, but also the consumption of dioxygen in the model wine in contact with the ceramic. It is also shown that coated ceramic (e. g. with beeswax; a traditional Armenian method) can drastically limit chemical exchange.



Analysis of the Proton Spin–Lattice Relaxation in Wine and Hydroalcoholic Solutions

Philippe R. Bodart¹ · Aymerick Batlogg¹ · Eric Ferret¹ · Adam Rachocki² · Magdalena Knapkiewicz² · Syuzanna Esayan^{1,3} · Nelli Hovhannisyan⁴ · Thomas Karbowski¹ · Régis D. Gougeon⁵

Received: 25 March 2021 / Accepted: 9 August 2021 / Published online: 6 September 2021
© The Author(s), under exclusive licence to Springer Science+Business Media, LLC, part of Springer Nature 2021

Abstract

NMR relaxometry is a powerful analytical method that can easily be applied to wine. Proton spin–lattice nuclear magnetic relaxation dispersion profiles of wines have revealed a signature dominated by paramagnetic manganese relaxation. However, manganese is a relatively scarce element in wine. With this study focusing on model wines, we analyse the impact of four factors: alcohol by volume (ABV), dissolved dioxygen, tartaric acid, and pH on the relaxation time, but important issues concerning high ABV systems are also discussed. Dissolved dioxygen concentration increases strongly with ABV, and paramagnetic O₂ can contribute significantly to the relaxation process. Moreover, ABV modifies the viscosity and also impacts the relaxation mechanisms. In contrast, the organic acid and the pH do not show a significant effect. Analysis of the profiles recorded for distinct ABVs confirms the influence of the viscosity.

Keywords Wine · Relaxation · NMR · Viscosity · Oxygen

Introduction

Fast field cycling (FFC) NMR relaxometry is a low-field NMR technique that allows measuring the longitudinal, or spin–lattice relaxation time (T_1), as a function of the magnetic field strength, over a wide range of frequencies (from a few kilohertz to tens of megahertz), corresponding to T_1 values of the order of seconds to a fraction of a millisecond. The experimental data are displayed in the form of a nuclear magnetic relaxation dispersion (NMRD) profile, where the relaxation rate ($R_1 = 1/T_1$) is reported as a function of the

Larmor frequency of the observed nuclei. Generally, the benefit of exploring the nuclear spin–lattice relaxation rate over a large range of frequencies is to isolate typical NMRD features associated with different molecular dynamics. Varying the static magnetic field (B_0) changes the Larmor pulsation ($\omega = \gamma B_0$, where γ is the gyromagnetic ratio of the observed nuclei) and therefore the time and length scales of the fluctuations responsible for the nuclear spin–lattice relaxation rate R_1 (Kimmich 2013; Kruk 2007, 2016). It is possible to record NMRD profiles of almost any material, including solids, liquids, or colloids. In food science, FFC NMR has been applied to seeds (Rachocki et al. 2012), oil (Conte et al. 2011, 2010; Rachocki and Tritt-Goc 2014), fruits (Capitani et al. 2014; Conte et al. 2009; Lo Scalzo et al. 2016), cocoa butter (Ladd-Parada et al. 2019), starch (Tavares et al. 2019), bread (Curti et al. 2011), honey (Cimo' and Conte 2015; Płowaś-Korus et al. 2018), eggs and meat (Bajd et al. 2016; Laghi et al. 2005; Uguz et al. 2019), cheese (Conte et al. 2020; Godefroy et al. 2003; Kruk et al. 2021), gelatin-based soft candies (Pocan et al. 2021a, b), and for quality and anti-fraud controls (Baroni et al. 2009). In recent communication, NMR relaxometry has proven to be a promising in situ tool for revealing fingerprints in wine that could be used for wine control (Bodart et al. 2020). Manganese has been shown to be the dominant relaxation agent in wines and

✉ Philippe R. Bodart
philippe.bodart@u-bourgogne.fr

¹ UMR PAM A02.102, Univ. Bourgogne Franche-Comté, Agrosup Dijon, 1 Esplanade Erasme, 21000 Dijon, France

² Institute of Molecular Physics, Polish Academy of Sciences, M. Smoluchowskiego 17, 60-179 Poznań, Poland

³ Research Institute of Biology, Yerevan State University, 1 Alex Manoogian Str., Yerevan, Armenia

⁴ Department of Ecology and Nature Protection, Yerevan State University, 1 Alex Manoogian Str, Yerevan, Armenia

⁵ UMR PAM A02.102, Univ. Bourgogne Franche-Comté, Institut Universitaire de la Vigne et du Vin, 1, Esplanade Erasme, 21000 Dijon, France

a fine quantification of this element, down to a few of $\mu\text{g/L}$ can be achieved. However, wine is a very complex system with tens of thousands of components (Jeandet et al. 2015), and we report here on model wines the additional impacts of several physicochemical factors on the proton spin–lattice relaxation rate. The model wines studied are mixtures of water, ethanol, tartaric acid, oxygen, and manganese. The effect of manganese concentration on the proton spin–lattice relaxation of wines was discussed in a previous communication (Bodart et al. 2020) and is not further detailed here. However, for comparison purposes, relaxation rates of some model wines or solutions with manganese are reported.

Materials and Methods

Sample Preparation

The model wines and solutions were prepared from ultrapure water (VWR), ethanol (Sigma-Aldrich $\geq 99.9\%$), and L-tartaric acid (Sigma-Aldrich $\geq 99.7\%$). $\text{MnSO}_4 \cdot x\text{H}_2\text{O}$ (Sigma-Aldrich $\geq 99.99\%$) was heated at $450\text{ }^\circ\text{C}$ for 14 h to remove the residual water (Krepelka and Rejha 1931; Sinha et al. 1987). The laboratory glassware was cleaned three times with Milli-Q water and ultrapure water prior to the preparation of the model wines. Samples are referenced as follows: E12ta5Mn1.2 represents a model wine composed of 12% in volume of ethanol and contains 5 g/L of tartaric acid and 1.2 mg/L of Mn^{2+} ions. Consistently, WMn1.2 is a water solution containing 1.2 mg/L of Mn^{2+} and no tartaric acid. In order to probe the impact of the addition of tartaric acid, independently of any pH effect, the pH of the solutions was adjusted with HCl to 2.3, 3.5, and 3.4 for E12taMn1.2, E12ta, and Wta, respectively. The uncertainty on manganese concentration in E12ta5Mn5.8 and E60ta5Mn5.7 is estimated to be 0.1 mg/L.

Viscosity Measurement

The kinematic viscosities were measured at $25\text{ }^\circ\text{C}$ using an Ostwald viscometer (SI Analytics) and a water bath to control the temperature. Dynamic viscosities were calculated as the product of the measured kinematic viscosity and the density of the hydroalcoholic solutions. The measurements were repeated four times and the calculated standard deviations ($<0.3\%$) fall within drawn symbols. If not specified otherwise, viscosities discussed in the text correspond to values at $25\text{ }^\circ\text{C}$.

Oxygen Measurement

Dissolved O_2 concentrations were measured by chemiluminescence using PreSens PST3 oxygen sensors (PreSens

GmbH, Regensburg, Germany), with a detection range between 0 and 45 mg/L. The samples placed in 10-mm NMR tubes were first N_2 -degassed and sealed. Prior to measurement, NMR tubes were opened, briefly exposed to air (to allow for atmospheric dioxygen penetrating the headspace), closed, and left 2 h at $25\text{ }^\circ\text{C}$ for gas absorption equilibrium. Dioxygen concentration was measured before and after the relaxation experiment. The cycle was repeated several times until atmospheric equilibrium was gradually reached in the samples.

Low-Field NMR

Low-field NMR experiments were recorded at $25\text{ }^\circ\text{C}$ on a minispec mq20 (Bruker) operating at 19.65 MHz. For each acquisition, four scans were collected. Longitudinal relaxation times were measured with an inversion recovery pulse sequence. For model wines with low ABV ($<20\%$), the relaxation curves can be approximated with good accuracy to a single exponential decrease, but for high ABV, bi-exponential curves are observed. If not specified otherwise, experiments were carried out at equilibrium and normal atmospheric dioxygen pressure. The measurements were repeated at least four times; the calculated standard deviations of the relaxation rates were within drawn points.

Field Cycling NMR Relaxometry

A field cycling relaxometer from Stellar company (Mede, Italy) with a magnetic field, covering the proton Larmor frequencies from 0.001 to 40 MHz, was used to record the proton spin–lattice relaxation profiles (Anoardo et al. 2001; Kimmich and Anoardo 2004; Noack 1986). The spectrometer switches the magnetic field from a polarising field (B_{pol}), corresponding to a proton Larmor frequency of 24 MHz, to a field of interest (B_{rel}) for a variable relaxation period (τ). After each τ delay, the B_{rel} field is switched to a proton Larmor frequency of 16 MHz corresponding to the acquisition field (B_{acqu}) at which a $\pi/2$ pulse allows for magnetisation detection. The measurements were carried out at a temperature of $25\text{ }^\circ\text{C}$. Four scans were recorded, with $\pi/2$ pulses of 10 μs , field-switching time of 3 ms, spectrometer dead time of 18 μs , and spectral width of 1.25 MHz. Points number 5 to 50 of fids were summed to produce the relaxation curves. The decay/recovery curves at each B_{rel} value were fitted, using a single exponential function. The R_1 uncertainties resulting from the exponential fit of the relaxation curves are reported in Fig. 5 (for most points, uncertainties were smaller than the size of the drawn symbols).

Results and Discussion

Effect of Ethanol Concentration

For historical and practical reasons, winegrowers and oenologists measure the alcoholic strength of wines in terms of alcohol by volume (ABV) at 20 °C. It is defined as:

$$ABV = \frac{V_{ethanol}}{V_{wine}} \quad (1)$$

however, volumes are temperature dependent and the ABV varies with temperature (e.g. ABV increases from 12.4 to 12.5% when the temperature increases from 20 to 25 °C). Alcoholic strength is simpler handled when defined as a weight ratio (ABW):

$$ABW = \frac{W_{ethanol}}{W_{wine}} \quad (2)$$

or with the molar fraction of water (or ethanol) in the wine:

$$X_{water} = \frac{n_{water}}{n_{water} + n_{ethanol}} \quad (3)$$

where n_{water} ($n_{ethanol}$) represents the number of moles of water (ethanol). The alcoholic strength can vary significantly in alcoholic beverages, from 0 to 0.09% ABV (natural fruit juice) to more than 90% in rectified spirits. According to the International Organisation of Vine and Wine (OIV) (“International Code of Oenological Practices” 2020), “Wine results exclusively from the partial or complete alcoholic fermentation of fresh grapes, whether crushed or not or of grape must. Its actual alcohol content shall not be less than 8.5% vol.” A maximal limit is not reported, but above 20%,

spirituous beverages generally result from distillation. Hereafter, the term wine refers to the OIV definition.

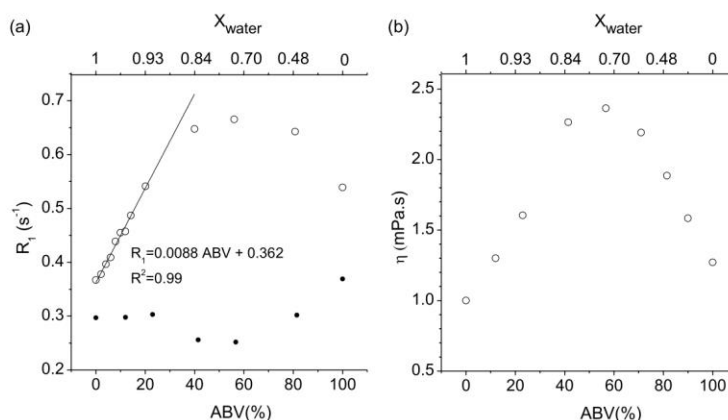
The proton spin–lattice relaxation rates dependency of ethanol solutions from pure water (ABV = 0%) to pure ethanol (ABV = 100%) are reported in Fig. 1a.

The relaxation rate varies strongly with ABV. This variation can be reasonably approximated by a linear relation up to 20% but large deviations appear when the ABV is above 40%. This is to be put in perspective with the variation of the solution viscosity (Fig. 1b). The same trend is observed on both curves with a maximum ABV value of around 60%.

The measured viscosity reported in Fig. 1b fully agrees with the literature data (Jora et al. 2017; Song and Peng 2008). Many semi-theoretical and empirical models have been presented to predict the viscosity of an ideal binary solution (Dey et al. 2008; McAllister 1960; Mehrotra et al. 1996). However, in a highly non-ideal solution (like methanol, ethanol, and propanol solutions), there is a strong interaction between the alcohol and water molecules in the solution and the modelling is not straightforward (Shirota and Castner 2000; Song and Peng 2008). When the amount of ethanol is low, because of the hydrophobic nature of the hydrocarbon chain of ethanol molecules, ethanol acts as a surfactant and forms micelles (Song and Peng 2008). Near the micelles’ surface, water molecules tend to spatially organise themselves by forming a hydration shell with a higher density and viscosity than in the bulk.

As the number of clusters formed of hydrated ethanol micelles increases, the viscosity of the mixture increases. This picture holds up to $ABV \cong 60\%$ ($X_{water} \cong 0.7$). Above 60% for ABV, as the amount of ethanol continues to increase, the overall interaction between ethanol and water molecules decreases, the solution tends towards pure ethanol and its viscosity decreases consistently (Onori 1996).

Fig. 1 **a** Open circles (○) represent the proton spin–lattice relaxation rate at 19.65 MHz and 25 °C of hydroalcoholic solutions versus ABV and X_{water} . Filled circles (●) correspond to the ratio of the relaxation rate of the hydroalcoholic solution corrected by the dioxygen contribution over the viscosity (i.e. R_1^* ratio, see below in the text); **b** open circles (○) represent the dynamic viscosity of the hydroalcoholic solution, measured at 25 °C, versus ABV and X_{water}



From a physical point of view, the mixtures are composed of two major distinct populations of a proton with distinct relaxation times: (i) the exchangeable OH proton from water and ethanol and (ii) the proton from the carbon chain of ethanol. This is an additional complication for the exploitation of relaxometry data. However, for model wines (12% ABV, i.e. 9.64 ABV) (“International Alcoholometric Tables” 1975), a simple calculation shows that the number of exchangeable hydroxyls represents 91% of the proton in the mixture, and in a first approximation, it could be considered the only population (at 20% ABV, the exchangeable OH represents 85% of the total proton present in the mixture).

From a NMR relaxation theory point of view, the spin–lattice relaxation rate can be correlated to the viscosity of the sample. In simple diamagnetic liquids, the relaxation rate is described by two contributions related to intramolecular and intermolecular interactions in the nuclear spin system. In the static magnetic field, the rotation of the molecules is the main source of modulation in time of the intramolecular interactions. Intermolecular interactions are also sensitive to molecular rotations but translational dynamics is usually considered the principal source of time modulation. Consequently, the overall relaxation rate can in general be expressed as the sum of the two main contributions:

$$R_1 = R_1^{\text{intra}} + R_1^{\text{inter}} = R_1^{\text{intra,rot}} + (R_1^{\text{inter,rot}} + R_1^{\text{inter,trans}}) \cong R_1^{\text{rot}} + R_1^{\text{trans}} \quad (4)$$

The simplest description of the rotational relaxation mechanism results from the stochastic fluctuations of dipolar interactions between pairs of protons of the same molecule. In the extreme narrowing limit, ($\omega\tau_R \ll 1$), the relaxation rate caused by rotational dynamics of the molecules can be written in the case of a two-spin system as follows (Abragam 2006; Kimmich 2013; Kruk 2016):

$$R_1^{\text{rot}} = \frac{3}{2} \left(\frac{\mu_o \gamma^2 \hbar}{4\pi r^3} \right)^2 \tau_R \quad (5)$$

where μ_o is the vacuum permeability, r the distance between the two nuclei within the molecules, and τ_R the rotational correlation time. Using the Stokes–Einstein relation (Abragam 2006; Korb et al. 2015):

$$\tau_R = \frac{4\pi a^3 \eta}{3KT} \quad (6)$$

where a is the radius of rotating molecules, η the dynamic viscosity, and K and T the Boltzmann constant and temperature, respectively, Eq. (5) can be written as:

$$R_1^{\text{rot}} = 2\pi \left(\frac{\mu_o \gamma^2 \hbar}{4\pi r^3} \right)^2 \frac{a^3 \eta}{KT} \quad (7)$$

Always in the extreme narrowing limit, assuming the force-free hard-sphere model in which two translating molecules are represented by two hard spheres of radius a that cannot interpenetrate, the translational motion is given by (Abragam 2006):

$$R_1^{\text{trans}} = \frac{\pi}{5} \left(\frac{\mu_o \gamma^2 \hbar}{4\pi r^3} \right)^2 \frac{N}{aD} = \frac{6\pi^2}{5} \left(\frac{\mu_o \gamma^2 \hbar}{4\pi r^3} \right)^2 N \frac{\eta}{KT} \quad (8)$$

where N is the spin density per unit volume and D is the self-diffusion coefficient, which can be expressed as $D = KT/6\pi a\eta$ (Stokes formula for translational diffusion).

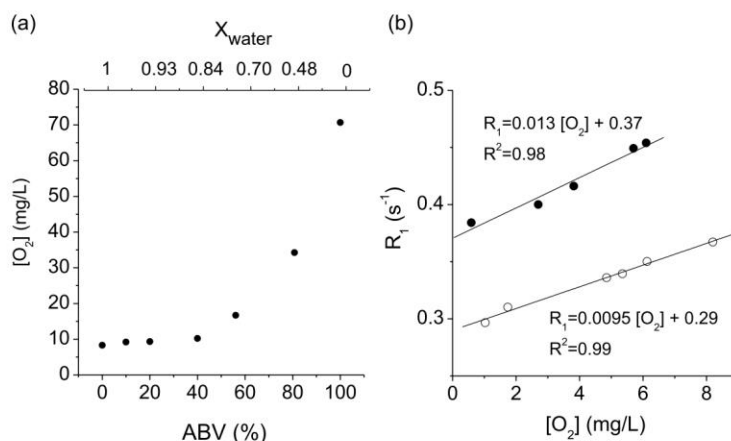
The crude equations [Eqs. (7) and (8)] suggest that if viscosity governs the evolution of the relaxation, the ratio R_1/η should be constant. However, to calculate such a ratio, it is necessary to subtract all other relaxation mechanisms that have a significant impact on the overall relaxation rate of the solution. The paramagnetic relaxation due to dissolved dioxygen in the solution cannot be neglected. For water, its contribution to R_1 is calculated to be 0.08 s^{-1} (see below). Figure 1a (filled circles) shows the variation of the ratio of the relaxation rate of alcoholic solution corrected from paramagnetic dioxygen (in pure water) by the solution viscosity ($R_1^* = (R_1 - 0.08)/\eta$) versus the alcoholic strength of the solution. Despite the crudeness of the above approximations, it is gratifying to observe that the variation of R_1^* is less pronounced than that of R_1 . This is all the more true as one gets closer to pure water, which confirms that the observed variation of relaxation rate of the alcoholic solution as a function of ABV is likely governed by the variation of the viscosity of the solution. When ABV increases, R_1^* is no longer constant for two reasons: (i) the dissolved dioxygen contribution strongly increases with ABV since more dioxygen is dissolved (Fig. 2a), the dioxygen correction on R_1 is no longer valid and should be adjusted for each point. (ii) As ABV increases, the amount of protons of the carbon chain (C–H) of ethanol, with respect to the total quantity of proton in the ethanol solution (OH and C–H) increases in the mixture and their contribution to the relaxation becomes more and more significant.

Effect of Dissolved Oxygen Concentration

It is well known that because of its paramagnetic nature, dissolved dioxygen directly impacts the relaxation rate of water (Hausser and Noack 1965).

The measured dissolved dioxygen concentrations at the atmospheric equilibrium of hydroalcoholic solutions are reported in Fig. 2a; the results agree very well with the literature (Shchukarev and Tolmacheva 1968) and are consistent with few measurements realised on wine (Moutounet and Mazauric 2001). At high ABV, the dissolved dioxygen concentration becomes very important. The proton

Fig. 2 **a** Atmospheric equilibrium dissolved dioxygen concentration in hydroalcoholic solutions at 25 °C versus ABV and water molar fraction X_{water} **b** Proton spin–lattice relaxation rate at 19.65 MHz and 25 °C versus the dissolved dioxygen concentration in water (○) and 12% ABV hydroalcoholic solution (●, E12)



relaxation rate is strongly affected by the paramagnetic O_2 and increased, contributing to the more pronounced asymmetry of the curve of Fig. 1a (relaxation rate vs. ABV) with respect to Fig. 1b curve (viscosity vs. ABV). The variation of the proton spin–lattice relaxation rate versus the concentration of dissolved dioxygen for water and hydroalcoholic solution (12% ABV) is reported in Fig. 2b. A linear correlation is observed in both cases. The measured correlation for water agrees very well with the correlation reported in the literature ($R_1 = 0.284 + 0.0088[O_2]$) (Franks 1972). The intercept value (0.29 s^{-1}) is the relaxation rate of dioxygen-free water, which leads to a T_1 value of 3.5 s in good agreement with reported data (3.57 s at 25 °C) (Abragam 2006; Franks 1972). Dioxygen contribution can then be measured as the difference between the relaxation rates of water at equilibrium in the atmosphere (0.36 s^{-1}) and when degassed (0.29 s^{-1}). The slope of the linear relationship of E12 hydroalcoholic solution is reasonably close to that of water. For the E12 solution, the relaxation rate at the intercept is 0.37 s^{-1} , and there is a difference of 0.08 s^{-1} with the intercept for water solutions (Fig. 2b). Under atmospheric conditions, the difference between the relaxation rates of water and hydroalcoholic solution (12% ABV) is about 0.1 s^{-1} . This means that the amount of dissolved dioxygen in water and ethanol solutions is comparable, and the difference in relaxation times is mainly due to the physical properties of the solutions (their viscosity). It is worth noting that this is a particular case for ABV ~ 12%, at lower and higher ABV, wine and water do not have comparable Ostwald coefficient, and the amount of dissolved oxygen can vary significantly between water and wine (Moutounet and Mazaurec 2001; Schlapfer et al. 1949; Tokunaga 1975).

Effect of Tartaric Acid Concentration

The most abundant acid in wine (tartaric acid) was chosen to model the impact on the proton relaxation rate (Fig. 3).

Figure 3 reveals that varying the level of tartaric acid has very little impact on the measured relaxation rate of hydroalcoholic solutions. In order to separate the effect of pH from other tartaric acid adjunction effects, measurements were performed at fixed pH values. The maximum variation

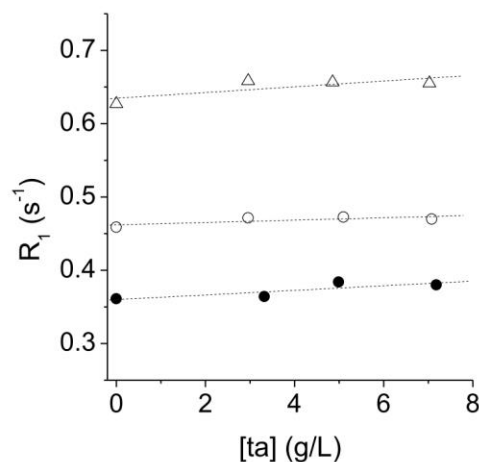


Fig. 3 Proton spin–lattice relaxation rate at 19.65 MHz and 25 °C of water (●, Wta), hydroalcoholic solution (○, E12ta), and model wine containing 1.2 mg/L of manganese (Δ, E12taMn1.2) versus tartaric acid concentration. For each solution, the pH was fixed to 2.3, 3.5, and 3.4 for E12taMn1.2, E12ta, and Wta, respectively

observed is below 3.5%. For water and E12 solutions, when the tartaric acid concentration increases from 0 to 7 g/L, the Jones–Dole equation shows a nearly linear increase in viscosity of only 3% at 30 °C (Parmar et al. 2004). In close agreement, the measured viscosities in E12 at 25 °C show a 1.3% linear increase in the same domain (Fig. 1S in Supplementary Information). In fact, in E12ta5, the molar concentration of tartaric acid is 1.6% that of ethanol; it is therefore not surprising that in the observed range of tartaric acid concentration ([0–7] g/L), the relaxation rate hardly shows a variation. We may expect the contribution of organic acids to the viscosity of wine to be small and it should barely infer the relaxation rate.

Effect of pH

Most wines have a pH between 3 and 4, with white wines being often more acidic than reds. The proton spin–lattice relaxation rates of various solutions containing water, tartaric acid, ethanol, and manganese over wide pH ranges are reported in Fig. 4.

In pure water, albeit spin–spin relaxation rate (R_2) shows a dependency on pH, R_1 is not affected (Meiboom et al. 1957), and for all reported solutions, the same trend is confirmed, without a significant impact of pH on relaxation. The maximum observed variation is 3% of the average value, which is certainly within the limits of experimental error. In wine, the pH variation is less than the range covered in

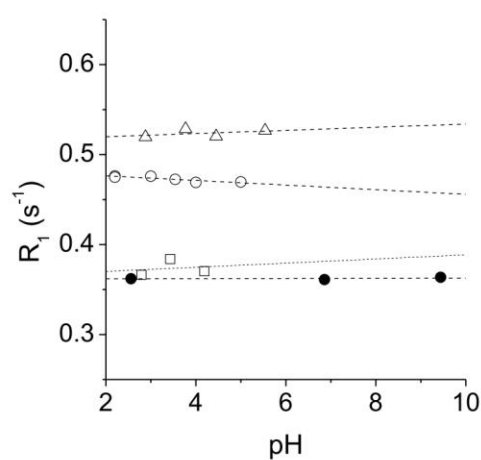


Fig. 4 Proton spin–lattice relaxation rates at 19.65 MHz and 25 °C of water (●), tartaric acid solutions (□, Wta5), hydroalcoholic solution (○, E12ta5), and manganese solutions (Δ, WMn1.2) versus pH values

Fig. 4, and the pH impact on wine relaxation rate could be considered insignificant.

NMRD Profiles

From the above-reported data, ABV has the strongest impact on the relaxation rate of wines. Figure 5 reports the NMRD profiles in two very distinct cases: E12ta5Mn5.8 and E60ta5Mn5.7, containing 12% and 60% ABV, respectively.

An interpretation of these NMRD profiles can be accomplished by using the Solomon–Bloembergen–Morgan equation: (Bertini et al. 2005; Bloembergen and Morgan 1961; Koenig and Brown 1984; Pell et al. 2018; Solomon 1955)

$$R_1 = R_0 + R_D + R_C \quad (9)$$

where R_0 is the diamagnetic contribution. The paramagnetic relaxation is decomposed in two contributions: (i) the dipolar (R_D), modelled by considering that the unpaired electrons are localised at the centre of the paramagnetic ion. The relaxation is then described by an interaction between an electronic point and a nuclear point dipole

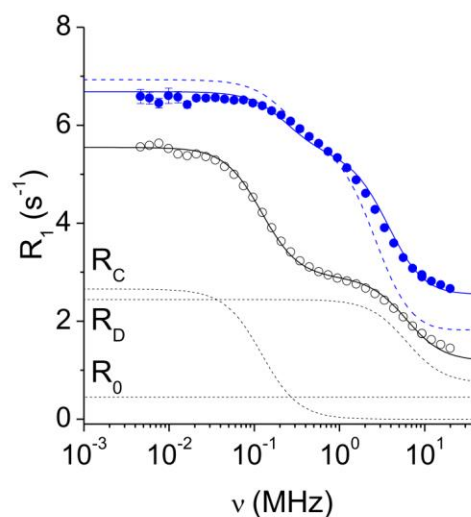


Fig. 5 Proton spin–lattice NMRD profiles of E12ta5Mn5.8 (○) and E60ta5Mn5.7 (●) recorded at 25 °C. Dotted black lines are R_0 , R_D , and R_C contributions; continuous black line is a refinement of E12ta5Mn5.8 relaxation rate. The upper dotted blue line is an illustrative calculation of the effect of the electron-thermal bath interaction ($\tau_{S0} = 10^{-9}$ s, $\tau_v = 810^{-12}$ s, and $\tau_R = 10^{-10}$ s, at 15 °C, (Bertini et al. 1993)), the continuous blue line is obtained with $\tau_{S0} = 10^{-9}$ s, $\tau_v = 810^{-12}$ s, and $\tau_R = 0.6910^{-10}$ s. In both calculations, τ_M is set to 10^{-4} s, ($\tau_R \ll \tau_M \ll T_1$)

(Solomon mechanism). (ii) The contact (R_C) contribution (fermi-contact interaction) arises from delocalization of the electronic wave function of the paramagnetic nuclei to the physical location of I-nuclei (Bloembergen mechanism). In the case of a two-spin system, these contributions are expressed as:

$$R_D = \frac{2}{15} \left(\frac{\mu_0}{4\pi} \right)^2 \frac{S(S+1)(\gamma_I \gamma_S \hbar)^2}{r_{IS}^6} \left[\frac{7\tau_D}{1 + (\omega_S \tau_D)^2} + \frac{3\tau_D}{1 + (\omega_I \tau_D)^2} \right] \quad (10)$$

and

$$R_C = \frac{2A^2 S(S+1)}{3\hbar^2} \left[\frac{\tau_C}{1 + (\omega_S \tau_C)^2} \right] \quad (11)$$

where A is the scalar coupling constant of the spin-exchange interaction between nucleus and electron, S is the electron spin number of the paramagnetic ion, γ_I , ω_I , and γ_S , ω_S are the proton and electron gyromagnetic ratio and Larmor pulsation, respectively, r_{IS} is the electron-nucleus distance, and τ_C and τ_D are the correlation times.

E12ta5Mn5.8 shows a dispersion of R_1 at ~ 0.1 MHz assigned to the contact contribution, whilst the dispersion for the dipolar coupling occurs at ~ 8 MHz. The refinement of the E12ta5Mn5.8 profile gives correlation times ($\tau_C = 1.98 \cdot 10^{-9}$ s and $\tau_D = 3.97 \cdot 10^{-11}$ s) in good agreement with previous measurements (Bodart et al. 2020). The calculated manganese concentration gives a satisfactory concentration of 5.5 ± 0.2 mg/L for a model wine with a given Mn concentration of 5.8 ± 0.1 mg/L. The situation is very different in the case of E60ta5Mn5.7 where dipolar and contact dispersions cannot be distinguished. This can be attributed to the dependence of the electronic correlation time on the magnetic field induced by a modulation of the quadratic zero-field splitting (Banci et al. 1985; Bloembergen and Morgan 1961; Hausser and Noack 1964; Rubinstein et al. 1971):

$$\frac{1}{\tau_D} = \frac{1}{\tau_S} + \frac{1}{\tau_R} + \frac{1}{\tau_M} \quad (12)$$

$$\frac{1}{\tau_C} = \frac{1}{\tau_S} + \frac{1}{\tau_M} \quad (13)$$

with

$$\frac{1}{\tau_S} = \frac{1}{5\tau_{S0}} \left[\frac{1}{1 + (\omega_S \tau_v)^2} + \frac{4}{1 + 4(\omega_S \tau_v)^2} \right] \quad (14)$$

where τ_M is the chemical exchange time (time of residence of the water molecules in the hydration shell of the paramagnetic nuclei), τ_R and τ_S the rotational and electronic

correlation time, respectively, τ_{S0} the electronic correlation time at zero field, and τ_v the correlation time that describes the spin-lattice time-dependent interactions.

A simplistic analysis of the high-frequency domain of Fig. 5 shows that the turnover point occurs at about 3 and 1.5 MHz for E12ta5Mn5.8 and E60ta5Mn5.7, respectively. If we assume that τ_R is dominating the dipolar paramagnetic correlation time τ_D (Eq. (12), $\tau_R \ll \tau_S, \tau_M$), then since the rotational correlation time is proportional to the viscosity (6), the viscosity of E60ta5Mn5.7 is expected to be twice that of E12ta5Mn5.8, which is in good agreement with Fig. 1b. An increase in viscosity is expected to slow down the dynamics, decrease the chemical exchange time τ_M of water, and increase the rotational correlation time τ_R . However, the modulation of the zero-field splitting (either through rotation of a static zero-field splitting is present or through induction of transient zero-field splitting by collision with solvent molecules) may also depend heavily on the viscosity of the solvent. These mechanisms have been discussed in detail for paramagnetic ions in ethylene glycol and hexaqua Mn^{2+} in water-glycerol mixtures at different temperatures (Banci et al. 1985; Bertini et al. 1993). They have shown that if the viscosity of the solution remains low (up to 20% glycerol, corresponding to a viscosity of ~ 2.1 mPa.s at 15 °C (Segur and Oberstar 1951)), the zero-field splitting has a moderate effect on the profile and the dipolar and contact dispersion remain discernible. However, at 35% glycerol ($\eta \sim 3$ mPa.s at 15 °C), the singularities are barely distinguishable.

Because of the increasing number of parameters to adjust when τ_S varies with the magnetic field, a refinement of the E60ta5Mn5.7 profile would require a multi-profile fitting with points at higher magnetic fields and recorded at various viscosities and temperatures. Moreover, other factors could also be considered: water not being the only source of protons, the substitution of water by ethanol or tartaric acid in the hydration sphere of manganese, and outer-sphere contribution (Bertini et al. 1993). Nevertheless, for illustrative purposes, Fig. 5 (top dotted blue line) reproduces the calculated NMRD profile of a solution with 35% glycerol at 15 °C ($\eta \sim 3$ mPa.s) (Bertini et al. 1993). The profile is similar to that of E60ta5Mn5.7 for which the viscosity is comparable ($\eta = 2.4$ mPa.s). The calculated profile can be adjusted by eye (continuous blue line) to the data with a slight decrease of τ_R , which is physically satisfactory since our data are recorded at higher temperature (25 °C) where a smaller rotational correlation time would be expected.

High viscosity wines could therefore lead to complex profiles masking the manganese signature (Bodart et al. 2020). To make this point concrete, the viscosity of various wines collected in the literature is reported in Fig. 6.

It appears that dry wines have rather low viscosity and show moderate variation. In consequence, the interpretation

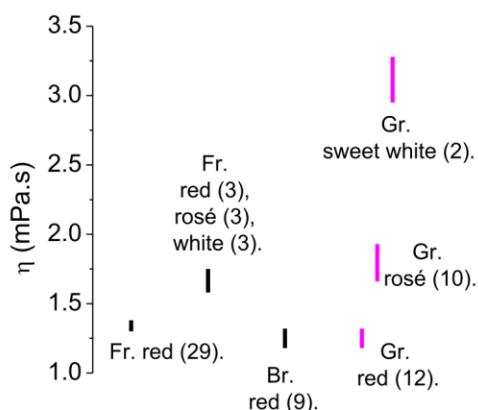


Fig. 6 Viscosity domains of various wines. Labels indicate the country, the type, and in brackets, the number of wines measured. (fr. red (29)) corresponds to 29 red wines of the same grape variety (Loire Valley Cabernet Franc) elaborated with a standard protocol but coming from two distinct areas, Anjou and Touraine (Siret et al. 2010); (Fr. red (3), rosé (3), and white (3)) reports 9 wines of 2 vintages from Loire Valley selected according to their typicity and probable differences in terms of viscosity and texture (Siret et al. 2008). (Br. Red (9)) is for 9 types of Brazilian dry red wines from different cultivars and produced by different wineries (Neto et al. 2015). Twenty-four different Greek wines (Yanniotis et al. 2007) of 2 vintages (in fuchsia) are also reported but the measurement was done at 16 °C whilst they were done at 23 and 26 °C for French and Brazilian wines, respectively

of relaxation time of most of these wines could be achieved with ease. However, when the viscosity increases (≥ 2 mPa.s) the viscosity impact significantly the profiles and it becomes rapidly less straightforward to analyse relaxation times unless the measurement is performed at sufficiently high temperature to decrease the viscosity effect.

Conclusion

An important viscosity of the wine can clearly complicate the interpretation of NMRD profiles and relaxation times, (e.g. precluding the determination of the manganese concentration by NMR relaxometry (Bodart et al. 2020)). However, the literature shows that a rather low and narrow range of viscosity (particularly for red and dry white wines) characterises wines and the relaxation times could be interpreted with ease. As the alcoholic strength increases (e.g. in distilled alcohols), the situation is less straightforward. (i) The amount of dissolved dioxygen strongly increases and has to be taken into account; (ii) the viscosity increases and relaxation mechanisms are further complicated; (iii) two main sources of proton may have to be considered simultaneously:

exchangeable hydroxyl groups of water and ethanol, and methyl and methylene groups of ethanol. The two last points being likely the more challenging aspect to handle.

Supplementary Information The online version contains supplementary material available at <https://doi.org/10.1007/s12161-021-02118-w>.

Acknowledgements The authors are grateful to COST Action CA15209 European Network on NMR Relaxometry (EURELAX). P.B. is thankful for the attentive reading of the manuscript by a referee and for his comment if τ_R is governing the relaxation in Eq. 12.

Author Contribution The manuscript was written through the contributions of all authors. All authors have given approval to the final version of the manuscript. Philippe R. Bodart: conceptualization, methodology, formal analysis, and writing the manuscript; Aymeric Batlogg: performing the experiments, formal analysis; Eric Ferret: formal analysis; Adam Rachocki: performing the experiments, formal analysis, and resources; Magdalena Knapkiewicz: performing the experiments; Syuzanna Esayan: performing the experiments; Nelli Hovhannissyan: formal analysis; Thomas Karbowski: formal analysis and securing funds; Régis D. Gougeon: writing the manuscript and securing funds.

Availability of Data and Material Upon request.

Code Availability Not applicable.

Declarations

Ethics Approval This article does not contain any studies with human or animal subjects.

Consent to Participate Not applicable.

Consent for Publication Not applicable.

Competing Interests The authors declare no competing interests.

References

- Abraham A (2006) The principles of nuclear magnetism Reprinted The international series of monographs on physics. Oxford Univ. Press, Oxford
- Anoardo E, Galli G, Ferrante G (2001) Fast-field-cycling NMR: applications and instrumentation. *Appl Magn Reson* 20:365–404
- Bajd F, Gradišek A, Apih T, Serša I (2016) Dry-cured ham tissue characterization by fast field cycling NMR relaxometry and quantitative magnetization transfer: FFC/qMT-NMR study of dry-cured hams. *Magn Reson Chem* 54:827–834. <https://doi.org/10.1002/mrc.4462>
- Banci L, Bertini I, Luchinat C (1985) ¹H NMRD studies of solutions of paramagnetic metal ions in ethyleneglycol. *Inorg Chim Acta* 100:173–181. [https://doi.org/10.1016/S0020-1693\(00\)88305-X](https://doi.org/10.1016/S0020-1693(00)88305-X)
- Baroni S, Consonni R, Ferrante G, Aime S (2009) Relaxometric studies for food characterization: the case of balsamic and traditional balsamic vinegars. *J Agric Food Chem* 57:3028–3032. <https://doi.org/10.1021/jf803727d>
- Bertini I, Briganti F, Xia Z, Luchinat C (1993) Nuclear magnetic relaxation dispersion studies of hexaaquo Mn(II) ions in water-glycerol mixtures. *J Magn Reson Ser A* 101:198–201

- Bertini I, Luchinat C, Parigi G (2005) ¹H NMRD profiles of paramagnetic complexes and metalloproteins. In: *Advances in Inorganic Chemistry*. Elsevier, pp 105–172. [https://doi.org/10.1016/S0898-8838\(05\)57003-X](https://doi.org/10.1016/S0898-8838(05)57003-X)
- Bloembergen N, Morgan LO (1961) Proton relaxation times in paramagnetic solutions. effects of electron spin relaxation. *J Chem Phys* 34:842–850. <https://doi.org/10.1063/1.1731684>
- Bodart PR, Rachocki A, Tritt-Goc J, Michalke B, Schmitt-Kopplin P, Karbowiak T, Gougeon RD (2020) Quantification of manganese ions in wine by NMR relaxometry. *Talanta* 209:120561. <https://doi.org/10.1016/j.talanta.2019.120561>
- Capitani D, Sobolev AP, Delfini M, Vista S, Antiochia R, Proietti N, Bubici S, Ferrante G, Carradori S, Salvador FRD, Mannina L (2014) NMR methodologies in the analysis of blueberries: general. *Electrophoresis* 35:1615–1626. <https://doi.org/10.1002/elps.201300629>
- Cimo G, Conte P (2015) Conformational redistribution of honey components following different storage conditions. *Int J Spectrosc* 2015:1–7. <https://doi.org/10.1155/2015/354327>
- Conte P, Bubici S, Palazzolo E, Alonzo G (2009) Solid-state ¹H-NMR relaxation properties of the fruit of a wild relative of eggplant at different proton Larmor frequencies. *Spectrosc Lett* 42:235–239. <https://doi.org/10.1080/00387010902895038>
- Conte P, Maccotta A, Pasquale CD, Alonzo G (2010) Supramolecular organization of triglycerides in extra-virgin olive oils as assessed by NMR relaxometry. *Fresenius Environ Bull* 19:6
- Conte P, Mineo V, Bubici S, De Pasquale C, Aboud F, Maccotta A, Planeta D, Alonzo G (2011) Dynamics of pistachio oils by proton nuclear magnetic resonance relaxation dispersion. *Anal Bioanal Chem* 400:1443–1450. <https://doi.org/10.1007/s00216-011-4904-8>
- Conte P, Cinquanta L, Lo Meo P, Mazza F, Micalizzi A, Corona O (2020) Fast field cycling NMR relaxometry as a tool to monitor Parmigiano Reggiano cheese ripening. *Food Res Int* 109845. <https://doi.org/10.1016/j.foodres.2020.109845>
- Curti E, Bubici S, Carini E, Baroni S, Vittadini E (2011) Water molecular dynamics during bread staling by nuclear magnetic resonance. *LWT Food Sci Technol* 44:854–859. <https://doi.org/10.1016/j.lwt.2010.11.021>
- Dey R, Singh AK, Pandey JD (2008) A temperature dependent viscometric study of binary liquid mixtures. *J Mol Liq* 137:88–91. <https://doi.org/10.1016/j.molliq.2007.03.010>
- Franks F (ed) (1972) *The physics and physical chemistry of water*. Springer: New York. <https://doi.org/10.1007/978-1-4684-8334-5>
- Godefroy S, Korb J-P, Creamer LK, Watkinson PJ, Callaghan PT (2003) Probing protein hydration and aging of food materials by the magnetic field dependence of proton spin-lattice relaxation times. *J Colloid Interface Sci* 267:337–342. [https://doi.org/10.1016/S0021-9797\(03\)00589-7](https://doi.org/10.1016/S0021-9797(03)00589-7)
- Hausser R, Noack F (1964) Kernmagnetische relaxation und korrelation in zwei-spin-systemen. *Z Angew Phys* 182:93–110. <https://doi.org/10.1007/BF01387090>
- Hausser R, Noack F (1965) Kernmagnetische relaxation und korrelation im system wasser - Sauerstoff. *Zeitschrift Für Naturforschung A* 20:1668–1675. <https://doi.org/10.1515/zna-1965-1220>
- International Alcoholometric Tables [WWW Document], 1975. URL https://www.oiml.org/fr/files/pdf_r/r022-f75.pdf. Accessed 2.23.21
- International Code of Oenological Practices [WWW Document], 2020. The International Organisation of Vine and Wine. URL <http://www.oiv.int/fr/normes-et-documents-techniques/pratiques-%C5%93nologiques/code-international-des-pratiques-%C5%93nologiques>. Accessed 11.23.20
- Jeandet P, Heinzmann SS, Roullier-Gall C, Cilindre C, Aron A, Deville MA, Moritz F, Karbowiak T, Demarville D, Brun C, Moreau F, Michalke B, Liger-Belair G, Witting M, Lucio M, Steyer D, Gougeon RD, Schmitt-Kopplin P (2015) Chemical messages in 170-year-old champagne bottles from the Baltic Sea: revealing tastes from the past. *Proc Natl Acad Sci* 112:5893–5898. <https://doi.org/10.1073/pnas.1500783112>
- Jora MZ, Cardoso MVC, Sabadini E (2017) Correlation between viscosity, diffusion coefficient and spin-spin relaxation rate in ¹H NMR of water-alcohols solutions. *J Mol Liq* 238:341–346. <https://doi.org/10.1016/j.molliq.2017.05.006>
- Kimmich R (2013) *NMR tomography, diffusometry, relaxometry*. Springer, Berlin
- Kimmich R, Anardo E (2004) Field-cycling NMR relaxometry. *Prog Nucl Magn Reson Spectrosc* 44:257–320. <https://doi.org/10.1016/j.pnmrs.2004.03.002>
- Koenig SH, Brown RD (1984) Relaxation of solvent protons by paramagnetic ions and its dependence on magnetic field and chemical environment: implications for NMR imaging. *Magn Reson Med* 1:478–495. <https://doi.org/10.1002/mrm.1910010407>
- Korb J-P, Vorapalawut N, Nicot B, Bryant RG (2015) Relation and correlation between NMR relaxation times, diffusion coefficients, and viscosity of heavy crude oils. *J Phys Chem C* 119:24439–24446. <https://doi.org/10.1021/acs.jpcc.5b07510>
- Krepelka JH, Rejha B (1931) The anhydrous and the hydrated manganese sulphates.- part I. *Collect Czech Chem Commun* 3:517–535
- Kruk D (2007) Theory of evolution and relaxation of multi-spin systems: application to nuclear magnetic resonance and electron spin resonance. arima publ, Bury St Edmunds
- Kruk D (2016) *Understanding spin dynamics*. Pan Stanford Publishing, Singapore
- Kruk D, Florek-Wojciechowska M, Masiewicz E, Oztop M, Ploch-Jankowska A, Duda P, Wilczynski S (2021) Water mobility in cheese by means of nuclear magnetic resonance relaxometry. *J Food Eng* 110483. <https://doi.org/10.1016/j.jfoodeng.2021.110483>
- Ladd-Parada M, Povey MJ, Vieira J, Ries ME (2019) Fast field cycling NMR relaxometry studies of molten and cooled cocoa butter. *Mol Phys* 117:1020–1027. <https://doi.org/10.1080/00268976.2018.1508784>
- Laghi L, Cremonini MA, Placucci G, Sykora S, Wright K, Hills B (2005) A proton NMR relaxation study of hen egg quality. *Magn Reson Imaging* 23:501–510. <https://doi.org/10.1016/j.mri.2004.12.003>
- Lo Scalzo R, Fibiani M, Francesc G, D'Alessandro A, Rotino GL, Conte P, Mennella G (2016) Cooking influence on physico-chemical fruit characteristics of eggplant (*Solanum melongena* L.). *Food Chem* 194:835–842. <https://doi.org/10.1016/j.foodchem.2015.08.063>
- McAllister RA (1960) The viscosity of liquid mixtures. *AIChE J* 6:427–431. <https://doi.org/10.1002/aic.690060316>
- Mehrotra AK, Monnery WD, Svrcek WY (1996) A review of practical calculation methods for the viscosity of liquid hydrocarbons and their mixtures. *Fluid Phase Equilib* 117:344–355. [https://doi.org/10.1016/0378-3812\(95\)02971-0](https://doi.org/10.1016/0378-3812(95)02971-0)
- Meiboom S, Luz Z, Gill D (1957) Proton relaxation in water. *J Chem Phys* 27:1411–1412. <https://doi.org/10.1063/1.1744015>
- Moutounet M, Mazauric J-P (2001) L'oxygène dissous dans les vins. *Revue Française d'Œnologie* 12–15
- Neto FS, de Castilhos MB, Telis VR, Telis-Romero J (2015) Effect of ethanol, dry extract and reducing sugars on density and viscosity of Brazilian red wines. *J Sci Food Agric* 95:1421–1427. <https://doi.org/10.1002/jsfa.6835>

- Noack F (1986) NMR field-cycling spectroscopy: principles and applications. *Prog Nucl Magn Reson Spectrosc* 18:171–276. [https://doi.org/10.1016/0079-6565\(86\)80004-8](https://doi.org/10.1016/0079-6565(86)80004-8)
- Onori G (1996) Dynamical and structural properties of water/alcohol mixtures. *J Mol Liq* 69:161–181. [https://doi.org/10.1016/0167-7322\(96\)85154-3](https://doi.org/10.1016/0167-7322(96)85154-3)
- Parmar ML, Awasthi RK, Guleria MK (2004) A study on viscosities of citric acid and tartaric acid in water and binary aqueous mixtures of ethanol at different temperatures. *Indian J Chem* 43A:41–44
- Pell AJ, Pintacuda G, Grey CP (2018) Paramagnetic NMR in solution and the solid state. *Prog Nucl Magn Reson Spectrosc*. <https://doi.org/10.1016/j.pnmrs.2018.05.001>
- Płowaś-Korus I, Masiewicz E, Szwengiel A, Rachocki A, Baranowska HM, Medycki W (2018) A novel method of recognizing liquefied honey. *Food Chem* 245:885–889. <https://doi.org/10.1016/j.foodchem.2017.11.087>
- Pocan P, Ilhan E, Florek-Wojciechowska M, Masiewicz E, Kruk D, Oztop MH (2021a) Exploring the water mobility in gelatin based soft candies by means of fast field cycling (FFC) nuclear magnetic resonance relaxometry. *J Food Eng* 294:110422. <https://doi.org/10.1016/j.jfoodeng.2020.110422>
- Pocan P, Knapkiewicz M, Rachocki A, Oztop MH (2021b) Detection of authenticity and quality of the Turkish delights (lokum) by means of conventional and fast field cycling nuclear magnetic resonance relaxometry. *J Agric Food Chem*. <https://doi.org/10.1021/acs.jafc.1c00943>
- Rachocki A, Latanowicz L, Tritt-Goc J (2012) Dynamic processes and chemical composition of *Lepidium sativum* seeds determined by means of field-cycling NMR relaxometry and NMR spectroscopy. *Anal Bioanal Chem* 404:3155–3164. <https://doi.org/10.1007/s00216-012-6409-5>
- Rachocki A, Tritt-Goc J (2014) Novel application of NMR relaxometry in studies of diffusion in virgin rape oil. *Food Chem* 152:94–99. <https://doi.org/10.1016/j.foodchem.2013.11.112>
- Rubinstein M, Baram A, Luz Z (1971) Electronic and nuclear relaxation in solutions of transition metal ions with spin $S=3/2$ and $5/2$. *Mol Phys* 20:67–80. <https://doi.org/10.1080/00268977100100081>
- Schlapfer P, Audikowski T, Bukowiecki A (1949) Untersuchungen über das maximale sauerstoffaufnahmevermögen organischer flüssigkeiten und die jodometrische Bestimmung des aufgenommenen Sauerstoffes. *Schweizer Arch Angew Wiss Tech* 15:299–307
- Segur JB, Oberstar HE (1951) Viscosity of glycerol and its aqueous solutions. *Ind Eng Chem* 43:2117–2120. <https://doi.org/10.1021/ie50501a040>
- Shchukarev SA, Tolmacheva TA (1968) Solubility of oxygen in ethanol ? Water mixtures. *J Struct Chem* 9:16–21. <https://doi.org/10.1007/BF00744018>
- Shirota H, Castner EW (2000) Solvation in highly nonideal solutions: a study of aqueous 1-propanol using the coumarin 153 probe. *J Chem Phys* 112:2367–2376. <https://doi.org/10.1063/1.480803>
- Sinha SG, Deshpande ND, Deshpande DA (1987) Dehydration of crystalline $MnSO_4 \cdot 4H_2O$. *Thermochim Acta* 113:95–104
- Siret R, Madieta E, Symonau R, Jourjon F (2008) Rheologic measurements of wine texture and viscosity. Correlations With Sensorial Analyses. [WWW Document]. REVUE INTERNET DE VITICULTURE ET OENOLOGIE. URL. https://www.infowine.com/fr/articles_techniques/mesures_rheologiques_de_la_texture_et_de_la_viscosite_des_vins_sc_6170.htm. Accessed 10 Jan 2021
- Siret R, Symoneaux R, Brossaud F, Forgerit V, Mongondry P (2010) Viscosité et texture des vins : comparaison de méthodes rhéologiques et sensorielles. *Rev Suisse Vitic Arboric Hortic* 42:314–320
- Solomon I (1955) Relaxation processes in a system of two spins. *Phys Rev* 99:559–565. <https://doi.org/10.1103/PhysRev.99.559>
- Song S, Peng C (2008) Viscosities of binary and ternary mixtures of water, alcohol, acetone, and hexane. *J Dispersion Sci Technol* 29:1367–1372. <https://doi.org/10.1080/01932690802313006>
- Tavares MIB, da Silva EO, Silva PSRC, Sebastião PJ (2019) The use of fast field cycling to evaluate the time domain relaxation of starches from tropical fruit seeds. *Mol Phys* 117:1028–1033. <https://doi.org/10.1080/00268976.2018.1540803>
- Tokunaga J (1975) Solubilities of oxygen, nitrogen, and carbon dioxide in aqueous alcohol solutions. *J Chem Eng Data* 20:41–46. <https://doi.org/10.1021/je60064a025>
- Uguz SS, Ozvural EB, Beira MJ, Oztop MH, Sebastião PJ (2019) Use of NMR relaxometry to identify frankfurters of different meat sources. *Mol Phys* 117:1015–1019. <https://doi.org/10.1080/00268976.2018.1542162>
- Yanniotis S, Kotseridis G, Orfanidou A, Petraki A (2007) Effect of ethanol, dry extract and glycerol on the viscosity of wine. *J Food Eng* 81:399–403. <https://doi.org/10.1016/j.jfoodeng.2006.11.014>

Publisher's Note Springer Nature remains neutral with regard to jurisdictional claims in published maps and institutional affiliations.